NASA CR-72410

RECIRCULATION AND INGESTION CHARACTERISTICS OF A LARGE-SCALE VTOL LIFT ENGINE POD

by

Gordon R. Hall

prepared for

NATIONAL AERONAUTICS AND SPACE ADMINISTRATION

CONTRACT NAS3-10498

NORTHROP NORAIR

Requests for copies of this report should be referred to

NASA
Scientific and Technical Information Facility
P.O. Box 33

College Park, MD 20740

COPY NO. 21

N69-12232

NASA CR-72410

TOPICAL REPORT

RECIRCULATION AND INGESTION CHARACTERISTICS OF A LARGE-SCALE VTOL LIFT ENGINE POD

by

Gordon R. Hall

prepared for

NATIONAL AERONAUTICS AND SPACE ADMINISTRATION

August 1968

CONTRACT NAS3-10498

Technical Management
NASA Lewis Research Center
Cleveland, Ohio
James J. Watt, Project Manager
Nestor Clough, Research Advisor

REVISIONS

CHANGE	DATE	ENGINEER	PAGES AFFECTED OR REMARKS
"A"	3-7-69	Gordon R. Hall	iii, iv, v

NORTHROP NORAIR
3901 W. Broadway
Hawthorne, California 90250

TABLE OF CONTENTS

LIST OF FIGURES

FIGURE NO.		PAGE NO.
31	EFFECT OF ANGLE OF ATTACK ON INGESTION CHARACTERISTICS	75
32	TYPICAL INLET PROXIMITY TEMPERATURE HISTORY	76
33	VARIATION IN GROUND PLANE TEMPERATURE WITH R/D AND H/D FOR TWO ENGINE OPERATION	77
34	VARIATION IN GROUND PLANE TEMPERATURE WITH R/D AND H/D FOR SINGLE ENGINE OPERATION	79
35	EFFECT OF H/D AND WIND ON GROUND JET DYNAMIC PRESSURE FOR TWO ENGINE OPERATION	81
36	EFFECT OF WIND ON GROUND PLANE TEMPERATURE FOR TWO ENGINE OPERATION	82
37	EFFECT OF WIND ON GROUND PLANE TEMPERATURE FOR SINGLE ENGINE OPERATION	84
38	EFFECT OF ANGLE OF ATTACK ON GROUND PLANE TEMPERATURE FOR TWO ENGINE OPERATION	86
39	EFFECT OF ANGLE OF ATTACK ON GROUND JET DYNAMIC PRESSURE FOR TWO ENGINE OPERATION	88
40	POD UNDERSURFACE PRESSURE DISTRIBUTION AT LOW WIND CONDITIONS	89
41	POD UNDERSURFACE PRESSURE DISTRIBUTION AT HIGH WIND CONDITIONS	90
42	POD UNDERSURFACE PRESSURE DISTRIBUTION AT ANGLE OF ATTACK	91
43	EFFECT OF H/D, WIND, AND ANGLE OF ATTACK ON POD UNDERSURFACE PRESSURE	92
44	EFFECT OF ANGLE OF ATTACK ON POD PEAK PRESSURE AMPLITUDE AND LOCATION	93
45	POD UNDERSURFACE PRESSURE DISTRIBUTION FOR SINGLE JET OPERATION	45
46	NOMINAL FLOW STRUCTURE BETWEEN GROUND PLANE AND POD FOR TWO ENGINE OPERATION	95

NOMENCLATURE

D	nozzle diameter
H	height of pod undersurface from ground plane
P_n	nozzle stagnation pressure
P_∞	ambient pressure
ΔP	pod pressure minus ambient pressure
q	jet stagnation pressure minus ambient pressure
q_n	nozzle stagnation pressure minus ambient pressure
R_x, R_{xy}, R_y	lateral distance from origin along X, XY, and Y axes, respectively, (Figure 6)
S	engine centerline spacing
T	inlet temperature indicated by an individual thermocouple
$\bar{T}$	spatial average inlet temperature, $\bar{T} = \frac{1}{n}\sum_{i=1}^{n} T_i$, where n equals number of inlet thermocouples
$\Delta\bar{T}$	spatial average inlet temperature increment above ambient, $\bar{T} - T_\infty$
$\dot{\bar{T}}$	rate of rise of spatial average inlet temperature
ϵ_{max}	maximum temperature distortion within inlet, $T_{max} - T_{min}$
ϵ_{rms}	RMS temperature distortion about spatial average inlet temperature, $\sqrt{\frac{1}{n}\sum_{i=1}^{n}(T_i - \bar{T})^2}$, where n equals the number of inlet thermocouples
Z	vertical distance from nozzle exit (Figure 9)
α	pod angle of attack (Figure 2)

Subscripts

1	engine #1
4	engine #4
c.l.	engine centerline

Superscript

$\wedge$	time average (applied to temperature indices)

COPY NO 25

NASA CR-72410

TOPICAL REPORT

RECIRCULATION AND INGESTION CHARACTERISTICS OF A LARGE-SCALE VTOL LIFT ENGINE POD

by

Gordon R. Hall

prepared for

NATIONAL AERONAUTICS AND SPACE ADMINISTRATION

August 1968

CONTRACT NAS3-10498

Technical Management
NASA Lewis Research Center
Cleveland, Ohio
James J. Watt, Project Manager
Nestor Clough, Research Advisor

NORTHROP NORAIR
3901 W. Broadway
Hawthorne, California 90250

PREFACE

This report documents the results of an investigation of recirculation and ingestion characteristics of a full-scale engine pod. The investigation was performed as a part of NASA Contract NAS 3-10498 entitled "Concepts to Reduce Hot Gas Ingestion in VTOL Lift Engines." This contract provides for a series of exploratory experimental investigations, the primary objective being to determine the relative effectiveness and merits of various exhaust gas ingestion control concepts for potential application to VTOL aircraft. A secondary objective of the contract is to establish modeling criteria and test techniques required for proper simulation of full-scale recirculation and ingestion phenomena in small-scale investigations.

The investigations are to be conducted with a small-scale engine pod model in which both dual turbojet and turbofan engines are simulated, and with a geometrically similar full-scale engine pod containing dual turbojet engines. For the small-scale tests, both open nozzles and jet suppression nozzles (which promote rapid mixing of the exhaust gases with the external ambient environment) are to be tested at turbojet exhaust conditions. Testing at turbofan exhaust conditions will be limited to an open nozzle configuration. Potential ingestion control concepts (which are limited to investigation in the small-scale tests) are to include: (1) devices located in the proximity of the engine inlet that deflect the upwash gases away from the inlet; and (2) ground surface configurations or devices which alter the impingement process of the exhaust jet on the ground so that the potential upwash is laterally removed from the engine proximity.

Prior to performing the small-scale investigation of various ingestion control concepts, it is essential that the validity of small-scale investigations of recirculation and ingestion phenomena be demonstrated more thoroughly than has been demonstrated heretofore. Thus, full-scale and small-scale tests with geometrically similar configurations (and similarly instrumented) are to be conducted prior to the investigation of ingestion control concepts, with detailed comparison of the results from these tests providing information necessary to assess the extent of reproducibility of full-scale recirculation phenomena in small-scale.

Considering the contract objectives, a separate report documenting only the results of the full-scale investigation would not be required. However, in performing the full-scale investigation, new approaches to instrumentation, test techniques, data reduction, and data analysis were taken. As a result, several new and interesting features of exhaust gas ingestion phenomena were found. Additionally, more comprehensive measurements of the ground jet flow and upwash flow were made than in previous full-scale investigations of recirculation phenomena. Accordingly, separate documentation of the full-scale results is warranted and provided herein.

TABLE OF CONTENTS

LIST OF FIGURES

FIGURE NO.		PAGE NO.
31	EFFECT OF ANGLE OF ATTACK ON INGESTION CHARACTERISTICS	71
32	TYPICAL INLET PROXIMITY TEMPERATURE HISTORY	72
33	VARIATION IN GROUND PLANE TEMPERATURE WITH R/D AND H/D FOR TWO ENGINE OPERATION	73
34	VARIATION IN GROUND PLANE TEMPERATURE WITH R/D AND H/D FOR SINGLE ENGINE OPERATION	75
35	EFFECT OF H/D AND WIND ON GROUND JET DYNAMIC PRESSURE FOR TWO ENGINE OPERATION	77
36	EFFECT OF WIND ON GROUND PLANE TEMPERATURE FOR TWO ENGINE OPERATION	78
37	EFFECT OF WIND ON GROUND PLANE TEMPERATURE FOR SINGLE ENGINE OPERATION	80
38	EFFECT OF ANGLE OF ATTACK ON GROUND PLANE TEMPERATURE FOR TWO ENGINE OPERATION	82
39	EFFECT OF ANGLE OF ATTACK ON GROUND JET DYNAMIC PRESSURE FOR TWO ENGINE OPERATION	84
40	POD UNDERSURFACE PRESSURE DISTRIBUTION AT LOW WIND CONDITIONS	85
41	POD UNDERSURFACE PRESSURE DISTRIBUTION AT HIGH WIND CONDITIONS	86
42	POD UNDERSURFACE PRESSURE DISTRIBUTION AT ANGLE OF ATTACK	87
43	EFFECT OF H/D, WIND, AND ANGLE OF ATTACK ON POD UNDERSURFACE PRESSURE	88
44	EFFECT OF ANGLE OF ATTACK ON POD PEAK PRESSURE AMPLITUDE AND LOCATION	89
45	POD UNDERSURFACE PRESSURE DISTRIBUTION FOR SINGLE JET OPERATION	90
46	NOMINAL FLOW STRUCTURE BETWEEN GROUND PLANE AND POD FOR TWO ENGINE OPERATION	91

NOMENCLATURE

D	nozzle diameter
H	height of pod undersurface from ground plane
P_n	nozzle stagnation pressure
P_∞	ambient pressure
ΔP	pod pressure minus ambient pressure
q	jet stagnation pressure minus ambient pressure
q_n	nozzle stagnation pressure minus ambient pressure
R_x, R_{xy}, R_y	lateral distance from origin along X, XY, and Y axes, respectively, (Figure 6)
S	engine centerline spacing
T	inlet temperature indicated by an individual thermocouple
$\overline{T}$	spatial average inlet temperature, $\overline{T} = \frac{1}{n}\sum_{i=1}^{n} T_i$, where n equals number of inlet thermocouples
$\Delta\overline{T}$	spatial average inlet temperature increment above ambient, $\overline{T} - T_\infty$
$\dot{\overline{T}}$	rate of rise of spatial average inlet temperature
ϵ_{max}	maximum temperature distortion within inlet, $T_{max} - T_{min}$
ϵ_{rms}	RMS temperature distortion about spatial average inlet temperature, $\sqrt{\frac{1}{n}\sum_{i=1}^{n}(T_i - \overline{T})^2}$, where n equals the number of inlet thermocouples
Z	vertical distance from nozzle exit (Figure 9)
α	pod angle of attack (Figure 2)

Subscripts

1	engine #1
4	engine #4
c.l.	engine centerline

Superscript

$\wedge$	time average (applied to temperature indices)

I. ABSTRACT

A full-scale investigation of the recirculation and ingestion characteristics of a model VTOL lift engine pod was conducted. Variables of the test included pod height above the ground plane, pod angle of attack, single engine/two engine operation, and wind speed. A new approach was taken to sensing, recording, reducing, and analyzing the inlet thermal environment. High response thermocouples were used to sense the inlet environment with the output recorded on magnetic tape. Some new characteristics of the instantaneous environment were thus revealed. Objective characterization of the environment, in the form of temperature indices describing both the dynamics and time average characteristics of the inlet temperature level, distortion, and rate of rise, was accomplished through a semi-statistical approach to data reduction and analysis with the aid of an analog computer. In addition to the usual parametric trends, spatial, temporal, and frequency distributions of the ingestion characteristics were determined. Comprehensive data are thus provided for subsequent correlations with data of a similar nature to be obtained under the same contract with a small-scale geometrically similar model. Other significant features of the investigation included closer control and measurement of exhaust jet alignment, and more comprehensive measurements of the ground jet flow and upwash flow than reported in previous large-scale investigations of recirculation and ingestion.

II. INTRODUCTION

Various phenomena associated with jet lift VTOL aircraft operating in ground proximity have drawn recent attention. Recirculation of exhaust gases about the aircraft resulting from interaction of the vertically directed lifting jets with the ground plane is one such phenomenon. Ingestion of the recirculating exhaust gases by the engines is of primary concern due to the rather strong effect that hot gas ingestion can have on engine performance. In particular, ingestion of hot exhaust gases by the engines results in thrust degradation which, in turn, reduces net lift capability and, generally, would introduce aircraft imbalance in hover. Additionally, high rates of inlet temperature rise and/or large temperature distortions across the inlet face can result in engine stall.

Ingestion of exhaust gases in large-scale jet lift VTOL models has been the subject of several recent investigations (e.g., References 1-5). These investigations have generally shown that the extent of exhaust gas ingestion is highly dependent upon the vehicle configuration and can, indeed, be a serious problem -- especially for split-engine configurations in which the wing location of the model relative to the propulsion system is ineffective in shielding the engine inlets from the recirculating upwash flow.

Perhaps the most salient feature of the results of References 1-5 is the nature of the inlet temperature field. In particular, for configurations in which significant ingestion occurred, the individual inlet temperature measurements were found to be of a highly transient, or sporadic nature, exhibiting characteristics of quasi-random phenomena. Upon detailed analyses, it was determined that the actual temperature transients (i.e., rate of rise and peaks levels) experienced were in most cases much more severe than the transients indicated, a result attributed to utilizing relatively slow responding temperature sensing elements within the engine inlets. Furthermore, attempts to really quantize the data of References 1-5 have been obscured due to its quasi-random character. That is, for an inlet continuously experiencing large temporal and spatial variations in temperature, the term "inlet temperature rise" becomes a rather nebulous quantity, being defined in different ways by different observers. Additionally, describing the ingestion characteristics of a particular configuration only in terms of "inlet temperature rise," even under a standardized definition, does not adequately describe the actual inlet thermal environment.

Quantizing data of the nature described above requires a statistical approach to data reduction and analysis which provides a series of indices yielding information about the temperature levels, spatial distortion, and transient character. At the same time, such an approach inherently provides objective characterization of the data (i.e., characterization which is independent of the observer).

Considering the above comments on previous large-scale investigations, a full-scale investigation of the recirculation and ingestion characteristics of a model VTOL lift engine pod was performed in which a new approach to temperature sensing, recording, reduction, and analysis was undertaken. Specifically, high response thermocouples were used to sense the transient inlet temperature environment. The output of these thermocouples was recorded on magnetic tape thereby providing raw data in a form which could be processed by an analog computer utilizing statistical approaches to data reduction and analysis. In addition to providing objective characterization of the effects of the parameters investigated in terms of various temperature indices, comprehensive reference data for both the dynamics and time-average characteristics of ingestion are provided for subsequent comparisons to data of a similar nature to be obtained in the same program from small-scale tests with a geometrically similar model, thereby allowing assessment of the extent of reproducibility of full-scale recirculation phenomena in small-scale.

Other significant features of the investigation included closer control (and measurement) of exhaust jet alignment than in prior large-scale investigations. This was prompted by the results of the small-scale investigation reported in Reference 6 (and later reported in greater detail in Reference 7) which showed high sensitivity of ingestion characteristics to relatively small perturbations in exhaust jet angle. In addition, more comprehensive measurements of the ground jet flow and upwash flow (fountain) were made than in previous large-scale recirculation investigations.

III. TEST FACILITY AND MODEL

The tests were performed at the NASA-Ames Research Center VTOL Ground Effects Test Facility (Figure 1). This facility is an outdoor complex designed to support powered VTOL models in static tests. The complex consists of a fixed 78' x 80' ground plane and a model support structure (Figure 2). The support structure is mechanized to provide variation of model height above the ground plane and angle of attack. Two trailers were located near the ground plane; one served as an office, the second accommodated instrumentation readout equipment and an engine control console.

The test vehicle investigated was the lift engine pod model shown in Figures 1 and 3. The pod was designed to accommodate four YJ-85 engines, although for the tests reported here only engines #1 and #4 were utilized. The selection of YJ-85 engines was based primarily upon availability considerations along with the wealth of experience obtained in utilizing these engines in other programs.

The spacing between engines #1 and #4, S, in terms of the 12.5 inch YJ-85 engine nozzle diameter, D, was S/D = 7.3. In terms of relative engine spacing, pod height, and pod width, the configuration investigated was designed to be geometrically similar (and similarly instrumented) to a small-scale engine pod which is also to be investigated as a part of the same contract, with direct comparison of the full-scale and small-scale results providing important information on scaling of recirculation phenomena.

Cover plates were provided for the inlet and exhaust ports located between engines #1 and #4. Hinged side panels were installed to allow for rapid ventilation of the engine bay in the event that overheating of critical engine components was experienced. An "engine heating" check run subsequently indicated that rapid ventilation of the engine bay was not required.

Alignment of the engine axes normal to the longitudinal axis of the pod was accomplished by rotation of the engines about the engine mounts via a turnbuckle mechanism attached to the tail pipes. This longitudinal alignment, which was considered to be critical based on the results of the small-scale investigation of Reference 6, was subsequently checked by measurements of the exhaust flows issuing from the nozzles.

The pod was mounted to the support struts by a horizontal support beam normal to the longitudinal axis of the pod and by a toggle mechanism located at the vehicle nose. The main support beam was located forward of engine #1 so as not to interfere with the upwash flow between the engines which is known to exist at the value of engine spacing investigated.

Configuration variables of the test included pod height (H/D = 2 to 8), angle of attack (α = -6° to +6°), and single engine/two engine operation.

IV. INSTRUMENTATION

1. Inlet Temperatures - The inlets to the compressor face of engines #1 and #4 were instrumented with twelve and twenty-four, respectively, high response bare bead thermocouples. The locations and details of the construction of these thermocouples are shown in Figure 4. The locations of the thermocouples were selected to represent equal flow areas.

The sensing element of the thermocouples was fabricated from .003" chromel/alumel wire. Based on Reference 8, the time constant for the thermocouple/flow environment combination was approximately 18 m.s. (or in terms of response to a sinusoidal input signal, flat response within 10% up to a frequency of about 5 cps), assuming an ideal butt weld junction through which the local thermal mass is not increased above that of the parent wire. The twelve thermocouples of engine #1, and the twelve thermocouples in engine #4 with common locations to those of engine #1, were recorded on magnetic tape. The remaining twelve thermocouples of engine #4 were recorded on oscillograph.

The selection of the wire size of .003", the chromel/alumel junction material, and the general thermocouple construction concept (Figure 4) was based on simple endurance/reliability tests of various thermocouples conducted prior to the large-scale tests. The problem of thermocouple optimization to sense the highly transient thermal environment of the inlets during ingestion is critical. One is faced with compromise in the thermocouple response in order to maintain component reliability. The problem is to minimize the sensing element wire diameter in order to enhance response characteristics (i.e., time constant, $\tau \alpha d^{3/2}$), without serious compromise in the mechanical integrity of the element when installed in the relatively high acoustic, vibration, and velocity environment of an engine inlet. In addition, corrosion resistance of the sensing element materials becomes a critical factor as the wire diameter becomes small. For example, the pre-test thermocouple evaluation demonstrated that for wire sizes in the neighborhood of .003" and smaller, an iron/constantan sensing element was unacceptable due to excessive corrosion of the iron leg.

The thermocouple design used for the large-scale tests proved to be a satisfactory selection. The reliability was reasonably good while the response characteristics did not constitute a significant compromise of the test results: approximately 10% failure was experienced within the first two or three tests, probably due to faulty initial construction. These early failures were repaired, after which time the total additional failures for the remainder of the test program was approximately 10%. All of the failures observed resulted from breakage at the juncture of the .003" wire with the 30 gage support wire, rather than at the sensing element junction or along the span of the .003" wire (Figure 4).

2. Inlet Proximity Temperatures - Twelve high response bare bead thermocouples (identical in construction to those described above for use in the engine inlets) were cantilevered from the sides of the engine pod in the plane of the inlets (Figure 5). These thermocouples, which were recorded on oscillograph, were situated to measure the temperature (and longitudinal concentration) of the upwash flow between the engines.

3. Ground Plane Temperatures - Eleven bare bead iron/constantan thermocouples (24 gage) were located within the NE quadrant of the ground plane (Figure 6) to measure steady state temperatures of the ground jet flow near the ground plane surface. These thermocouples were mounted 2" above the ground plane and were recorded on oscillograph.

4. Ground Jet Pressures and Temperatures - Five vertical rakes were positioned in the NE quadrant of the ground plane (Figure 7a) to measure the ground jet pressure and temperature profiles. The rakes consisted of an array of total pressure probes, static pressure probes, and temperature probes as indicated in Figure 7b. The rake pressures were recorded on manometers and the rake temperatures were recorded on a strip recorder.

5. Engine Pod Pressures - Six pressure taps were installed on the lower surface of the pod along the longitudinal centerline (Figure 8). These pressure measurements, which were recorded on manometers, provided information on the strength and location of the upwash flow between the engines.

6. Engine Performance Measurements - Engine exhaust pressure and temperature, RPM, and compressor discharge pressures were measured with high response sensing elements and recorded on oscillograph. Engine exhaust temperature and RPM were also monitored at the engine control console.

7. External Wind - External wind speed, azimuth, and elevation were monitored prior to testing and recorded continuously on oscillograph during the tests.

The sensing instrument (MRI Vector Vane Wind System) was located at the NW corner of the ground plane and mounted approximately 16' above the ground plane (Figure 2).

V. PROCEDURE

JET ALIGNMENT

Prior to conducting the recirculation tests, "vertical" alignment of the exhaust jets in the fore-aft direction was undertaken. Following the small-scale results reported in Reference 6, it was assumed that the fore-aft alignment of jets would be a critical factor affecting ingestion level.

The jet alignment was determined by raising the leveled engine pod to the maximum height ($H/D \approx 10$), suspending a plumb line from the engine centerline, and positioning the centerprobe of a cruciform total pressure rake coincident with the plumb line at about 8 nozzle diameters below the nozzle exit (Figure 9). The engine in question was then started and brought to full power and the exhaust jet pressure profiles measured. The angle of the jet centerline was determined by the fore-aft and left-right displacement, δ (Figure 9), of the dynamic pressure profile peak from the cruciform rake centerprobe. Considering the tolerances in establishing δ by fairing the pressure profiles the accuracy in determining the jet centerline is estimated to be about $\pm 0.2°$.

Alignment of the jets in the fore-aft direction was accomplished by rotation of the engine about the engine mounts with a turnbuckle mechanism attached to the engine tail pipe. There was no provision for engine alignment in the left-right direction, again based on the small-scale results of Reference 6, which showed that ingestion was relatively insensitive to small jet angular change in the lateral direction. Based on the method defined above, the final angular deviations of the jet centerlines from vertical for the nominally zero angle of attack tests are given below.

TABLE 1 - EXHAUST JET ALIGNMENT

	FORE-AFT ALIGNMENT	LEFT-RIGHT ALIGNMENT
Engine #1	0.1° Forward	0.7° Right
Engine #4	0.5° Forward	0.6° Left

JET PRESSURE PROFILES

Having aligned the exhaust jets, dynamic pressure profiles (i.e., jet total pressure minus ambient pressure) of the jets were measured at various distances, Z, from the nozzle exit, again using the cruciform pressure rake shown schematically in Figure 9. Measurements were made at values of Z/D from approximately zero to eight, with the rake aligned such that the centerprobe was coincident with a plumb line suspended from the engine centerline. The nominal value of the engine tail pipe pressure ratio was $P_n/P_\infty = 1.8$. The dynamic pressure profiles obtained, q, non-dimensionalized with respect to the average value of the engine tail pipe dynamic pressure, q_n, are shown in Figures 10 to 13.

The depression in the dynamic pressure in the central region of the jet at the smaller values of Z/D is indicative of flow separation from the tail pipe centerbody. The data scatter at the smaller values of Z/D is the result of circumferential variations in tail pipe pressure. At the larger values of Z/D, the relatively localized effects of the tail pipe centerbody are not apparent, with the profiles resembling a distribution characteristic of the asymptotic profiles for a conventional open nozzle. Also at the larger values of Z/D, an offset of the dynamic pressure peak from the vertical (i.e., zero position on the abscissa) is generally observed. These offset values were used to determine the final alignment of the jets indicated in Table 1.

Figure 14 shows the variation in jet centerline dynamic pressure with distance from the nozzle exit for engines #1 and #4. For comparative purposes, the dynamic pressure decay for a 3" open nozzle supplied by a plenum (i.e., low initial turbulence level) is also shown. Reservoir conditions for the reference nozzle (Reference 9) were $T_n = 1200°F$ and $P_n/P_\infty = 2.0$. The effect of the engine tail pipe centerbodies is clearly apparent in Figure 14 at the smaller values of Z/D. At the larger values of Z/D, the rate of dynamic pressure decay is seen to be similar to that of the small-scale reference nozzle.

TEST PROCEDURE

Table 2 presents a complete list of the recirculation tests reported. Prior to conducting the tests of Table 2, external wind conditions were monitored until satisfactory conditions were attained. For the majority of the nominally "no wind" tests, wind conditions were less than 3 mph. For the "wind" tests, winds ranging from 10-20 mph were experienced. Once the desired wind condition was attained, engine #4 was started and brought to the nominal idle condition (viz., 50% RPM). For "single engine" tests, after stabilizing

TABLE 2. TEST CONDITIONS

Test No.	Engines Operating	Pod Height H/D	Angle of Attack α	Wind Condition Speed	Wind Condition Direction
1	#1 & #4	2	0	<4 MPH	N
2	↓	3	↓	↓	NW
3		4			NW
4*		↓			NW
5*					W
6**					SW
7**					SW
8***					W
9****					W
10		6			NW
11		8			N
12	#4	2	0	<4 MPH	N
13	↓	4	↓	↓	W
14		6			NW
15		8			NW
16	#1 & #4	2	0	12±2 MPH	NE
17	↓	4	↓	16±4 "	W
18		6		16±4 "	NE
19		8		16±4 "	N
20	#4	2	0	10±2 MPH	NE
21	↓	4	↓	14±4 "	N
22		6		16±4 "	NE
23		8		20±2 "	N
24	#1 & #4	2	+6	<4 MPH	N
25	↓	4	+6	↓	NW
26		↓	+3		N
27			+1		W
28			-1		W
29			-3		N
30			-6		NW
31		6	+6		NW
32		8	+6		N

* - Repeatability tests
** - Reduced power tests
*** - #4 engine max. power, #1 engine slowly increased from 50% RPM to max. power
**** - #1 engine max. power, #4 engine slowly increased from 50% RPM to max. power

engine #4 at the idle condition, data acquisition was initiated, followed by acceleration of the engine to "full power." The nominal "full power" engine setting for the tests was 98% (16,170 RPM).

For "two engine" tests, after stabilizing engine #4 at the idle condition, engine #1 was started and brought to idle condition, after which time data acquisition was initiated and the two engines were simultaneously accelerated to "full power." Although some sporadic ingestion usually occurred even at idle conditions for both engines operating, there was no problem in determining the reference value of inlet temperature in that there were always some easily identifiable periods of time during which some of the inlet thermocouples were obviously recording ambient temperature.

Generally, "two engine" tests, run at the same H/D and wind conditions as single engine tests, were conducted after the single engine tests without shut-down of engine #4: that is, the single engine test was terminated by return of engine #4 to the idle condition, after which time engine #1 was started. General heating of the ambient environment during a two-test series of this nature was checked during pre-test runs and found to be negligible.

The nominal period of data acquisition for the tests was 30 sec.

DATA REDUCTION

Due to the random, or sporadic, nature of the inlet thermal environment, special data reduction techniques oriented toward a statistical analysis approach were employed to characterize the data. First of all, the temperatures were sensed with high response thermocouples and recorded on magnetic tape. Having the raw data on magnetic tape, it was then possible to perform operations on the raw data using an analog computer. The analog computer provided various temperature indices which individually yield information on the inlet temperature levels, spatial distortion, and transient characteristics. Considering the apparent random nature of the raw data, an approach of this type is essential for objective characterization of the inlet thermal environment, in that a single index (e.g., inlet temperature rise) cannot adequately describe the actual thermal environment experienced. On the other hand, a series of indices, considered collectively, can provide all the essential information contained within the data.

For each of the tests of Table 2, the raw data were played back on oscillograph tapes. In addition, the following temperature indices were computed by an analog computer for each of the tests:

(1) The instantaneous spatial average of the n[1] individual temperatures within the inlet:

$$\overline{T}(t) = \frac{1}{n}\sum_{i=1}^{n} T_i(t)$$

(2) The cumulative time average of (1):
(i.e., space-time average of temperature to time t)

$$\hat{T}(t) = \frac{1}{t}\int_{o}^{t}\overline{T}(t)dt$$

(3) The instantaneous maximum temperature distortion within the inlet:

$$\epsilon_{max}(t) = T_{max}(t) - T_{min}(t)$$

(4) The cumulative time average of (3):
(i.e., time average of the maximum distortion)

$$\hat{\epsilon}_{max}(t) = \frac{1}{t}\int_{o}^{t}\epsilon_{max}(t)dt$$

(5) The instantaneous RMS temperature distortion about the mean value:

$$\epsilon_{rms}(t) = \sqrt{\frac{1}{n}\sum_{i=1}^{n}\left[T_i(t) - \overline{T}(t)\right]^2}$$

(6) The cumulative time average of (5):
(i.e., time average of RMS distortion)

$$\hat{\epsilon}_{rms}(t) = \frac{1}{t}\int_{o}^{t}\epsilon_{rms}(t)dt$$

---

[1] The nominal value of n was twelve. For many of the tests, however, all the thermocouples within the inlet were not operative so that n was reduced accordingly for purposes of data reduction.

(7) The instantaneous rate of rise of (1):

$$\dot{\overline{T}}(t) = \frac{d\overline{T}}{dt}$$

(8) The cumulative time average of the absolute value of (7): (i.e., time average of the absolute rate of rise of (1))

$$\left|\hat{\dot{\overline{T}}}(t)\right| = \frac{1}{t}\int_{0}^{t} \left|\dot{\overline{T}}(t)\right| dt$$

In addition to the raw data and the above defined temperature indices which were computed for each of the tests, a limited amount of extended data reduction and analysis, providing standardized statistical representations of the data, was performed for selected tests with the aid of an analog computer and frequency analysis equipment. These statistical representations include probability density plots and power spectral density plots for the temperature indices (1), (3), (5), and (7), as well as for samples of the raw temperature data. These plots provide the relative distribution of the data in question in the time domain and in the frequency domain, respectively.

Finally, the effect of thermocouple response, resulting from finite-mass thermocouples, was examined for selected data samples to determine if the recorded data were significantly attenuated below that of the actual environment. Following Reference 8, the actual temperature is related to the temperature indicated by the thermocouple through the following simple relation:

$$T_{act} = T_{ind} + \tau \dot{T}_{ind}$$

where τ is the thermocouple time constant (approximately 18 ms. for the current investigation). As can be seen from the above relation, the indicated temperature approaches the actual temperature as the thermocouple time constant and/or the temperature gradient becomes small. Using an analog computer, the actual temperature time history was computed for several samples of the spatial average inlet temperature ($\overline{T}$) and for several samples of the raw data (t).

VI. DISCUSSION

Table A-1 (Appendix) presents a complete list of the tests reported herein. The variables of the test include pod height above the ground plane (H/D), pod angle of attack (α), single engine/two engine operation, and wind condition. A set of reduced data for each of the tests is presented in the Appendix. Table A-1 also serves as an index for the data presented in the Appendix and provides summary information on the various time average ingestion characteristics for each test.

Substantial data (most of which are not included in the Appendix) are also included within the body of the report. These data serve to illustrate the various points of discussion which follow.

EXHAUST PRESSURE AND TEMPERATURE

A typical time history of the engine exhaust pressure and temperatures is shown in Figure 15. This recording is taken from Test 3 whose data are used extensively in subsequent discussions to illustrate specific points regarding ingestion characteristics.

The nominal "full power" engine setting for the tests was 98% (16,170 RPM). This value of power setting resulted in exhaust pressure ratios of about 1.8 and exhaust temperatures about 1100°F. The acceleration time of engine #4 from the nominal idle RPM of 50% to full power was found to be consistently slower (by about one second) than the acceleration time of engine #1. The time lag of about one second for engine #4 was found to be incurred during the initial phase of the acceleration transient in that a test conducted with an idle RPM of 60% for both engines showed considerably less lag, while a test conducted with an idle RPM of 70% showed simultaneous acceleration of the two engines to full power. The selection of 50% RPM as a nominal idle condition was based on the consideration of minimizing ingestion prior to engine acceleration.

Typically, when both engines were operating, ingestion was significant in one of the two engines, thereby resulting in a significant time-varying (due to the nature of the ingestion) reduction in exhaust pressure. For example, for the test of Figure 15, significant ingestion of exhaust gases was experienced by engine #1 resulting in thrust variations (based on exhaust pressure variation) of about 15%. On the other hand, the thrust level of engine #4, which experienced little ingestion, is seen to be essentially constant. Although ingestion was generally significant in one of the two engines during operation with two engines, no engine stalls were encountered during the course of the tests.

INGESTION CHARACTERISTICS

Raw Data

Figures 16 and 17 show raw inlet temperature data typical of two engine and single engine operation. These data have been traced directly from oscillograph tapes, the oscillograph tapes having been obtained by playback of the raw data from magnetic tapes. The test conditions of Figures 16 and 17 are H/D = 4, zero angle of attack, and low wind conditions (i.e., wind = 3 mph). The general character of the data, however, as discussed in the following paragraphs, is typical of other values of H/D, angle of attack, and wind conditions.

Two Engine Operation - For two engine operation, in which hot gas ingestion is dominated by the upwash flow resulting from mutual interaction of the two jets and the ground plane, several general characteristics of the data are immediately obvious. First of all, in reference to Figure 16, it is observed that beyond approximately the first five seconds (i.e., the time required to establish full power, see Figure 15), the thermal environment of engine #1 (Figure 16a) is significantly higher than ambient, while that of engine #4 (Figure 16b) is essentially ambient except for occasional temperature spikes. Secondly, the sporadic nature of the data, typical of the ingestion prone engine, is clearly evident for engine #1. Temperature spikes are observed which persist typically for a few tenths of a second, or less, and frequently reach levels in excess of 100°F above ambient. These temperature spikes, or pulses, are sometimes very local in nature as evidenced by simultaneous response of only very few thermocouples, while at other times they are observed to encompass a large section of the inlet as evidenced by simultaneous response of the majority of the thermocouples.

During time intervals between temperatures spikes, the temperature level indicated is typically ambient. In no case was a prolonged temperature rise observed which might be considered a "steady" temperature, rather than a series of closely space temperature pulses.

The "return to ambient" characteristic of the data of Figure 16 between closely spaced temperature pulses has not been observed (to the author's knowledge) in previously reported investigations on hot gas recirculation.

One explanation which might be advanced is that the configuration of the current investigation is more prone to such a phenomenon in that the path of the upwash gases is shorter and relatively unimpeded compared to that for configurations in which the upwash is blocked by a wing or other surface, the latter constituting the great majority of configurations of previous investigations. As a result, mixing of the upwash flow with the ambient environment is more thorough for configurations employing surfaces in the path of the upwash than for the configuration reported herein.

In some of the previous work (e.g., Reference 3), however, configurations much like that of the current investigation (i.e., wingless configurations or wing location such as not to block the upwash flow) were investigated. The inlet temperature data from these configurations, however, did not exhibit the (return to ambient) characteristic of the data presented herein.

Previous analysis of data samples for both wingless and winged configurations of Reference 3, performed by the author of this document and the author of Reference 10 in accord with the method indicated in Section V, showed that the inlet temperature recordings from Reference 3 were, in general, highly attenuated due to the relatively slow responding temperature sensing elements used in this (and most other previous) investigations. Furthermore, the "true" inlet temperature histories from these previous tests, as derived from the recorded temperature and corrected for thermocouple lag, were found to exhibit, or have a strong tendency to exhibit, the "return to ambient" characteristics observed in the current investigation.

In summary, it is concluded that the primary reason for the observed "return to ambient" characteristic in the current investigation, but not in previous investigations, is that the thermocouples used to sense the inlet thermal environment in the current investigation were considerably more responsive than those of previous investigations.

Thermocouple Response - It is appropriate at this point to comment on the fidelity of the thermocouples of the current investigation in following the actual temperature spikes experienced in the engine inlets. Several traces of the spatial average inlet temperature, $\overline{T}$, and of the individual inlet temperatures, T, were analyzed in the manner indicated previously in Section V. Typical results are shown in Figure 18.

A comparison of the indicated time histories of two raw data samples of T with estimates of the actual time histories is shown in Figures 18(a) and 18(b).

The samples are taken from Test 3. As can be seen, the indicated time histories are reasonably good representations of the "actual" time histories -- the most obvious difference being increased sharpness of the "actual" temperature spikes compared to the indicated temperature spikes, and the associated increase in amplitude of temperature fluctuations occurring at frequencies above about 10 cps.

Figure 18(c) shows a similar comparison for the spatial average inlet temperature, $\overline{T}$, also for Test 3. Due to the damping effect associated with the spatial averaging process, the indicated value of $\overline{T}$ follows the "actual" value even more closely than for the raw temperature data. Again, some increase in amplitude of temperature fluctuations occurring above frequencies of about 10 cps is observed.

Considering the relatively good agreement between the indicated temperatures and the "actual" temperatures as demonstrated in Figure 18, no attempt was made to correct the temperature data presented in this report for thermocouple lag (other than, of course, the data samples of Figure 18 which were corrected in order to determine whether or not correction of all the data was desirable).

Single Engine Operation - In contrast to the data of Figure 16 (typical of operation with two engines) are the data of Figure 17, which are typical of operation with a single engine at low wind conditions. For single engine operation at low wind conditions, the engine exhaust strikes the ground, spreads radially along the ground, and eventually rises as a result of buoyancy forces. The resulting ingestion level is low, with peak temperatures generally less than 5°F above ambient, although for the example of Figure 17 somewhat higher temperatures are indicated during the period of engine acceleration.

At high wind condition (i.e., wind 12-16 mph), ingestion was found to be somewhat more significant than at low wind condition for single engine operation. At high wind conditions, temperature pulses of about 10-15°F were frequently observed, persisting typically for periods of about one-half second. These temperature pulses were generally found to be distributed over the entire inlet rather than localized as for the case of two engine operation. The above results suggest an external flow field in which the wind interacts with the far field ground jet[1], blowing portions of it back within the influence of the engine inlet.

It should be pointed out, however, that due to the limited extent of the ground plane at the NASA Ames Test Facility, the resulting interaction of the wind with the far field ground jet may not be indicative of a larger ground plane. Specifically, the "ground plane" is raised approximately 1½ ft above earth level and extends about 40 nozzle diameters from the engine centerline. As a result, the ground jet separates at the edge of the ground plane, and as a free flow, thereby becomes considerably more susceptible to an interaction effect with the external wind than would be an attached ground jet.

Ingestion Prone Engine

As noted previously, with both engines operating, significant ingestion was generally experienced in one engine, but not in both engines. In reviewing the data, an interesting correlation of the ingestion prone engine with "steady state" exhaust pressure levels was found -- namely, it was found that when the exhaust pressure of engine #1 exceeded that of engine #4 by more than about ½ psi during time intervals when ingestion was not significant, engine #4 was generally the ingestion prone engine. On the other hand, when the exhaust pressure of engine #1 exceeded that of engine #4 by less than about ½ psi, or was less than engine #4, during time intervals in which ingestion was not significant, engine #1 was generally the ingestion prone engine. This correlation is illustrated in Figure 19 for the two-engine tests at zero angle of attack. The data include the results from six "repeatability" tests not listed in Table 2 in order to provide a more complete summary.

The bias in the data (i.e., neutral point at $P_{n1} - P_{n4} \approx \frac{1}{2}$psi) might quite possibly be attributed to irregularities in the ground plane contour in the region between engines #1 and #4. The ground plane structure in the region of the near flow field (i.e., high temperature environment) consisted of steel plates bolted to the basic ground plane. Detailed measurement of the contour, or buckling, of these plates in the region between the engines, indicated local slopes of 1-2 degrees. As will be discussed subsequently, angularity asymmetries in the configuration/ground plane combination can have appreciable effects on ingestion characteristics.

[1]Subsequent discussions will demonstrate that for the range of winds investigated, interaction of the wind with the near field ground jet (i.e., $R/D \lesssim 20$) is negligible.

The correlation of Figure 19 suggests that the upwash flow is highly sensitive to a bias in nozzle pressure in that the "steady state" (i.e., without ingestion) nozzle pressures were generally within 1 psi of each other. Once ingestion occurs, the nozzle pressure bias is further increased as the result of an engine feedback effect, typically resulting in frequent instantaneous pressure biases of 1-2 psi. That is, ingestion of hot gases by the engine with the lower "steady state" nozzle pressure results in a further reduction of nozzle pressure for that engine.

In terms of the upwash flow, the more energetic ground jet from the engine with the higher pressure biases the fountain (which originates in the jet interaction plane) in the direction of the engine with the lower pressure. The resulting upwash asymmetry is further amplified by the increased influence of the closer inlet on the upwash flow.

The high sensitivity of the upwash flow and ingestion characteristics to nozzle pressure bias suggested here is in general agreement with the small-scale findings of References 6 and 7. The small-scale results of References 6 and 7, however, indicated a more continuous shift in the ingestion level from one inlet to the other rather than the discontinuous nature of the ingestion observed herein (i.e., significant ingestion in one inlet or the other, but not in both). The above difference is attributed, at least in part, to the engine feedback effect which was, of course, not present in the small-scale tests. The engine feedback effect would tend to stabilize the upwash asymmetry in the direction of one engine or the other.

Tests 8 and 9 illustrate further the effect of nozzle pressure bias on ingestion. For Test 8, engine #4 was held at full power throughout the run while engine #1 was progressively increased to full power. For Test 9, engine #1 was held at full power throughout the run while engine #4 was progressively increased to full power. The results obtained for the two tests, which are presented in the Appendix, are self-consistent and are described below.

During the initial portion of the tests, in which large nozzle pressure biases existed, neither engine experienced significant ingestion (Figures A8-1, A8-2 and A9-1, A9-2. At large values of nozzle pressure bias, the high pressure jet passes around and beneath the low pressure jet (this flow structure is clearly illustrated by oil streak photographs of the small-scale tests reported in Reference 6). At the high nozzle pressure bias conditions no upwash is developed as evidenced by the ambient condition of the inlet proximity thermocouples (Figures A8-3 and A9-3).

The above condition prevails until the nozzle pressure bias decreases to a value of about 4 psi at which time significant ingestion of hot gases by the low pressure engine begins. At this point the upwash development begins as evidenced by temperature spikes on the inlet proximity thermocouples. The onset of significant ingestion at a nozzle pressure bias of about 4 psi is in excellent agreement with the small-scale results of References 6 and 7.

As the nozzle pressure bias is further reduced, ingestion of hot gases by the lower pressure engine increases (as do the temperature spikes on the inlet proximity thermocouples) until a nozzle pressure bias of about 2 psi is obtained. For nozzle pressure biases between zero and about 2 psi, the ingestion level would appear to be relatively constant. Note that although the steady state nozzle pressure ratios are essentially equal at the end of the run for the two engines, for both Tests 8 and 9, the ingestion prone engine remains the same throughout the run (viz., engine #1 for Test 8 and engine #4 for Test 9), illustrating the stabilizing effect of the engine feedback mechanism on the upwash.

Temperature Indices

Figures 20 and 21 present time histories of the spatial average inlet temperature ($\overline{T}$), the maximum temperature distortion within the inlet (ϵ_{max}), the RMS temperature distortion about the spatial average inlet temperature (ϵ_{rms}), and the rate of rise of the spatial average temperature ($\dot{\overline{T}}$), for engines #1 and #4, respectively, of Test 3[1]. Similar data are presented in the Appendix for each of the tests listed in Table 2. The data of Figures 20 and 21, which are typical time histories for two engine operation, are discussed here for illustrative purposes.

Figure 20 shows the data for the ingestion prone engine of Test 3 (engine #1). From the graph of $\overline{T}$, it is seen that the average inlet temperature is essentially ambient (with the exception of a few minor temperature pulses) prior to t = 5 sec (i.e., the time required to reach full power, Figure 15). Beyond t = 5 sec, significant oscillations in $\overline{T}$ are observed, reaching instantaneous levels approximately 50°F above ambient. From the rate of rise trace, it is seen that the oscillations in $\overline{T}$ result in values of $\dot{\overline{T}}$ up to about 1000°F/sec for the example shown.

[1] See Section V, "Data Reduction," for mathematical definition of the various temperature indices.

Since the temperature spikes observed in the raw data (Figure 16a) are generally localized, peak values of $\overline{T}$ are accordingly significantly less than the localized peak values of the temperature observed in the raw data. It follows, of course, that the averaging process also attenuates local temperature spikes of lesser amplitude -- the result being that $\overline{T}$, while still rather sporadic in nature, is considerably smoother than the individual temperature traces of the raw data.

Turning to the temperature distortion indices of Figure 20, ϵ_{max} and ϵ_{rms}, two observations are made. First of all, as one might expect, there appears to be a definite correlation between ϵ_{rms} and ϵ_{max}, the instantaneous value of ϵ_{rms} being about 1/3 that of ϵ_{max} (the 1/3 factor relation between ϵ_{rms} and ϵ_{max} is typical for all tests). Secondly, large values of distortion are frequently observed without significant increase in $\overline{T}$, again illustrating the local nature of the hot gas ingestion. This is particularly evident during the first 5 sec of the test prior to reaching full power. Even when the value of $\overline{T}$ is not significantly above ambient, the distortion is still high, further illustrating highly non-uniform temperature distributions across the inlet. Typically the instantaneous value of ϵ_{max} is several times the value of the spatial average temperature rise, $\overline{T}$.

Figure 21 presents similar data for the non-ingestion prone engine of Test 3 (engine #4). The traces are seen to be rather inactive, with $\overline{T}$ essentially ambient (other than for a short period of rather significant ingestion during engine acceleration when the nozzle pressure of engine #4 was below that of engine #1). At full power conditions, a few significant temperature spikes of very localized nature (as indicated by the high ratio of distortion relative to rise in $\overline{T}$) are observed.

Time Dependence

The temperature indices discussed above were cumulatively time-averaged through the tests in order to provide a single run-average index for each of the quantities $\overline{T}$, ϵ_{max}, ϵ_{rms}, and $\dot{\overline{T}}$. These time average quantities were obtained by continuous integration and division by time of the quantities in question, the computing process beginning once full thrust level of the engines was established (i.e., $t \approx 5$ sec). For the case of $\dot{\overline{T}}$, the integral taken was that of the absolute value rather than of the algebraic value (the integral of the algebraic value of $\dot{\overline{T}}$ must be zero unless there is a <u>net</u> increase or decrease in $\overline{T}$ with time).

Figure 22 shows the cumulative time averages $\hat{\overline{T}}$, $\hat{\epsilon}_{max}$, $\hat{\epsilon}_{rms}$, and $|\hat{\dot{\overline{T}}}|$ for engine #1 of Test 3, the hat over the quantity indicating the cumulative time average. As can be seen, the cumulative time averages are essentially independent of time except during the initial stages of the computation where the time interval which is divided into the integral is not sufficiently large (say, $t \lesssim 1$ sec) to dampen the individual oscillations. In summary, although the quantities $\overline{T}$, ϵ_{max}, ϵ_{rms}, and $\dot{\overline{T}}$ are of a sporadic nature on a short time basis, there is virtually no net change (i.e., no "long time" time-dependence) in the average value of these quantities over the duration of the tests. Although only one example is used to demonstrate this point, the conclusion is generally applicable to all the tests.

Radial Distribution

For Tests 3 and 4, inlet temperature indices for the ingestion prone engines (engine #1 and engine #4, respectively) were computed for the inboard and outboard thermocouples separately. The evaluation of these data provides information on the radial distribution of the hot gas ingestion. These data are presented in Figures A3-3 and A3-4 for Test 3, and in Figures A4-3 and A4-4 for Test 4. Some general comments based on comparison of these figures with each other, and with the data for the total inlet, follow.

Considering first the inlet temperature level, it was found that the time average inlet temperature rise above ambient, $\hat{\Delta T}$, for the outboard region of the inlet was about 25-30% higher than that for the inboard region. The average inlet temperature considering the total inlet lies, of course, between that of the inboard and outboard levels.

A somewhat greater difference between outboard and inboard characteristics was found in the time average distortion levels, $\hat{\epsilon}_{max}$ and $\hat{\epsilon}_{rms}$. The outboard distortion was about 40% higher than the inboard distortion for Test 3, and about 70% higher for Test 4. For both tests the outboard time history of ϵ_{max} was found to be nearly identical to the time history of ϵ_{max} for the total inlet, thereby indicating that the maximum local temperature occurs almost exclusively in the outboard region of the inlet.

For Test 3, the time-average rate of rise, $|\hat{\dot{\overline{T}}}|$, was found to be essentially the same for the inboard and outboard regions of the inlet and about 25% greater than the average rate for the total inlet (i.e., the spatial averaging process dampens the transients). In contrast, for Test 4, although the value of $|\hat{\dot{\bar{T}}}|$ for the outboard region was again about 25% greater than for the total inlet, the value of $|\hat{\dot{\bar{T}}}|$ for the inboard region was about 50% greater than for the total inlet. This latter result can be seen qualitatively by comparison of the time histories of $\bar{T}$ and $\dot{\bar{T}}$ for the various inlet regions. The result of such a direct comparison indicates that higher $\bar{T}$ peaks are experienced in the inboard region of the inlet than in the outboard region of the inlet, even though, as discussed above, ϵ_{max} is significantly greater in the outboard region of the inlet. That is (for Test 4 only), while the outboard region of the inlet experienced larger <u>spatial</u> variations in temperature than the inboard region, the inboard region experienced larger <u>temporal</u> variations in temperature than the outboard region.

<u>Temporal Distribution</u>

Figure 23 shows the relative distribution of $\Delta\bar{T}$, ϵ_{max}, and $|\dot{\bar{T}}|$ in the <u>time</u> domain (i.e., probability density) for engine #1 of Test 3. Also shown are the time average quantities $\hat{\Delta\bar{T}}$, $\hat{\epsilon}_{max}$, and $|\hat{\dot{\bar{T}}}|$ provided for comparison (note that $\hat{\Delta\bar{T}}$, $\hat{\epsilon}_{max}$, and $|\hat{\dot{\bar{T}}}|$ are the <u>moment</u> centers of the area under the distribution curves). Several characteristics of the probability densities are immediately evident.

The probability density of $\Delta\bar{T}$ (Figure 23a) is seen to be heavily skewed toward the lower temperature levels, with the most probable value (i.e., mode) of $\Delta\bar{T}$ being only about one-half the mean value. That is, most of the time is spent at temperature levels below the average value. Although similar distributions were not generated for the individual temperature (T), it may be inferred from the character of the raw data that the distributions would be even more skewed toward the lower temperatures as a result of the previously discussed "return to ambient" between temperature spikes. It follows that the most probable value of T would be the ambient temperature

Figure 23b shows the probability density of ϵ_{max}. The distribution is seen to be much more symmetrical with respect to the mean value than that for $\Delta\bar{T}$, the most probable value of ϵ_{max} being close to the mean value. Figure 23c shows the probability density of $|\dot{\bar{T}}|$. The probability density is seen to be heavily skewed with respect to the mean value, with the most probable value of $|\dot{\bar{T}}|$ being about zero.

Although only Test 3 is used to illustrate the probability densities of $\Delta\bar{T}$, ϵ_{max}, and $|\dot{\bar{T}}|$, the trends indicated are indicative of other tests.

Frequency Distribution

Figure 24 shows the distribution of $\overline{T}$ in the frequency domain (i.e., power spectral density) for engine #1 of Test 3. The power spectral density representation of $\overline{T}$ characterizes the frequency composition of the oscillations by showing the relative energy associated with each frequency. To illustrate the concept, the power spectral density of a pure sine wave is simply a delta function (i.e., infinite spike) at the frequency of the wave since the total "energy" of the curve is contained within a single frequency. As a second example of the other extreme, the power spectral density of "white noise" is a constant amplitude across the frequency spectrum since by definition, "white noise" contains all frequencies with equal energy contents. For any real fluctuating process, a power spectral density curve exists which lies somewhere between the two extremes illustrated, and for many cases, will have one or more dominant frequencies as indicated by peaks in the power spectral density plot.

With reference to Figure 24, no dominant frequency appears to exist, but rather a large number of peaks are observed which generally decrease with decreasing frequency. As can be seen, little energy is contained in frequencies above about 5 cps. Similar spectral plots of $\overline{T}$ were generated for other tests in an effort to determine if any correlations might exist for the different run conditions. In general, the various plots appeared to be about the same (Figure 24 being a typical example). In addition, spectral density plots of individual temperatures (T) were generated. Again, the data were much like that of Figure 24, although the frequency content of T was found to be generally somewhat higher than for $\overline{T}$.

In the process of generating the power spectral density plots of $\overline{T}$, the RMS fluctuation of $\Delta\overline{T}$ about its mean value, $\hat{\Delta T}$, may be obtained. The RMS fluctuation about the mean, commonly referred to as the standard deviation (symbolized by σ), is an index to the amplitude of the temperature fluctuations. Figure 25 shows $\hat{\Delta T}$ and the standard deviation of $\hat{\Delta T}$ (i.e., $\hat{\Delta T} \pm \sigma$) as a function of H/D at zero angle of attack and low wind conditions. In the range of H/D = 2-6, the ratio of σ to $\hat{\Delta T}$ ranges from about 0.6-0.8.

Parametric Trends

The effects of H/D, wind, and angle of attack on the ingestion characteristics (as defined by the time average temperature indices $\hat{\Delta T}$, $\hat{\epsilon}_{max}$, $\hat{\epsilon}_{rms}$, and $|\dot{T}|$) with two engines operating are discussed in the paragraphs which follow. The period of the time average indices extended from the time at which "steady state" exhaust conditions were established (i.e., $t \approx 5$ sec) to $t = 30$ sec. As noted previously, the selection of the termination point for the time-average indices is not critical in that the time-average quantities are relatively independent of the averaging time beyond the first few seconds (Figure 22).

Repeatability - Prior to discussing the parametric trends, it is appropriate to examine some repeatability aspects of the data. Figure 26 shows the time average quantities $\hat{\Delta T}$, $\hat{\epsilon}_{max}$, $\hat{\epsilon}_{rms}$, and $\left|\hat{\dot{T}}\right|$ for six tests conducted at the same nominal condition: $H/D = 4$, zero angle of attack, and low wind conditions (i.e., wind < 4 mph). In general, the tests were not consecutive and not conducted on the same day. Although the repeatability of the data is not as good as one might desire, it is reasonably good considering the nature of the raw data -- the majority of the data being within ±10% of the six-text average value of the respective temperature indices. The accuracy of $\hat{\Delta T}$, $\hat{\epsilon}_{max}$, and $\hat{\epsilon}_{rms}$ is about ±2°F, so that the actual repeatability of inlet thermal environment from run to run is most likely better than the repeatability indicated by the data. This would be particularly true in the case of $\hat{\Delta T}$ where ±2°F constitutes a sizeable percent of $\hat{\Delta T}$. Detailed data of three of the six tests used for the repeatability comparison of Figure 26 are presented in the Appendix (tests 3-5).

Effect of H/D - The effect of H/D on ingestion characteristics for low wind condition, high wind conditions, and angle of attack is presented in Figures 27-30. First of all, in comparing Figures 27-30 at $\alpha = 0$, it is observed that the curves for $\hat{\Delta T}$, $\hat{\epsilon}_{max}$, $\hat{\epsilon}_{rms}$, and $\left|\hat{\dot{T}}\right|$ show similar (and very substantial) variations with H/D. Such a comparison of the various temperature indices tends to confirm the rather curious variation with H/D observed -- namely, that for both low wind and high wind conditions at zero angle of attack, there is an H/D interval (i.e., $H/D \approx 3\text{-}5$) in which the ingestion characteristics increase, rather than decrease, with increasing H/D. Although conjectural explanations which are consistent with the observed results can readily be generated, it is perhaps more realistic to present the data without rationalizing explanations.

Effect of Wind

The effect of wind (Figures 27-30) is seen to result in a significant reduction in ingestion characteristics for values of $H/D \gtrsim 3$ where, presumably, the upwash strength is reduced to a level where the wind effectively deflects it before reaching the level of the inlets: in all cases, the ingestion prone engine was downstream of the wind (i.e., engine #1). Based on the exhaust pressure levels, however, it is anticipated that engine #1 would have been the ingestion prone engine even without wind, as per Figure 19.

Effect of Angle of Attack

The 6° angle of attack is seen to be very effective in reducing ingestion characteristics at all values of H/D, with no apparent tendency for ingestion characteristics to increase with increasing H/D as for the case of $\alpha = 0$. Based on Figures 27-30, ingestion would seemingly be virtually eliminated at $\alpha = 6°$; however, review of the Appendix data (viz., Tests 24 and 25) indicates that sporadic localized ingestion occurs at H/D = 2 and 4.

Figure 31 shows the variation in ingestion characteristics with angle of attack. Data are shown for the ingestion prone engine. The variation in ingestion characteristics with angle of attack is seen to be quite significant, with major reductions in ingestion characteristics resulting from relatively small angles of attack. This result is in general agreement with the small-scale findings reported in References 6 and 7 (which also provide a detail discussion of the effects of jet angle on the structure of the upwash). Based on the findings of References 6 and 7, the effect of engine cant angle on ingestion characteristics (and flow structure) is equivalent to the effect of angle of attack. Thus, it would appear that a small engine cant angle might be effectively used as an ingestion suppression concept in the design of a VTOL aircraft.

Also of interest in Figure 31 is the negative angle of attack bias indicated. That is, engine #1, the ingestion prone engine at positive values of α (and $\alpha = 0$), is also the ingestion prone engine at $\alpha = -1$. This bias is apparently not the result of a bias in P_n/P_∞ (the zero angle of attack ingestion prone engine criterion discussed previously) in that the steady state values of P_n/P_∞ was essentially equal for the two engines at $\alpha = -1$ (and $\alpha = 0$). Rather, it is suggested that it is a result of the ground plane contour in the region between engines #1 and #4. As noted previously, the ground plane structure in the region of the near flow field consisted of steel plates bolted caused by exposure to the high temperature jet impingement) of 1-2 degrees were to the basic ground plane in which permanant local slopes (due to warping of the plates caused by exposure to the high temperature jet impingement) of 1-2 degrees were measured. Even greater buckling may have been experienced during the tests when the plates were hot.

UPWASH ENVIRONMENT

Figure 32 shows the inlet proximity temperature history for Test 3. As can be seen, the activity in the proximity of the ingestion prone engine (engine #1) is considerably greater than in the proximity of the non-ingestion prone (engine #4), with temperature peaks of about 150°F observed. Correlation of inlet proximity temperature activity with the ingestion prone engine is a general trend typical of all tests examined. In addition, the extent of the activity of the inlet proximity temperature field was found to be indicative of the level of ingestion -- this result supporting the concept of the upwash, or fountain, being the predominant source of hot gas ingestion.

The inlet proximity temperature traces of Figure 32 are seen to be considerably smoother than those for the inlet (Figure 16), although still of a rather sporadic nature. The "smoother" traces result from the lower velocity of the flow past the inlet proximity thermocouples compared to that past the inlet thermocouples. The lower velocity has a two-fold smoothing effect on the temperature traces. First of all, for a given spatial gradient in temperature, the time gradient is proportional to the velocity of the flow. Secondly, the thermocouple response is reduced (i.e., time constant $\tau \alpha V^{-1}$) as a result of the lower velocity.

The nature of the inlet proximity temperature field suggests an upwash environment of predominately large clumps of hot gas (as evidenced by the simultaneous response of several inlet proximity thermocouples). In approaching the inlet, acceleration of the flow results in stretching of the clumps, or bubbles, into elongated stream tubes. Based on typical duration of the temperature pulses within the inlet, hot gas stream tubes of the order of 10-100 ft in length are typically indicated, and may occupy anywhere from a very small fraction of the inlet cross-section to the major portion of the inlet cross-section.

GROUND JET CHARACTERISTICS

Dynamic pressure and temperature profile maps of the ground jet for various tests are presented in the Appendix. These maps (indexed in Table A-1) show the vertical dynamic pressure and temperature profiles provided by the rakes shown in Figure 7, and the lateral ground plane temperature distributions provided by the ground plane thermocouples shown in Figure 6. As noted in Figure 6, the "ground plane" temperatures were sensed by thermocouples located 2" above the ground. For the majority of the temperature maps presented in the

Appendix, the ground plane temperature pattern in the proximity of the engines is not complete due to frequent thermocouple breakage in this local high temperature-high dynamic pressure environment.

Pressure/Temperature Profiles

In reviewing the ground jet profile maps of the Appendix, several general observations of the ground jet characteristics can be made immediately. First of all, for tests in which both engines #1 and #4 are operating, the thickness of the "ground jet" in the interaction plane (i.e., along the X-axis) is much greater than in the common plane of the jets (i.e., along the Y-axis). This is at least partially explained by the fact that the flow in the interaction plane is not parallel to the ground plane, even at moderate distances from the Y-axis, but instead exhibits some upwash characteristics due to the mergence of the two non-parallel (in the plan view) ground jet flows. Secondly, the maximum temperatures of the "ground jet" in the interaction plane are generally higher than in the common plane of the jets, even though the nearest vertical rake in the interaction plane is about 60% farther from the jet source than is the nearest vertical rake in the common plane. The above observations (viz., increase in thickness and temperature, and flow with an upward component of velocity in the interaction plane) lead to aggravation of ingestion characteristics.

For tests performed with single engine operation (i.e., engine #4), the dynamic pressure and temperature profiles along the Y-axis were virtually the same as for equivalent test conditions with two engines operating. Dynamic pressure and temperature profiles along the X-axis for single engine operation were, of course, noticeably different from those for two engine tests -- the single engine profiles along the X-axis being considerably thinner, having lower values of maximum temperature, and, generally, higher values of maximum dynamic pressure.

Figures 33-39, in supplementing the profile maps of the Appendix, present summary data of the ground jet characteristics by illustrating particular trends which are not immediately obvious from data of the Appendix. These figures will be discussed in the following paragraphs.

Effect of H/D

Figure 33 shows the ground plane temperature distribution along the X, XY, and Y axes (non-dimensionalized with respect to nozzle diameter) for the various values of H/D investigated with both engines #1 and #4 operating, and at relatively low wind conditions (i.e., wind < 4 mph). Figure 34 shows similar data for single engine (i.e., engine #4) operation. The effect of H/D on ground plane temperature is seen to be small except within a radial distance of a few diameters from engine #4 centerline. The general trend is a decrease in temperature with increasing H/D, with the exception of the interaction plane when both engines are operating, for which case an <u>increase</u> in temperature with H/D is indicated. This rather curious trend, which might have been considered to be within the band of data scatter in Figure 34c, is substantiated by the independent ground jet temperature profiles measured with the rakes of Figure 7 and presented in the Appendix.

Figure 35 shows the variation in the maximum value of the ground jet dynamic pressure (non-dimensionalized with respect to $P_n - P_\infty$) with H/D. The same trends are indicated as with the ground plane temperature data -- namely, that the maximum dynamic pressure decreases with H/D except in the interaction plane, in which case, an <u>increase</u> with H/D is observed.

<u>Effect of Wind</u>

Figures 35-37 compare dynamic pressure and ground plane temperature data at relatively low wind conditions (i.e., wind = 3 mph) to data at high wind conditions (i.e., wind = 16 mph) for two engine and single engine operation. No effect of wind is observed on either the maximum value of dynamic pressure or the ground plane temperatures within the range of the data.

<u>Effect of Angle of Attack</u>

The effects of angle of attack on ground plane temperature distribution are shown in Figure 38. A rather strong effect is observed along the R_y axis, considering the relatively narrow range of angle of attack investigated. Although there is a lateral shift in the ground plane stagnation point with the angle of attack, this factor alone is not sufficient to account for the variation in temperatures observed at the higher values of R_y/D. As might be expected, a lesser angle of attack effect is observed along the R_{xy} axis, while virtually no angle of attack effect is observed along the R_x axis.

Figure 39 shows the effect of angle of attack on the maximum value of the ground jet dynamic pressure. As for the case of the ground plane temperatures, a strong effect of angle of attack is observed on the Y-axis, a lesser effect on the XY-axis, and virtually no effect on the X-axis.

ENGINE POD PRESSURES

Pressure distributions on the undersurface of the pod between engines #1 and #4 are shown in Figures 40-45 for both engines operating. Figure 40 presents the pressure distributions at low external wind conditions (i.e., wind < 4 mph) for various values of H/D. The effect of H/D on the level of the pressure distribution is seen to be significant, the level decreasing with increasing H/D.

Characteristic of the pressure distributions of Figure 40 is a positive pressure field approximately midway between the engines, with a negative field on either side. The positive pressure field results from the upwash flow, or fountain, impinging upon the engine pod. Based on the data of Figure 40, and assuming ambient density of the upwash flow prior to impingement on the pod surface, upwash flow velocities as high as about 200 ft/sec are indicated at H/D = 2. This is a conservative estimation in that the density of the upwash flow prior to impingement would actually be significantly less than ambient density, due to its relatively high temperature. As a result, higher upwash velocities than that indicated are most probably experienced.

The negative pressure field on either side of the positive pressure field results from high mass flow entrainment by the jets (and, to a lesser extent, by the upwash flow), coupled with limited area from which to draw the free air necessary to satisfy the scavenging characteristics of the jets. The flow model of Figure 46 illustrates the above described fountain and entrainment effects.

Figure 41 illustrates the effect of external wind (i.e., wind range 12-16 mph) on the pod pressure distribution. The general character of the data is similar to that for low wind conditions (i.e., fountain effect and entrainment effect), but the strength of the upwash is noticeably reduced, particularly at the higher values of H/D.

Figure 42 illustrates the effect of angle of attack (i.e., $\alpha = +6°$) on the pod pressure distribution. The effect of the 6° angle of attack on the strength of the upwash is seen to be very pronounced, the data indicating virtually no upwash for values of H/D greater than about 4. This inference, based on the data of Figure 42, is substantially in agreement with direct observations of the effect of small angles of attack on upwash flow structure as discussed in detail for the small-scale tests reported in References 6 and 7. The effects of wind and angle of attack on the magnitude of the pod pressures are also consistent with the trends of ingestion characteristics discussed previously for these conditions.

It is rather curious, however, that the pressure distributions of Figures 40-42 are not more asymmetric considering previous discussions under "Ingestion Prone Engine." That is, although with two engines operating, ingestion was generally significant in one engine or the other, but not in both, the peak of the pod pressure distribution occurs approximately midway between the engines. This result would indicate that the major asymmetry of the upwash flow occurs between the pod undersurface and the plane of the inlets rather than between the ground plane and the pod undersurface.

A summary plot of the data of Figures 40-42 is shown in Figure 43, in which the peak of the pressure distributions, ΔP_{max}, is plotted against H/D. The effect of wind and angle of attack in reducing the upwash strength is clearly illustrated.

Additional data on the effects of angle of attack are presented in Figure 44. These data serve to illustrate the decrease in the magnitude and the longitudinal shift of the peak pressure, ΔP_{max}, with angle of attack. The amplitude curve of ΔP_{max} is seen to be biased toward negative angles of attack (i.e., symmetrical about $\alpha \approx -1\frac{1}{2}°$) as was the ingestion level discussed previously in Figure 31. The longitudinal shift of ΔP_{max} is seen to be only about 2% of the distance between engine centerlines per degree of angle of attack. Again, one might have expected a more dramatic shift in the location of ΔP_{max} with angle of attack, based on previous discussions of the ingestion characteristics.

The pod pressure distribution for single engine operation is shown in Figure 45. For single engine operation, the induced pressures result solely from entrainment of free air by the jet, the resulting induced effects being considerably less than for two engine operation (note the change in scale of Figure 45 from that of previous figures).

VII. SUMMARY OF RESULTS

Comprehensive data on recirculation phenomena have been obtained for a full-scale lift engine pod model. These results will serve as reference data from which to compare the results of a similar small-scale investigation of a geometrically similar model, employing similar instrumentation and data reduction and analysis techniques, to be performed as a part of the same contract.

In addition to providing reference data for investigation of the effects of scaling on recirculation phenomena, several significant findings which provide new insight into recirculation phenomena as a whole were obtained. A summary of the principal results follows.

1. For two engine operation, significant ingestion of hot gases, and associated thrust loss, was generally experienced in one engine or the other, but <u>not</u> in both engines. For single engine operation, ingestion of hot gases was negligible at low wind condition but not negligible at high wind conditions. No engine stalls were encountered during the course of the tests.

2. The sensitivity of ingestion to difference in exhaust pressure level of the two engines was found to be acute. Small pressure biases were found to govern which engine experienced ingestion. Once ingestion is established in one engine or the other, a feedback effect is developed which stabilizes the ingestion asymmetry toward that engine.

3. The use of high response temperature sensing elements revealed some new transient characteristics of inlet thermal environment heretofore not observed. Similar high response thermocouples are recommended in future investigations.

4. For two engine operation, ingestion was of a sporadic nature, consisting of series of short duration, localized, temperature spikes. The temperature spikes were typically about 50-150°F above ambient, persisting for less than about 0.2 second, and encompassing anywhere from a small fraction of the inlet area to the majority of the inlet area. During time intervals between temperature spikes, the inlet thermal environment was typically ambient.

5. For single engine operation at high wind conditions, temperature increases of about 10°F above ambient, uniformily distributed over the inlet, and persisting for about one-half second were typically experienced.

6. Instantaneous values of the space average inlet temperature occasionally reach levels in excess of 80°F above ambient, and rate of rise levels occasionally

in excess of 1000°F/sec. The distribution of the space average temperature in the time domain was found to be heavily skewed toward ambient temperature, with the most probable temperature being significantly less than the time average temperature.

7. Severe inlet temperature distortions were experienced (frequently in excess of 100°F), with the distortion typically several times the value of the space average temperature rise. Ingestion in the outboard region of the inlet was found to be somewhat higher than in the inboard region of the inlet.

8. Excluding short duration temperature spikes, ingestion characteristics were found to be independent of time over the data acquisition period of 30 seconds.

9. The effects of H/D, wind, and angle of attack were found to have a strong effect on the ingestion characteristics: for example, a 6° angle of attack of the pod was found to result in major reductions in the ingestion level; a 12-16 MPH wind was found to generally result in a moderate reduction in the ingestion level; and increasing H/D was found to result in major reductions in ingestion level, except for a narrow H/D interval at zero pod angle of attack in which the ingestion level was found to increase with increasing H/D.

10. Correlation of the thermal environment along the sides of the pod (in the plane of the inlets) with the engine inlet thermal environment supports the concept of the upwash, or fountain, being the predominant source of ingestion.

11. The ground jet in the interaction plane was found to be thicker and have higher temperatures than the ground jet in the common plane of the exhaust jets.

12. An <u>increase</u> in ground jet temperature and pressure with increasing H/D was found to exist in the interaction plane. The effect of wind (i.e., 12-16 MPH) on the near field ground jet temperature and pressure profiles in both the interaction plane and common plane of the exhaust jets (i.e., $R/D \lesssim 20$) was negligible. A strong angle of attack effect on the near field ground jet temperature and pressure was found in the direction of the common plane of the jets.

13. Pressure distribution on the pod undersurface indicated strong upwash conditions, with indicated velocities as high as 200 ft/sec., or more, for

zero angle of attack and low wind conditions. Major reductions in the strength of the upwash were found at angle of attack and at higher wind conditions.

Acknowledgment

Acknowledgment is given to the NASA Ames Research Center for their cooperation in providing facilities and manpower, to the Northrop Research Laboratories test crew for their major role in the pre-test effort and data acquisition phases of the program, and to Miss Joyce Oshiro for her enduring persistence in reducing the data and in assisting the author in the preparation of this report.

VIII. REFERENCES

1. Tolhurst, W. H., Kelly, M. W.: "Characteristics of Two Large-Scale Jet-Lift Propulsion Systems." Conference on V/STOL and STOL Aircraft, NASA SP-116, April 1966.
2. McLemore, H. C.: "Consideration of Hot Gas Ingestion for Jet V/STOL Aircraft." Conference on V/STOL and STOL Aircraft, NASA SP-116, April 1966.
3. Lavi, R.: "Parametric Investigation of VTOL Hot Gas Ingestion and Induced Jet Effects in Ground Proximity." NOR67-32, Northrop Corporation, February 1967.
4. Hammond, A. D., McLemore, H. C.: "Hot-Gas Ingestion and Jet Interference Effects for Jet V/STOL Aircraft." Presented at AGARD Flight Mechanics Panel Meeting, Gottingen, West Germany, September 1967.
5. Lavi, R., Hall, G. R., Stark, W. W.: "Full-Scale Ground Proximity Investigation of a VTOL Fighter Model Aircraft." NASA CR-1098, June 1968.
6. Adarkar, D. B., Hall, G. R.: "The 'Fountain Effect' and VTOL Exhaust Ingestion." AIAA Paper No. 68-79, January 1968.
7. Hall, G. R., Rogers, H. K., Adarkar, D. B.: "Recirculation Effects Produced by a Pair of Heated Jets Impinging on a Flat Surface." NASA (CR number to be assigned), September 1968.
8. Hall, G. R., Bogdanovic, J. A.: "Response of Bare Wire Thermocouples to Temperature Variation in a Jet Engine Intake." AIAA Journal of Aircraft, July-August 1967.
9. Higgins, D. C., Kelly, D. P., Wainwright, T. W.: "Exhaust Jet Wake and Thrust Characteristics of Several Nozzles Designed for VTOL Downwash Suppression." NASA CR-383, January 1966.
10. Gunn, C. O.: "J-85 VTOL Experience." G. E. Technical Memorandum TM67FPD1639, September 1967.

FIGURE 1. NASA AMES VTOL GROUND EFFECTS TEST FACILITY

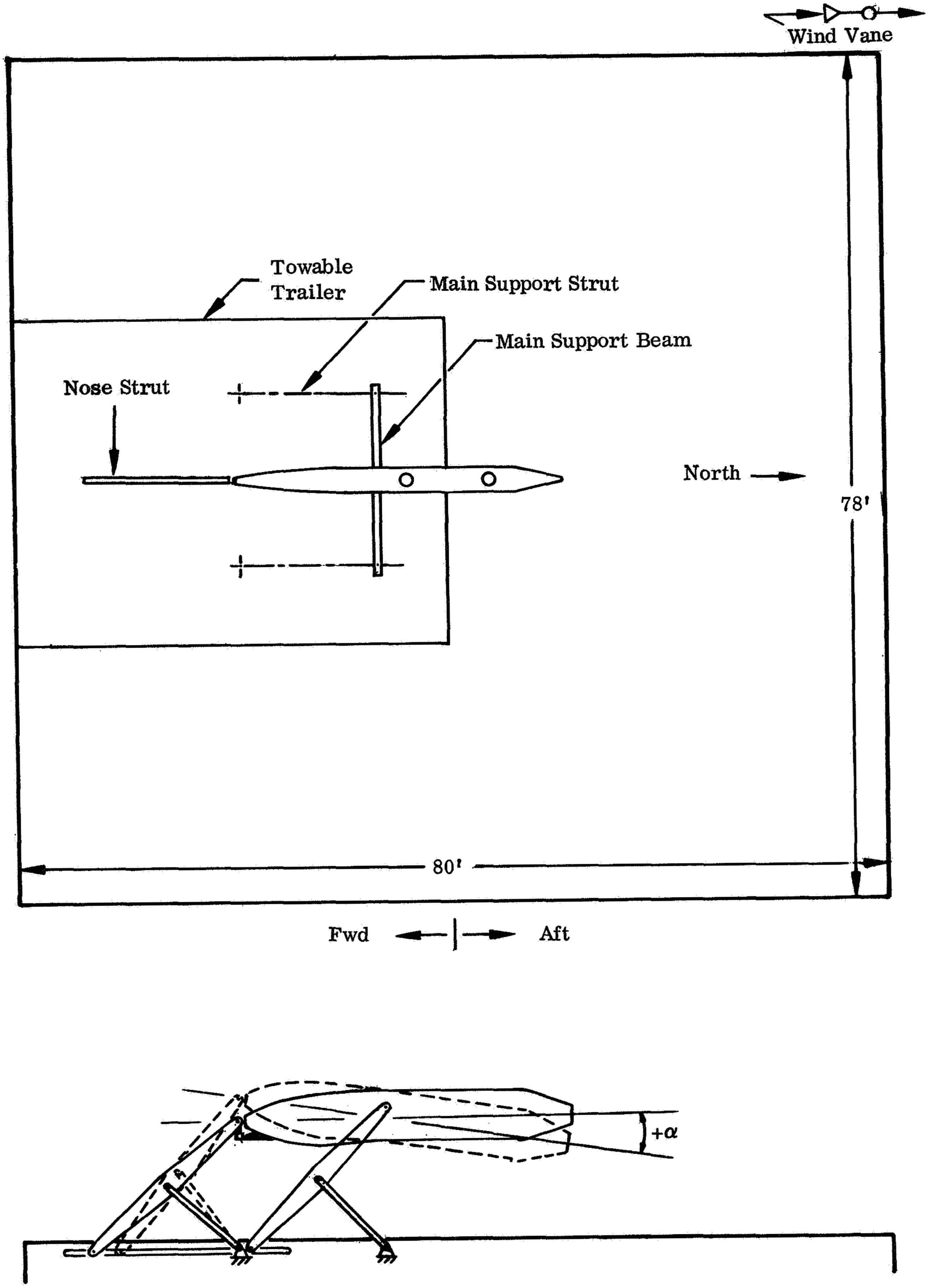

FIGURE 2. MODEL SUPPORT AND GROUND PLANE ARRANGEMENT

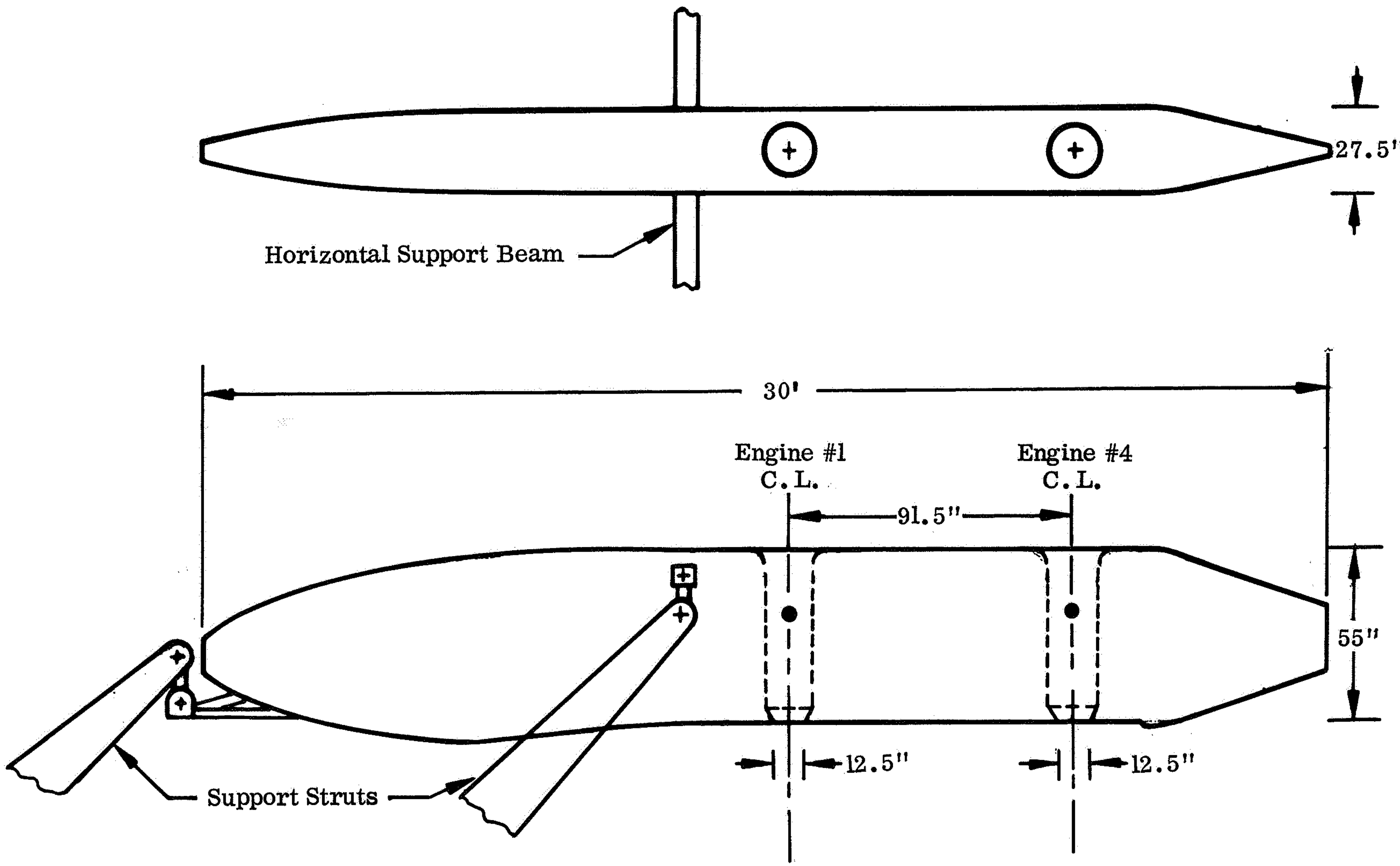

FIGURE 3. ENGINE POD MODEL

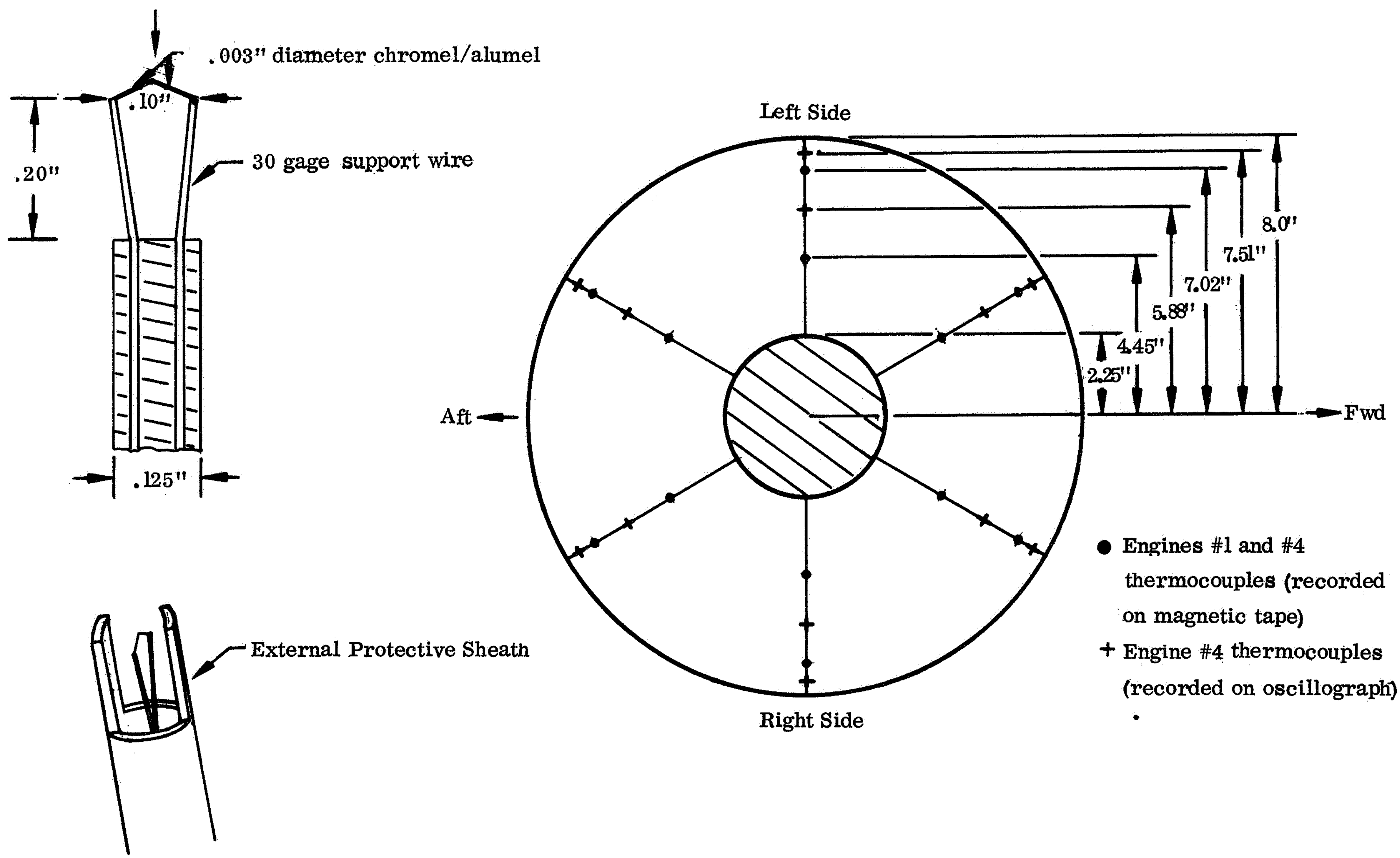

FIGURE 4. INLET THERMOCOUPLE LOCATION AND CONSTRUCTION DETAIL

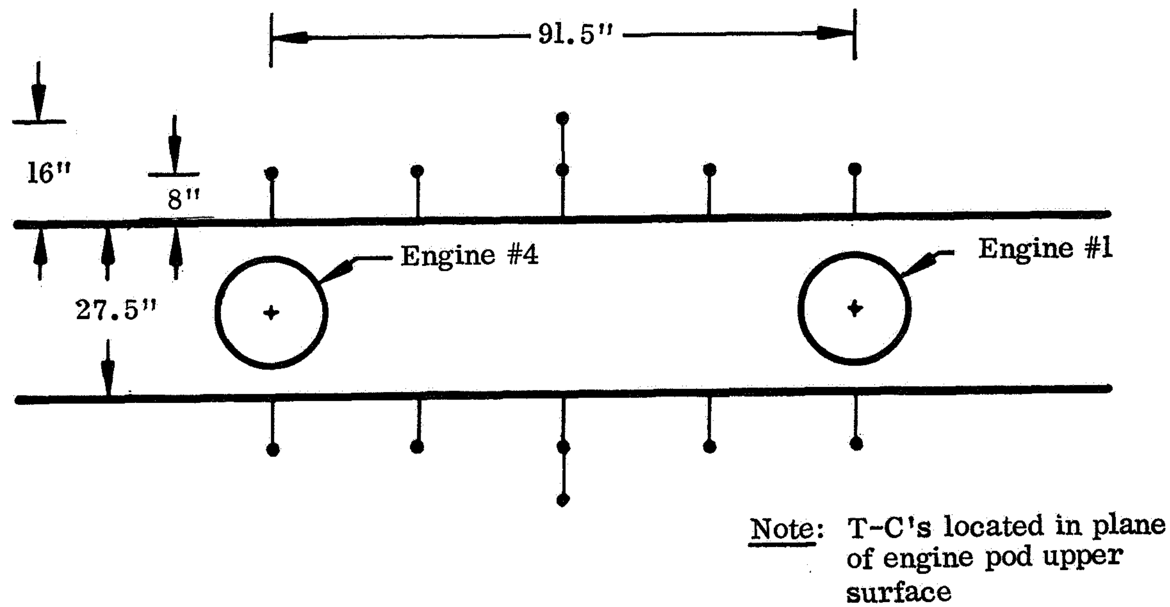

FIGURE 5. INLET PROXIMITY THERMOCOUPLES

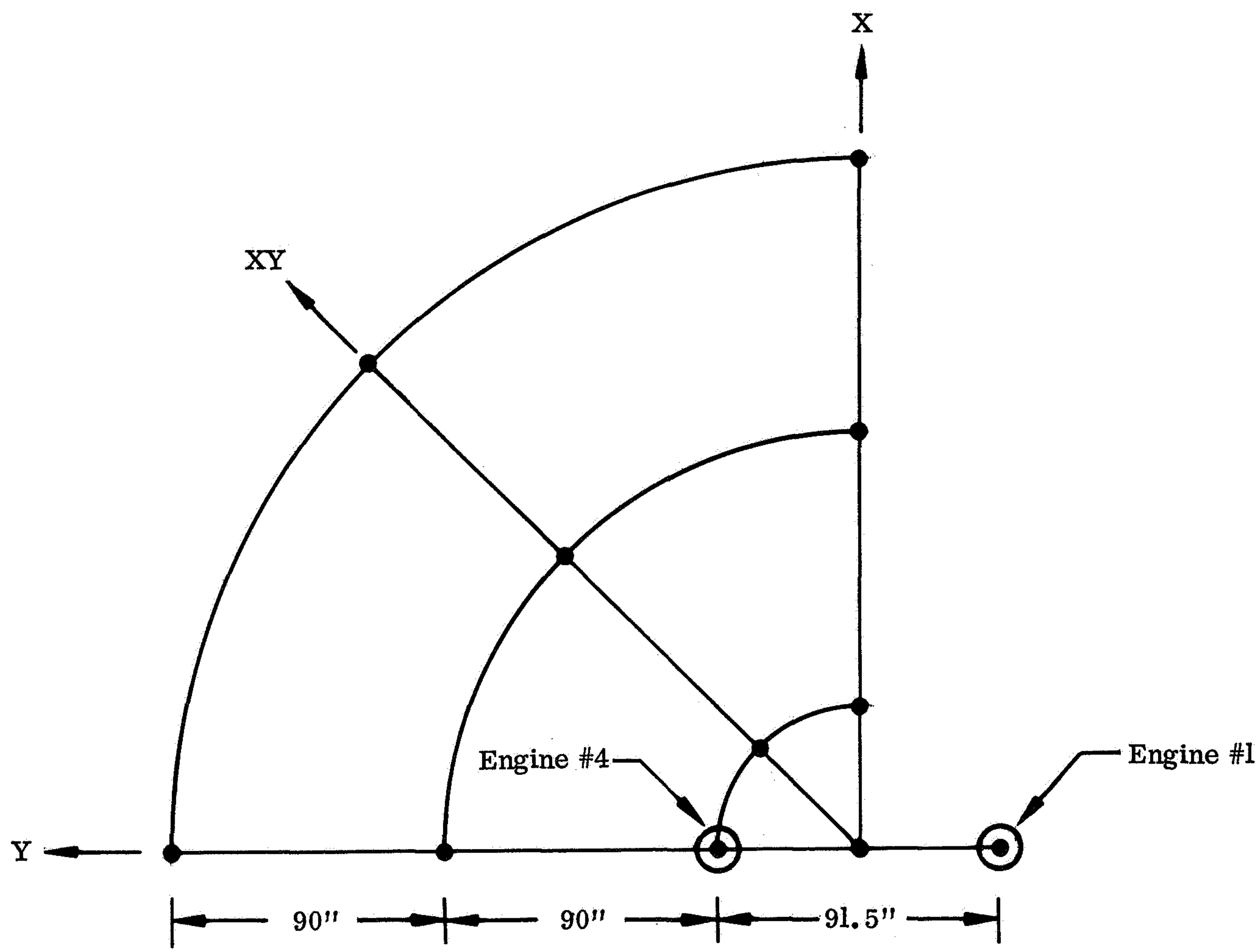

Note: All thermocouples mounted 2" above ground plane

FIGURE 6. GROUND PLANE THERMOCOUPLES

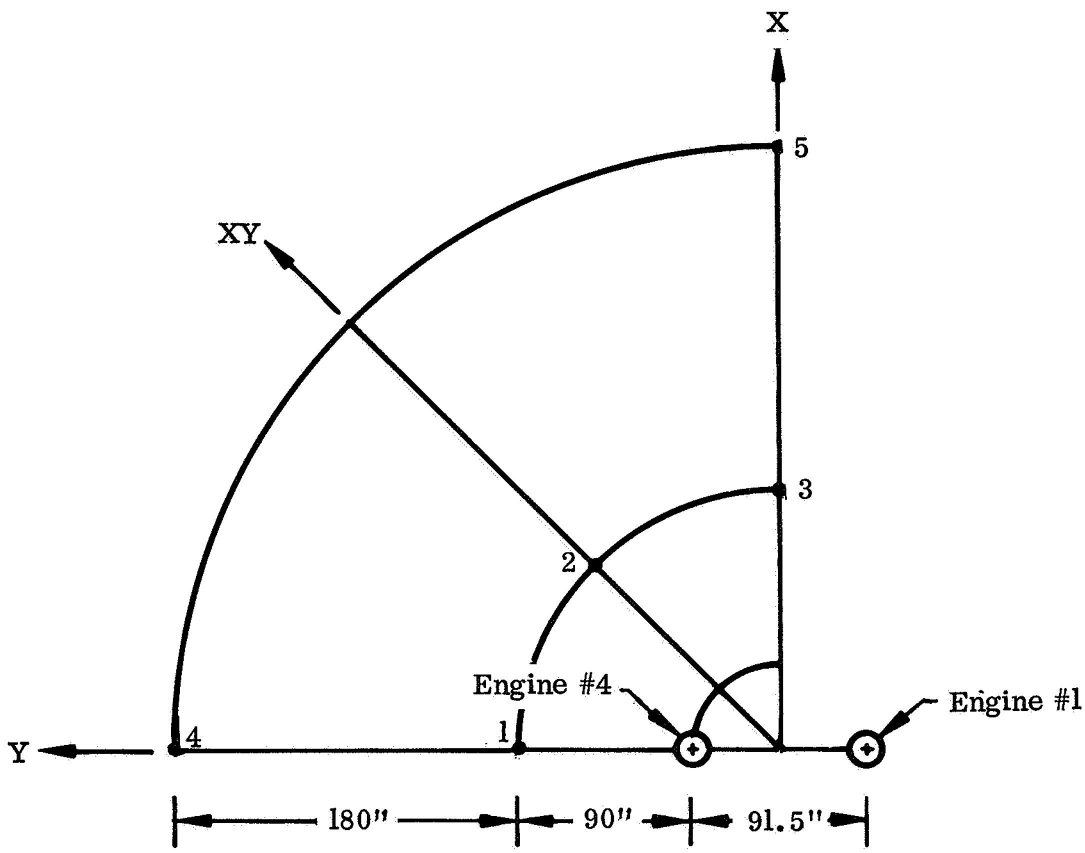

(a) Rake Planform Locations

Probe Height above Ground, h	Total Pressure, P_T	Static Pressure, P_S	Temperature, T*
.25"	X	X	X
.75"	X	X	X
1.50"	X		
3.00"	X	X	X
4.50"	X		
6.00"	X	X	X
10.00"	X		
15.00"	X	X	X
25.00"	X		
35.00"	X	X	X
50.00"	X	X	

* Temperature probes on rakes 1, 3, and 5 only

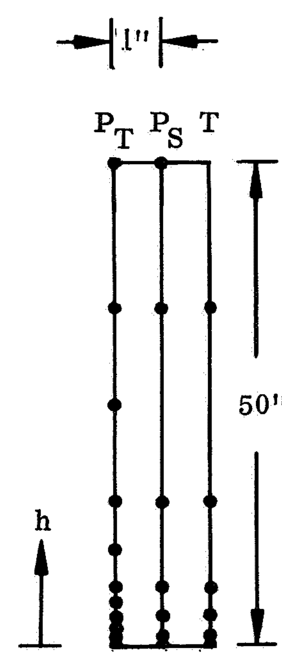

(b) Probe Vertical Locations

FIGURE 7. GROUND JET RAKES

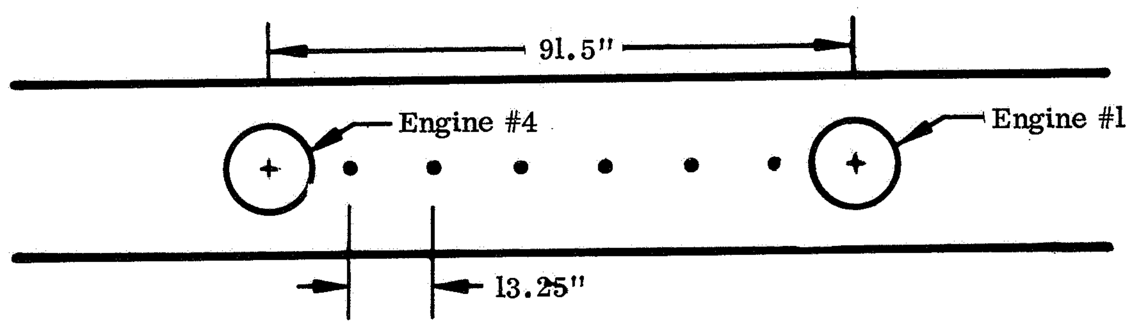

Note: Pressure taps located on engine pod lower surface

FIGURE 8. ENGINE POD PRESSURES

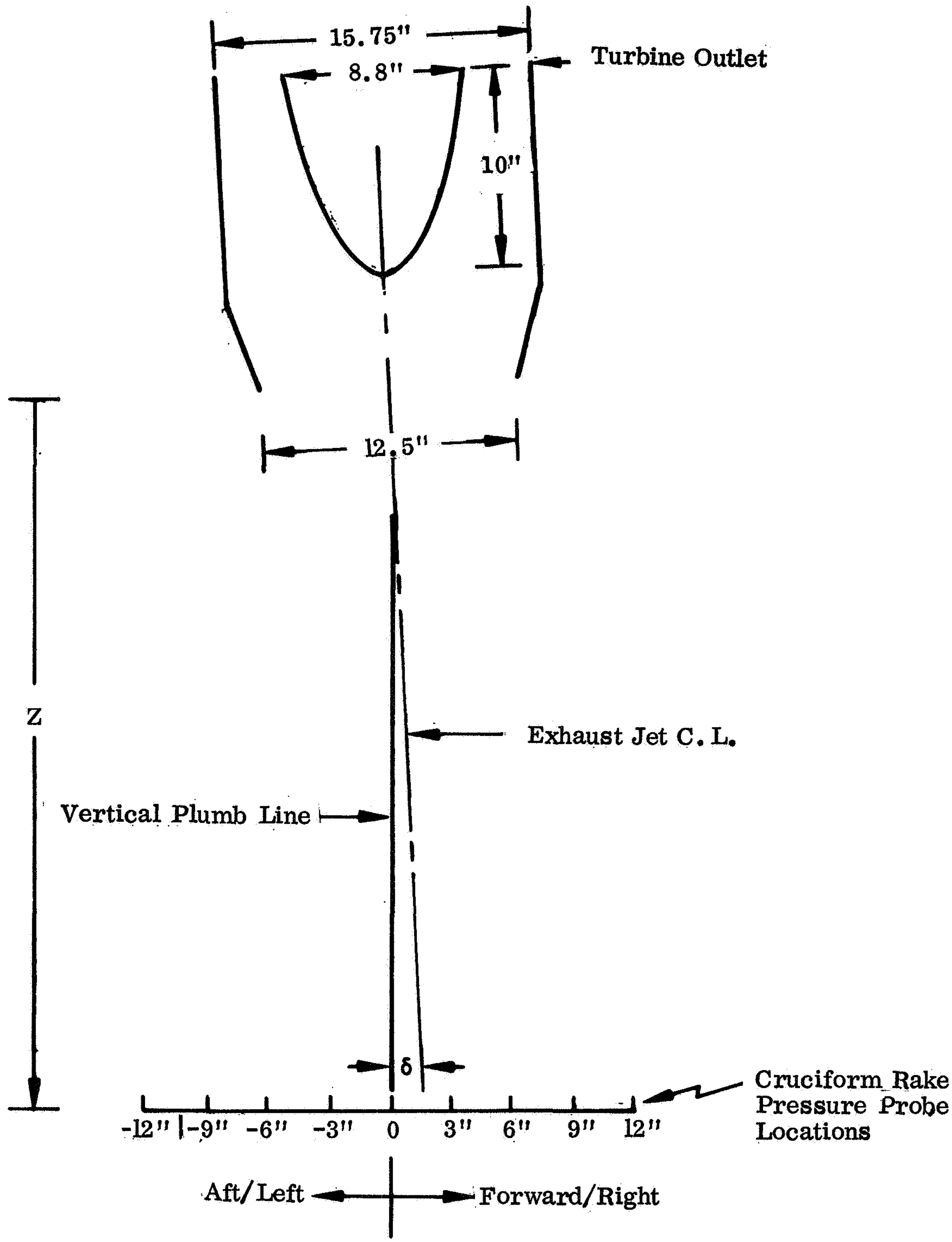

FIGURE 9. EXHAUST JET ALIGNMENT AND CALIBRATION

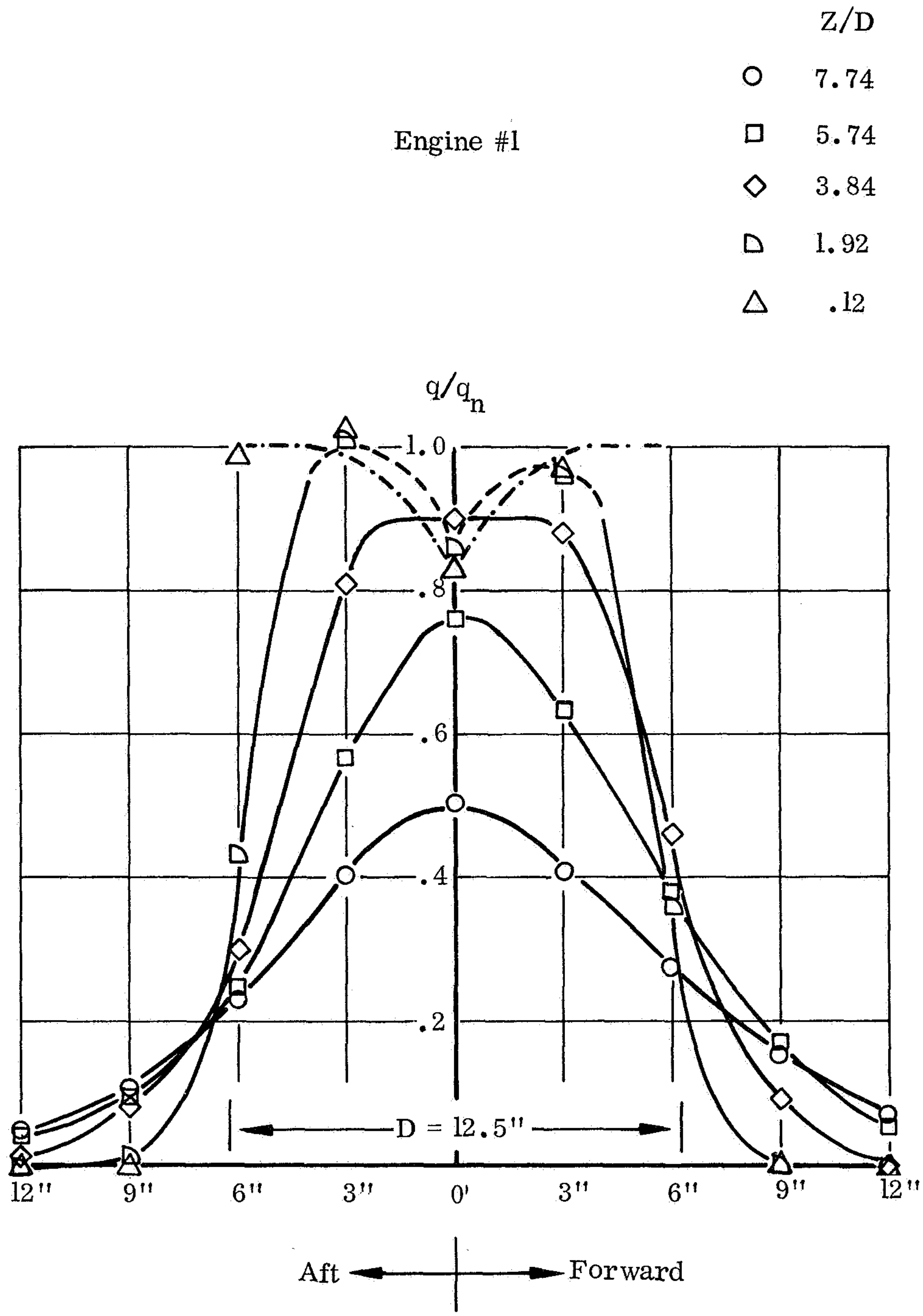

FIGURE 10. EXHAUST JET DYNAMIC PRESSURE PROFILES

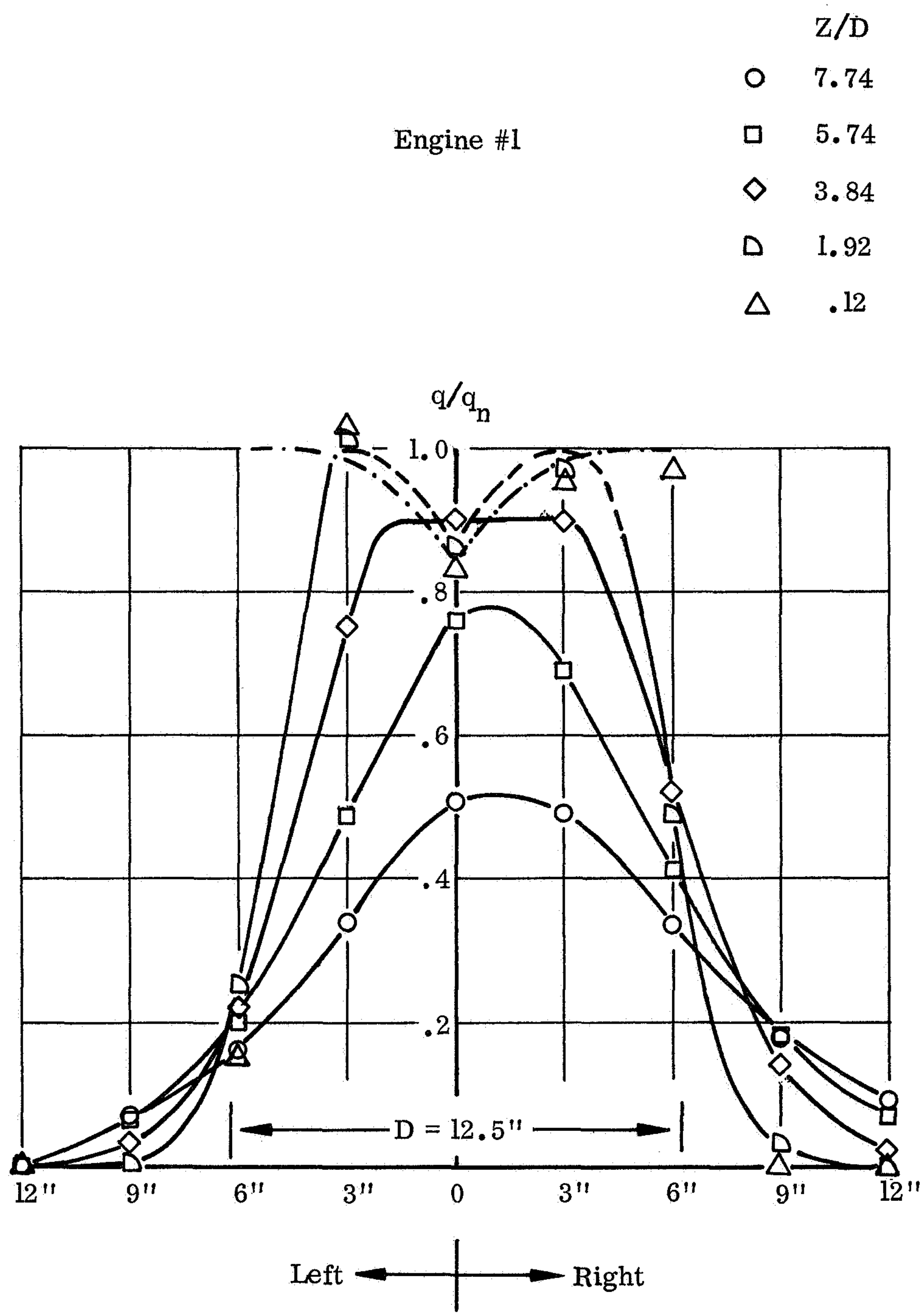

FIGURE 11. EXHAUST JET DYNAMIC PRESSURE PROFILES

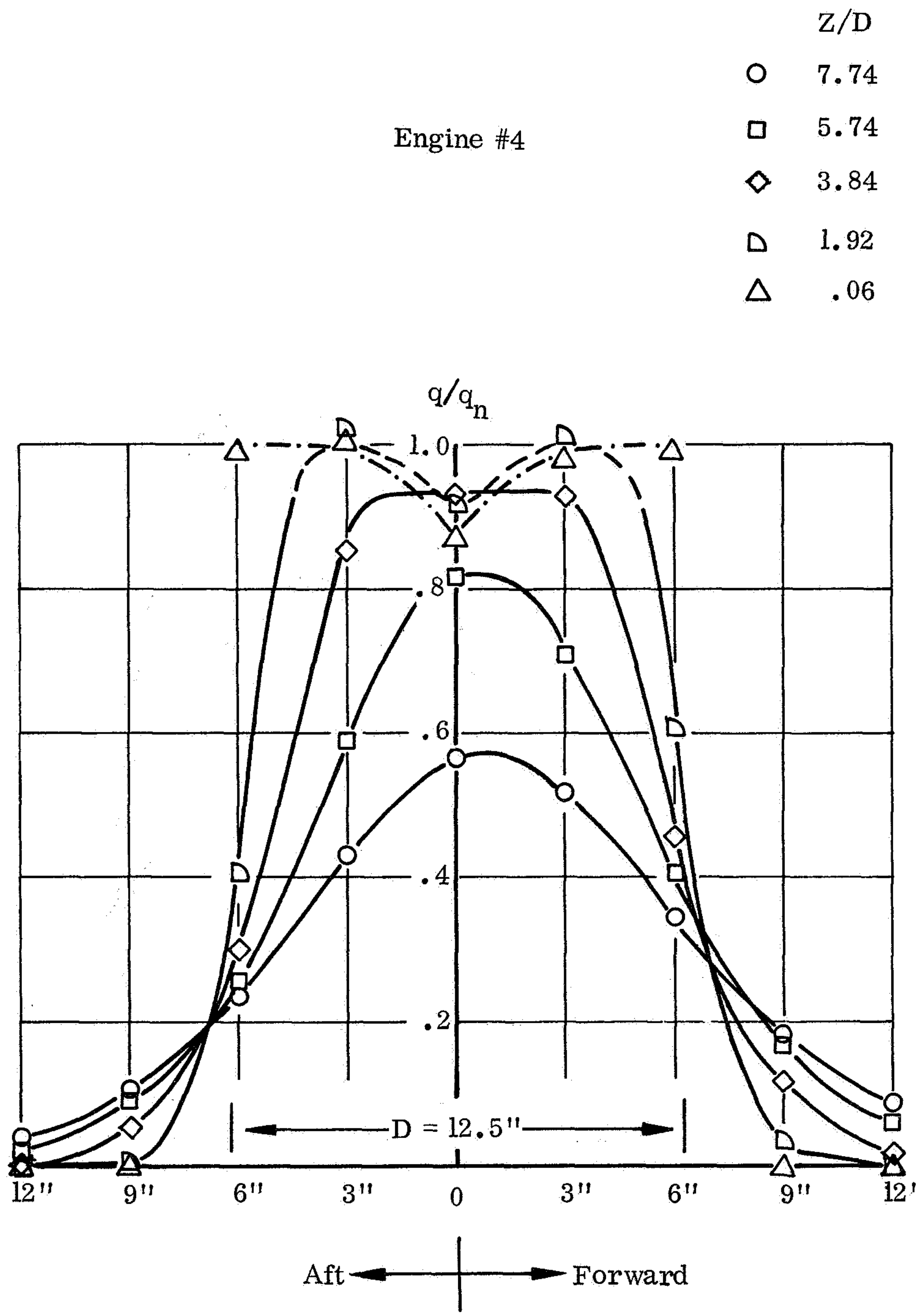

FIGURE 12. EXHAUST JET DYNAMIC PRESSURE PROFILES

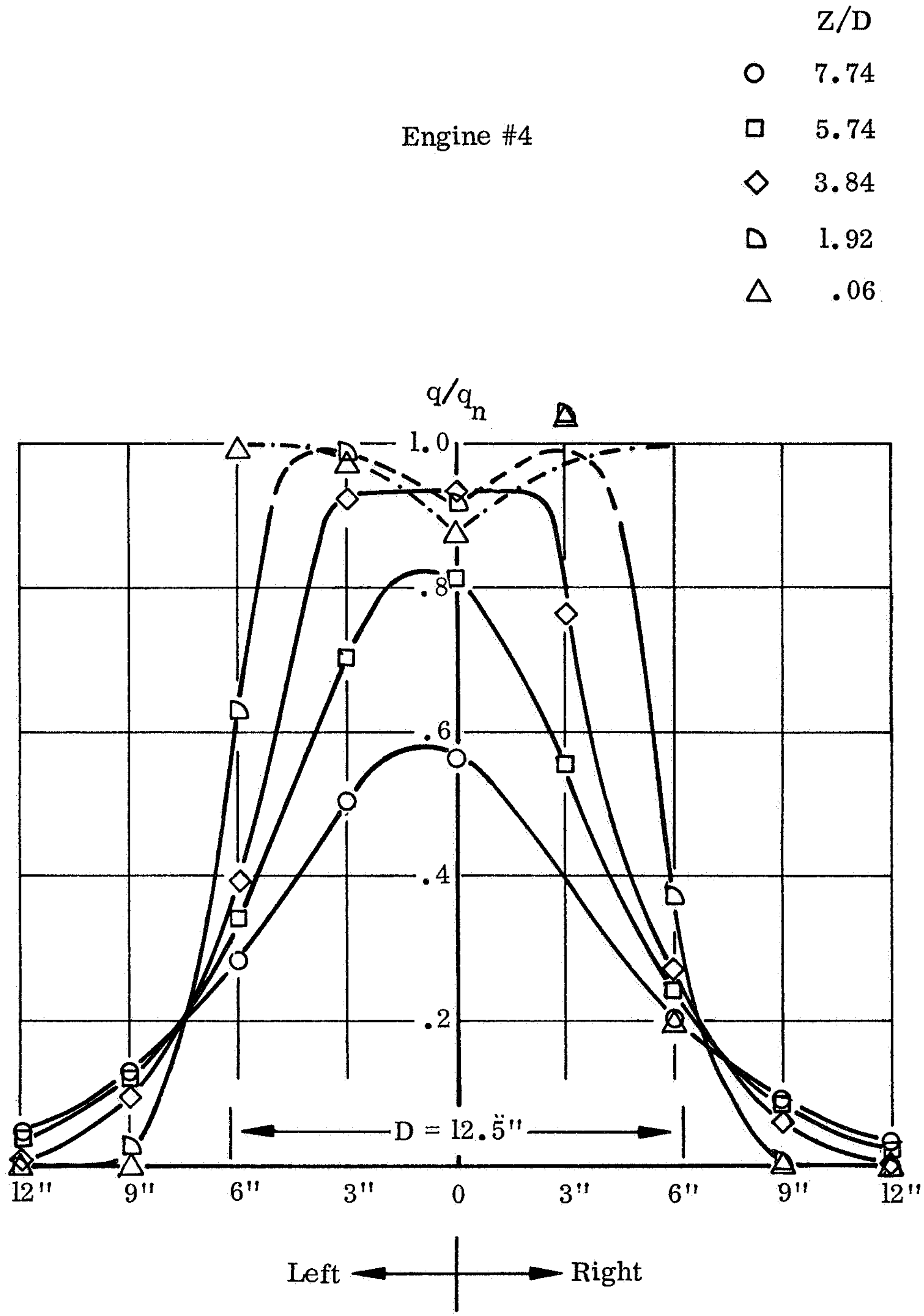

FIGURE 13. EXHAUST JET DYNAMIC PRESSURE PROFILES

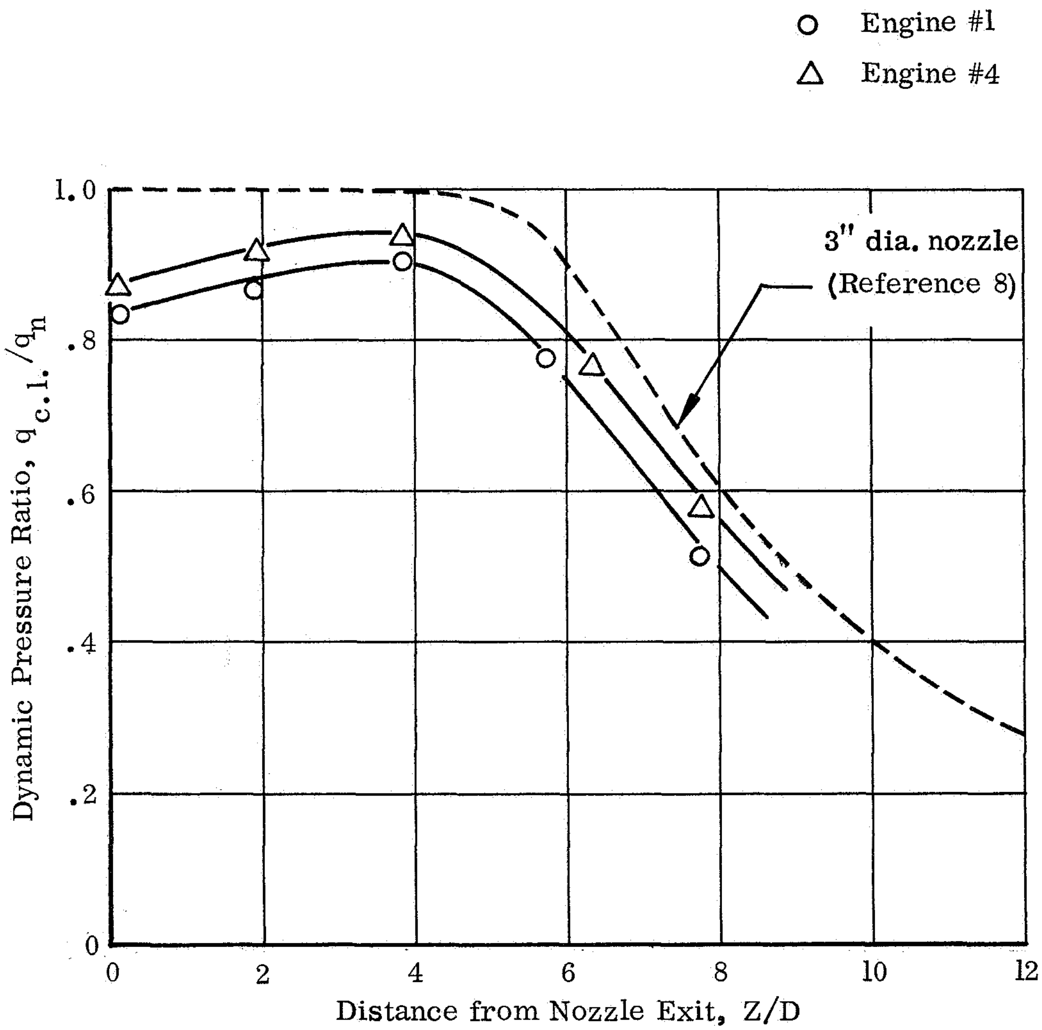

FIGURE 14. EXHAUST JET CENTERLINE DYNAMIC PRESSURE DECAY

Test 3

H/D = 4

α = 0

Wind = 3 MPH

Engines #1 and #4 operating

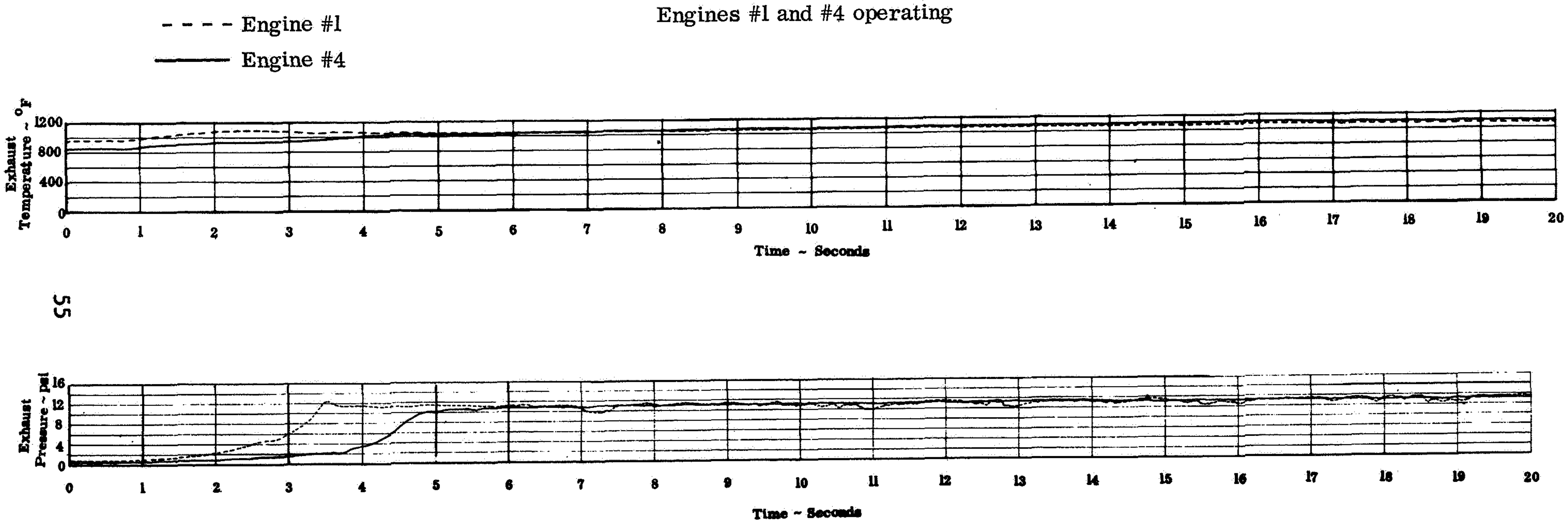

FIGURE 15. TYPICAL EXHAUST PRESSURE AND TEMPERATURE HISTORY

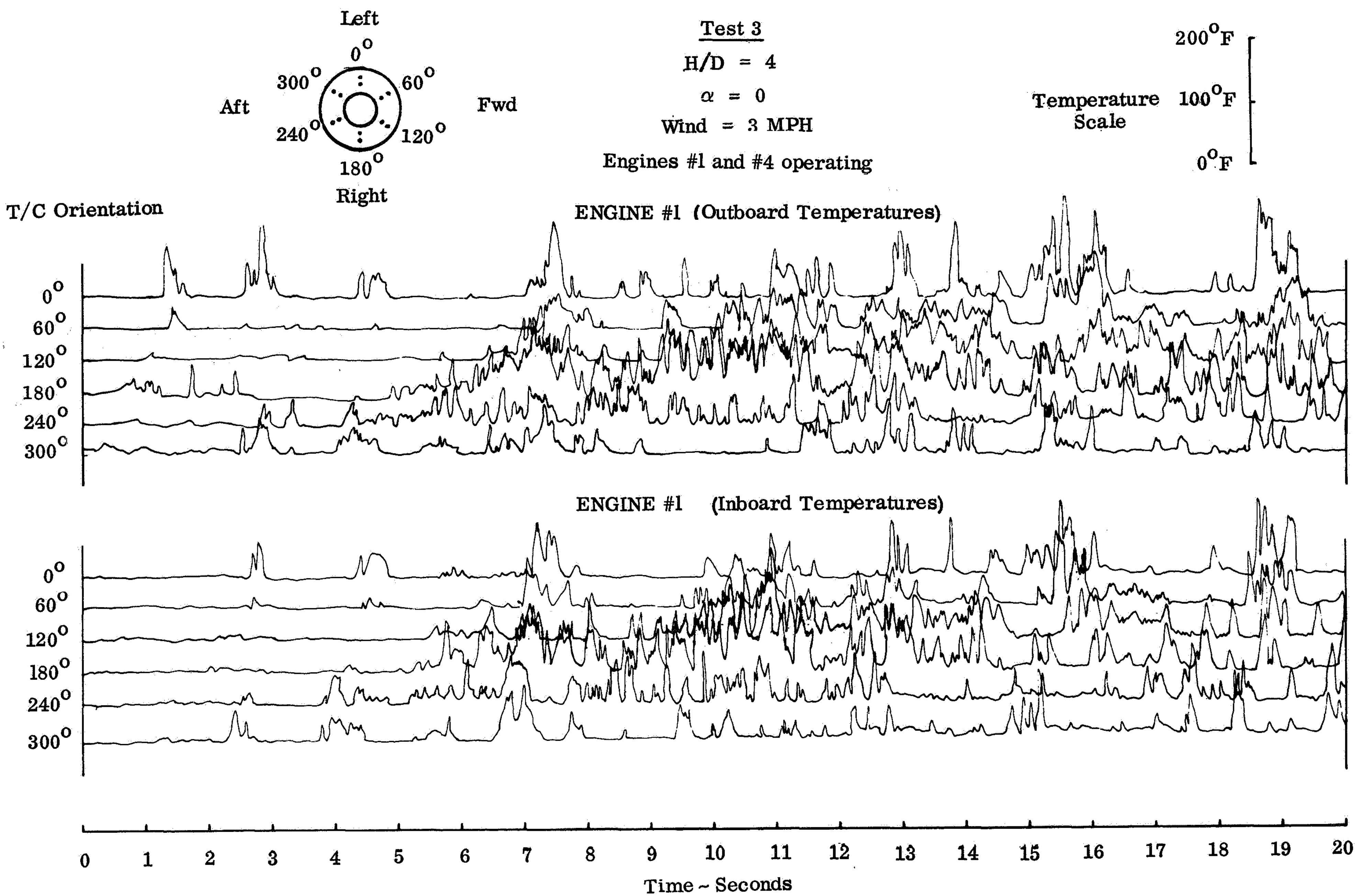

FIGURE 16a. TYPICAL INLET TEMPERATURE HISTORY - TWO ENGINE OPERATION, INGESTION PRONE ENGINE

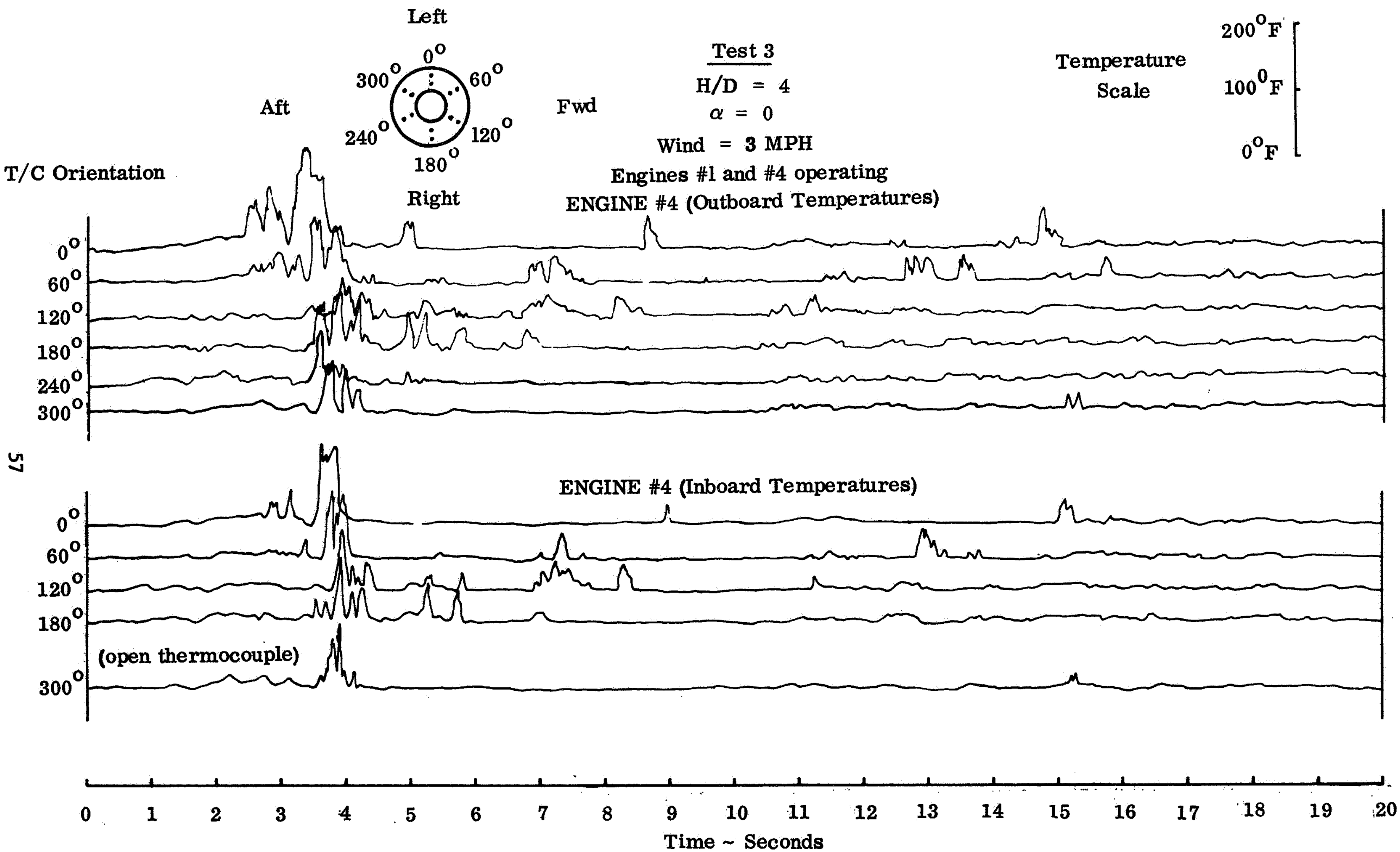

FIGURE 16b. TYPICAL INLET TEMPERATURE HISTORY - TWO ENGINE OPERATION, NON-INGESTION PRONE ENGINE

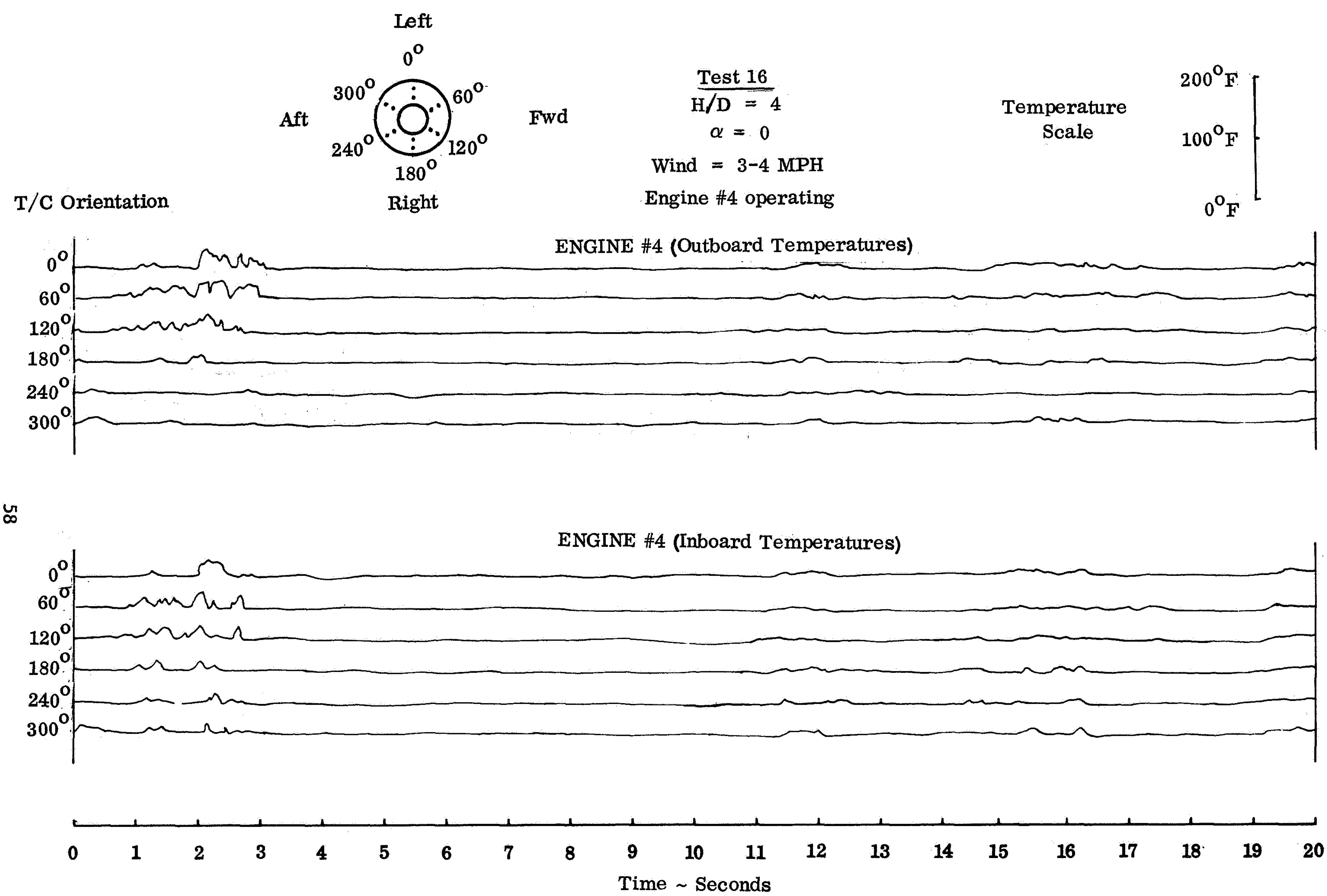

FIGURE 17. TYPICAL INLET TEMPERATURE HISTORY - SINGLE ENGINE OPERATION

Test 3

H/D = 4

α = 0

Engines #1 and #4 operating

ENGINE #1

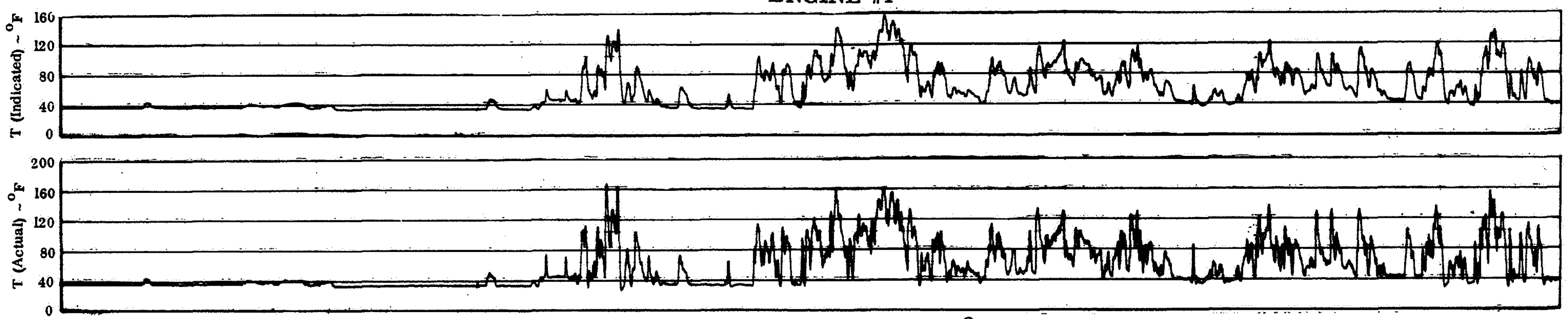

(a) Outboard Temperature (120°)

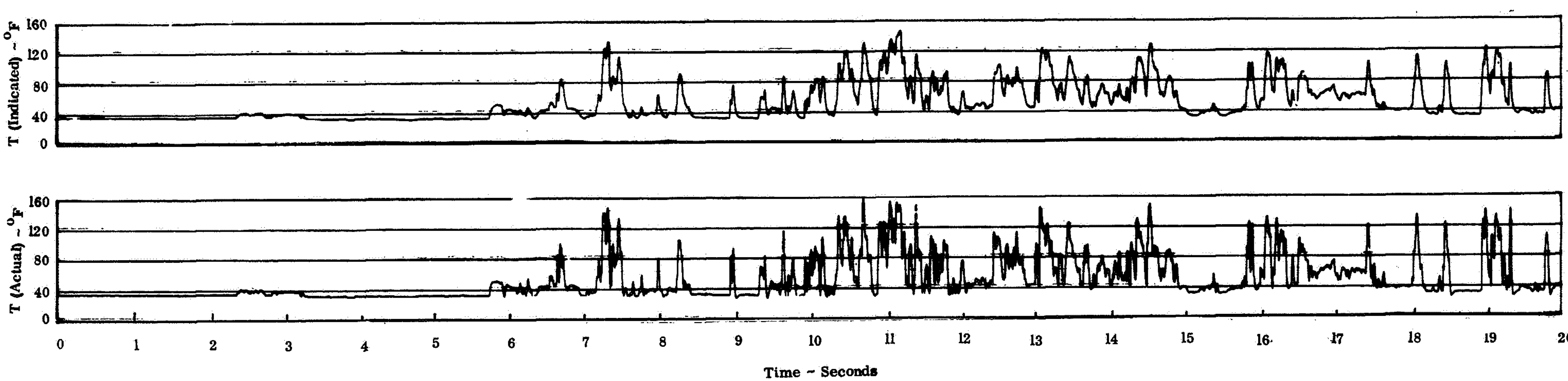

(b) Inboard Temperature (120°)

FIGURE 18. COMPARISON OF INDICATED AND ACTUAL TEMPERATURE HISTORIES

<u>Test 3</u>

H/D = 4

α = 0

Engines #1 and #4 operating

ENGINE #1

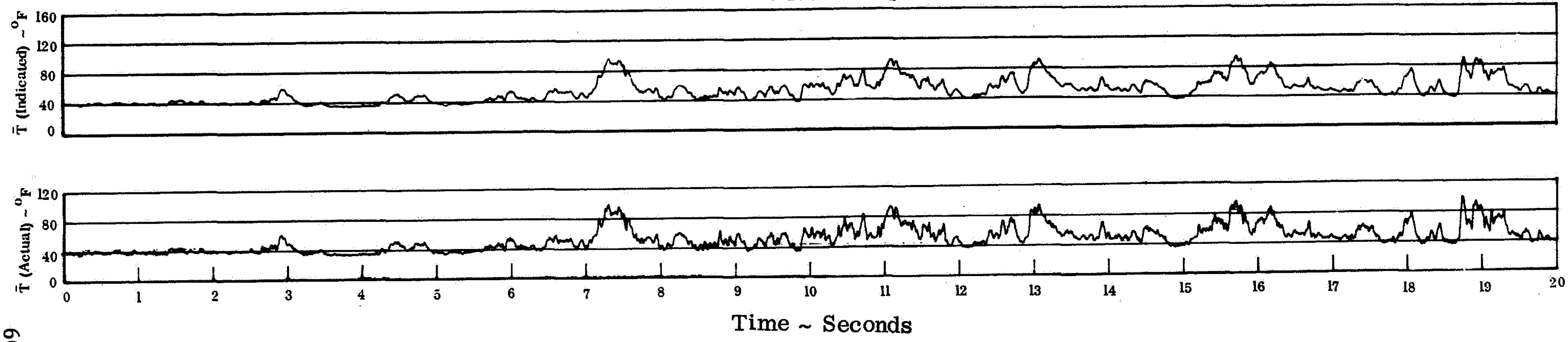

(c) Space Average Temperature

FIGURE 18 (Cont.). COMPARISON OF INDICATED AND ACTUAL TEMPERATURE HISTORIES

$\alpha = 0$

Engines #1 and #4 operating

<u>Note</u>: In order to provide a more complete summary, data from six "repeatability" tests not listed in Table A-1 are included in the data below.

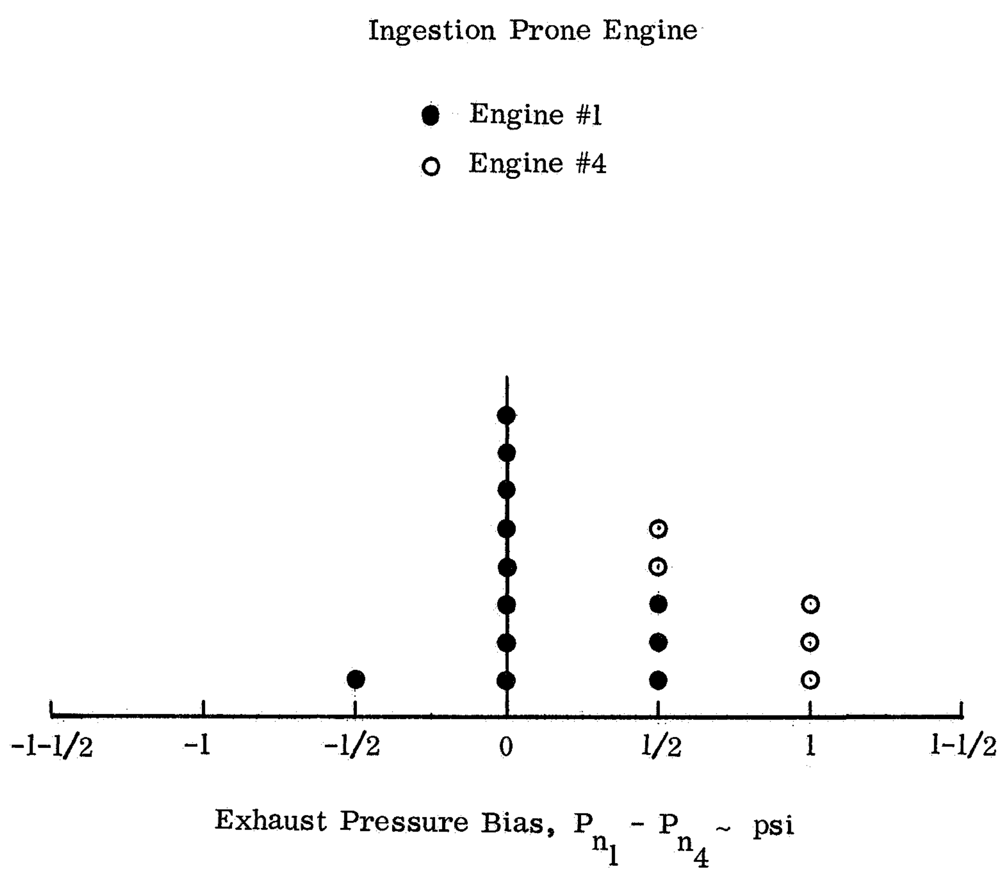

FIGURE 19. INGESTION PRONE ENGINE CORRELATION

Test 3

H/D = 4

$\alpha = 0$

Wind = 3 MPH

Engines #1 and #4 operating

ENGINE #1

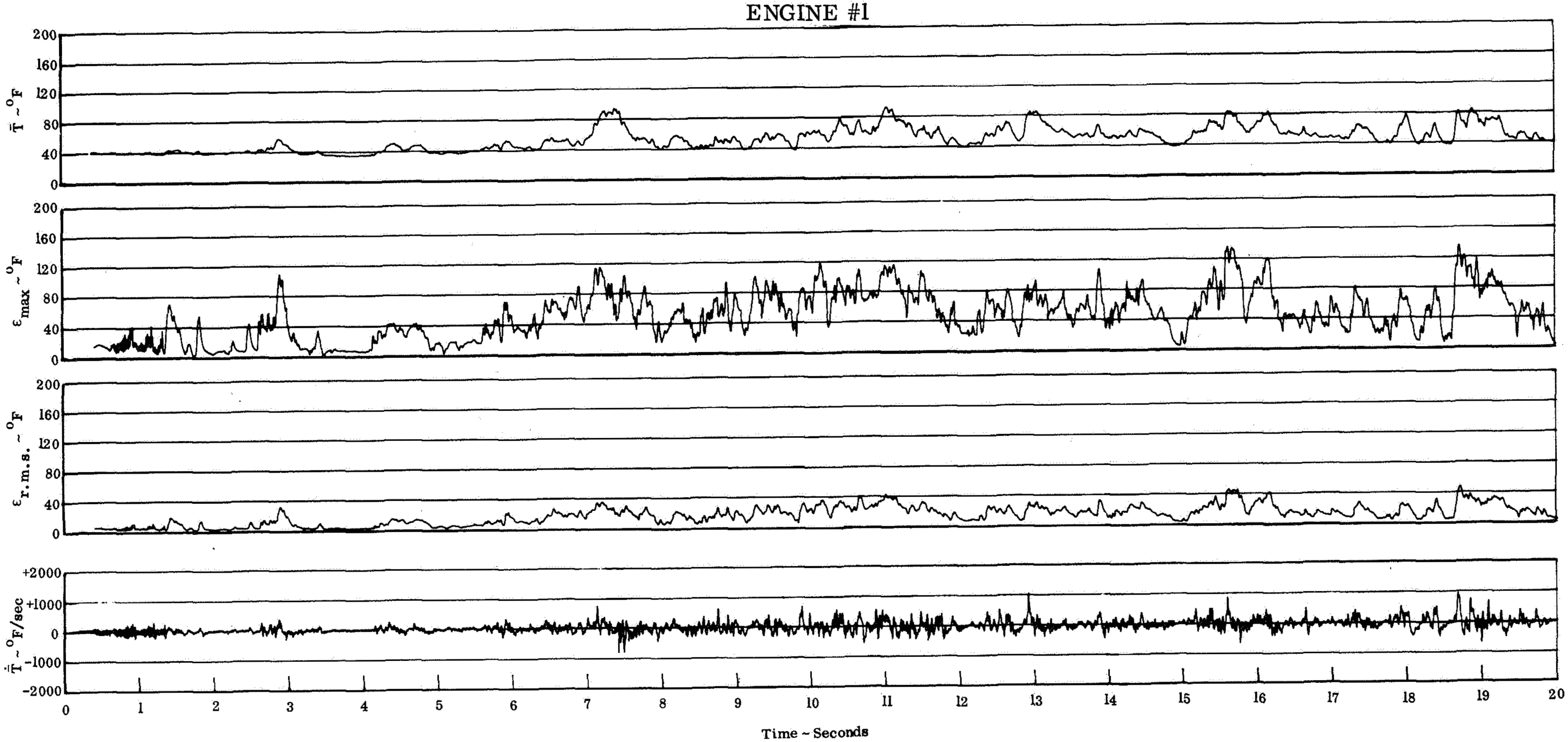

FIGURE 20 . TYPICAL INGESTION CHARACTERISTICS HISTORY - INGESTION PRONE ENGINE

Test 3

$\overline{H/D} = 4$

$\alpha = 0$

Engines #1 and #4 operating

ENGINE #4

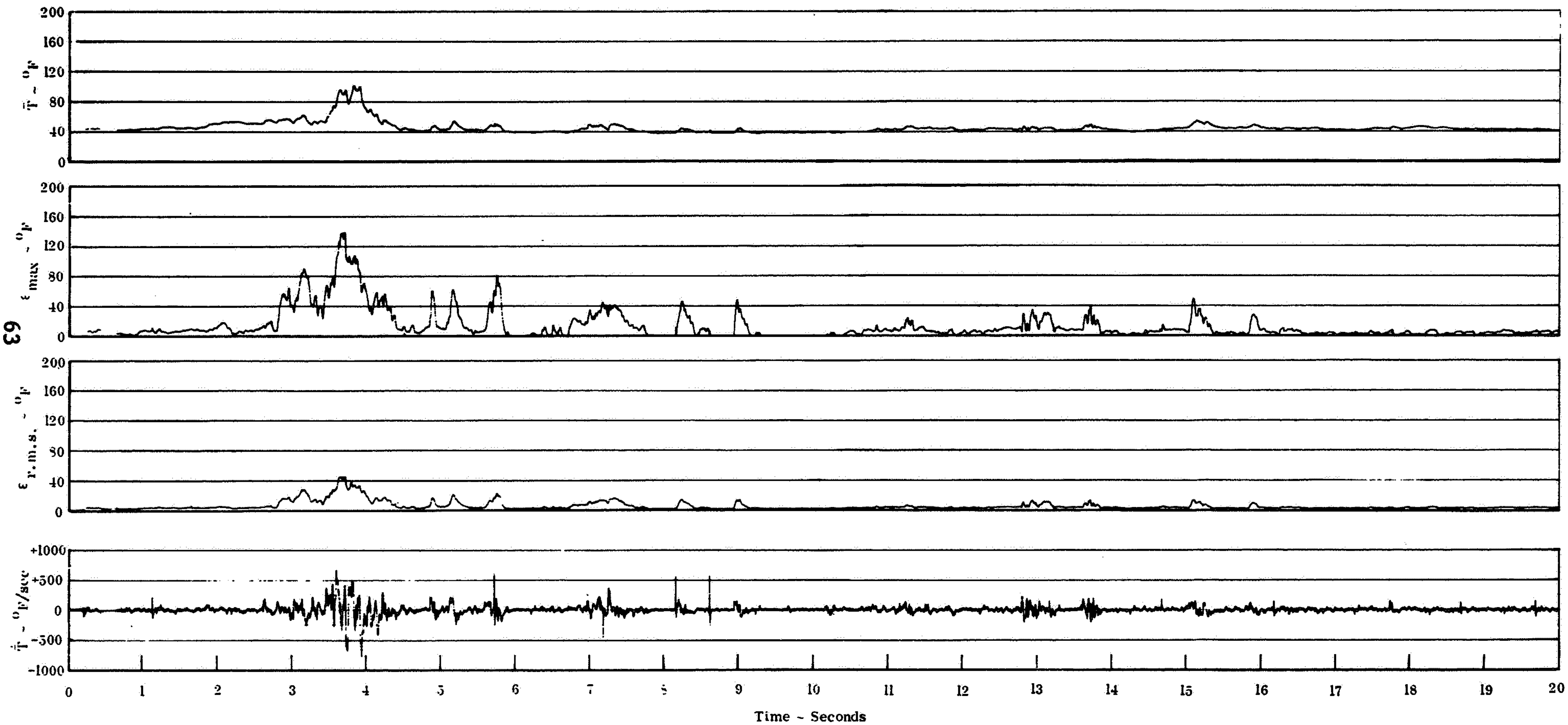

FIGURE 21. TYPICAL INGESTION CHARACTERISTICS HISTORY - NON-INGESTION PRONE ENGINE

Test 3

H/D = 4

α = 0

Wind = 3 MPH

Engines #1 and #4 operating

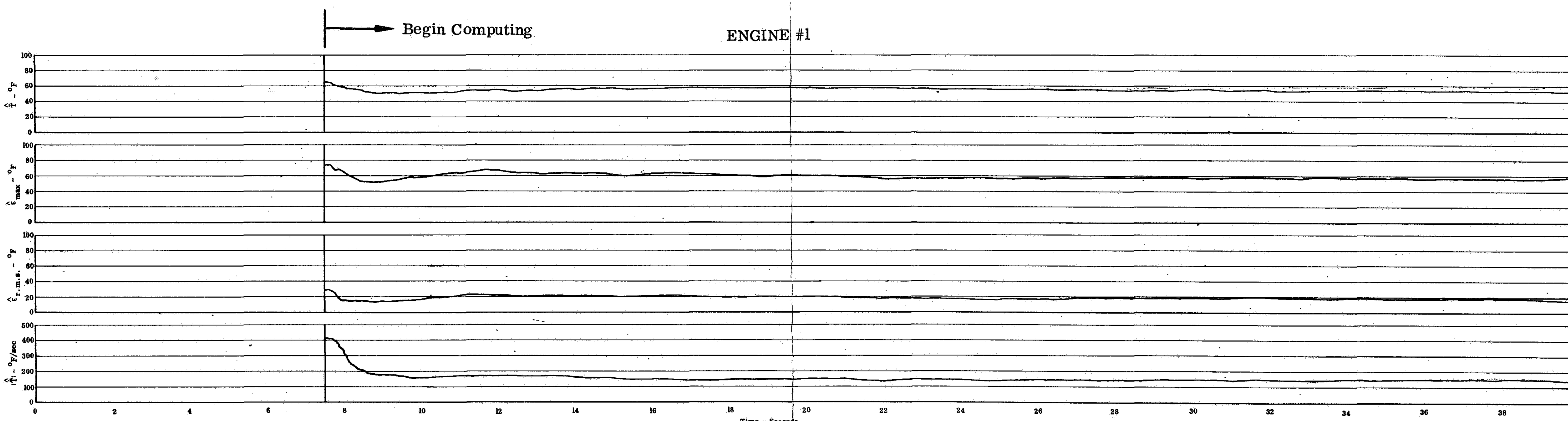

FIGURE 22. TYPICAL COMULATIVE TIME-AVERAGE OF INGESTION CHARACTERISTICS.

Test 3

H/D = 4

α = 0

Wind = 3 MPH

Engines #1 and #4 operating

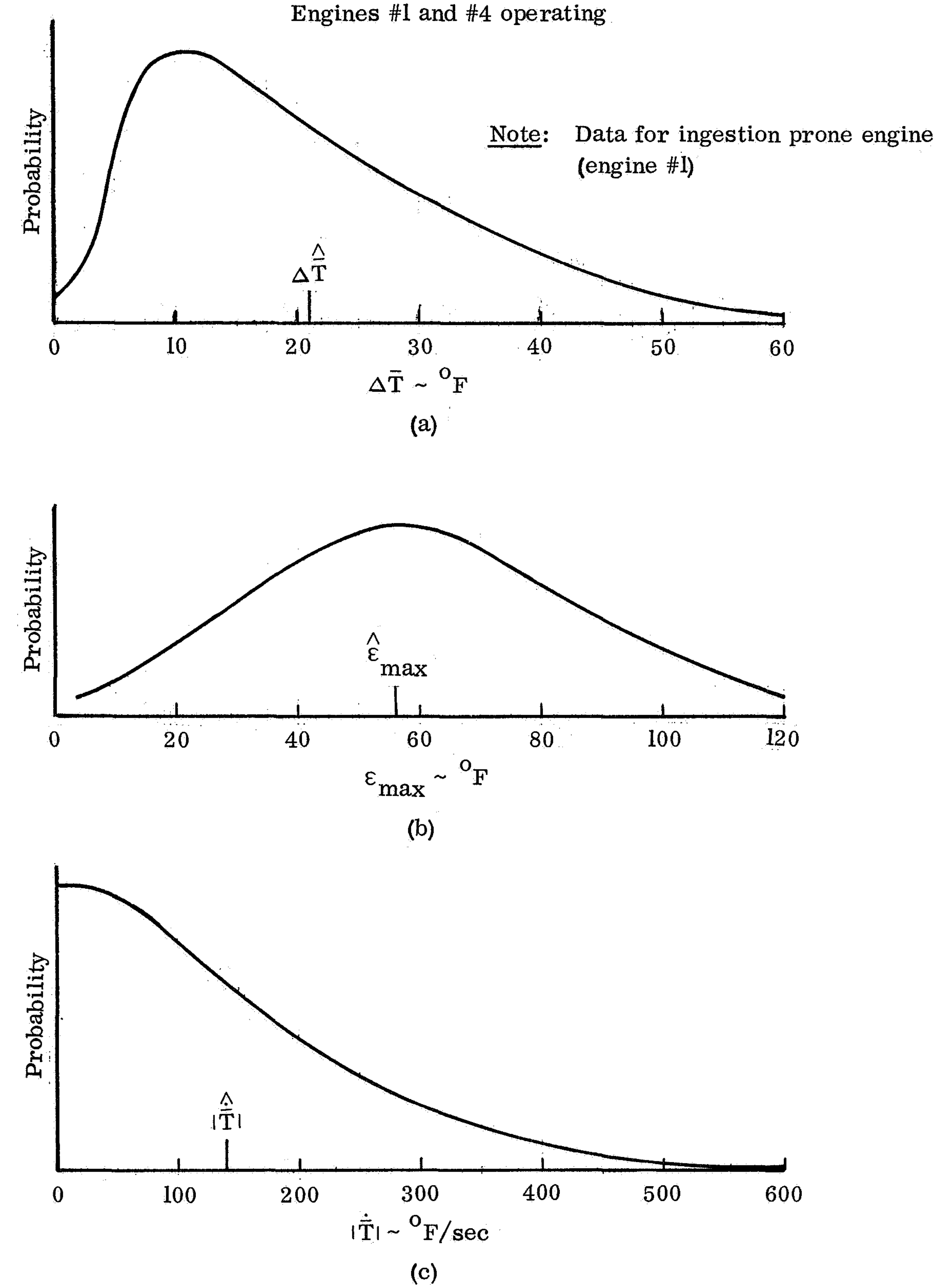

FIGURE 23. PROBABILITY DENSITY OF INGESTION CHARACTERISTICS

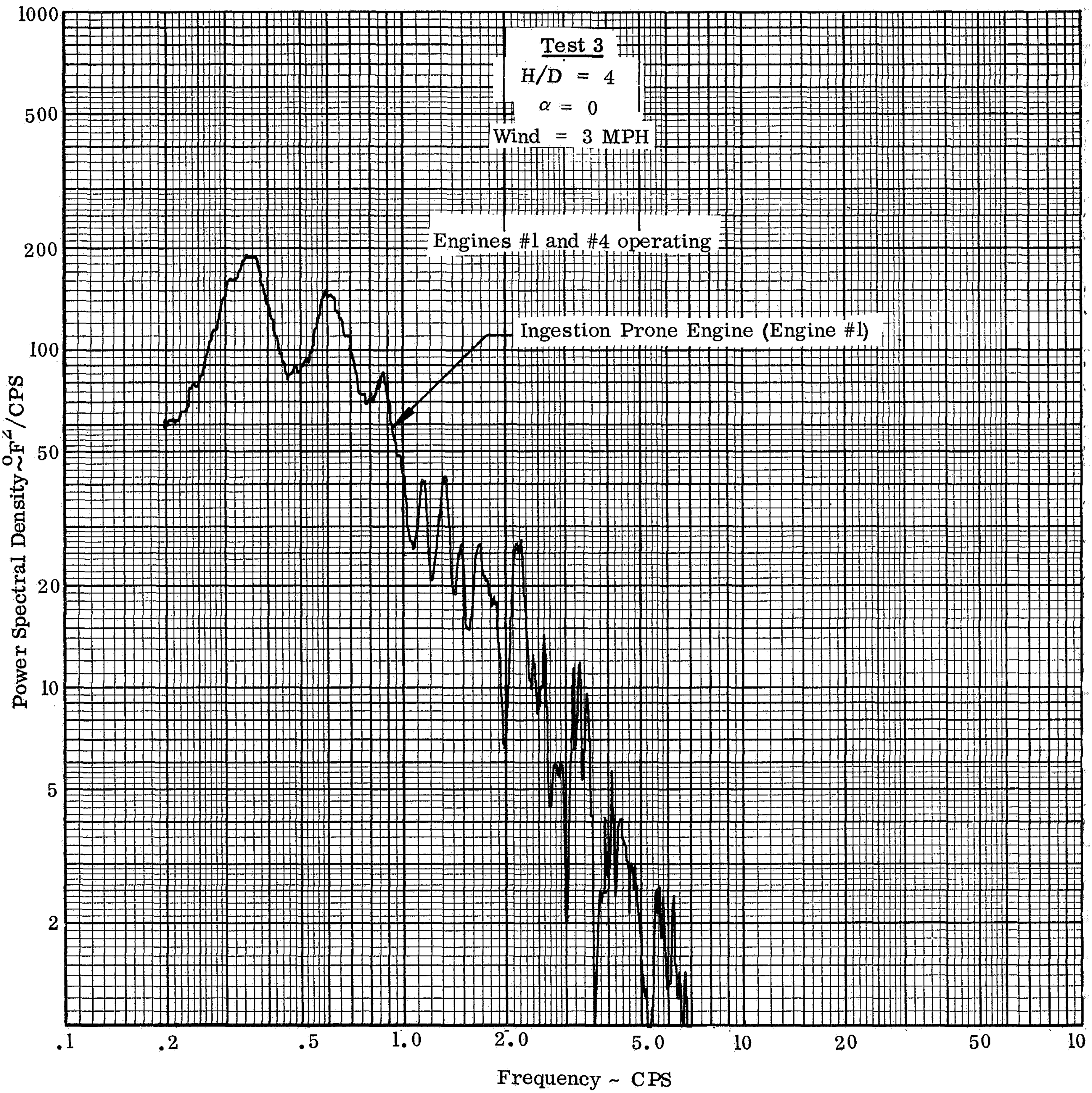

FIGURE 24. POWER SPECTRAL DENSITY OF $\overline{T}$ FLUCTUATIONS

Wind < 4 MPH

$\alpha = 0$

Engines #1 and #4 operating

Note: Data for ingestion prone engine

$$\sigma = \sqrt{\frac{1}{t}\int_0^t (\bar{T} - \hat{\bar{T}})^2 dt}$$

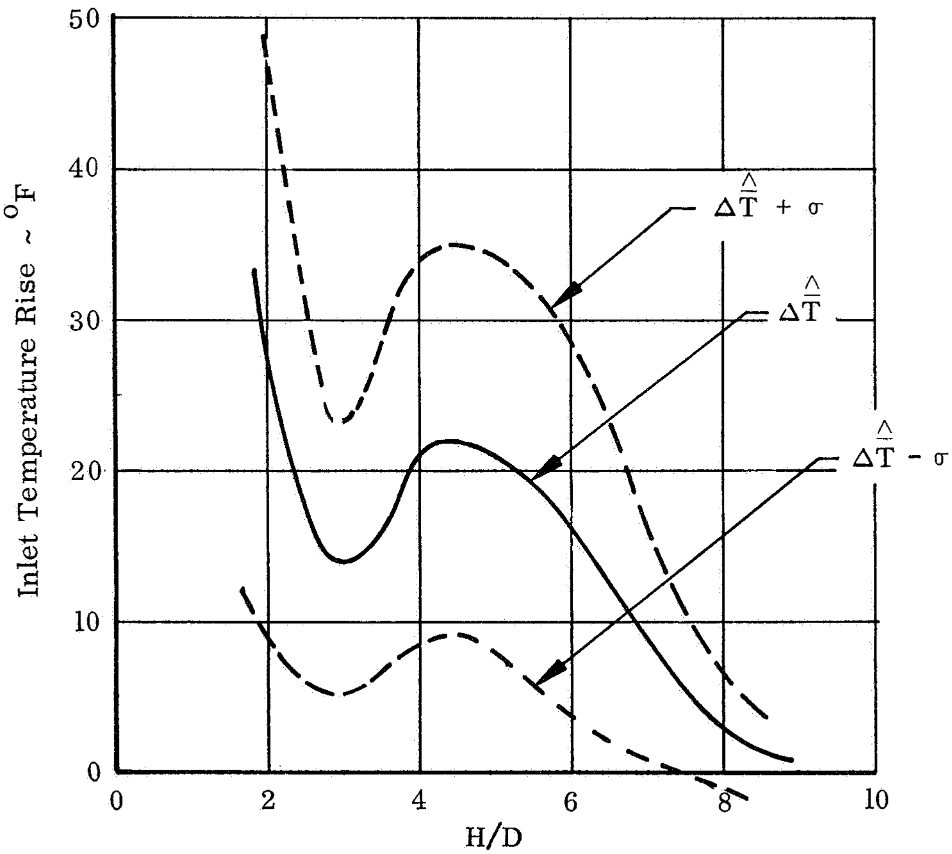

FIGURE 25. STANDARD DEVIATION OF THE MEAN TEMPERATURE RISE

Wind < 4 MPH

H/D = 4

α = 0

Engines #1 and #4 operating

Note: Data for ingestion prone engine

○ Engine #1

● Engine #4

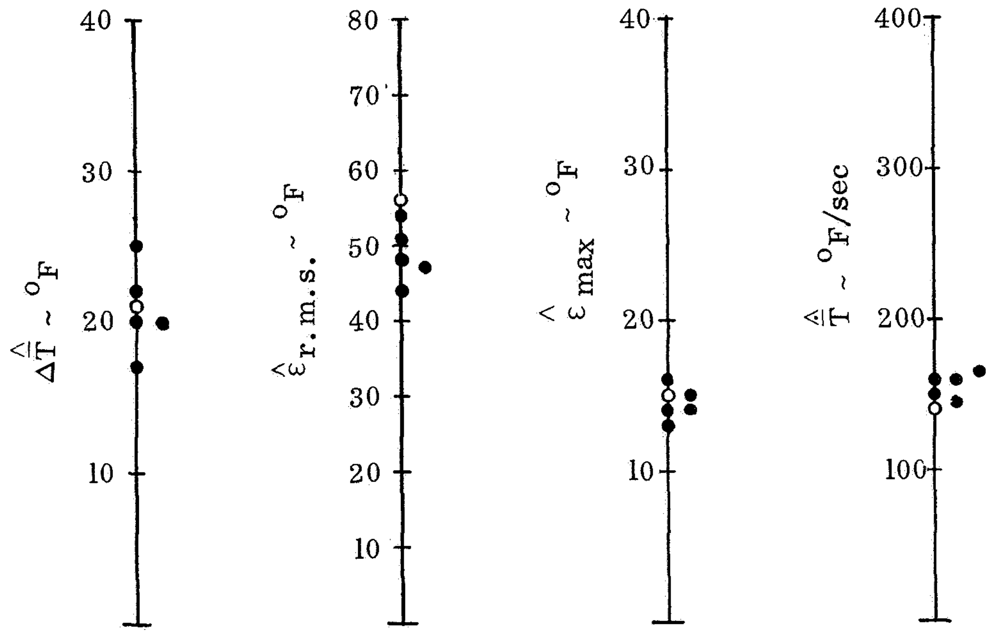

FIGURE 26 . REPEATABILITY OF INGESTION CHARACTERISTICS

○ α = 0, Wind < 4 MPH

△ α = 0, Wind 12-16 MPH

□ α = +6°, Wind < 4 MPH

Engines #1 and #4 operating

Note: Data for ingestion prone engine

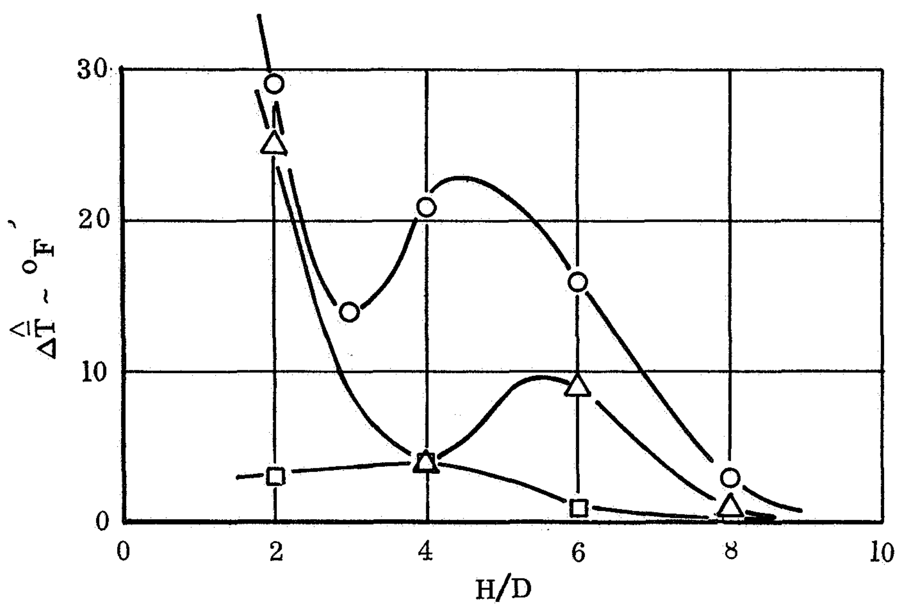

FIGURE 27. EFFECT OF H/D, WIND, AND ANGLE OF ATTACK ON INLET TEMPERATURE RISE

Engines #1 and #4 operating

○ α = 0, Wind < 4 MPH

△ α = 0, Wind = 12-16 MPH

□ α = +6°, Wind < 4 MPH

Note: Data for ingestion prone engine

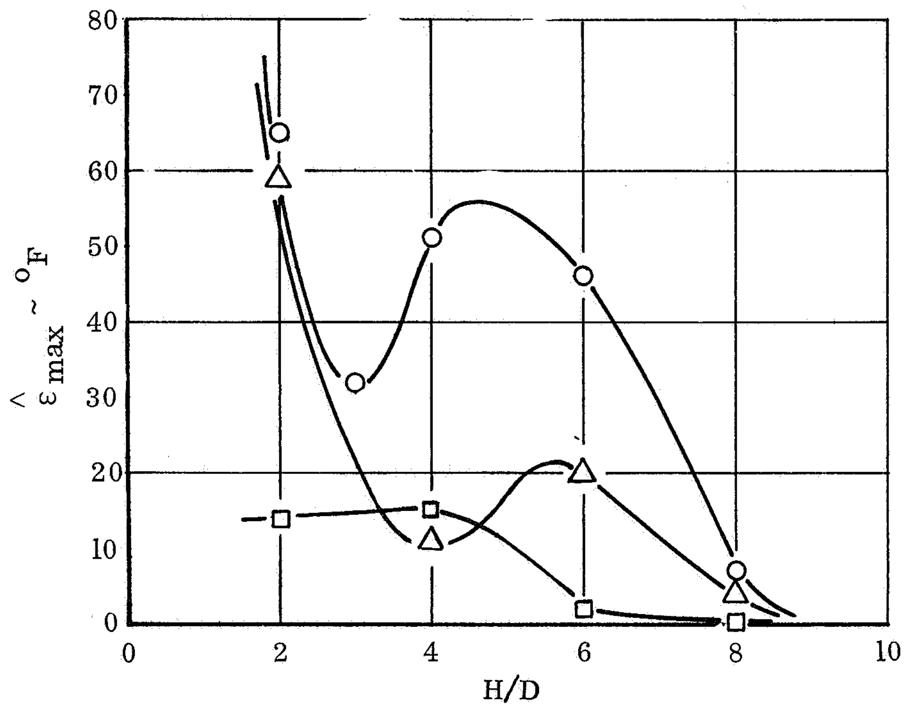

FIGURE 28. EFFECT OF H/D, WIND, AND ANGLE OF ATTACK ON INLET TEMPERATURE DISTORTION

○ α = 0, Wind < 4 MPH

△ α = 0, Wind = 12-16 MPH

□ α = +6°, Wind < 4 MPH

Engines #1 and #4 operating

<u>Note</u>: Data for ingestion prone engine

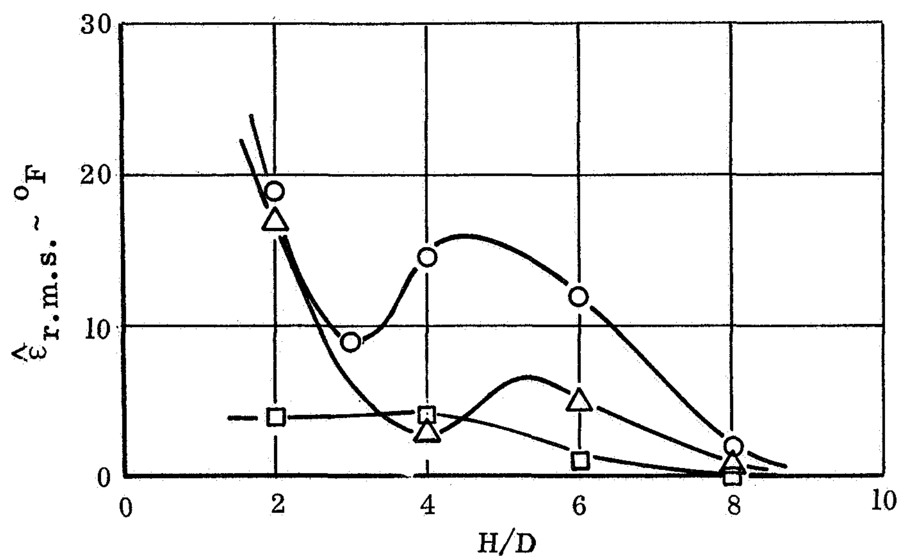

FIGURE 29. EFFECT OF H/D, WIND, AND ANGLE OF ATTACK ON INLET TEMPERATURE DISTORTION

○ α = 0, Wind < 4 MPH

△ α = 0, Wind = 12-16 MPH

□ α = +6°, Wind < 4 MPH

Engines #1 and #4 operating

Note: Data for ingestion prone engine

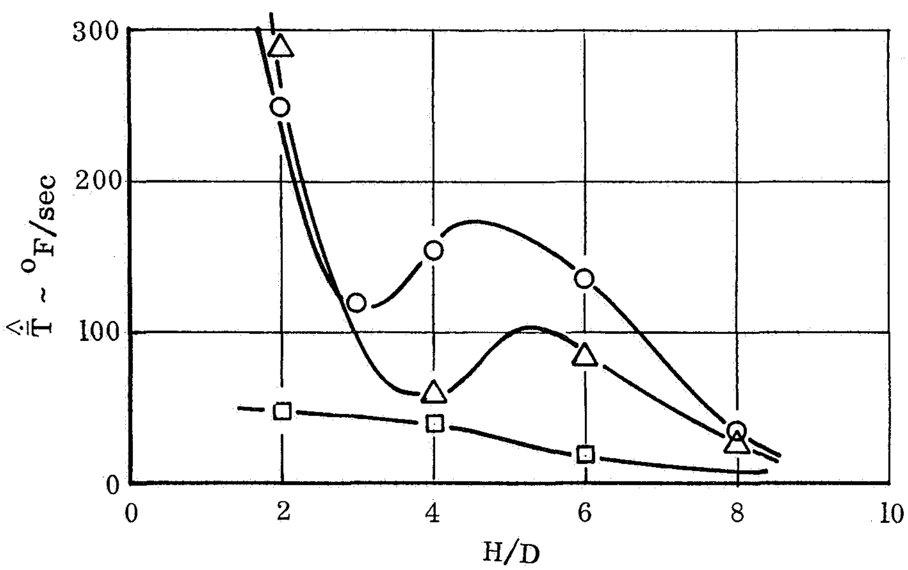

FIGURE 30. EFFECT OF H/D, WIND, AND ANGLE OF ATTACK ON INLET TEMPERATURE RATE OF RISE

H/D = 4
Wind < 4 MPH

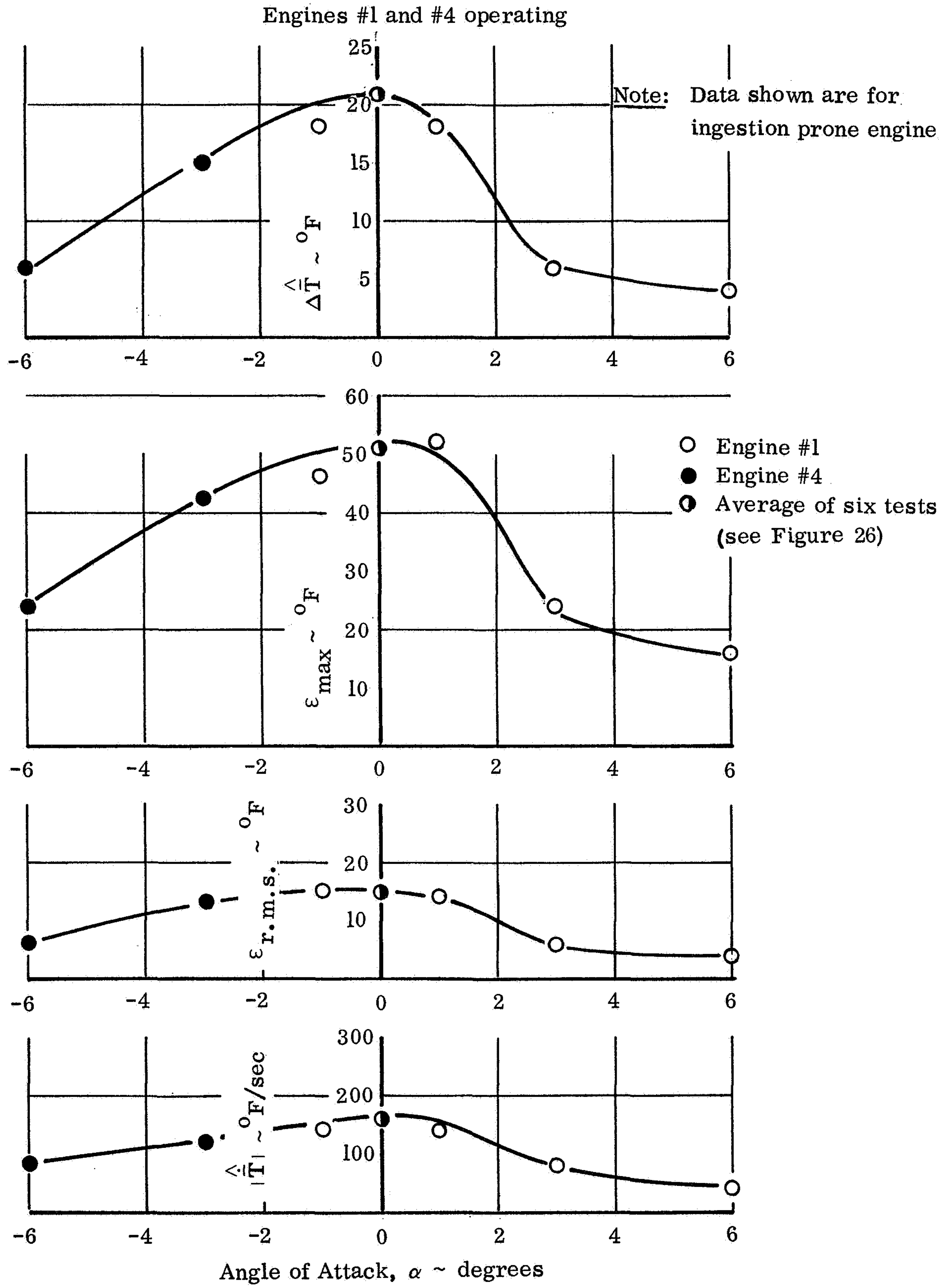

FIGURE 31. EFFECT OF ANGLE OF ATTACK ON INGESTION CHARACTERISTICS

Test 3

H/D = 4

α = 0

Wind = 3 MPH

Engines #1 and #4 operating

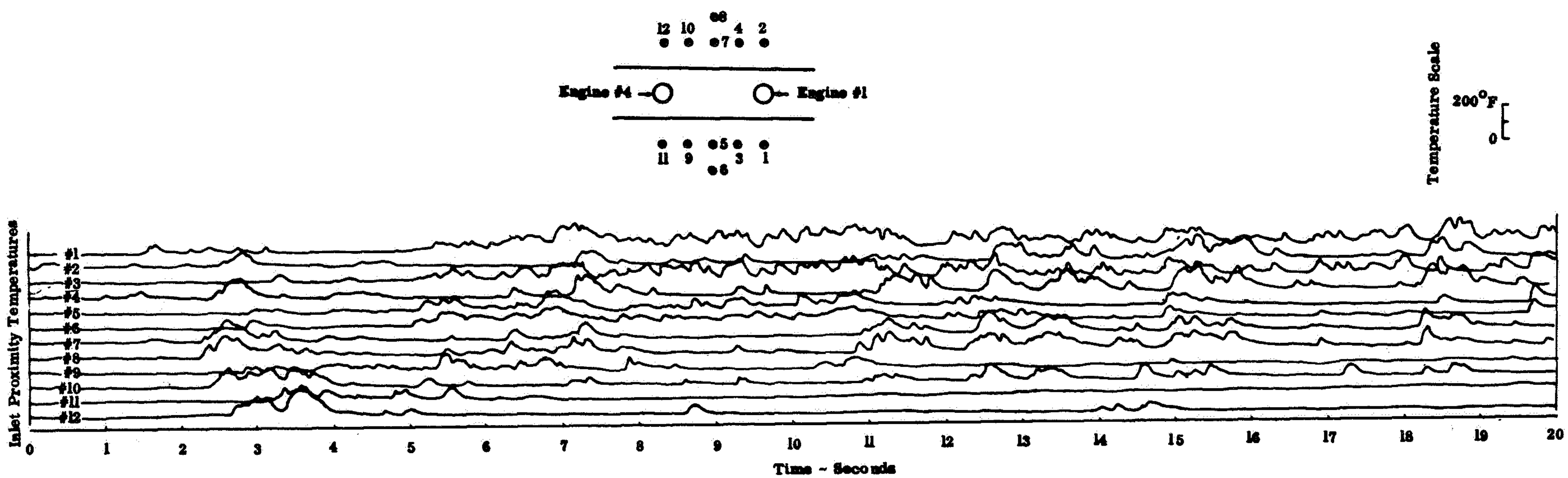

FIGURE 32. TYPICAL INLET PROXIMITY TEMPERATURE HISTORY

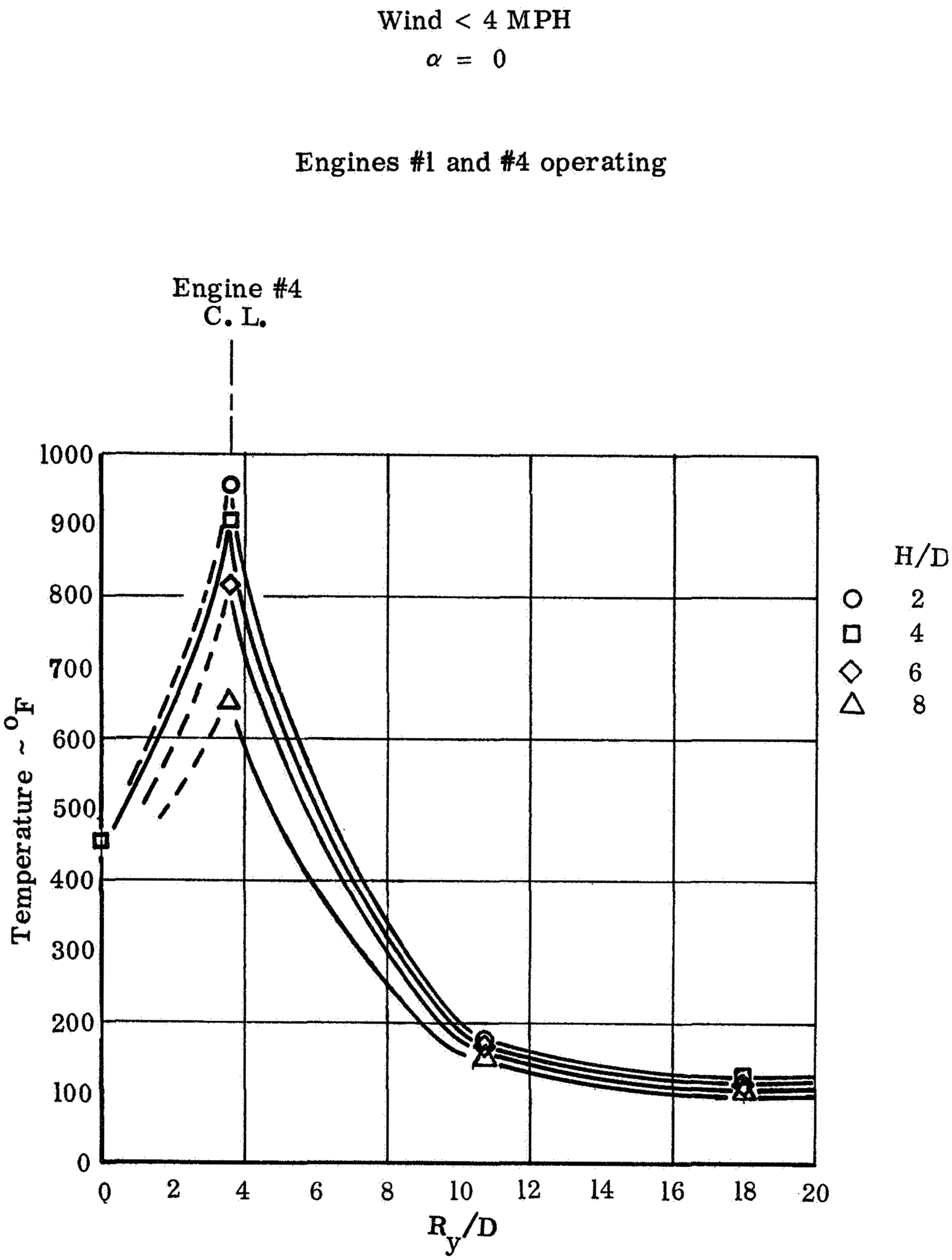

(a)

FIGURE 33. VARIATION IN GROUND PLANE TEMPERATURE WITH R/D AND H/D FOR TWO ENGINE OPERATION

Wind < 4 MPH

$\alpha = 0$

Engines #1 and #4 operating

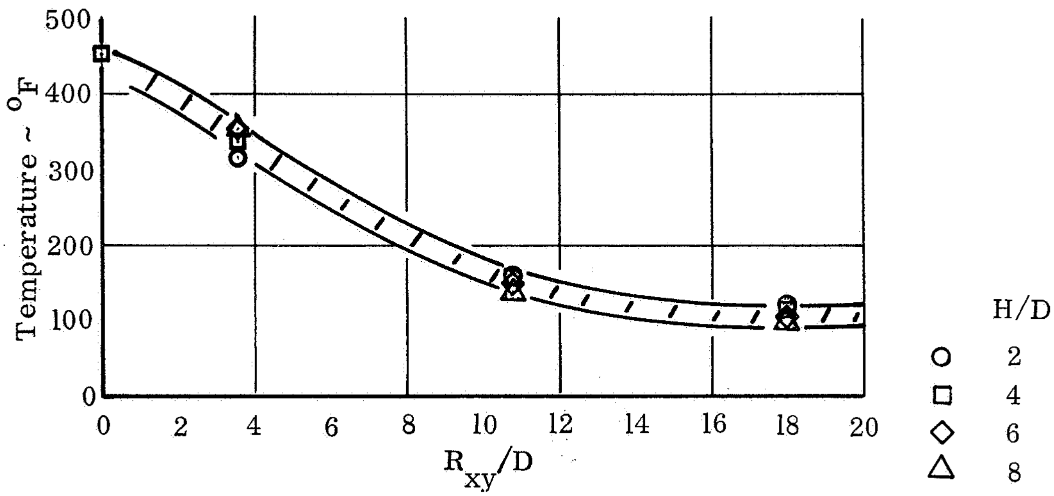

(b)

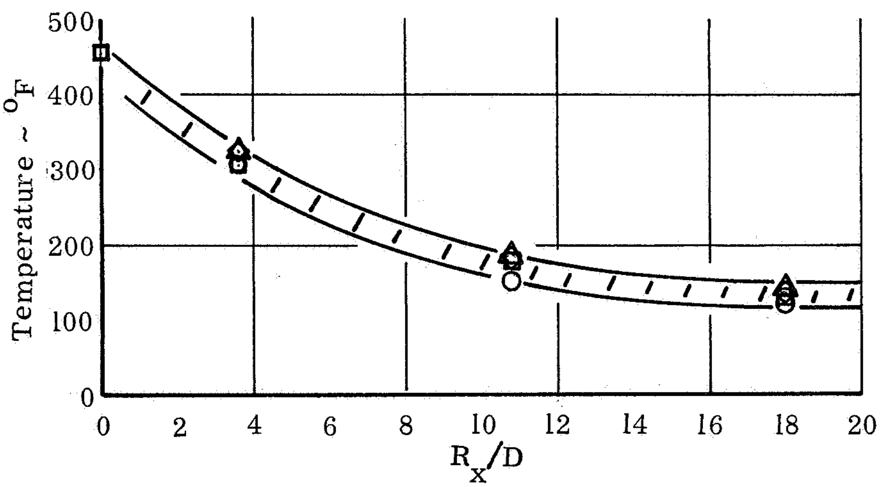

(c)

FIGURE 33 (CONT.). VARIATION IN GROUND PLANE TEMPERATURE WITH R/D AND H/D FOR TWO ENGINE OPERATION

Wind < 4 MPH
$\alpha = 0$

Engine #4 operating

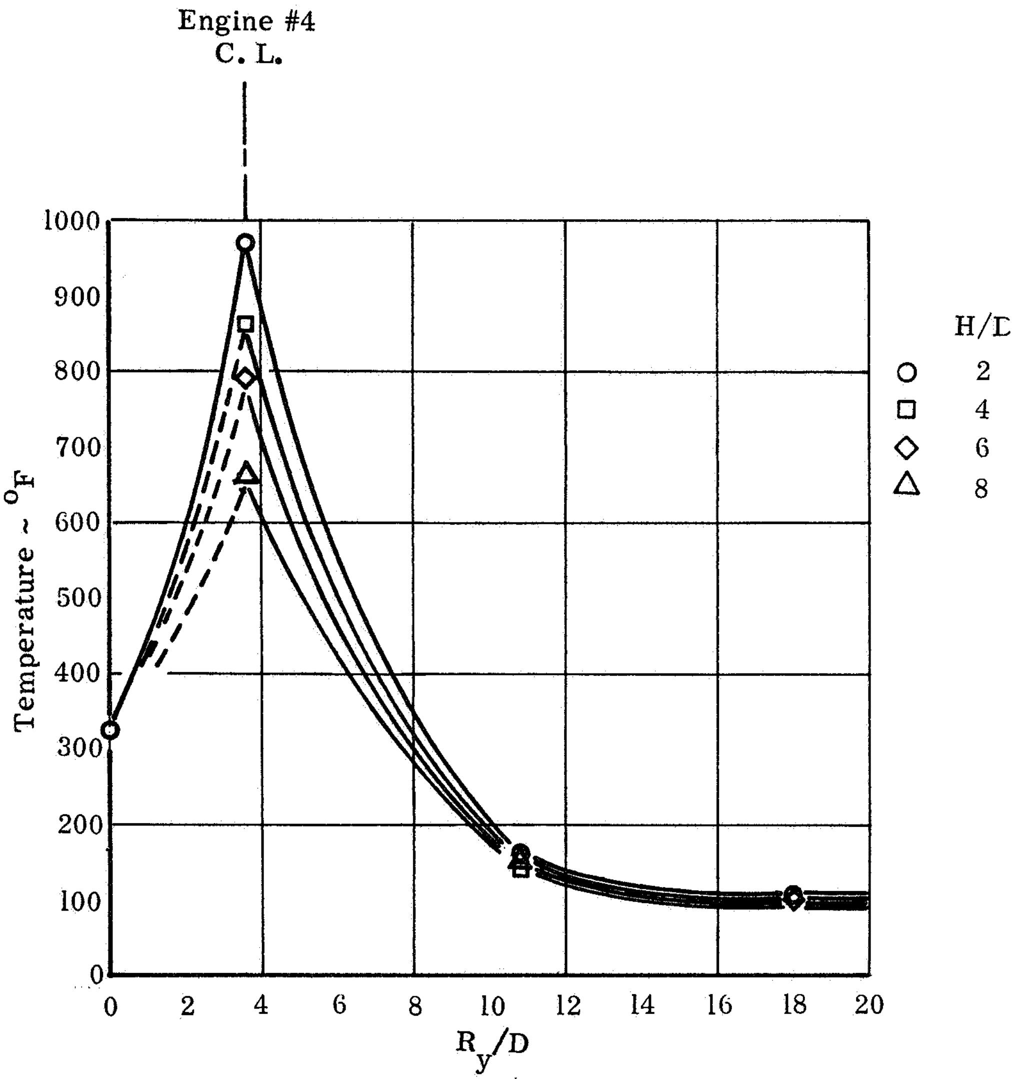

(a)

FIGURE 34. VARIATION IN GROUND PLANE TEMPERATURE WITH R/D AND H/D FOR SINGLE ENGINE OPERATION

Wind < 4 MPH

$\alpha = 0$

Engine #4 operating

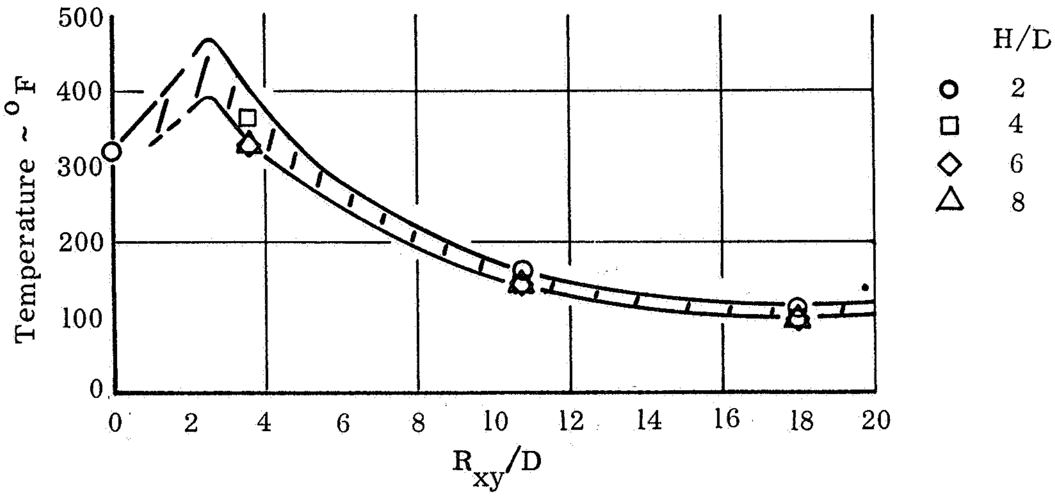

(b)

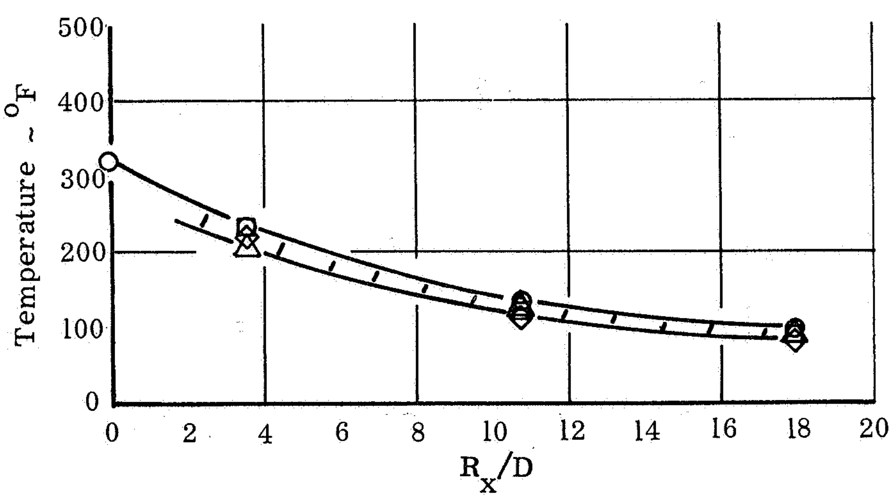

(c)

FIGURE 34 (CONT.). VARIATION IN GROUND PLANE TEMPERATURE WITH R/D AND H/D FOR SINGLE ENGINE OPERATION

$\alpha = 0$

Engines #1 and #4 operating

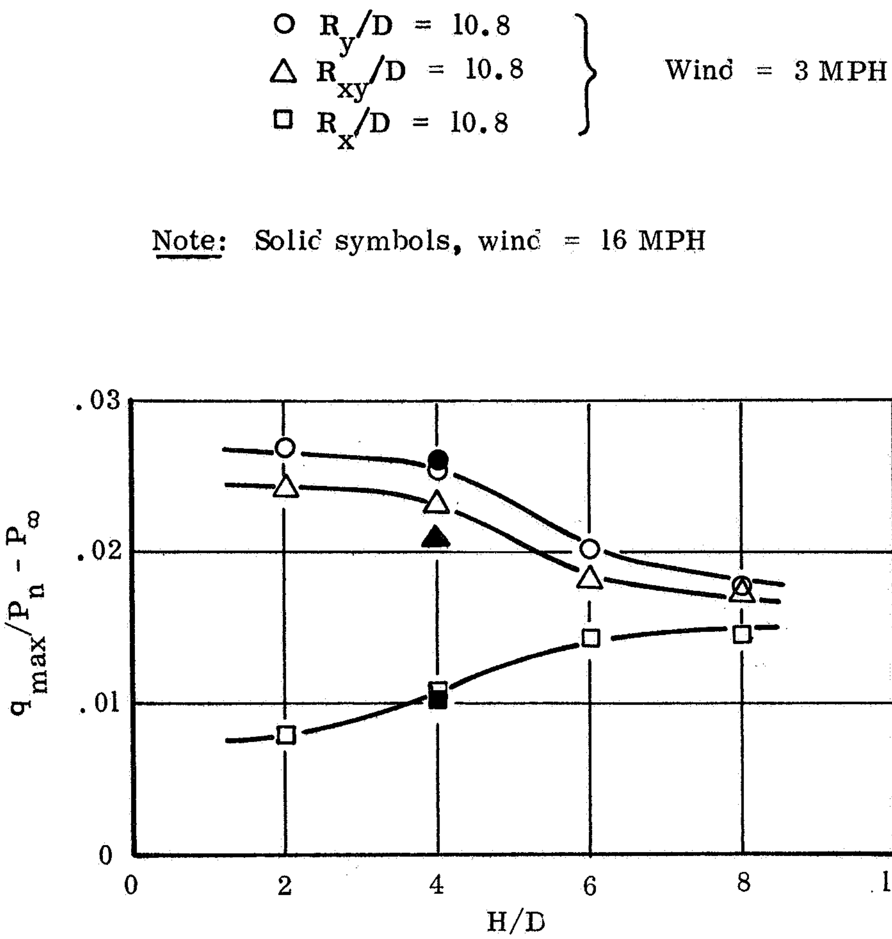

FIGURE 35. EFFECT OF H/D AND WIND ON GROUND JET DYNAMIC PRESSURE FOR TWO ENGINE OPERATION

H/D = 4
α = 0

Engines #1 and #4 operating

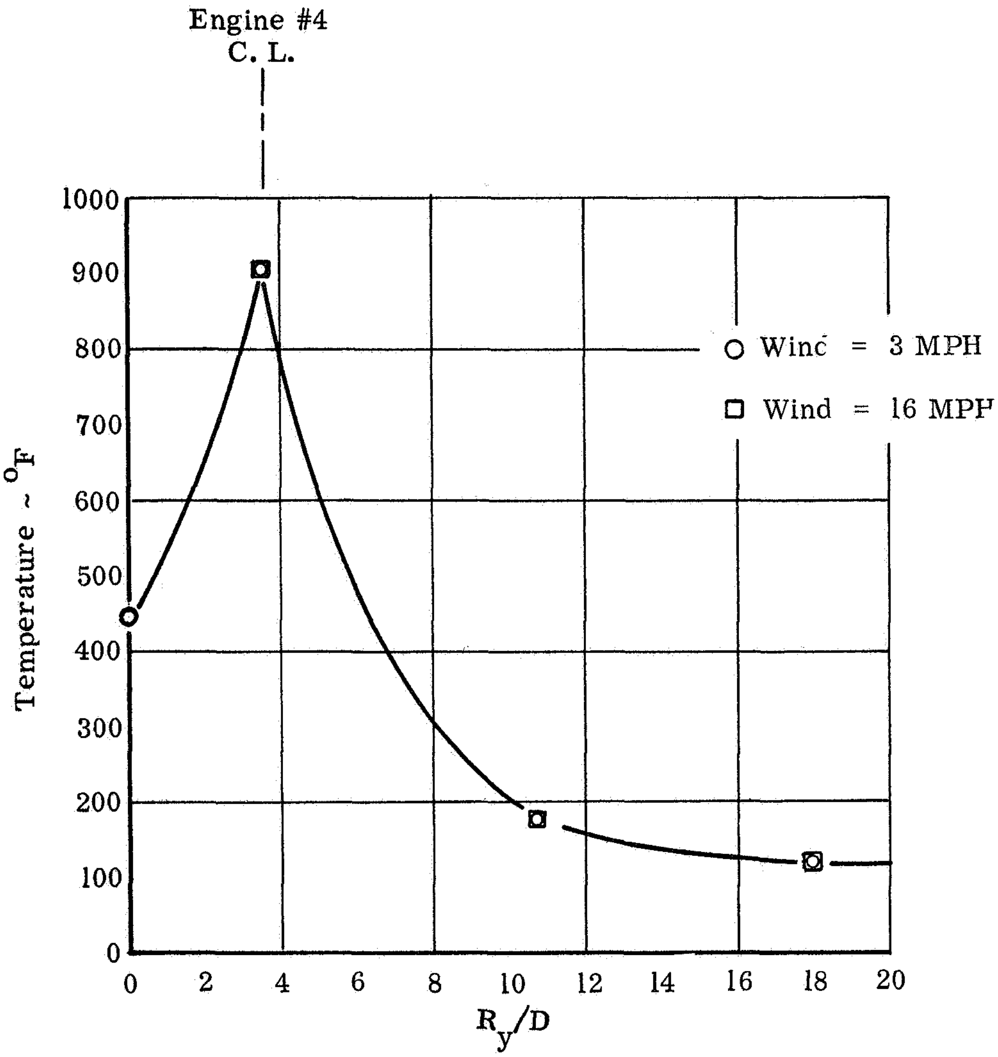

(a)

FIGURE 36. EFFECT OF WIND ON GROUND PLANE TEMPERATURE FOR TWO ENGINE OPERATION

H/D = 4

α = 0

Engines #1 and #4 operating

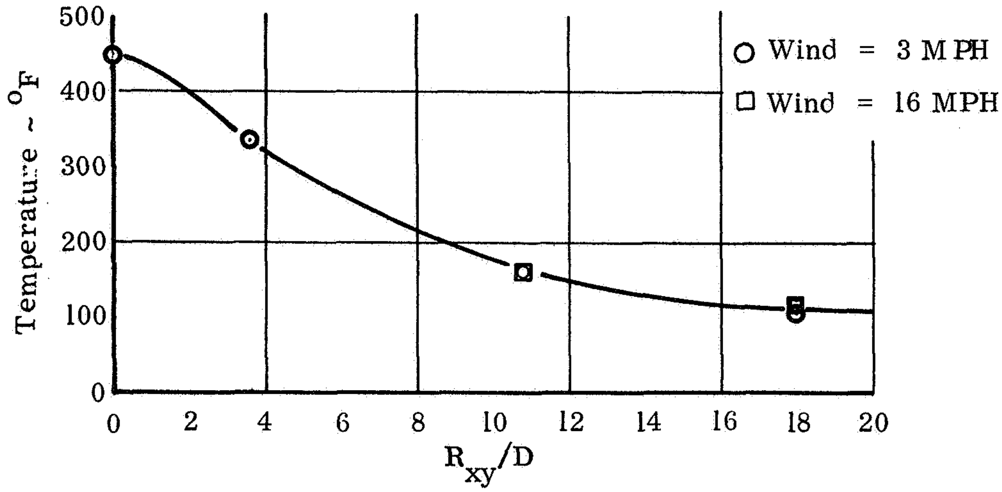

(b)

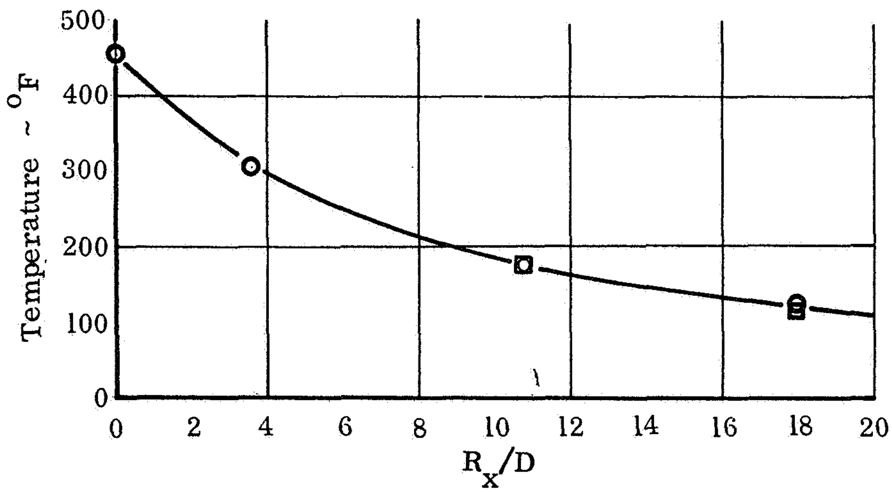

(c)

FIGURE 36 (CONT.). EFFECT OF WIND ON GROUND PLANE TEMPERATURE FOR TWO ENGINE OPERATION

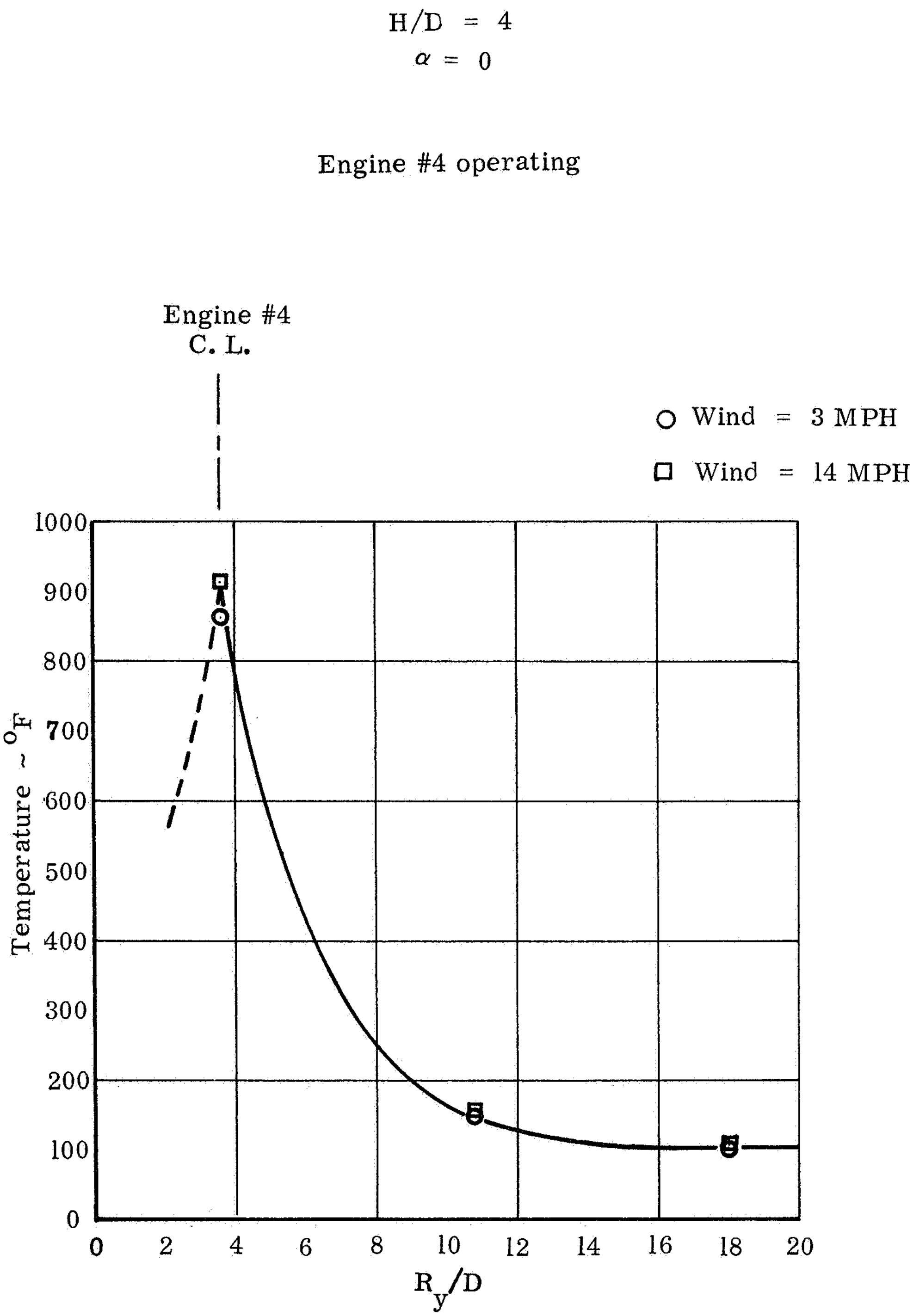

(a)

FIGURE 37. EFFECT OF WIND ON GROUND PLANE TEMPERATURE FOR SINGLE ENGINE OPERATION

H/D = 4

α = 0

Engine #4 operating

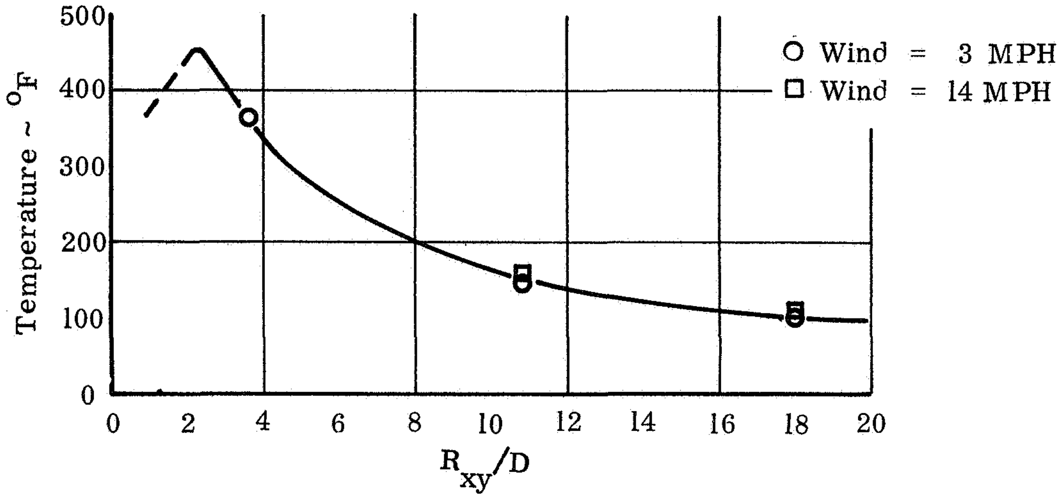

(b)

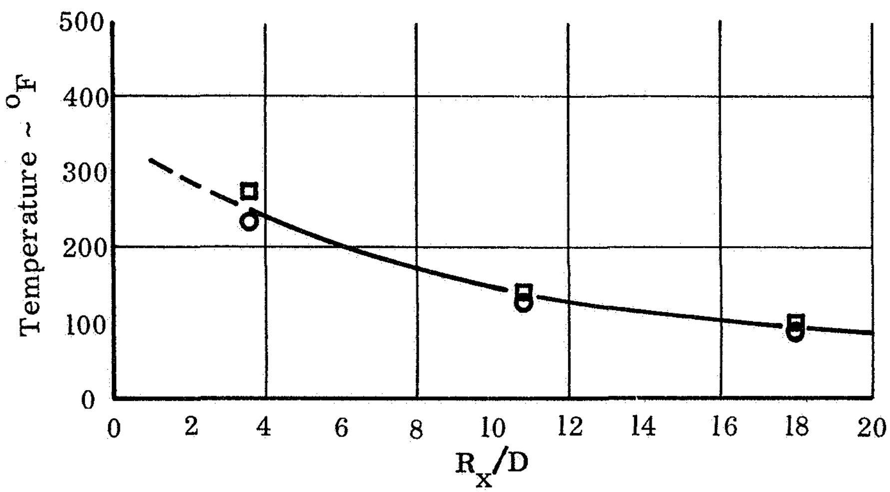

(c)

FIGURE 37 (CONT.). EFFECT OF WIND ON GROUND PLANE TEMPERATURE FOR SINGLE ENGINE OPERATION

H/D = 4

Wind < 4 MPH

Engines #1 and #4 operating

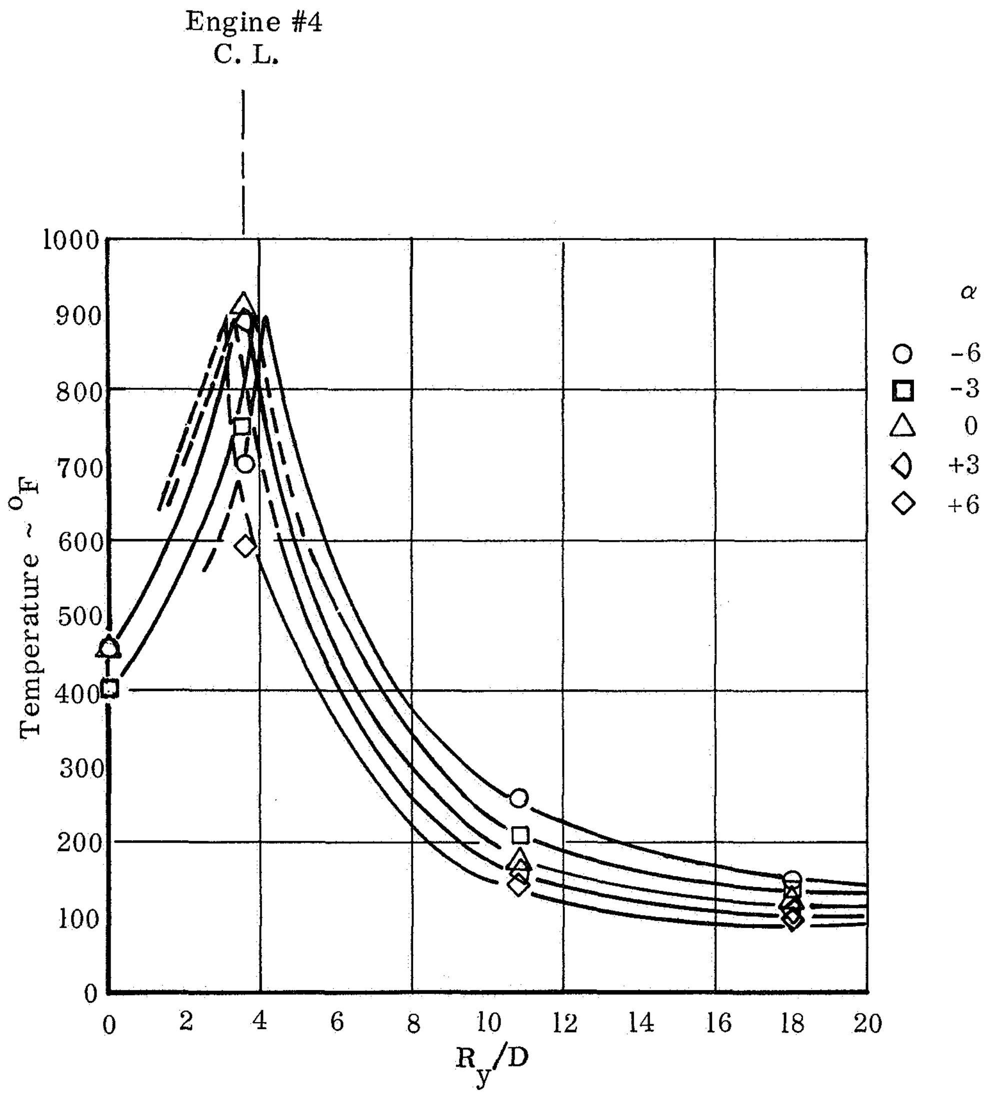

(a)

FIGURE 38. EFFECT OF ANGLE OF ATTACK ON GROUND PLANE TEMPERATURE FOR TWO ENGINE OPERATION

H/D = 4

Wind < 4 MPH

Engines #1 and #4 operating

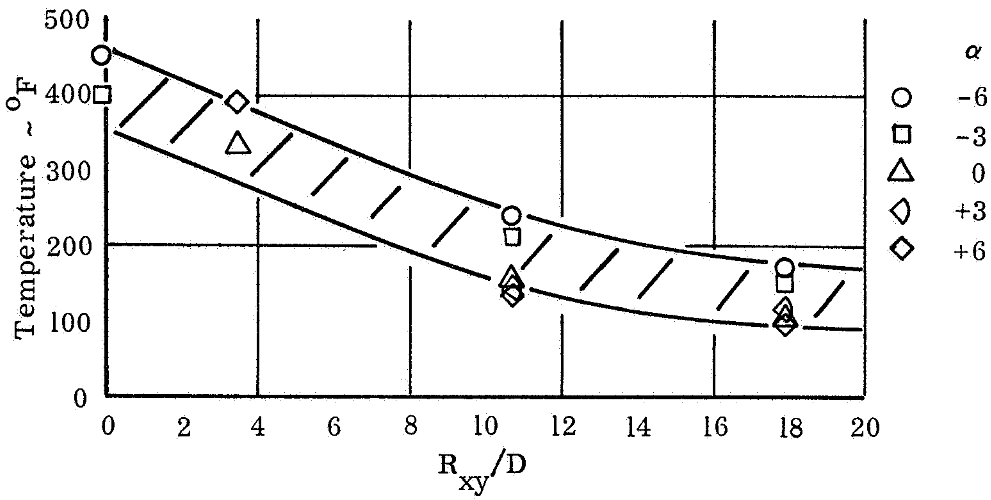

(b)

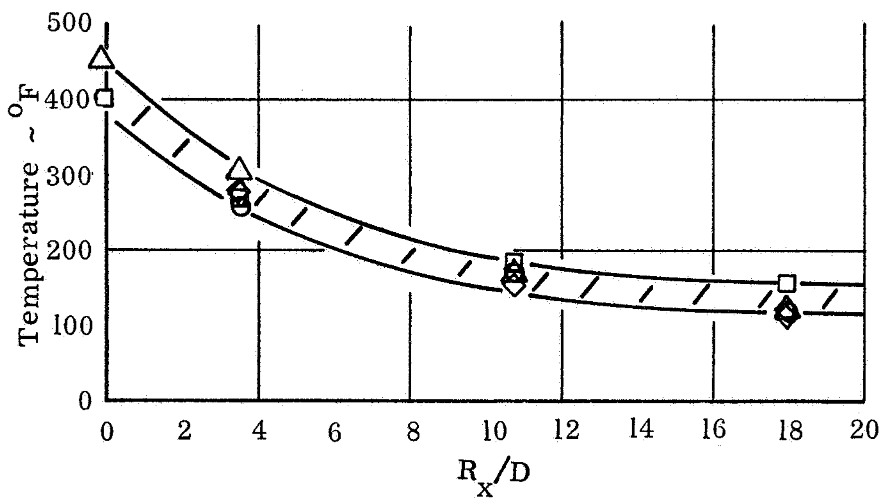

(c)

FIGURE 38 (CONT.). EFFECT OF ANGLE OF ATTACK ON GROUND PLANE TEMPERATURE FOR TWO ENGINE OPERATION

H/D = 4

Wind < 4 MPH

Engines #1 and #4 operating

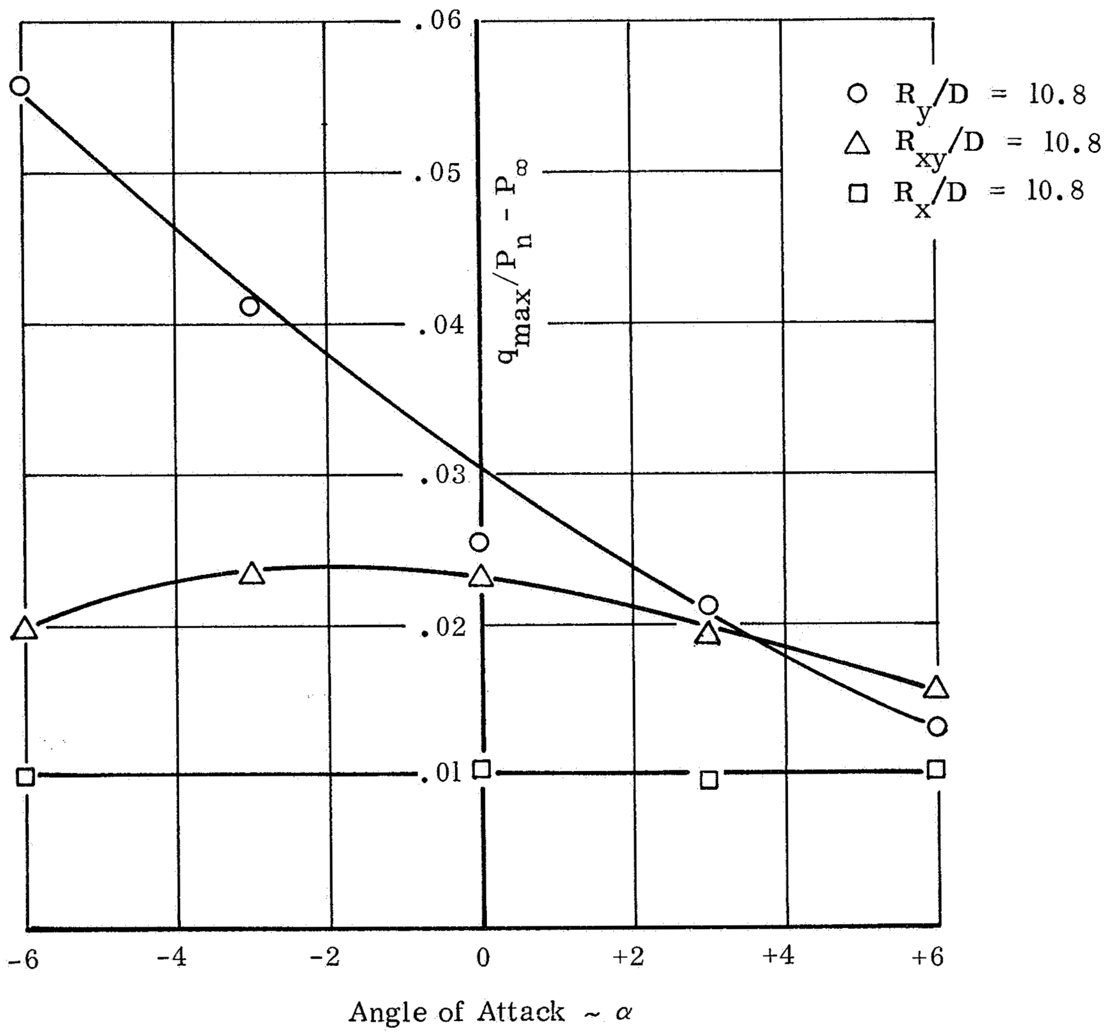

FIGURE 39. EFFECT OF ANGLE OF ATTACK ON GROUND JET DYNAMIC PRESSURE FOR TWO ENGINE OPERATION

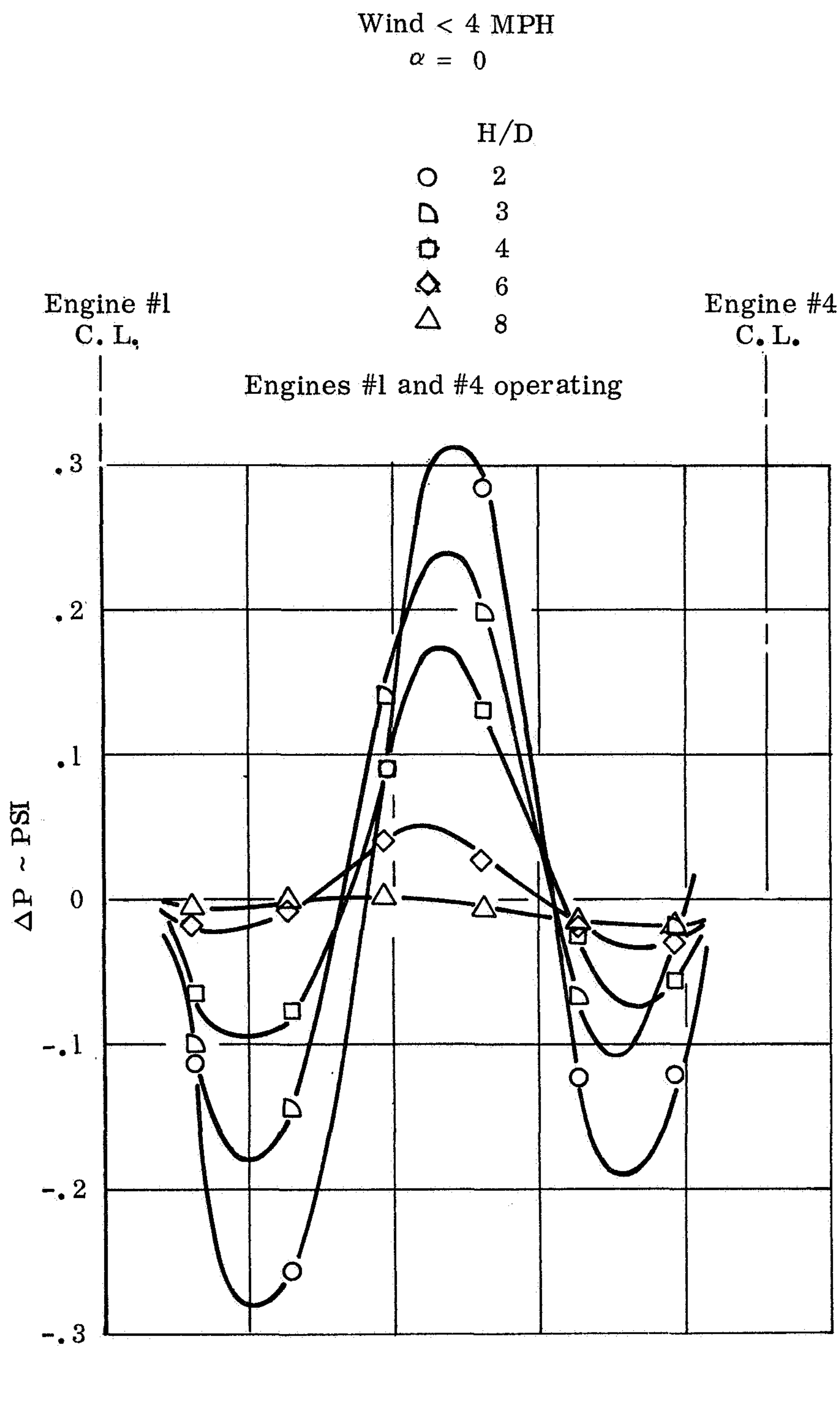

FIGURE 40. POD UNDERSURFACE PRESSURE DISTRIBUTION AT LOW WIND CONDITIONS

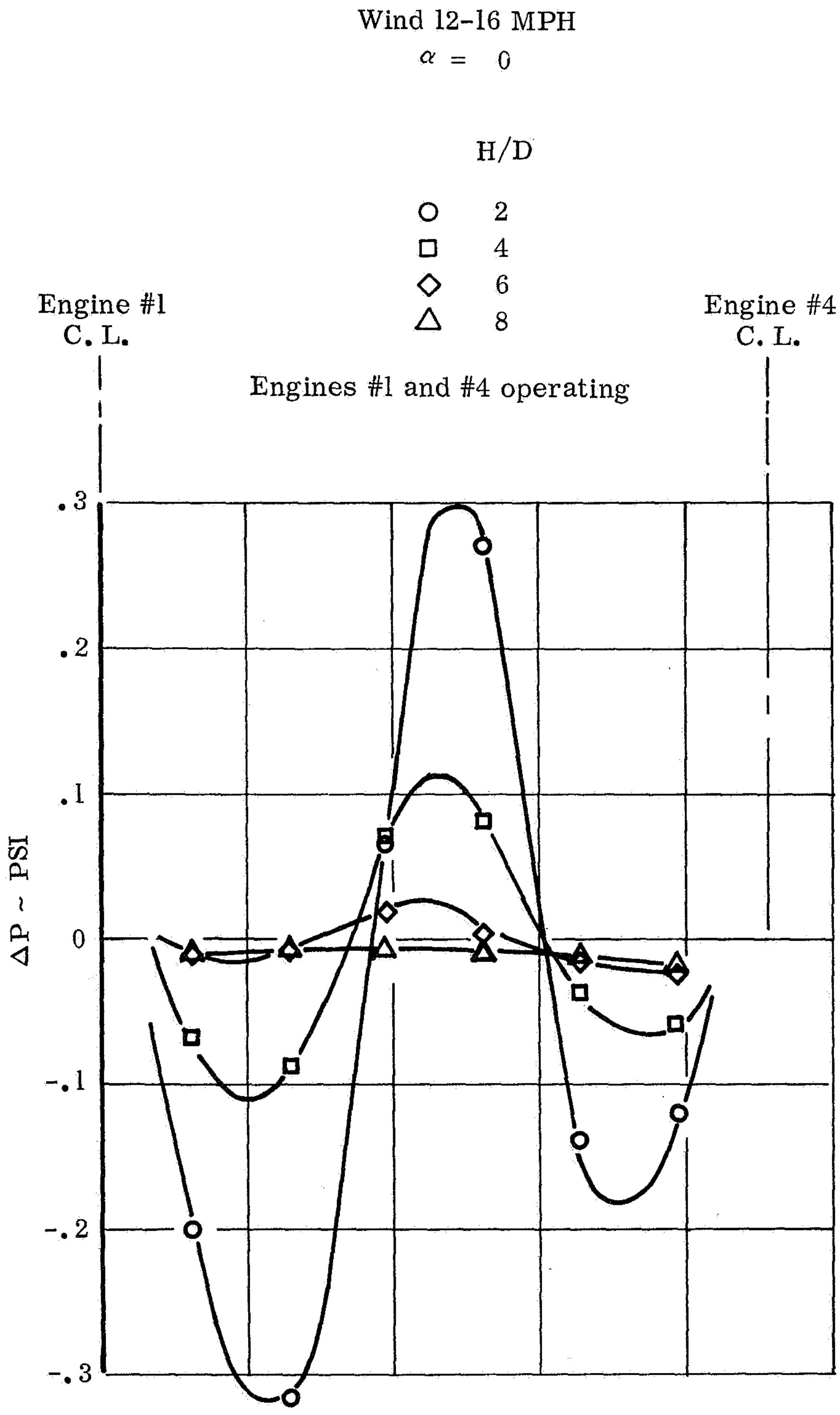

FIGURE 41. POD UNDERSURFACE PRESSURE DISTRIBUTION AT HIGH WIND CONDITIONS

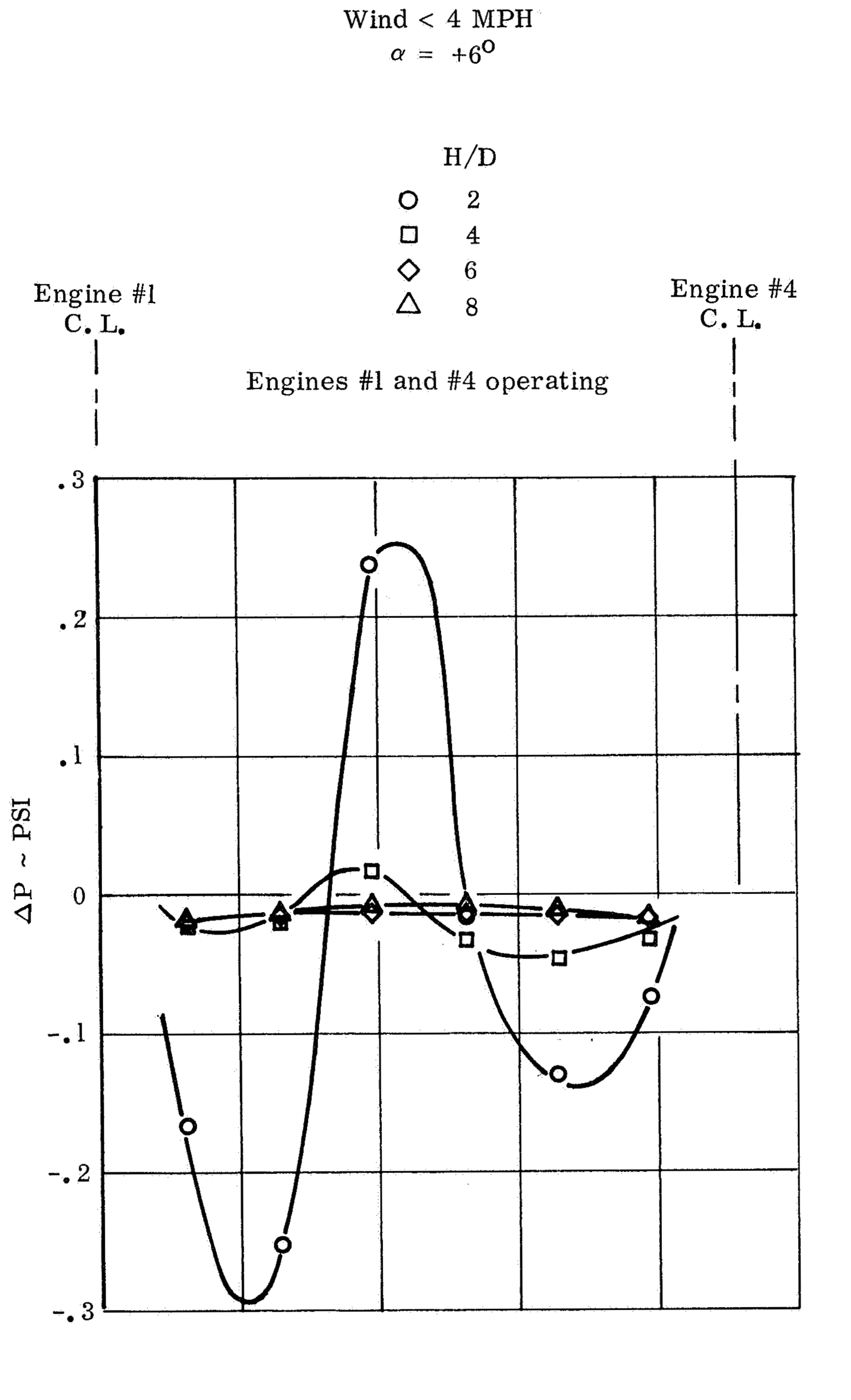

FIGURE 42. POD UNDERSURFACE PRESSURE DISTRIBUTION AT ANGLE OF ATTACK

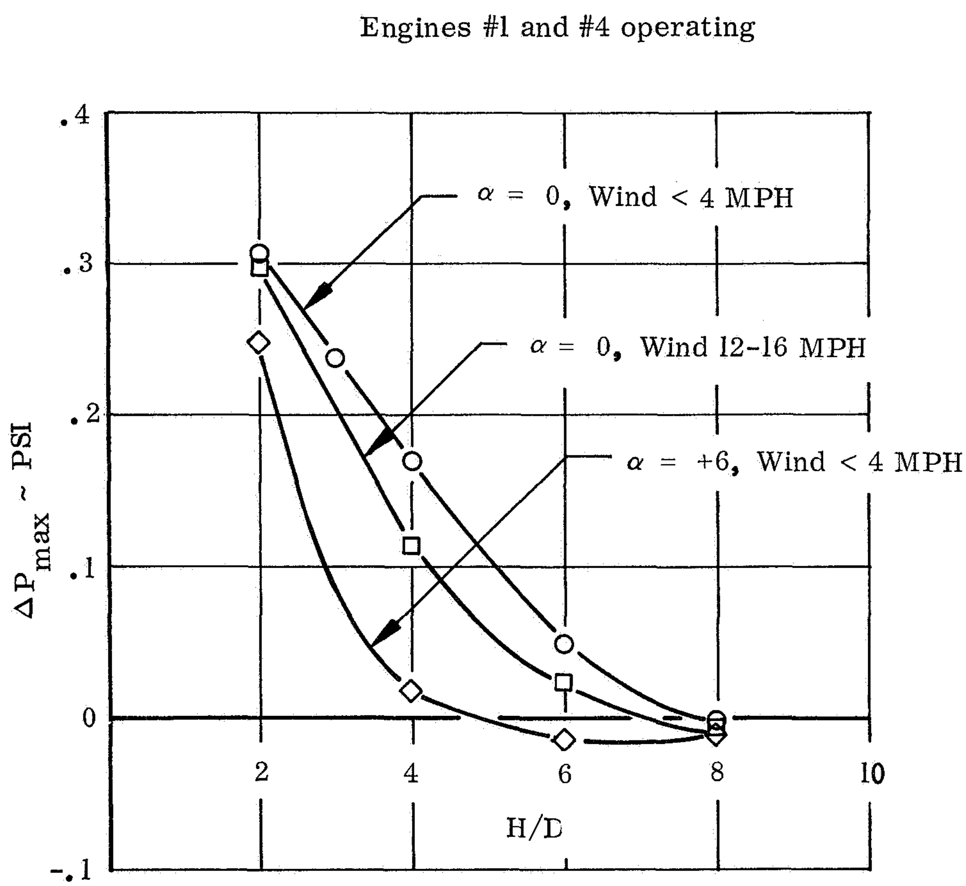

FIGURE 43. EFFECT OF H/D, WIND, AND ANGLE OF ATTACK ON POD UNDERSURFACE PRESSURE

H/D = 4
Wind < 4 MPH

Engines #1 and #4 operating

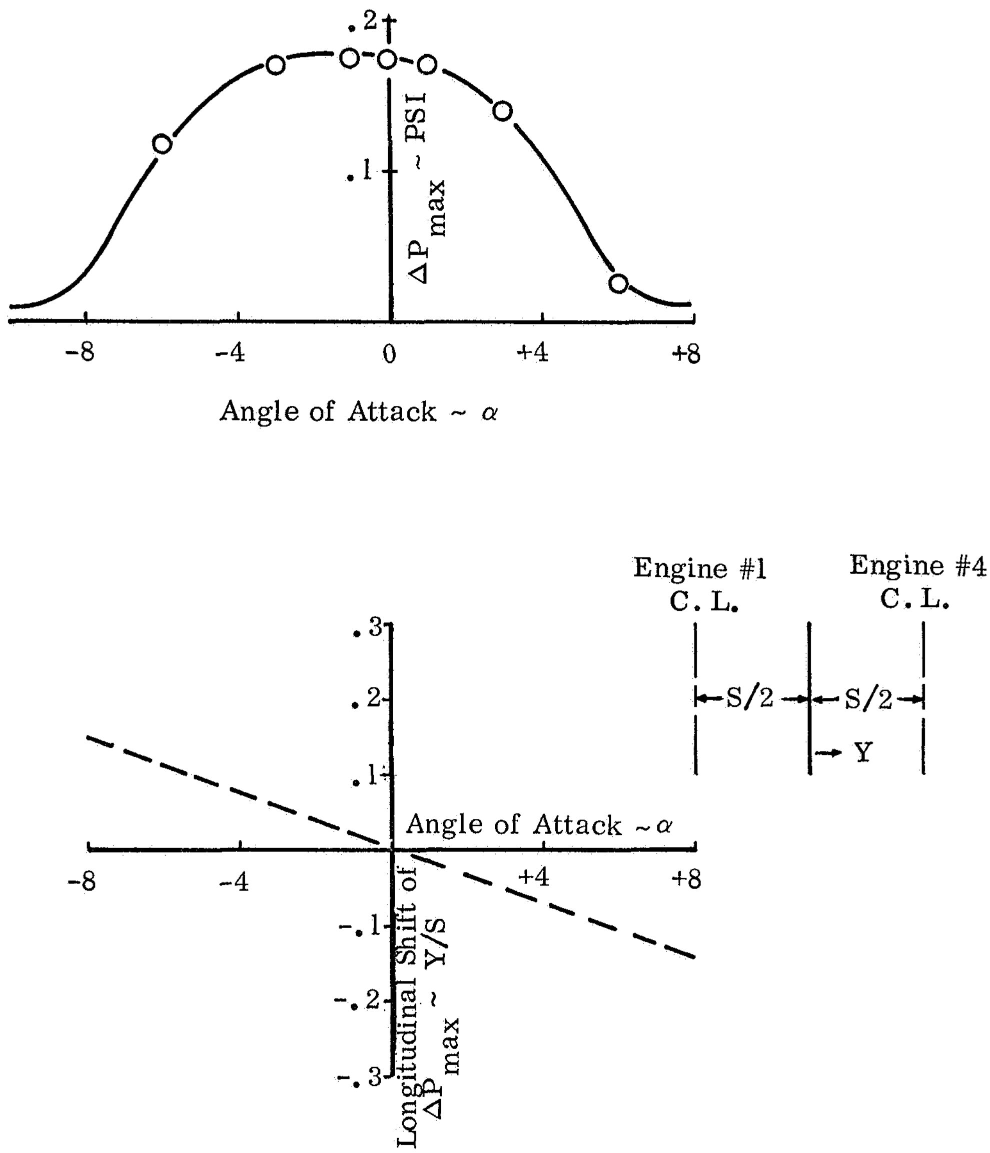

FIGURE 44. EFFECT OF ANGLE OF ATTACK ON POD PEAK PRESSURE AMPLITUDE AND LOCATION

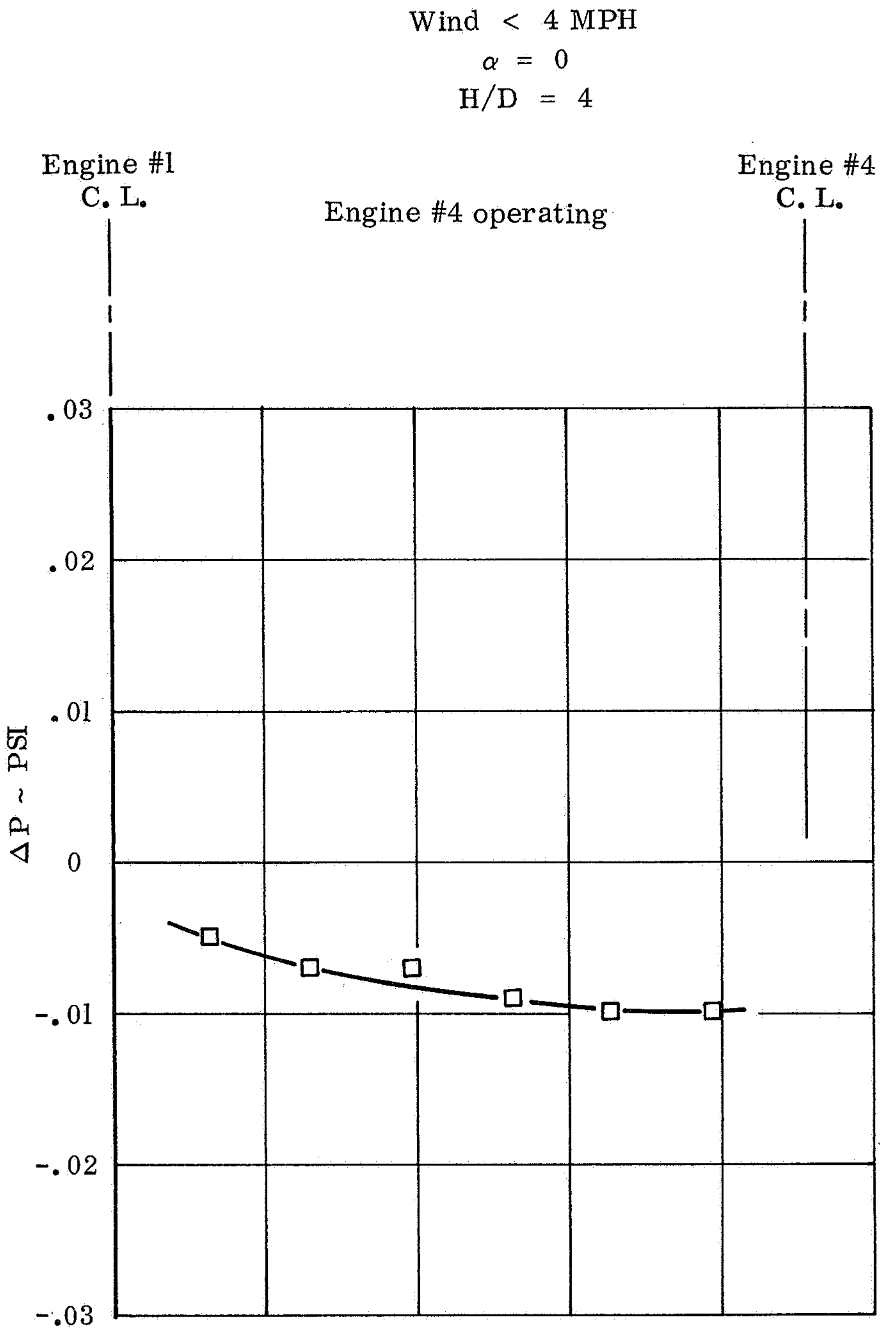

FIGURE 45. POD UNDERSURFACE PRESSURE DISTRIBUTION FOR SINGLE JET OPERATION

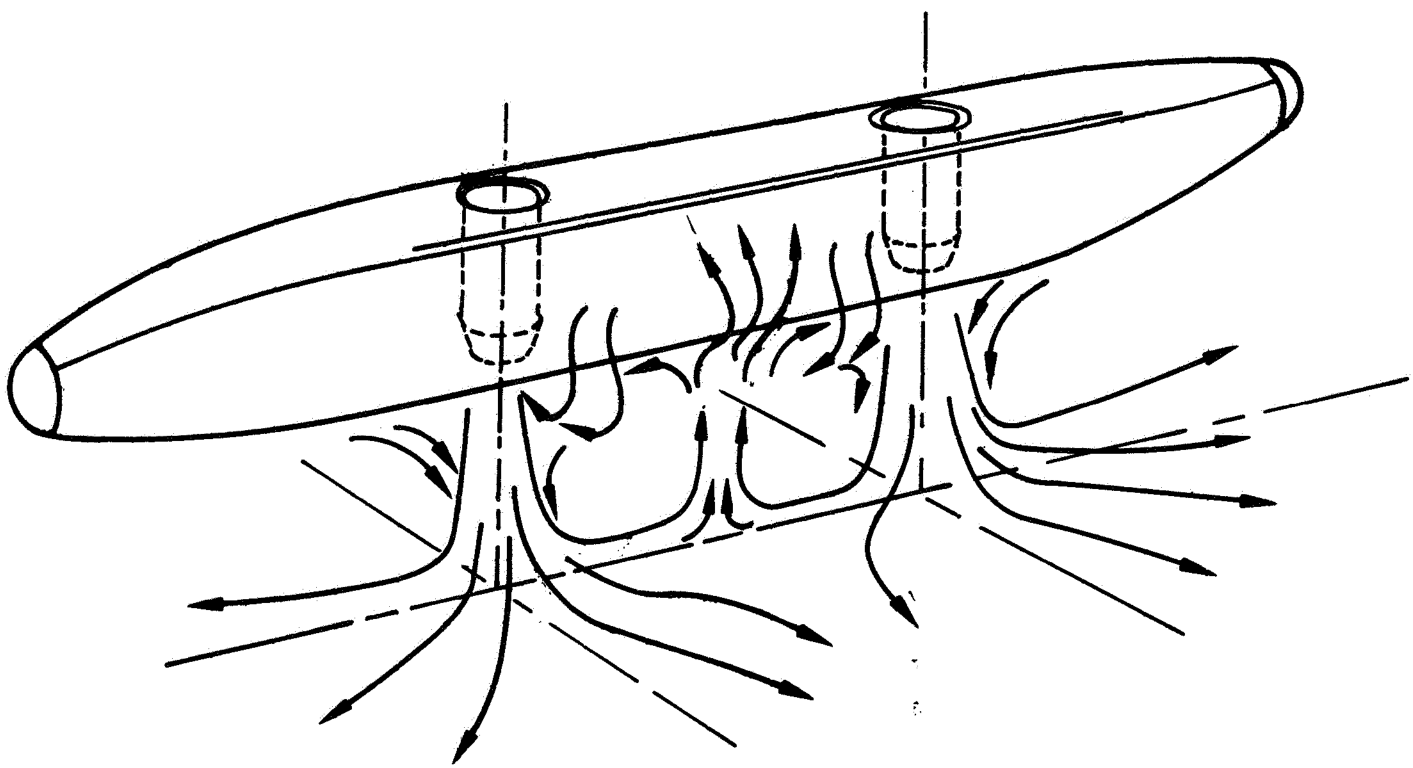

FIGURE 46. NOMINAL FLOW STRUCTURE BETWEEN GROUND PLANE AND POD FOR TWO ENGINE OPERATION

APPENDIX

Presented herein is a set of reduced data for each of the tests indicated in Table A-1. Table A-1 serves as an index for the data which follow and also provides summary information on the various time-average ingestion characteristics for each test. The nominal period of computation of the time-average ingestion indices was 30 sec. The absence of a numerical value for $\left|\dot{\hat{T}}\right|$ in Table A-1 indicates the value is less than 40°F/sec. The accuracy of the various time varying and time-average ingestion indices is considered to be about ±2°F.

/

TEST CONDITIONS						ENGINE		
Test No.	Engines Operating	Pod Height H/D	Angle of Attack α	Wind Conditions: Speed	Wind Conditions: Direction	$\hat{\Delta T}$ (°F)	$\hat{\varepsilon}_{max}$ (°F)	$\hat{\varepsilon}_{r.m}$
1	#1 & #4	2	0	<4 mph	N	**29**	**62**	
2	↓	3	↓	↓	NW	**14**	**32**	
3	↓	4	↓	↓	NW	**21**	**56**	
4[1]	↓	↓	↓	↓	NW	4	16	
5[1]	↓	↓	↓	↓	W	1	6	
6[2]	↓	↓	↓	↓	SW	2	12	
7[2]	↓	↓	↓	↓	SW	1	6	
8[3]	↓	↓	↓	↓	W	—	—	
9[4]	↓	↓	↓	↓	W	—	—	
10	↓	6	↓	↓	NW	**16**	**46**	
11	↓	8	↓	↓	N	**3**	**7**	
12	#4	2	0	<4 mph	N			
13	↓	4	↓	↓	W			
14	↓	6	↓	↓	NW			
15	↓	8	↓	↓	NW			
16	#1 & #4	2	0	12±2 mph	NE	**25**	**59**	
17	↓	4	↓	16±4 mph	W	**4**	**11**	
18	↓	6	↓	16±4 mph	NE	**9**	**20**	
19	↓	8	↓	16±4 mph	N	**1**	**4**	
20	#4	2	0	10±2 mph	NE			
21	↓	4	↓	14±4 mph	N			
22	↓	6	↓	16±4 mph	NW			
23	↓	8	↓	20±2 mph	N			
24	#1 & #4	2	+6	<4 mph	N	**3**	**14**	
25	↓	4	+6	↓	NW	**4**	**16**	
26	↓	↓	+3	↓	N	**6**	**24**	
27	↓	↓	+1	↓	W	**18**	**52**	
28	↓	↓	-1	↓	W	**18**	**46**	
29	↓	↓	-3	↓	N	6	24	
30	↓	↓	-6	↓	NW	3	10	
31	↓	6	+6	↓	NW	**1**	**2**	
32	↓	8	+6	↓	N	**0**	**2**	

1 Repeatability tests
2 Reduced power tests
3 #4 engine max. power, #1 engine slowly increased from 50% RPM to max. power
4 #1 engine max. power, #4 engine slowly increased from 50% RPM to max. power
5 Inlet outboard and inboard regions analyzed separately for ingestion prone engine

Bold type - Ingestion Prone Engine Data

2

TABLE A-1

INGESTION CHARACTERISTICS SUMMARY							APPENDIX - DATA INDEX				
#1		ENGINE #4				Exhaust Pressure & Temp.	Ingestion Charac.	Inlet Proximity Temp.	Ground Jet Press. & Temp. Maps	Pod Pressure Distribution
.s. (°F)	$\|\hat{\dot{T}}\|$ (°F/sec)	$\hat{\Delta T}$ (°F)	$\hat{\varepsilon}_{max}$ (°F)	$\hat{\varepsilon}_{r.m.s.}$ (°F)	$\|\hat{\dot{T}}\|$ (°F/sec)					
19	250	6	10	4	—	X	X		X	X
9	120	1	4	2	—	X	X			X
15	140	4	8	3	—	X	X 5		X	X
6	60	25	54	16	165	X	X 5			
2	—	20	48	14	160	X	X			
4	—	12	36	12	100	X	X			
2	—	10	38	12	110	X	X			
—	—	—	—	—	—	X	X	X		
—	—	—	—	—	—	X	X	X		
12	135	4	16	6	55	X	X		X	X
2	35	3	4	2	—	X	X		X	X
		0	2	0	—	X	X		X	
		0	4	2	—	X	X		X	X
		0	4	2	—	X	X		X	
		1	4	1	—	X	X		X	
17	290	4	8	4	50	X	X			X
3	60	3	6	2	50	X	X		X	X
5	85	4	6	2	50	X	X			X
1	25	1	4	1	—	X	X			X
		3	6	2	—	X	X			
		4	6	2	—	X	X		X	X
		4	8	4	—	X	X			
		2	2	0	—	X	X			
4	45	2	4	2	—	X	X			X
4	40	2	8	2	—	X	X		X	X
6	80	5	10	4	—	X	X		X	X
4	140	2	8	2	—	X	X			X
5	150	2	8	4	—	X	X			X
8	—	15	42	13	120	X	X		X	X
4	—	6	24	6	85	X	X		X	X
1	20	0	2	1	—	X	X			X
0	—	0	2	0	—	X	X			X

Test #1

H/D = 2

α = 0

Wind = <4 MPH

Engines #1 and #4 operating

INGESTION CHARACTERISTICS

	ENGINE #1	ENGINE #4
$\Delta \hat{\bar{T}}$	29°F	6°F
$\hat{\epsilon}_{max}$	62°F	10°F
$\hat{\epsilon}_{r.m.s.}$	19°F	4°F
$\lvert\hat{\dot{T}}\rvert$	250°F/sec	—

Test 1

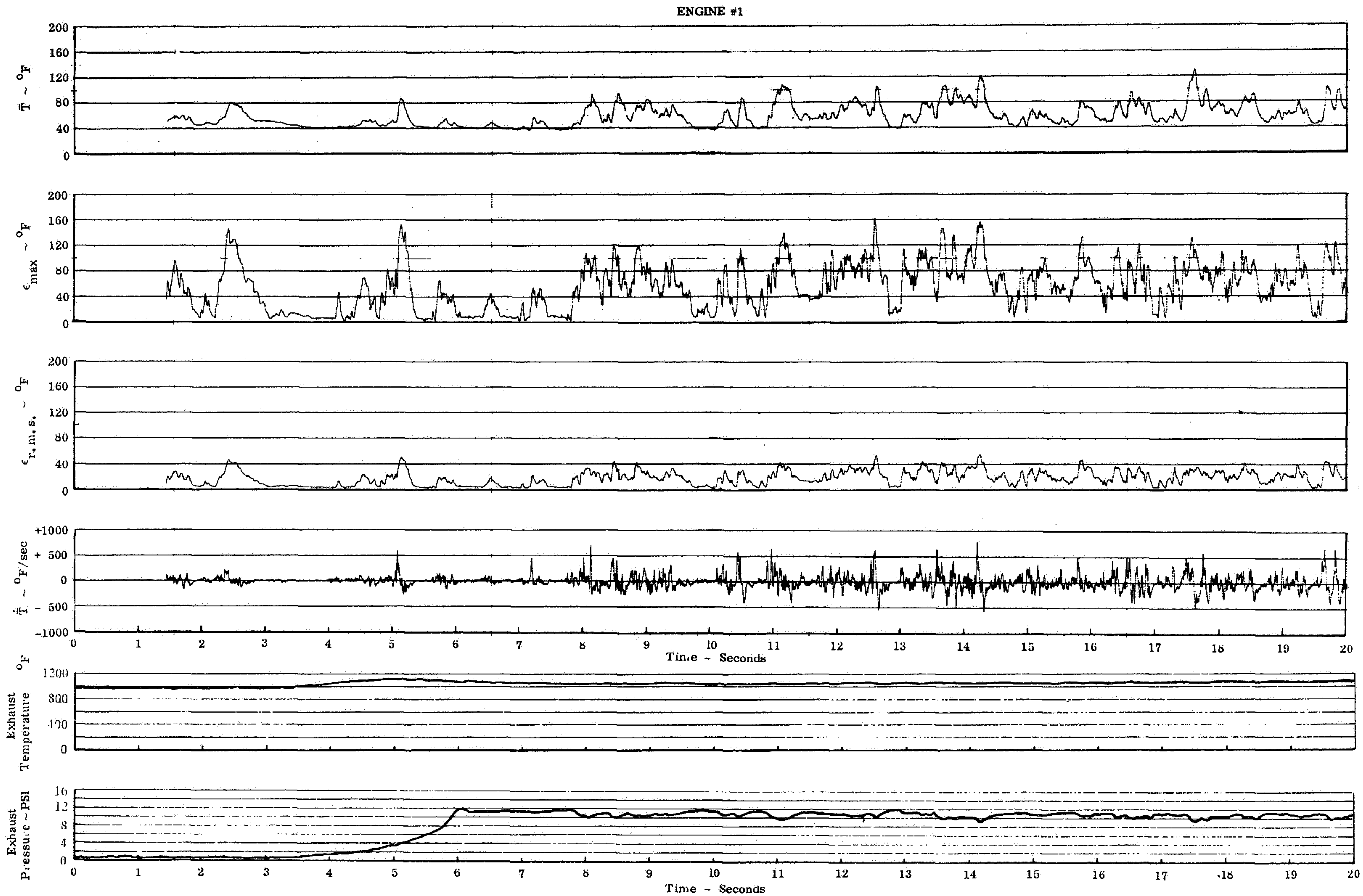

FIGURE A1-1. EXHAUST CONDITIONS AND INGESTION CHARACTERISTICS

Test 1

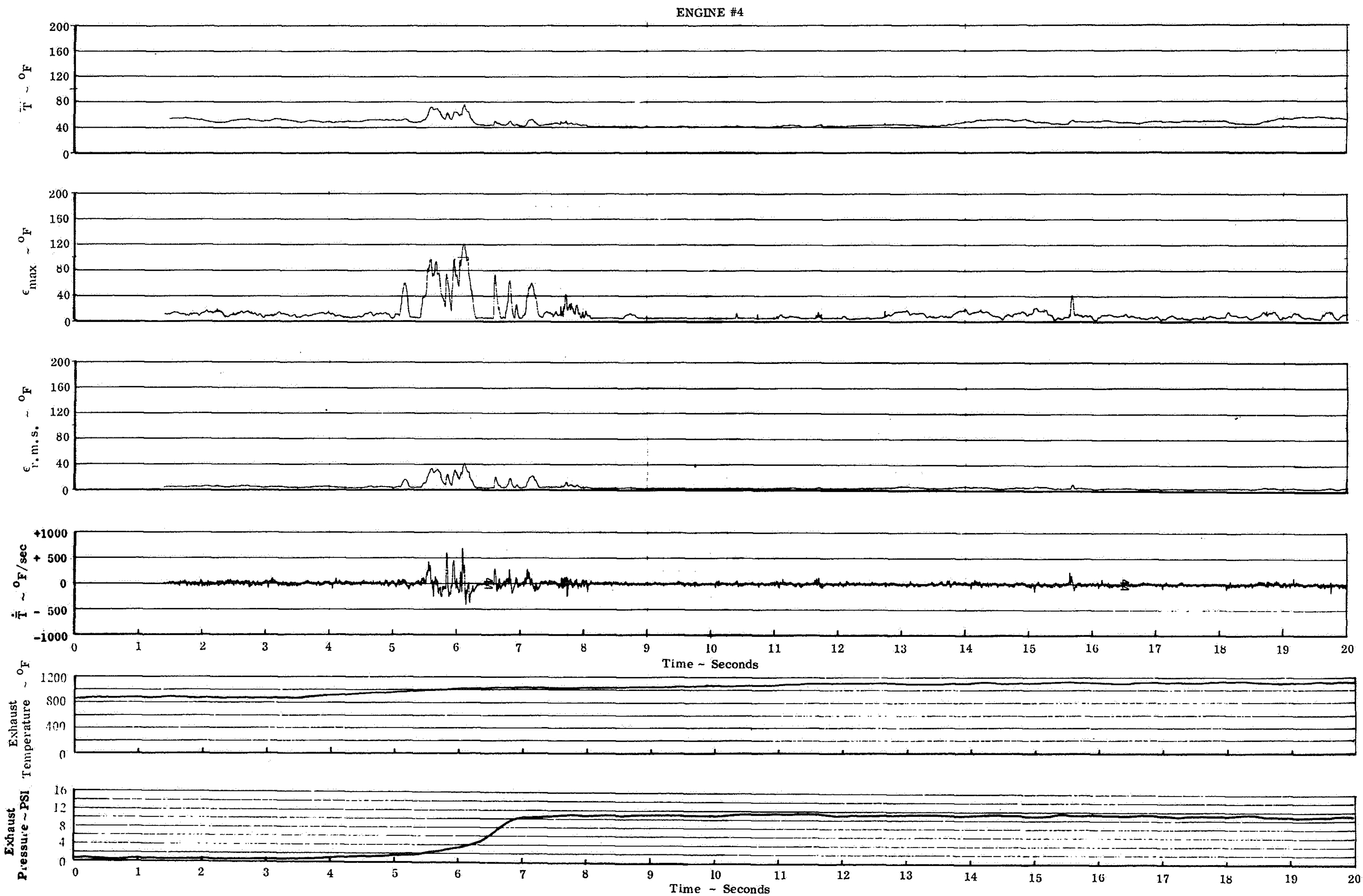

FIGURE A1-2. EXHAUST CONDITIONS AND INGESTION CHARACTERISTICS

Test 1

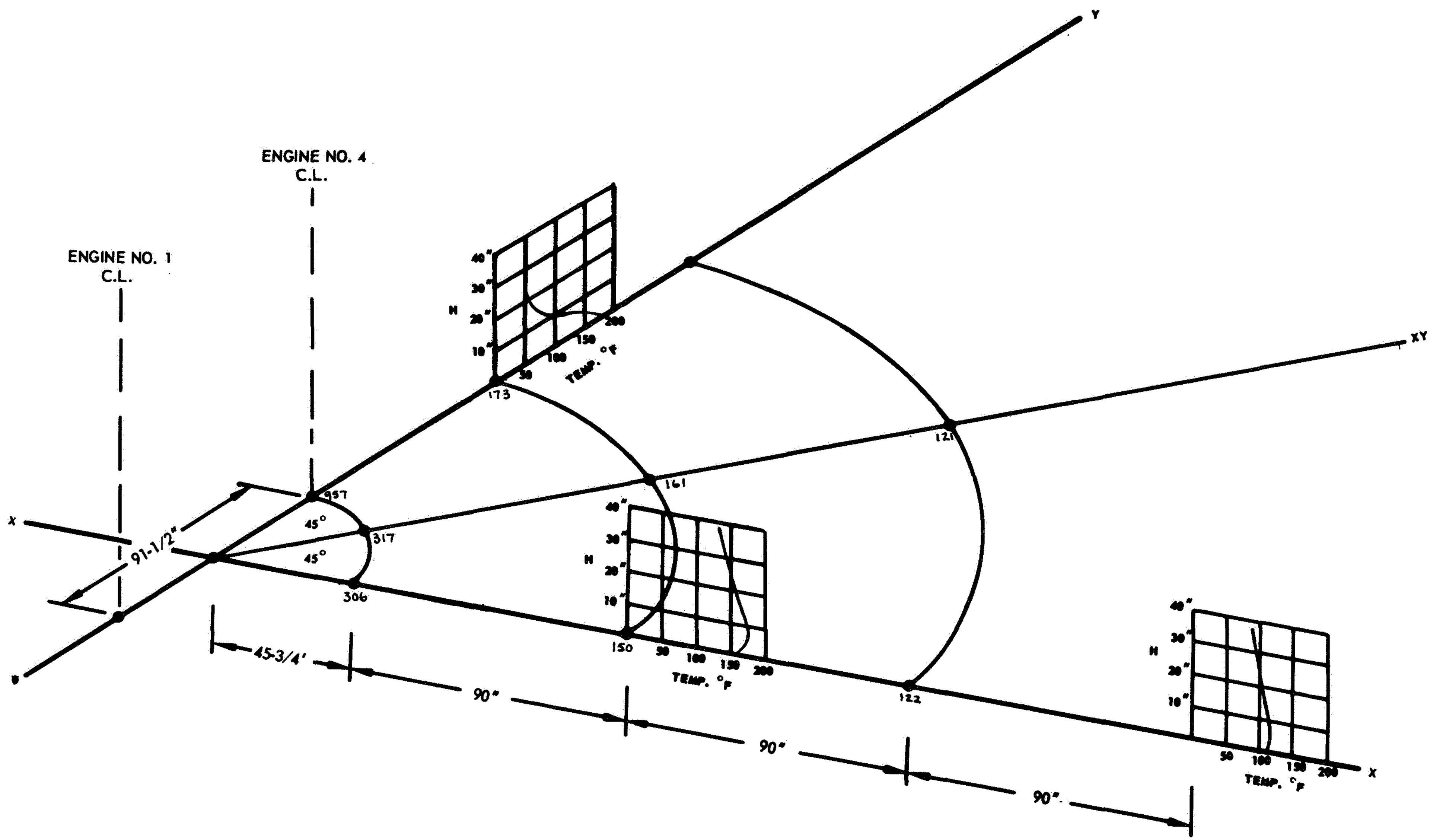

FIGURE A1-3. GROUND JET TEMPERATURE PROFILE

Test 1

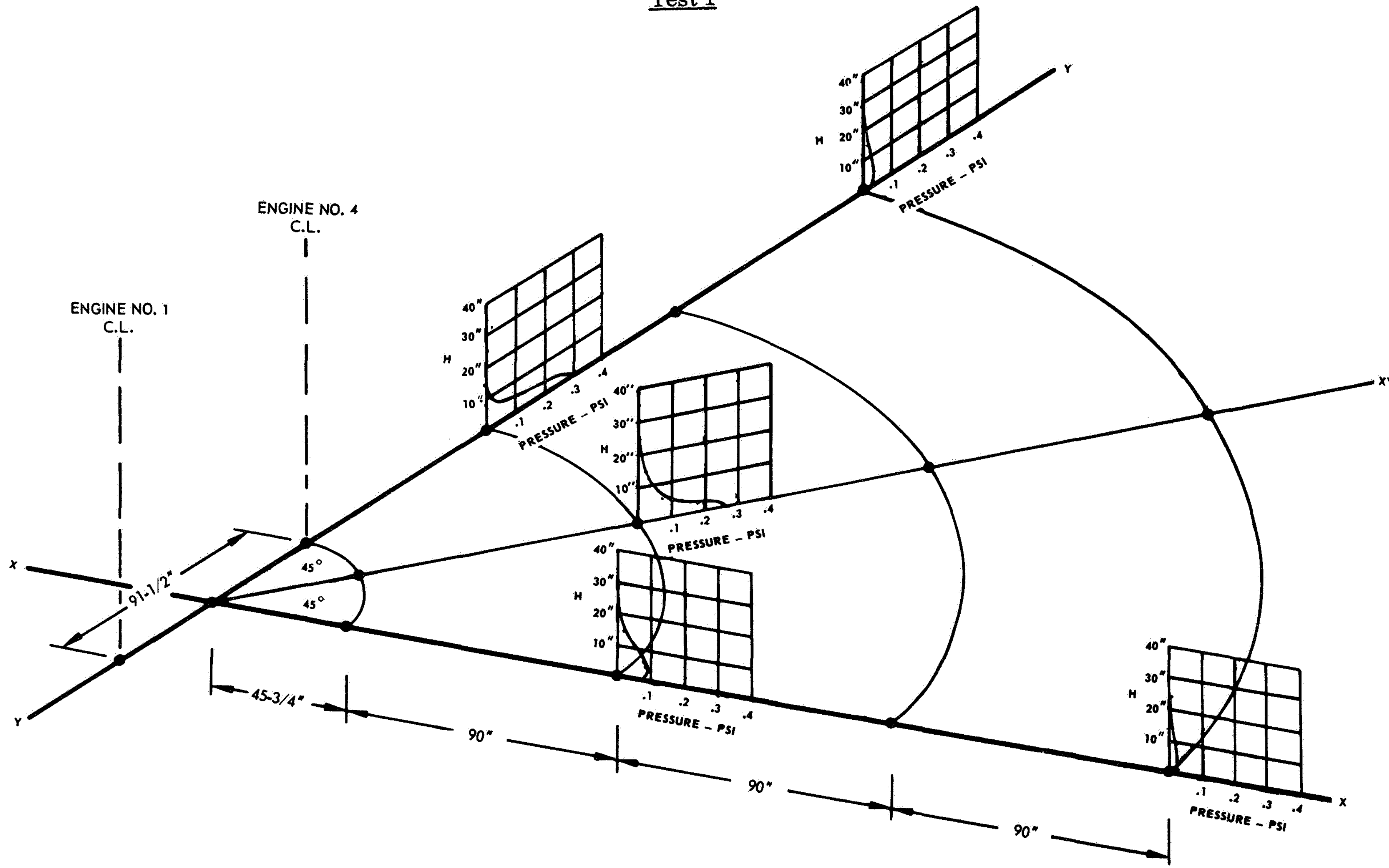

FIGURE A1-4. GROUND JET DYNAMIC PRESSURE PROFILE

Test 1

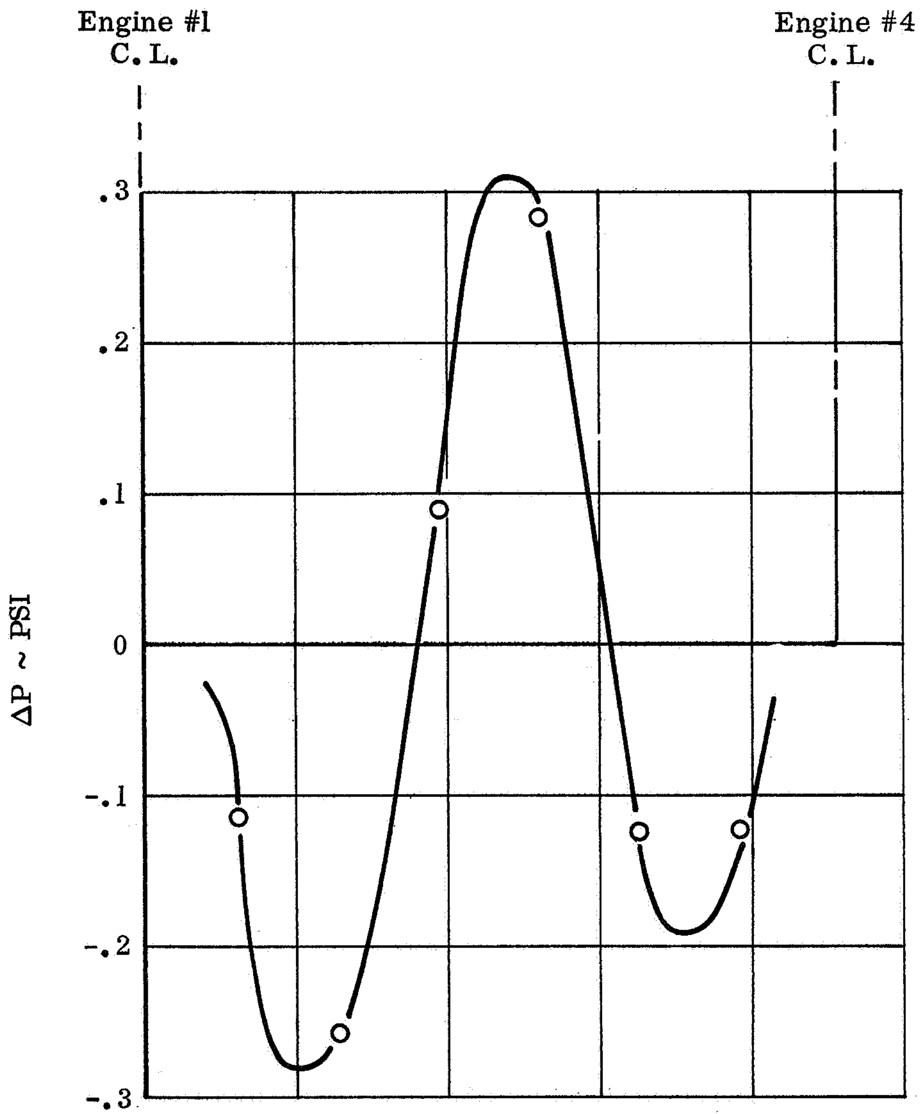

FIGURE A1-5. POD UNDERSURFACE PRESSURE DISTRIBUTION

Test #2

$H/D = 3$

$\alpha = 0$

Wind $= < 4$ MPH

Engines #1 and #4 operating

INGESTION CHARACTERISTICS

	ENGINE #1	ENGINE #4
$\Delta \hat{\bar{T}}$	14°F	1°F
$\hat{\epsilon}_{max}$	32°F	4°F
$\hat{\epsilon}_{r.m.s.}$	9°F	2°F
$\lvert\hat{\dot{T}}\rvert$	120°F/sec	—

Test 2

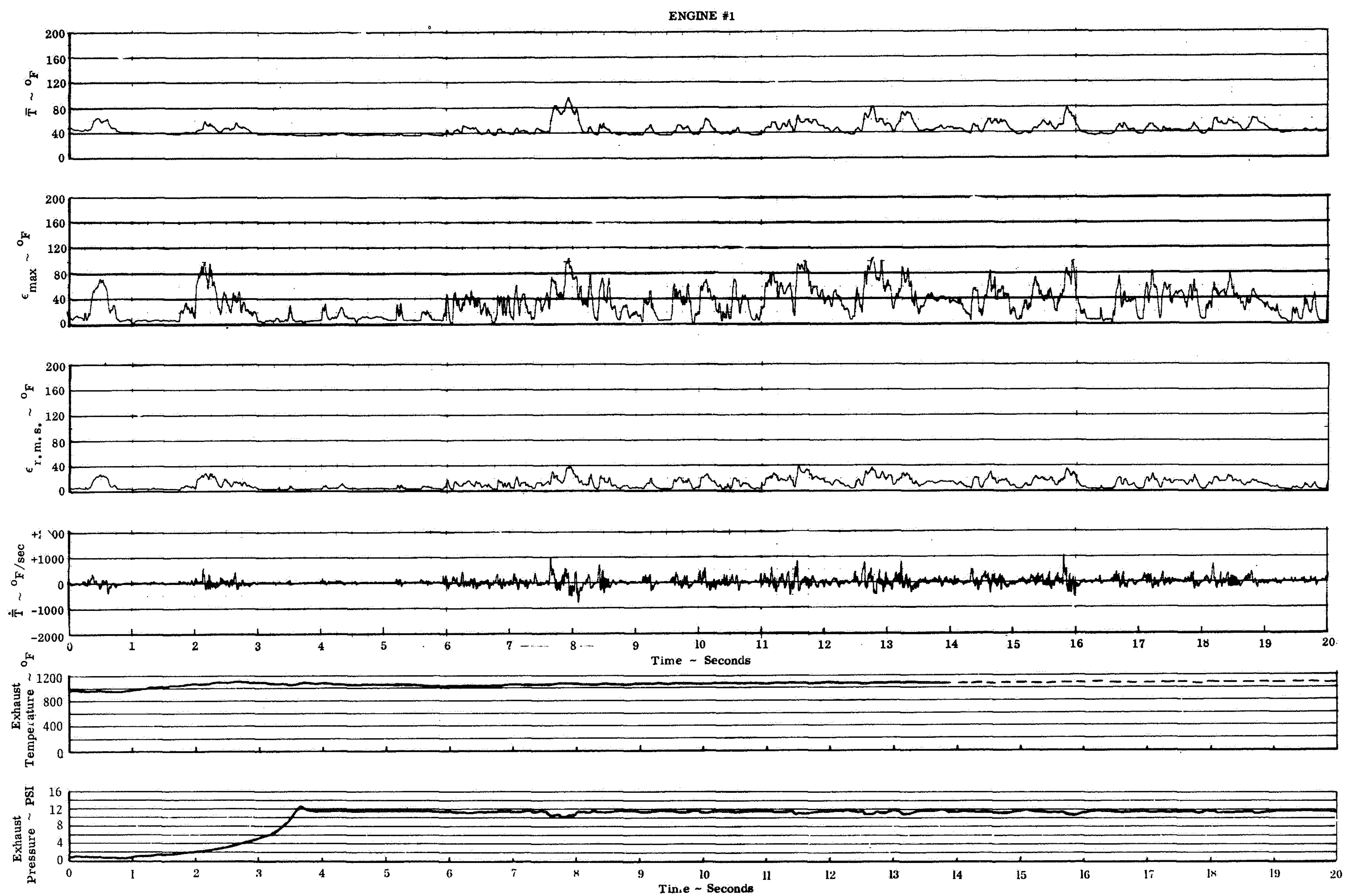

FIGURE A2-1. EXHAUST CONDITIONS AND INGESTION CHARACTERISTICS

Test 2

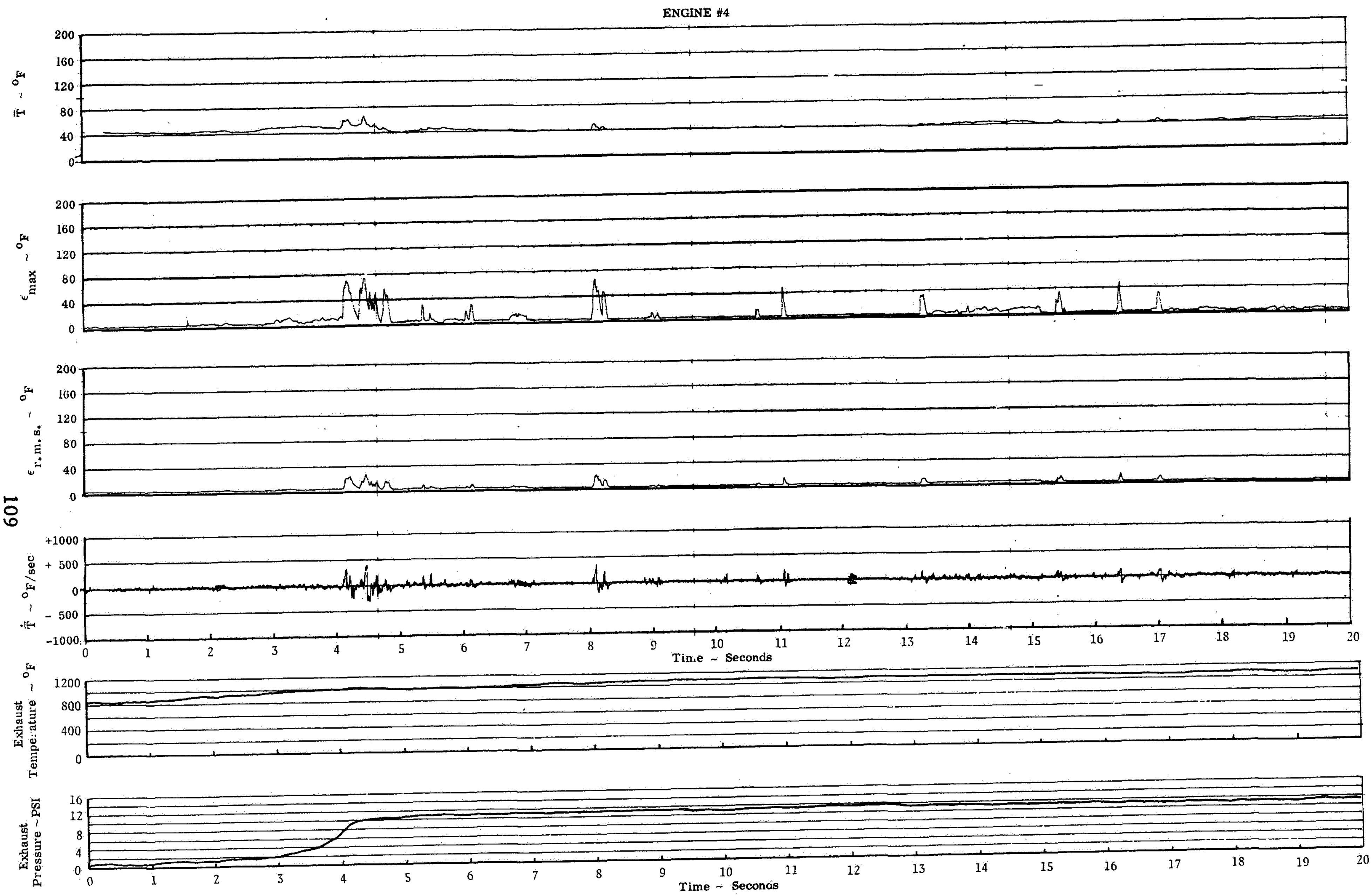

FIGURE A2-2. EXHAUST CONDITIONS AND INGESTION CHARACTERISTICS

Test #3

H/D = 4

α = 0

Wind = <4 MPH

Engines #1 and #4 operating

INGESTION CHARACTERISTICS

	ENGINE #1	ENGINE #4
$\Delta\hat{\bar{T}}$	21°F	4°F
$\hat{\epsilon}_{max}$	56°F	8°F
$\hat{\epsilon}_{r.m.s.}$	15°F	3°F
$\lvert\hat{\dot{T}}\rvert$	140°F/sec	—

Test 3

ENGINE #1

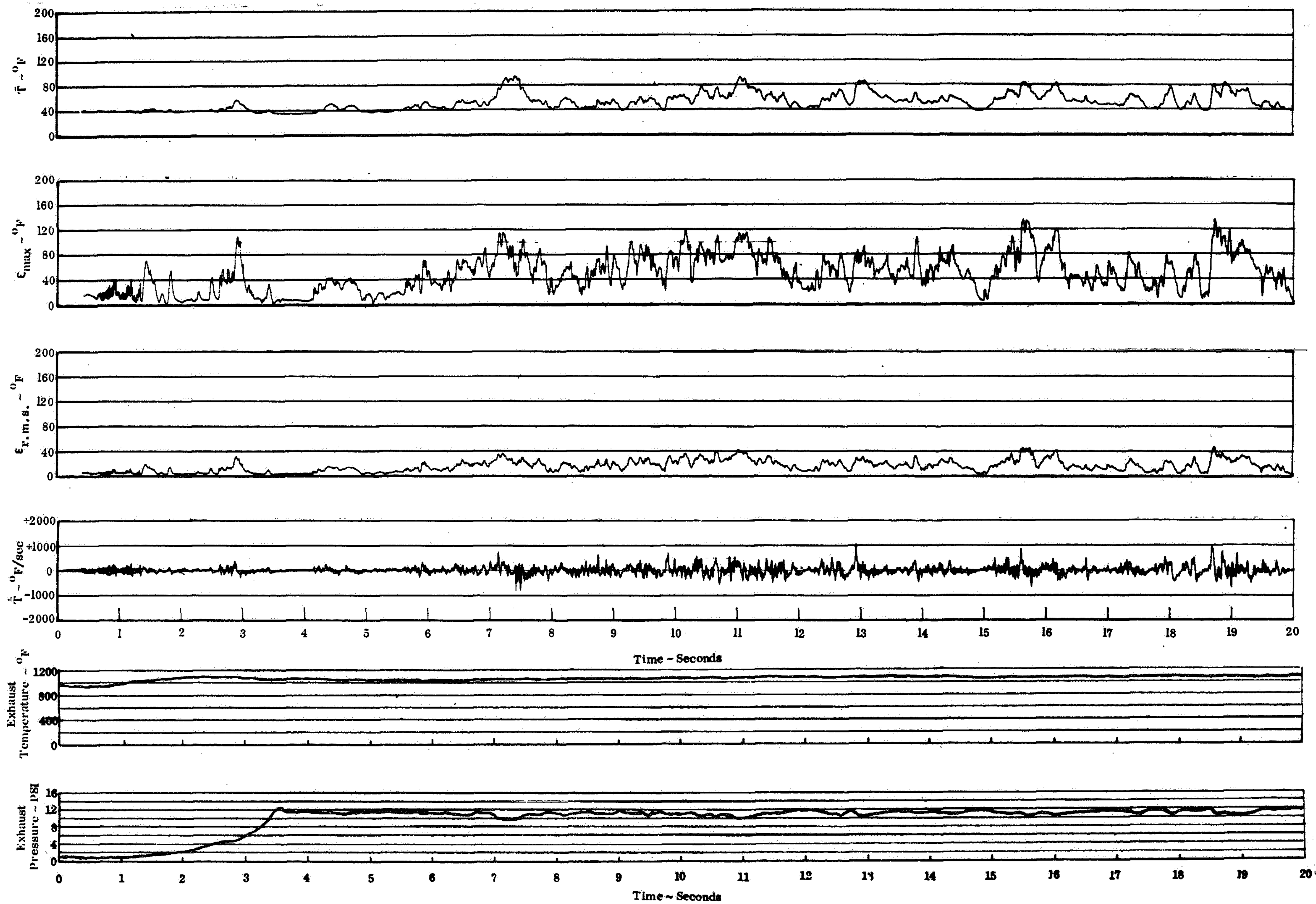

FIGURE A3-1. EXHAUST CONDITIONS AND INGESTION CHARACTERISTICS

Test 3

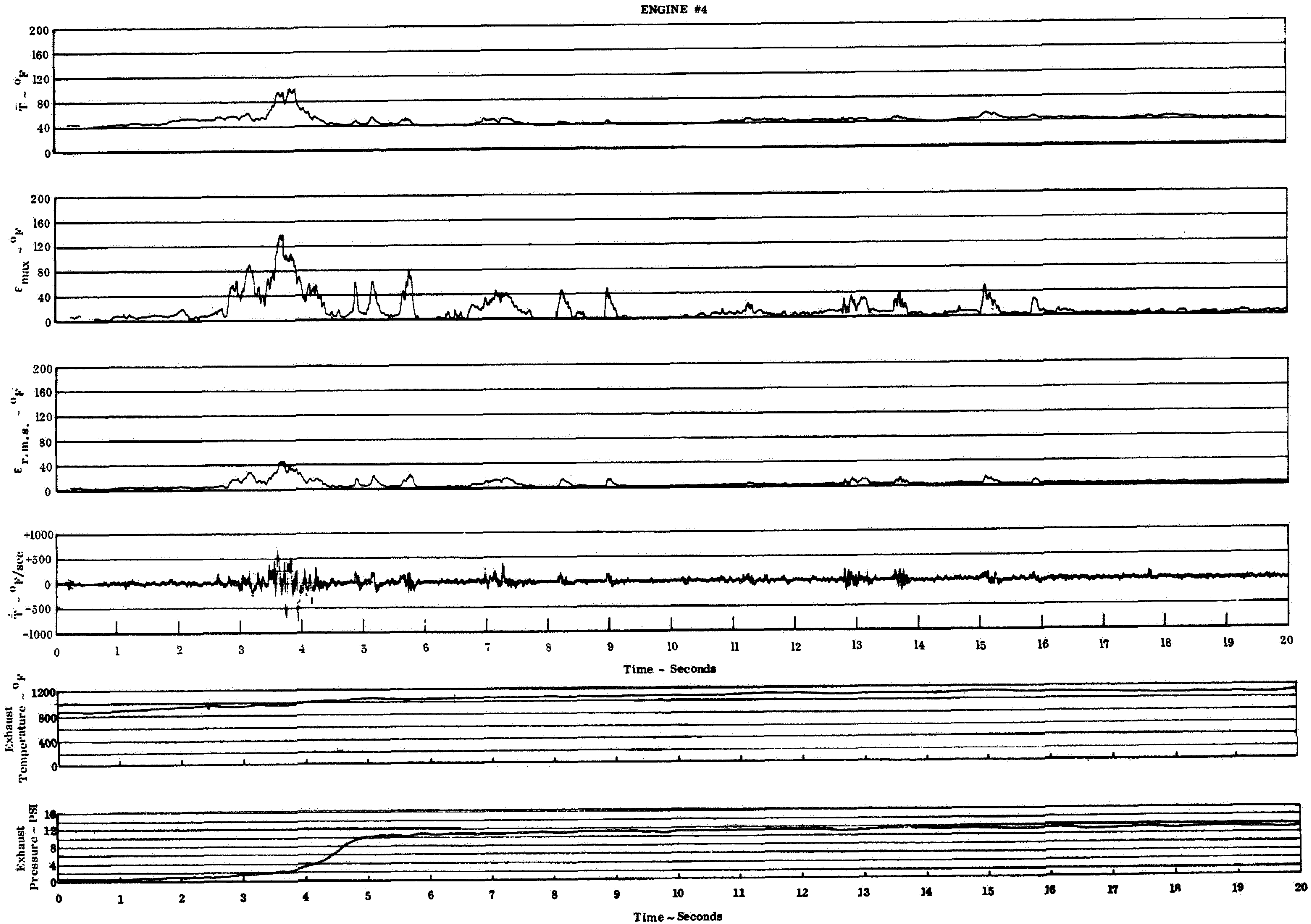

FIGURE A3-2. EXHAUST CONDITIONS AND INGESTION CHARACTERISTICS

Test 3

ENGINE #1 (Outboard Temperatures)

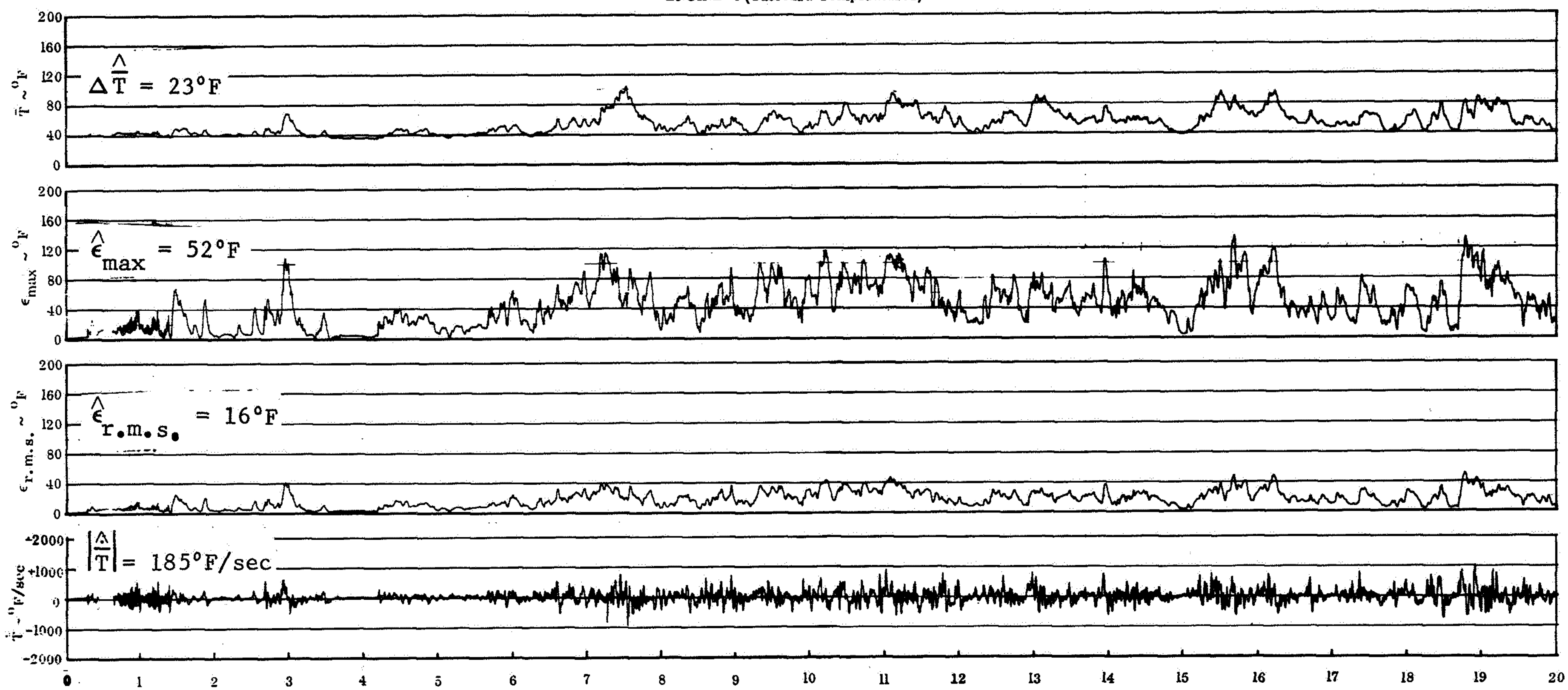

FIGURE A3-3. INGESTION CHARACTERISTICS

Test 3

ENGINE #1 (Inboard Temperatures)

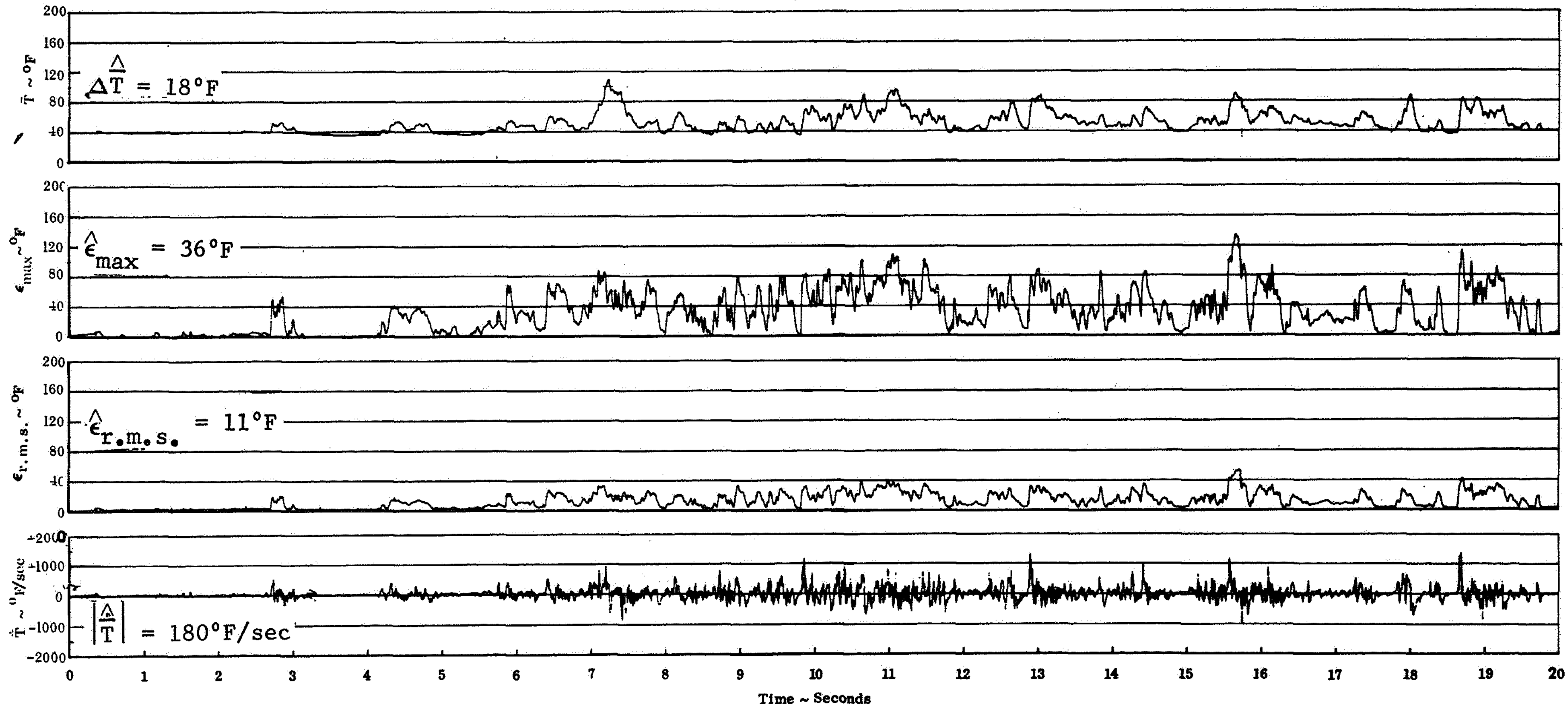

FIGURE A3-4. INGESTION CHARACTERISTICS

Test 3

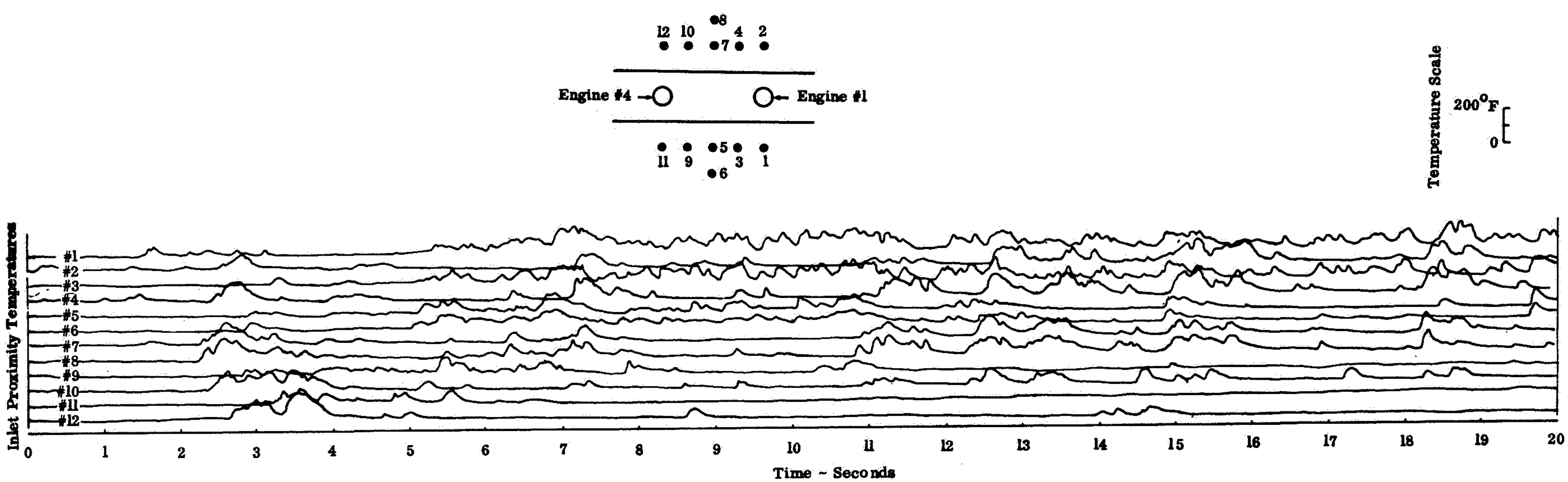

FIGURE A3-5. INLET PROXIMITY TEMPERATURES

Test 3

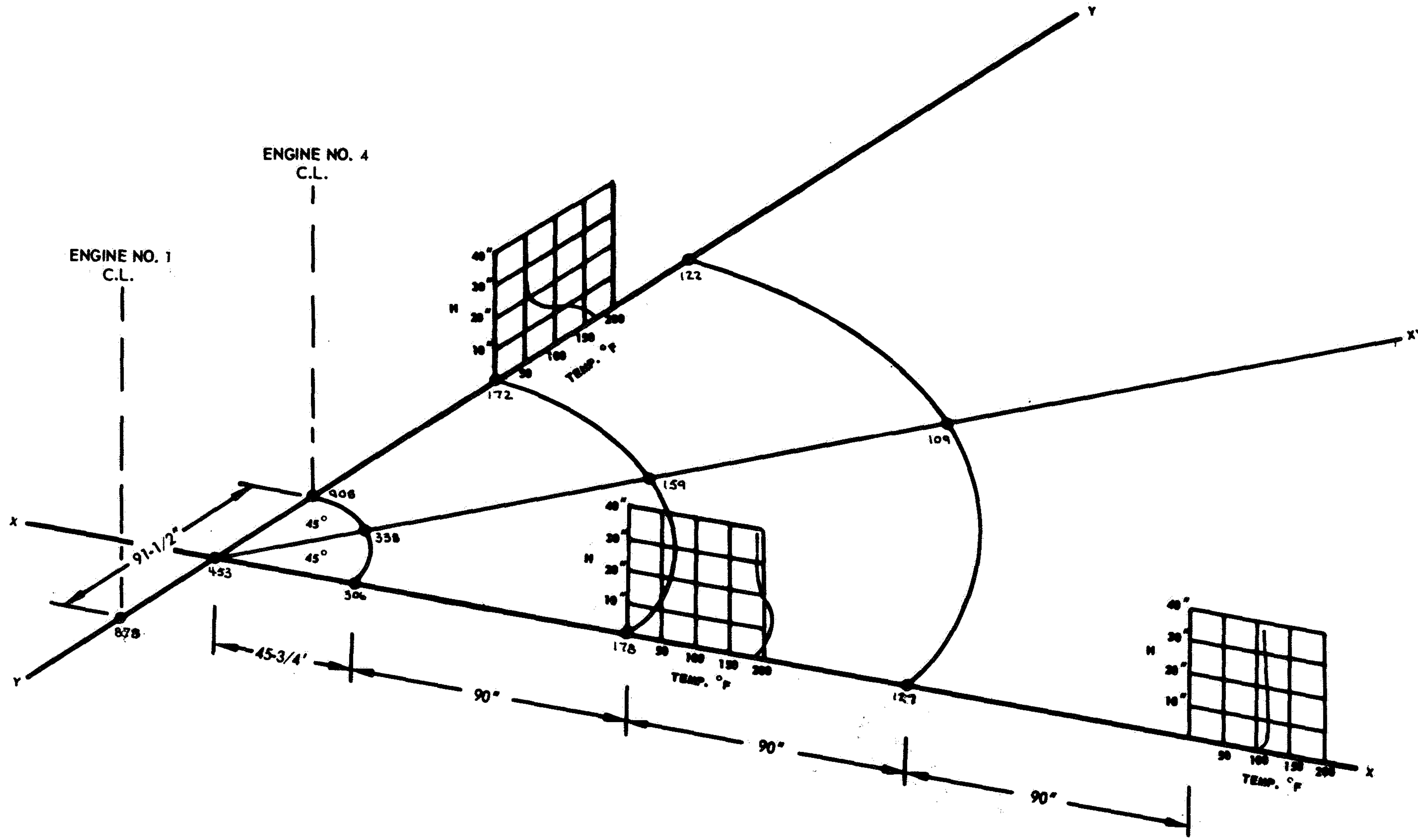

FIGURE A3-6. GROUND JET TEMPERATURE PROFILE

Test 3

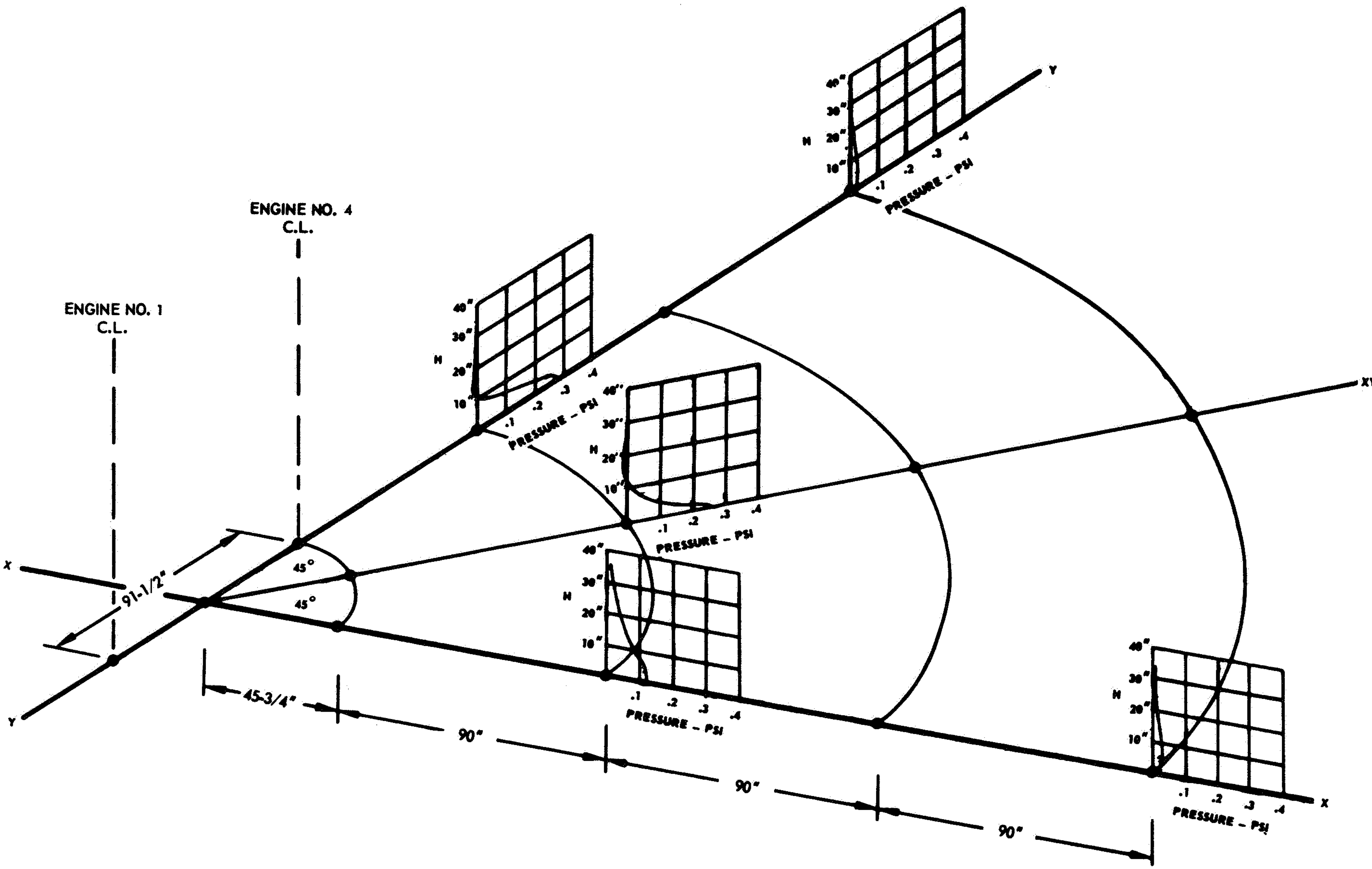

FIGURE A3-7. GROUND JET DYNAMIC PRESSURE PROFILE

Test 3

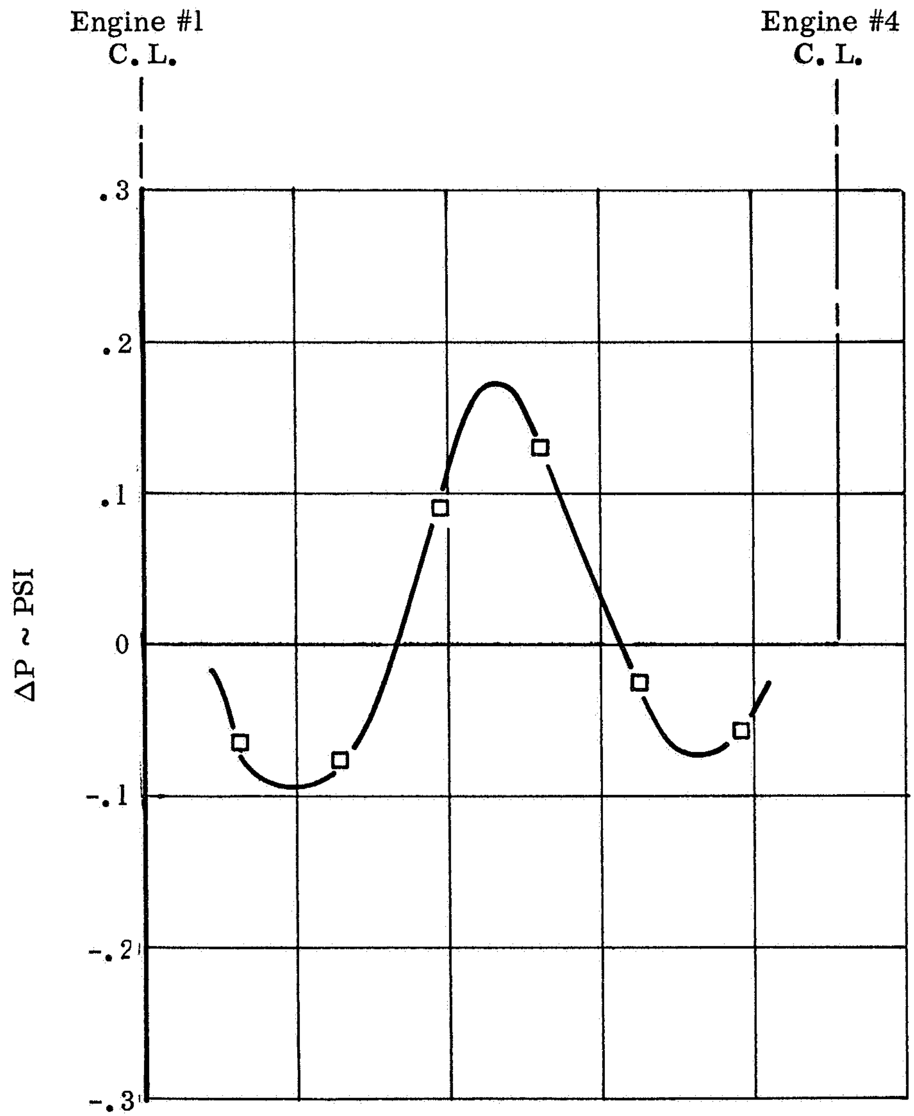

FIGURE A3-8. POD UNDERSURFACE PRESSURE DISTRIBUTION

Test #4

H/D = 4

α = 0

Wind = <4 MPH

Engines #1 and #4 operating.

INGESTION CHARACTERISTICS

	ENGINE #1	ENGINE #4
$\Delta \hat{\bar{T}}$	4°F	26°F
$\hat{\epsilon}_{max}$	16°F	54°F
$\hat{\epsilon}_{r.m.s.}$	6°F	16°F
$\lvert\hat{\dot{T}}\rvert$	60°F/sec	165°F/sec

Test 4

ENGINE #1

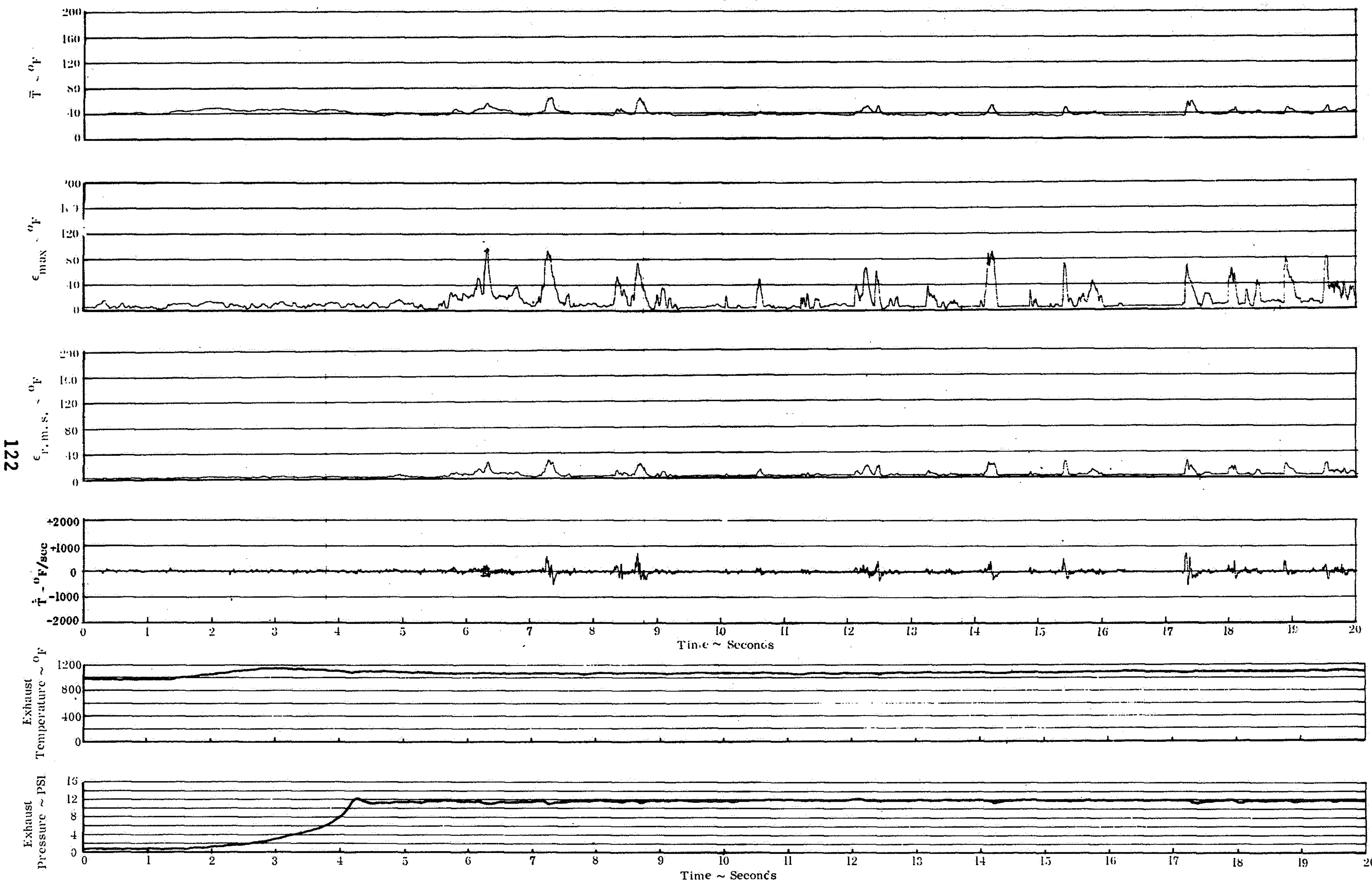

FIGURE A4-1. EXHAUST CONDITIONS AND INGESTION CHARACTERISTICS

Test 4

ENGINE #4

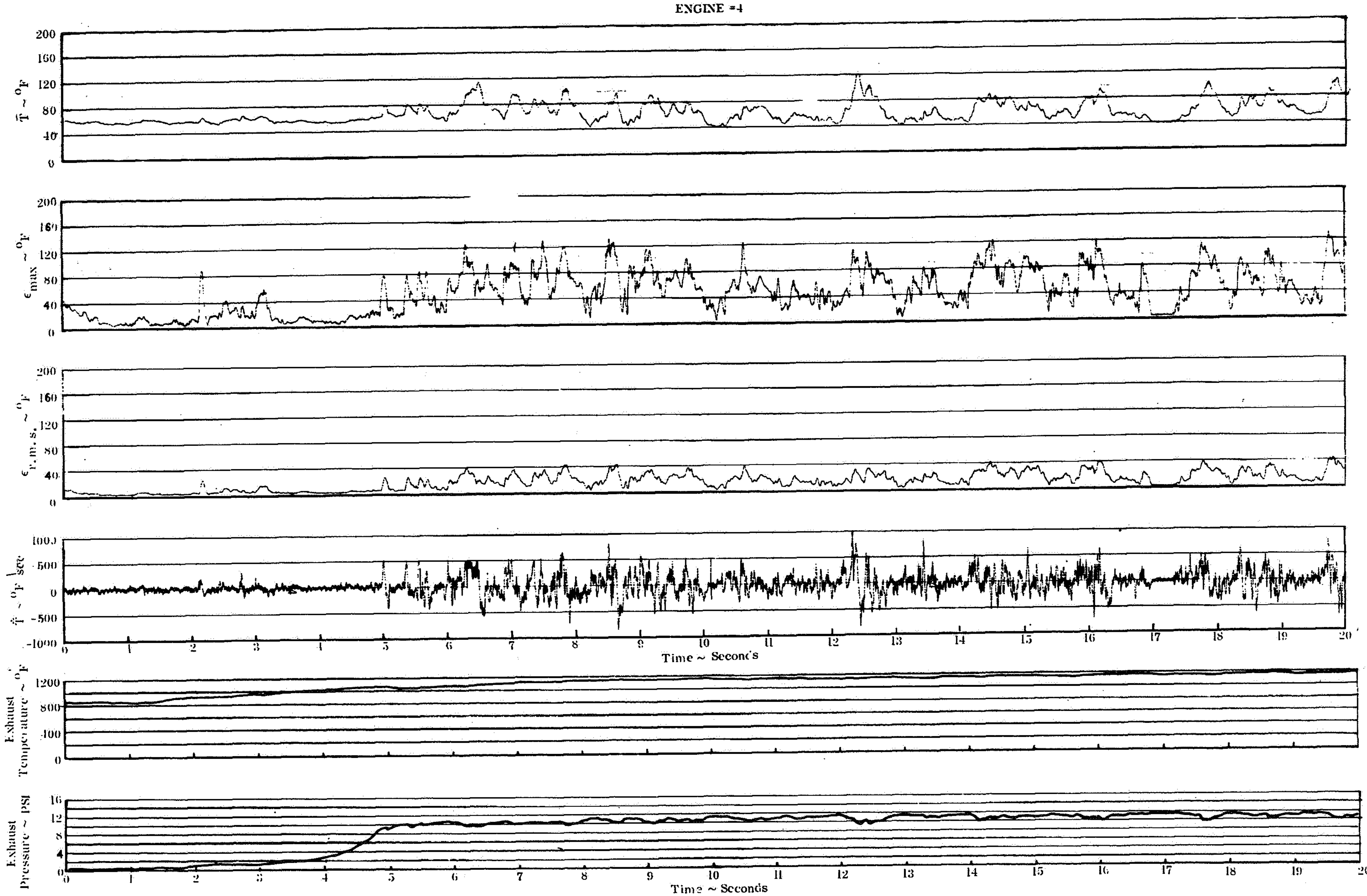

FIGURE A4-2. EXHAUST CONDITIONS AND INGESTION CHARACTERISTICS

Test 4

ENGINE #4 (Outboard Temperatures)

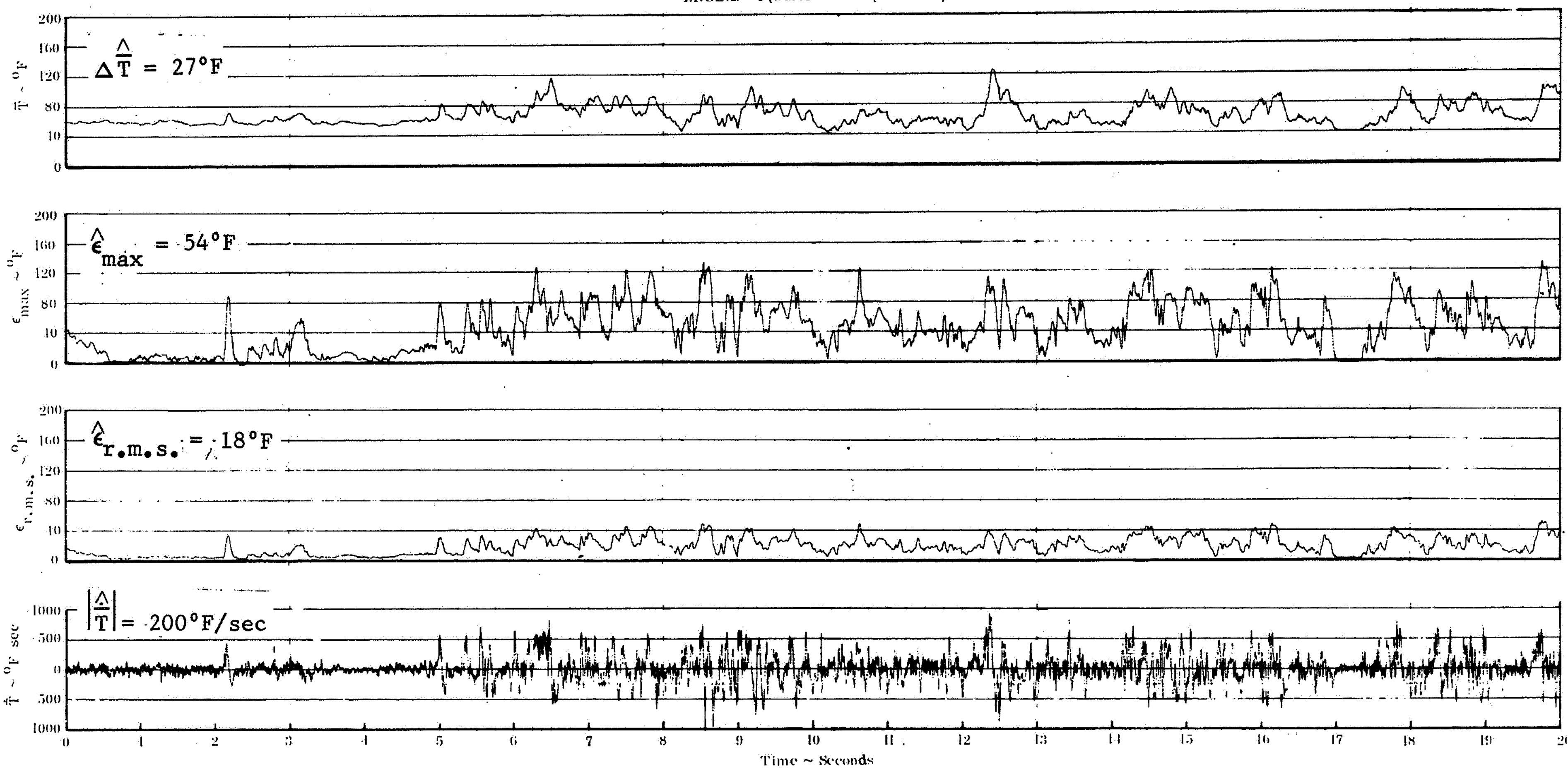

FIGURE A4-3. EXHAUST CONDITIONS AND INGESTION CHARACTERISTICS

Test 4

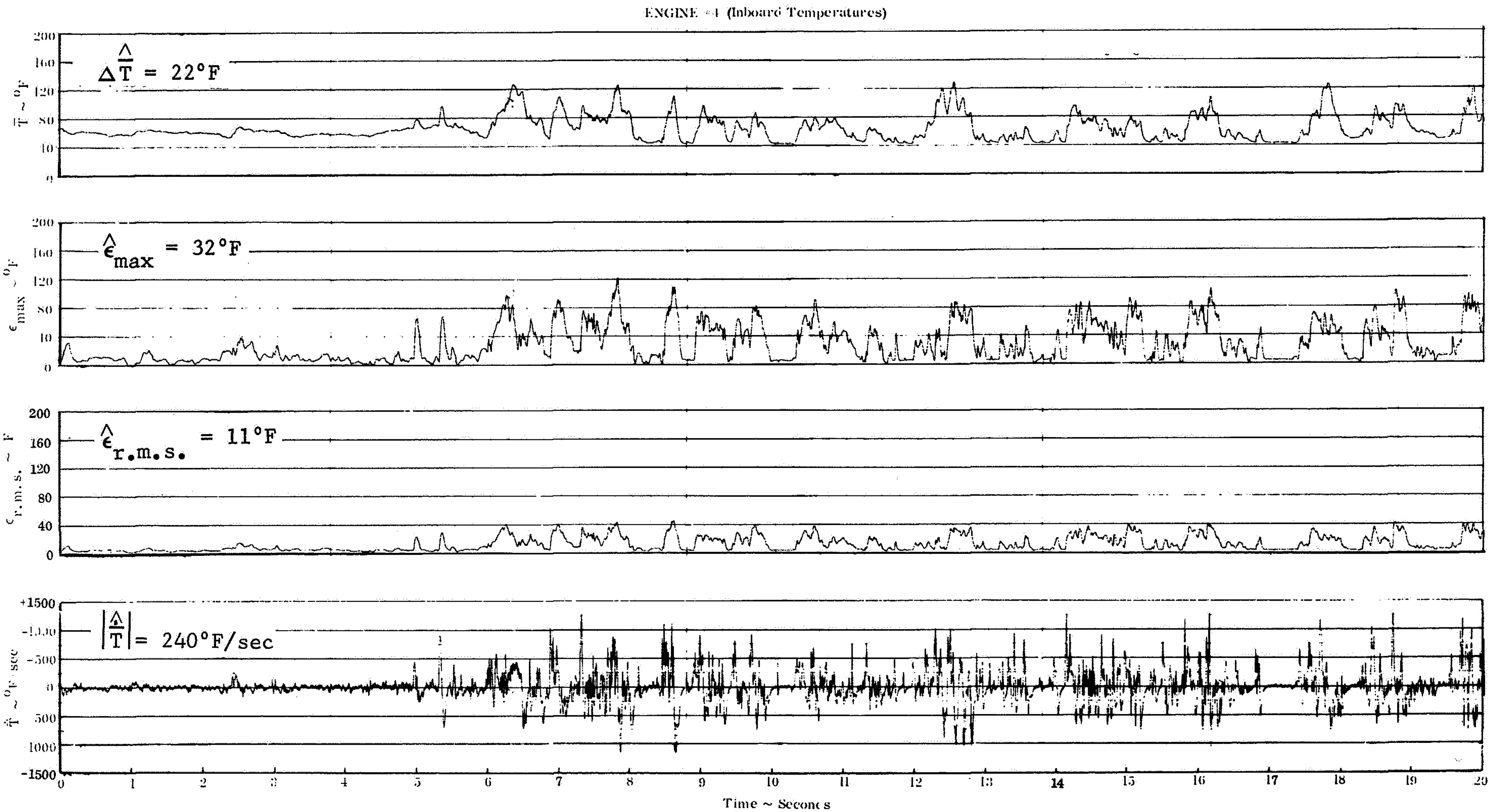

FIGURE A4-4. EXHAUST CONDITIONS AND INGESTION CHARACTERISTICS

Test #5

H/D = 4

α = 0

Wind = <4 MPH

Engines #1 and #4 operating

INGESTION CHARACTERISTICS

	ENGINE #1	ENGINE #4
$\Delta \hat{\bar{T}}$	1°F	20°F
$\hat{\epsilon}_{max}$	6°F	48°F
$\hat{\epsilon}_{r.m.s.}$	2°F	14°F
$\lvert\hat{\dot{T}}\rvert$	—	160°F/sec

Test 5

ENGINE #1

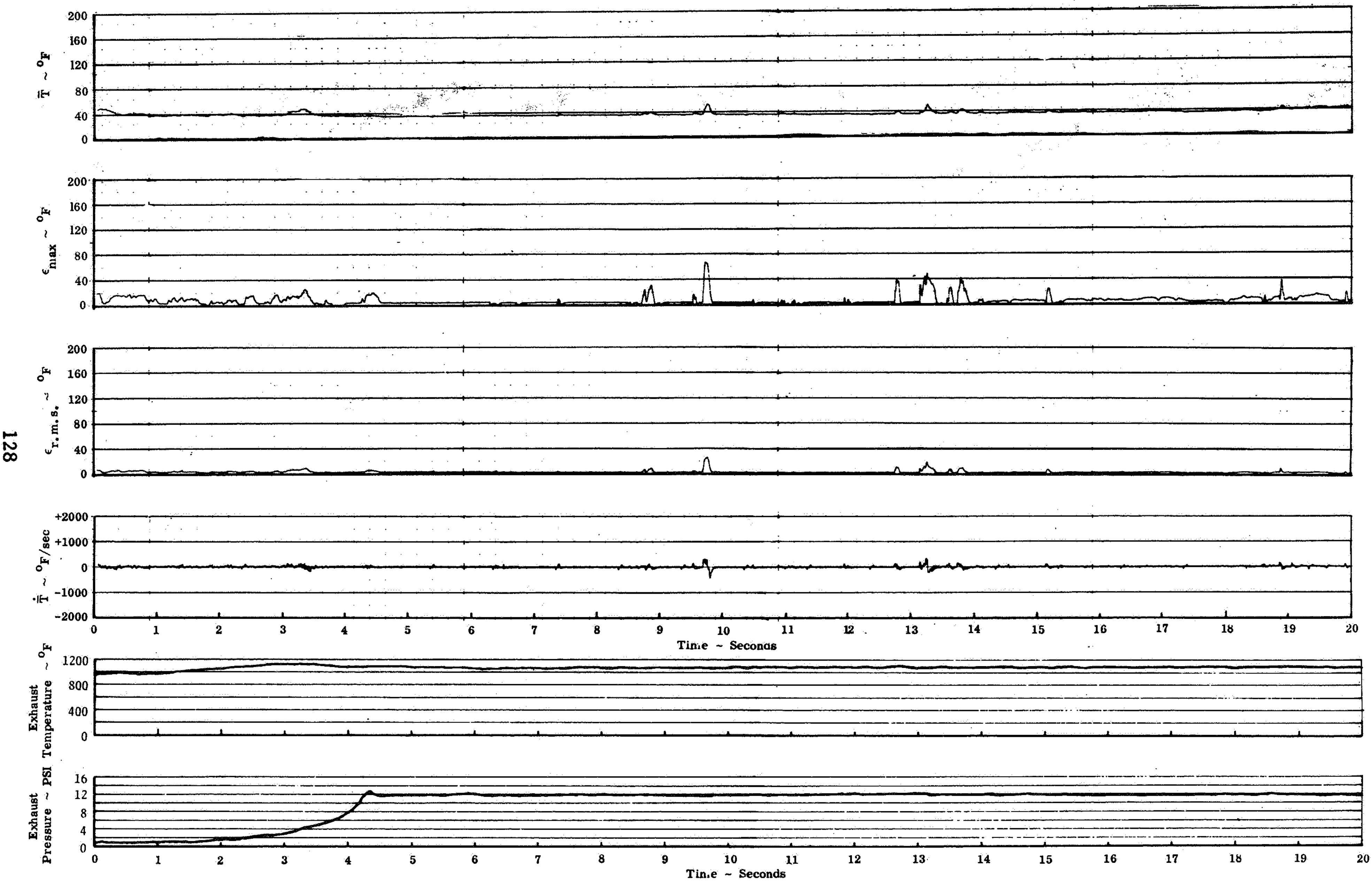

FIGURE A5-1. EXHAUST CONDITIONS AND INGESTION CHARACTERISTICS

Test 5

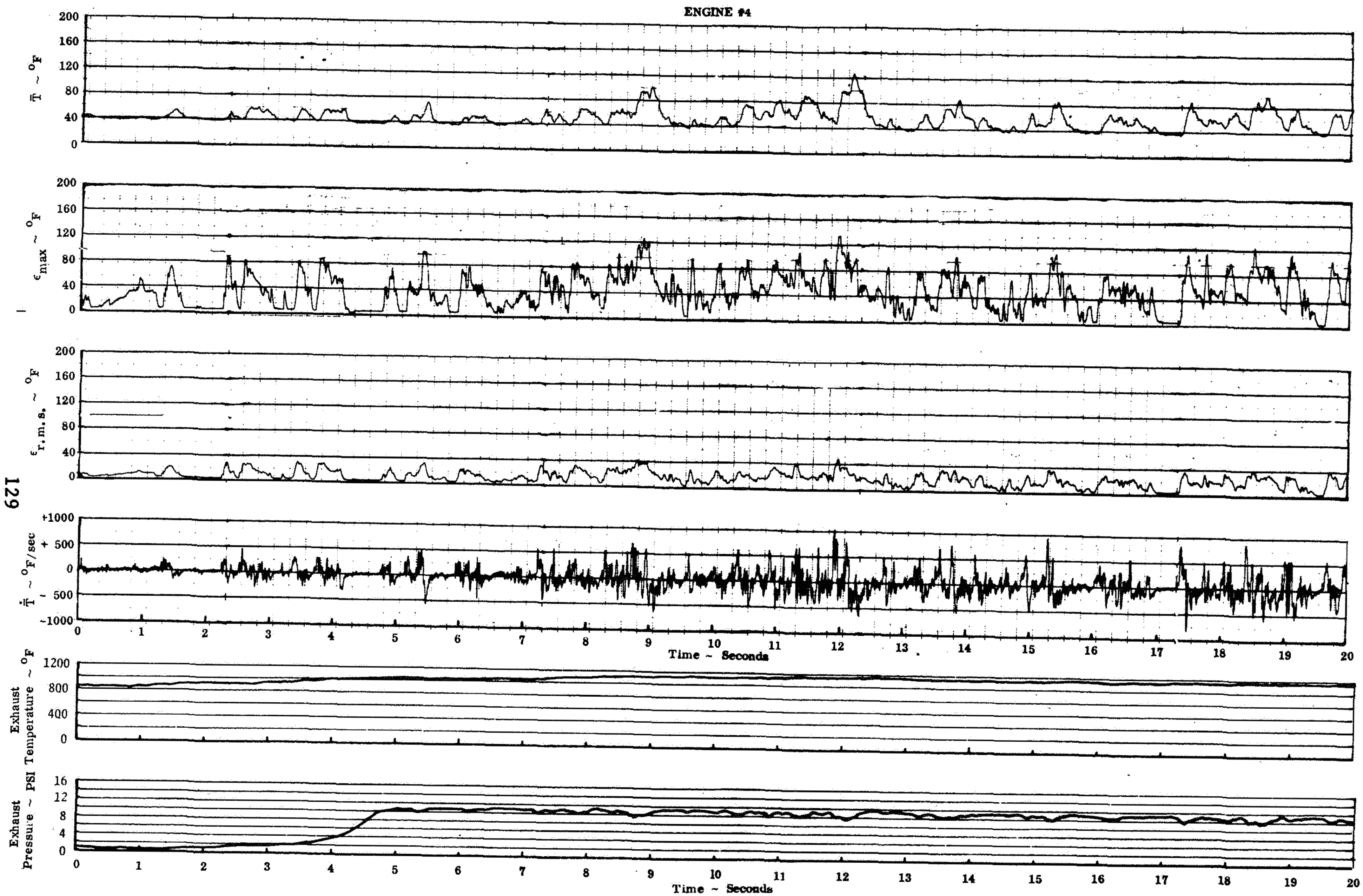

FIGURE A5-2. EXHAUST CONDITIONS AND INGESTION CHARACTERISTICS

Test #6

H/D = 4

α = 0

Wind = <4 MPH

Engines #1 and #4 operating

INGESTION CHARACTERISTICS

	ENGINE #1	ENGINE #4
$\Delta\hat{\bar{T}}$	2°F	12°F
$\hat{\epsilon}_{max}$	12°F	36°F
$\hat{\epsilon}_{r.m.s.}$	4°F	12°F
$\lvert\hat{\dot{T}}\rvert$	—	100°F/sec

Test 6

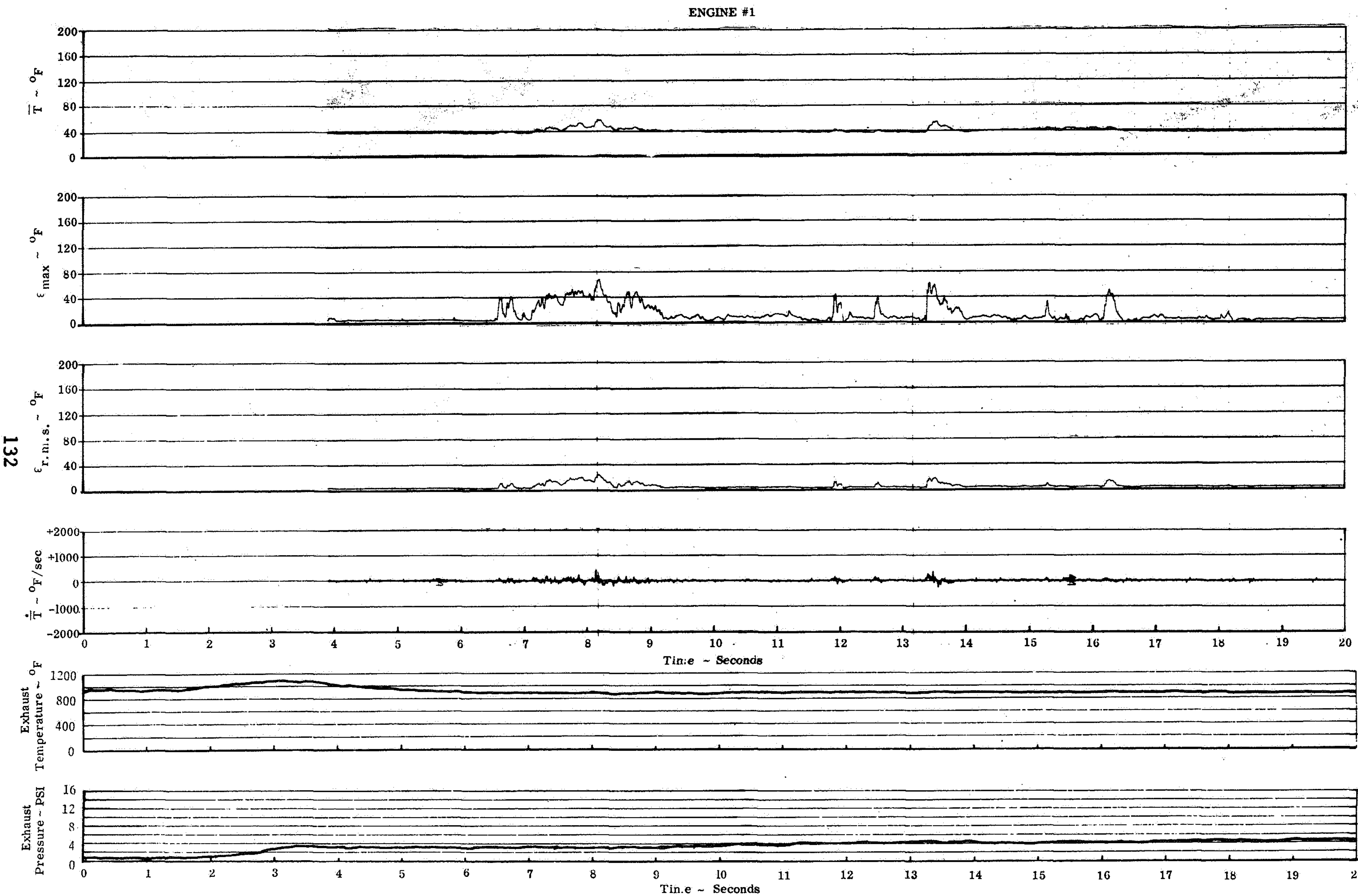

FIGURE A6-1. EXHAUST CONDITIONS AND INGESTION CHARACTERISTICS

Test 6

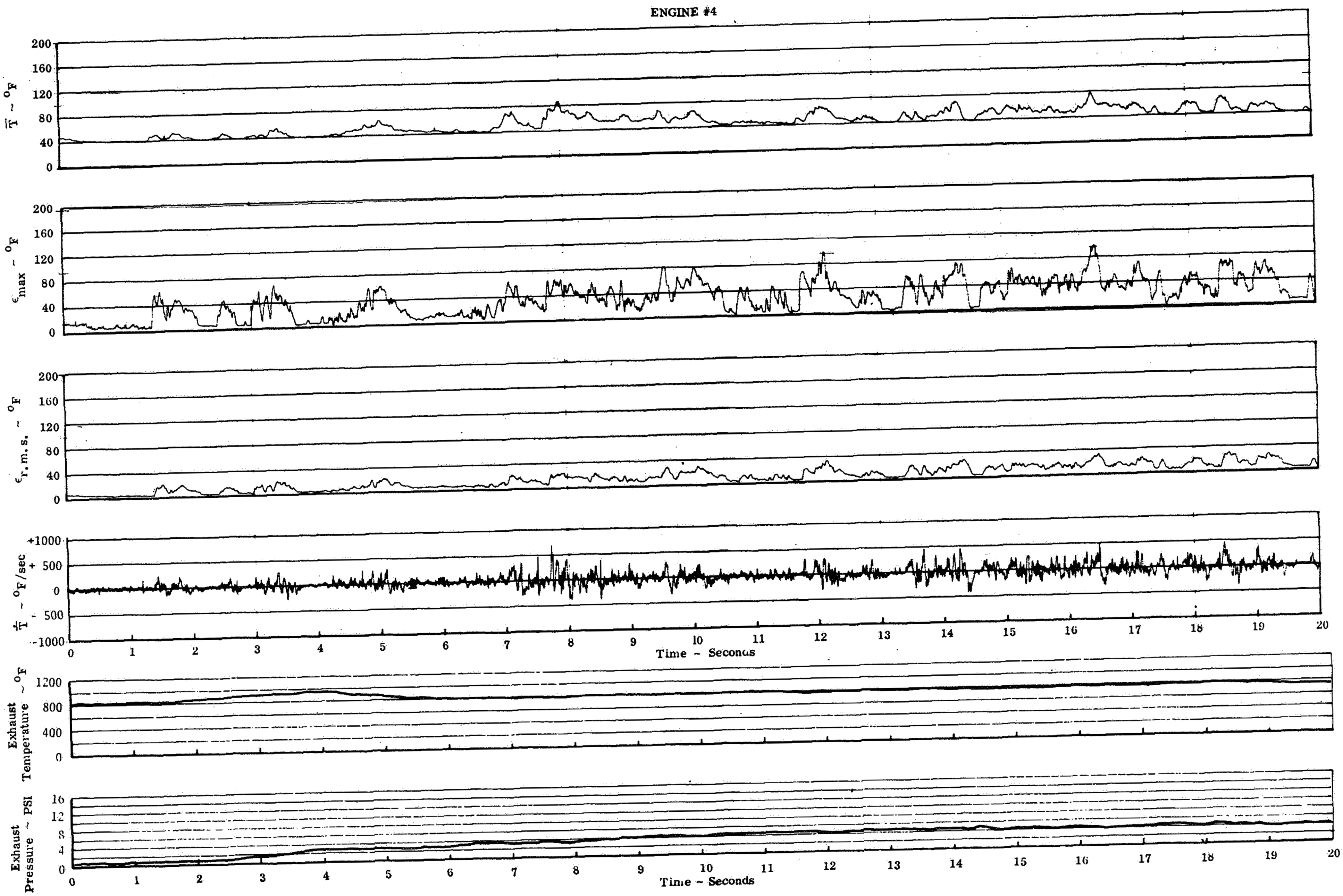

FIGURE A6-2. EXHAUST CONDITIONS AND INGESTION CHARACTERISTICS

Test #7

H/D = 4

α = 0

Wind = <4 MPH

Engines #1 and #4 operating

INGESTION CHARACTERISTICS

	ENGINE #1	ENGINE #4
$\Delta\hat{\bar{T}}$	1°F	10°F
$\hat{\epsilon}_{max}$	6°F	36°F
$\hat{\epsilon}_{r.m.s.}$	2°F	12°F
$\lvert\hat{\dot{T}}\rvert$	—	110°F/sec

Test 7

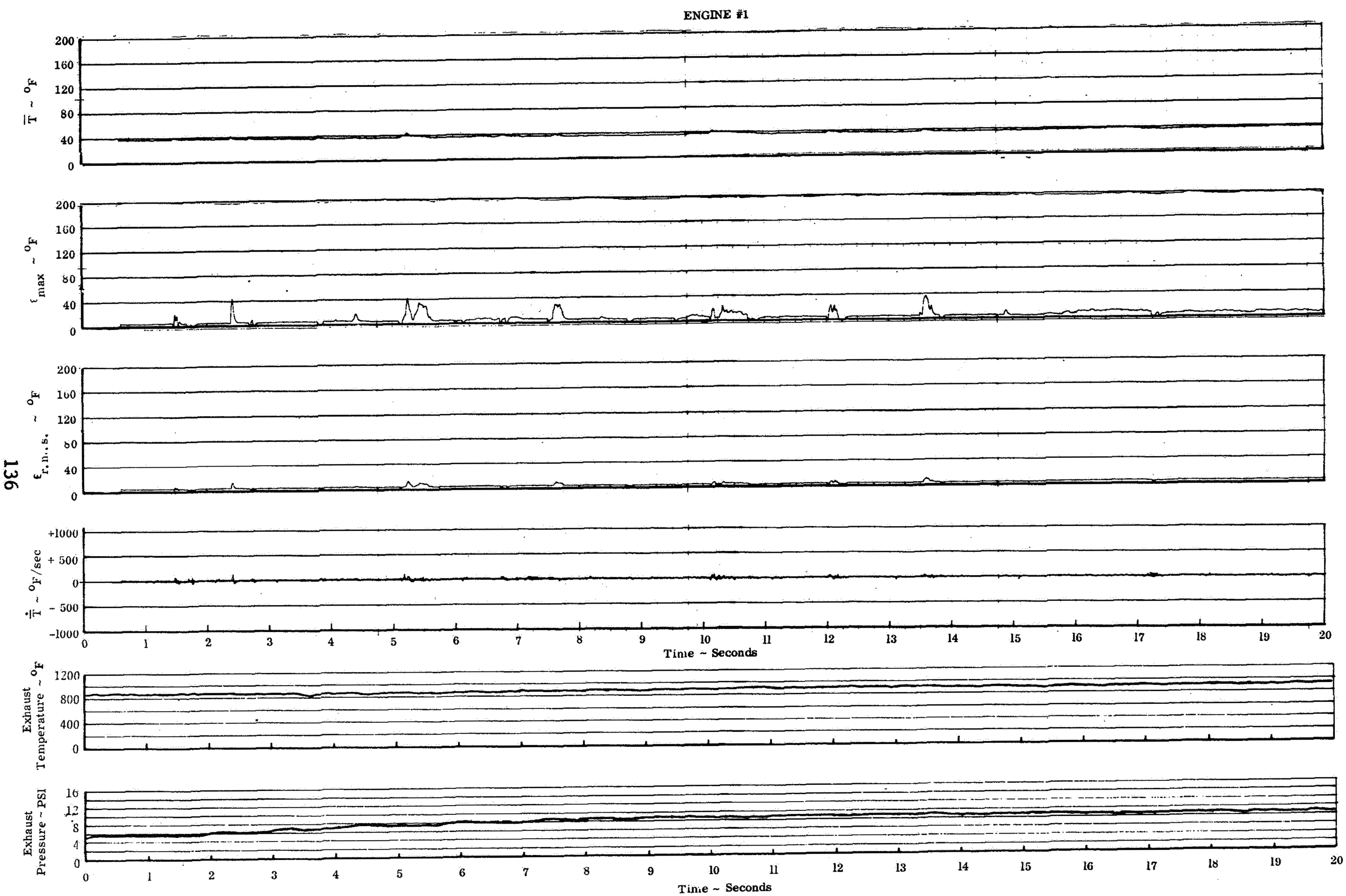

FIGURE A7-1. EXHAUST CONDITIONS AND INGESTION CHARACTERISTICS

Test 7

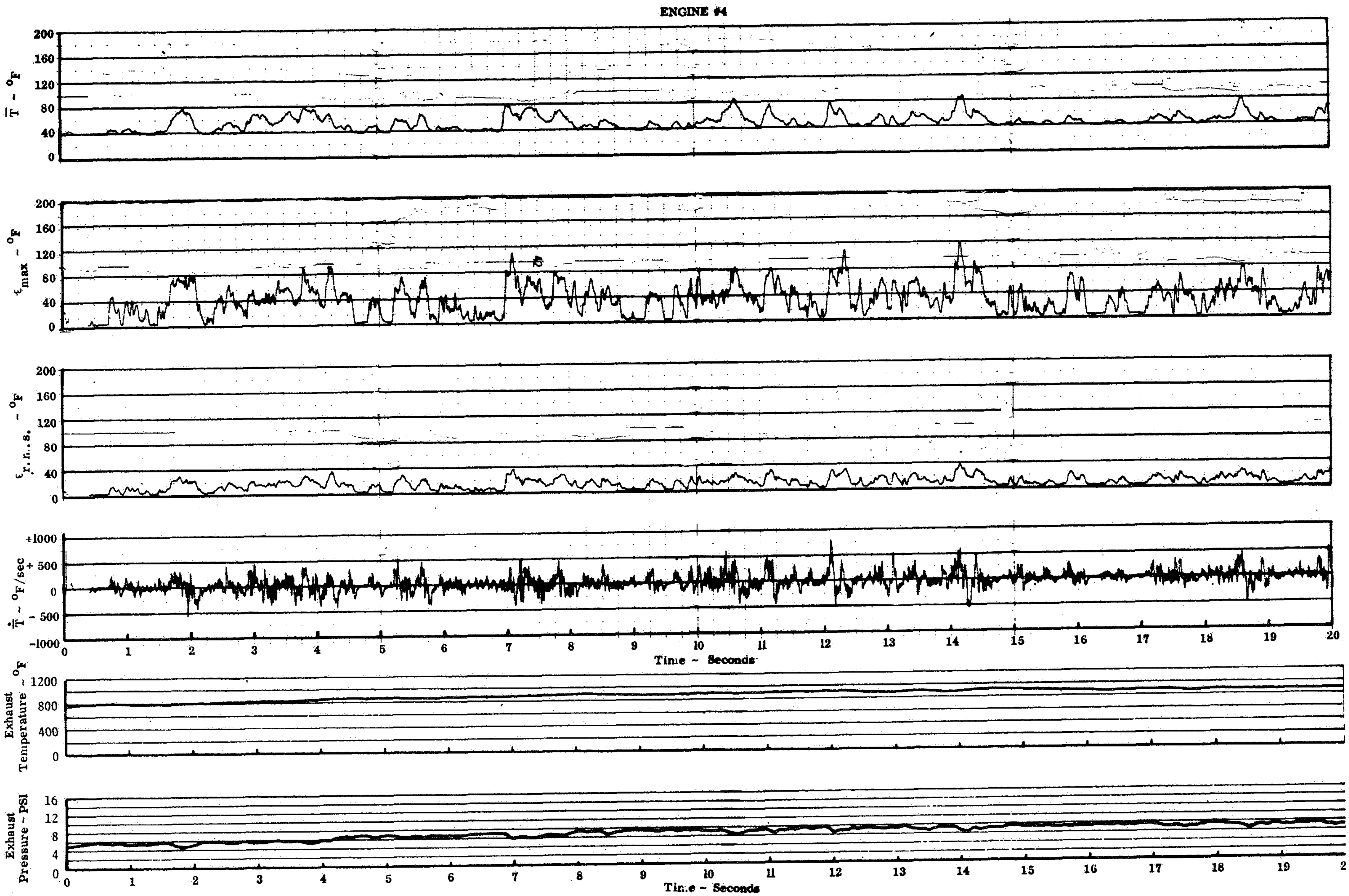

FIGURE A7-2. EXHAUST CONDITIONS AND INGESTION CHARACTERISTICS

Test #8

$H/D = 4$

$\alpha = 0$

Wind = <4 MPH

Engines #1 and #4 operating

INGESTION CHARACTERISTICS

	ENGINE #1	ENGINE #4
$\Delta \hat{\bar{T}}$	—	—
$\hat{\epsilon}_{max}$	—	—
$\hat{\epsilon}_{r.m.s.}$	—	—
$\lvert\hat{\bar{T}}\rvert$	—	—

Test 8

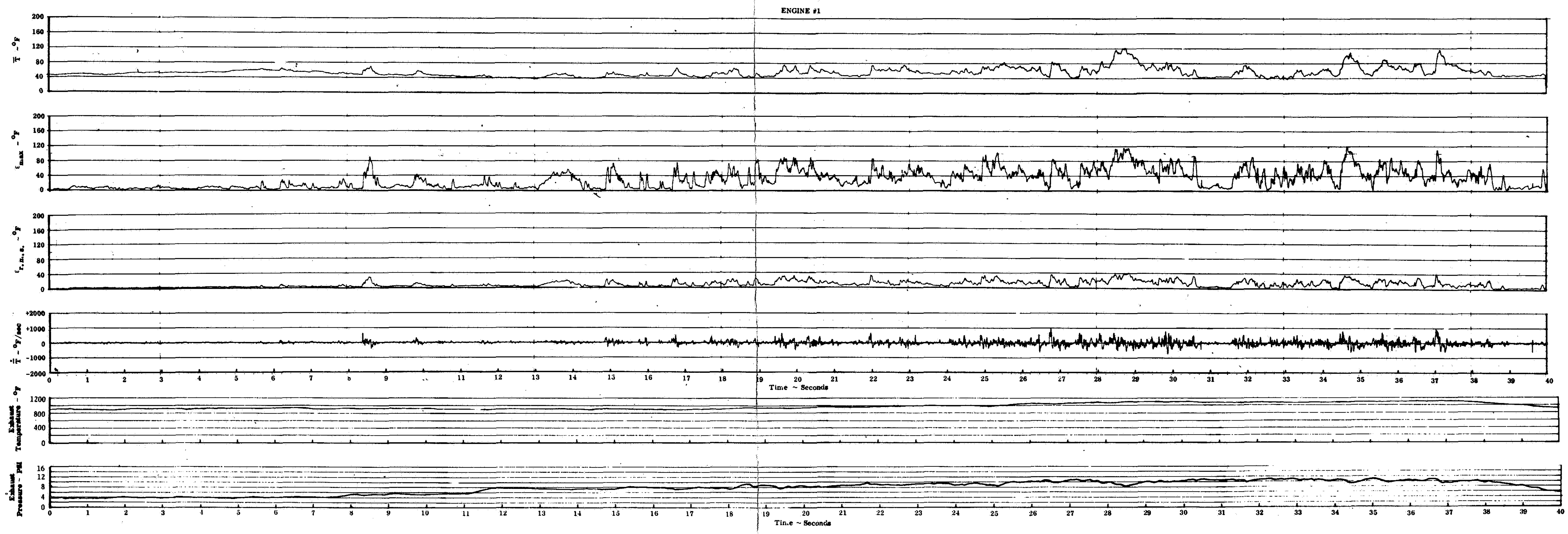

FIGURE A8-1. EXHAUST CONDITIONS AND INGESTION CHARACTERISTICS

Test 8

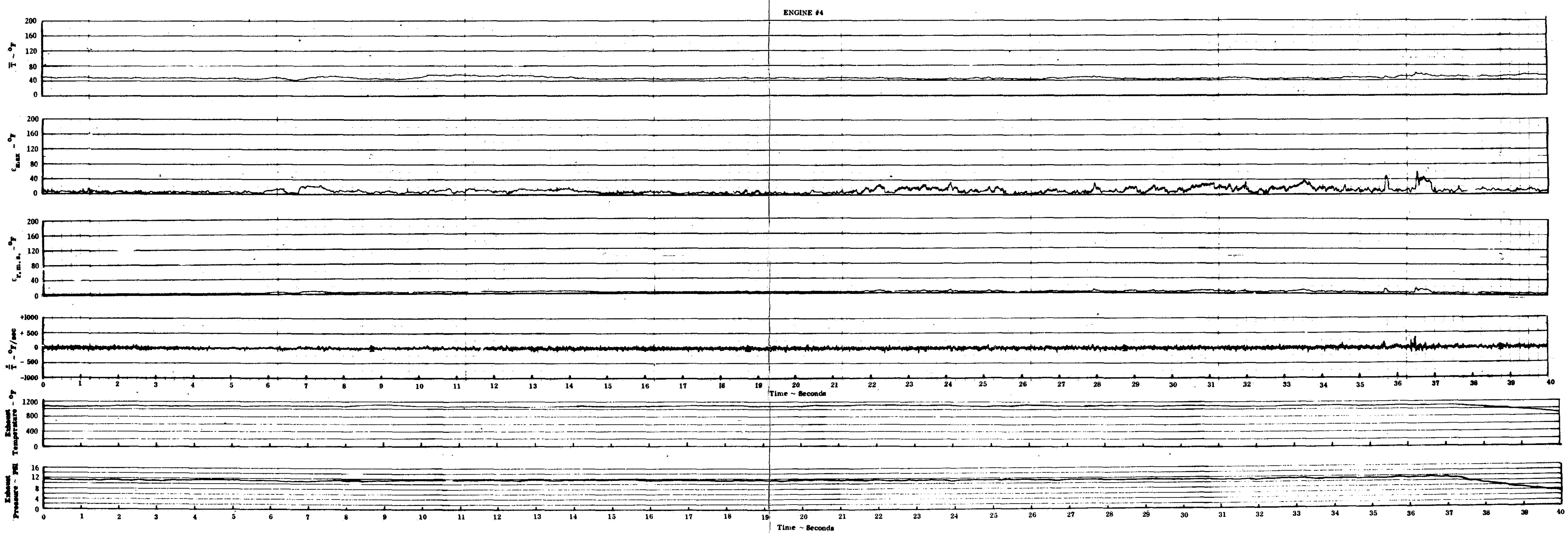

FIGURE A8-2. EXHAUST CONDITIONS AND INGESTION CHARACTERISTICS

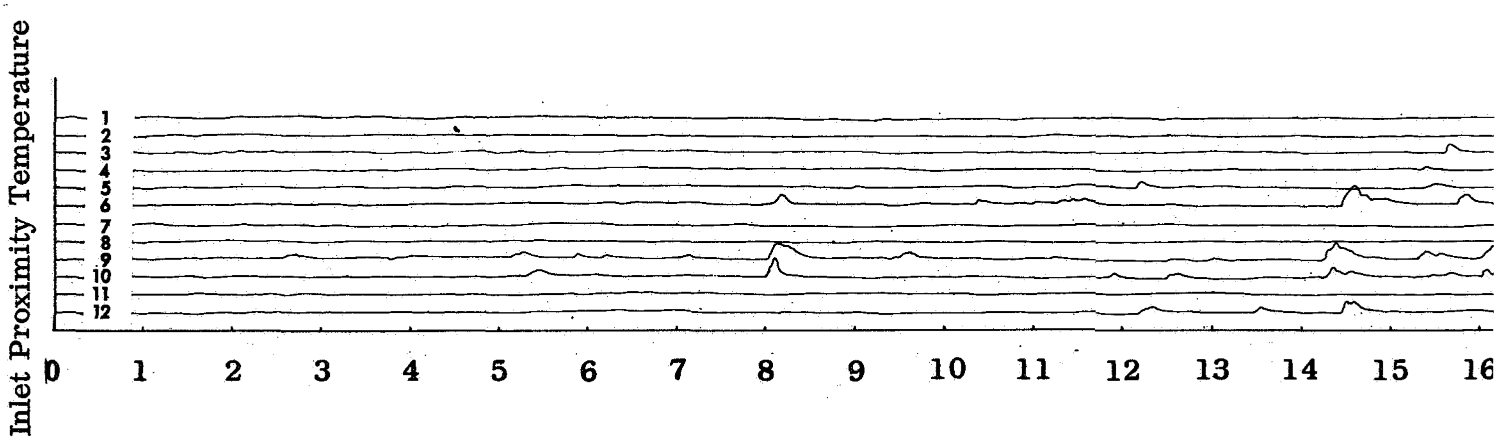
Inlet Proximity Temperature
1
2
3
4
5
6
7
8
9
10
11
12
0 1 2 3 4 5 6 7 8 9 10 11 12 13 14 15 16

2

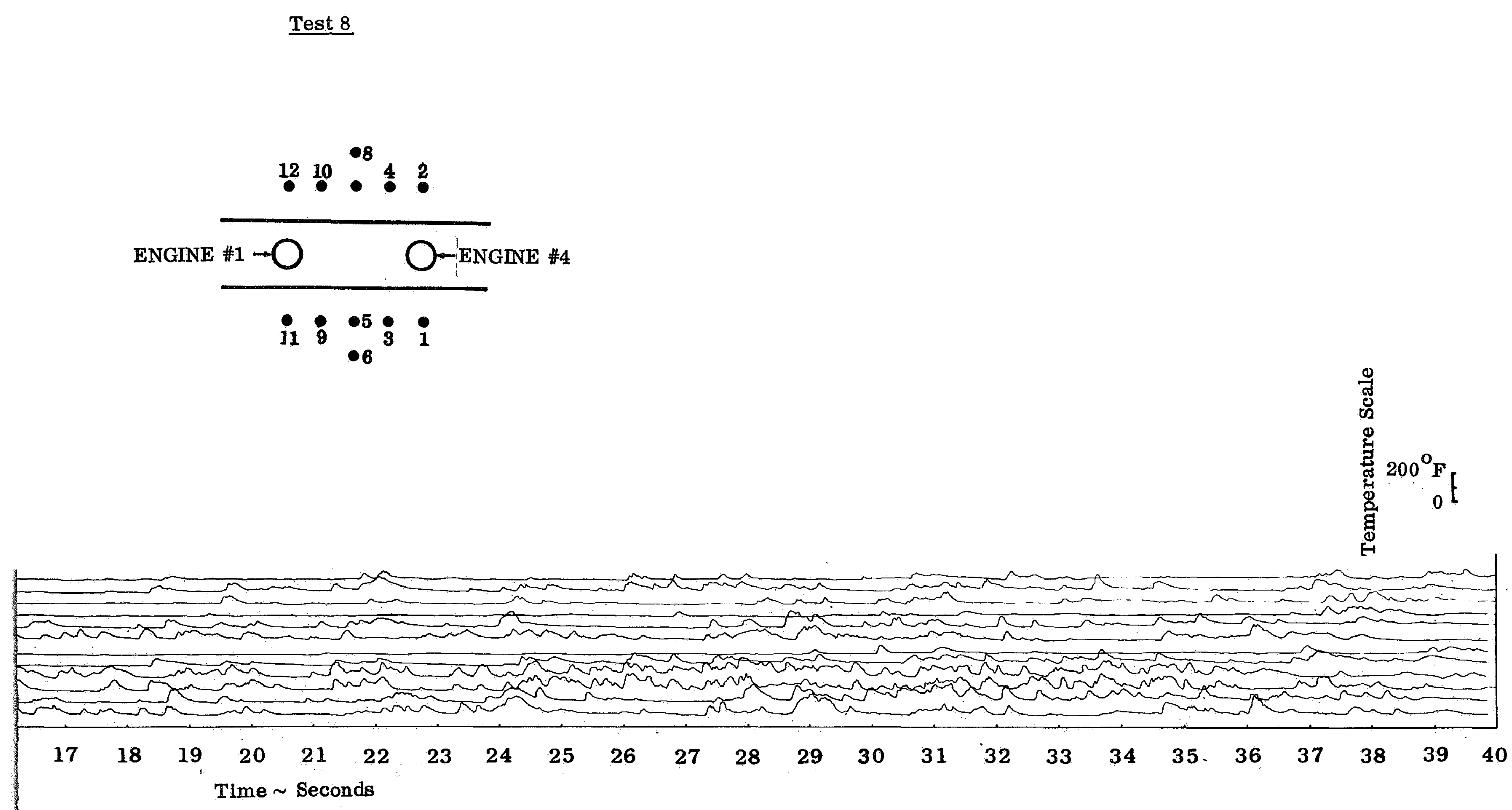

FIGURE A8-3. INLET PROXIMITY TEMPERATURES

Test #9

H/D = 4

α = 0

Wind = <4 MPH

Engines #1 and #4 operating

INGESTION CHARACTERISTICS

	ENGINE #1	ENGINE #4
$\Delta \hat{\bar{T}}$	—	—
$\hat{\epsilon}_{max}$	—	—
$\hat{\epsilon}_{r.m.s.}$	—	—
$\lvert\hat{\bar{T}}\rvert$	—	—

Test 9

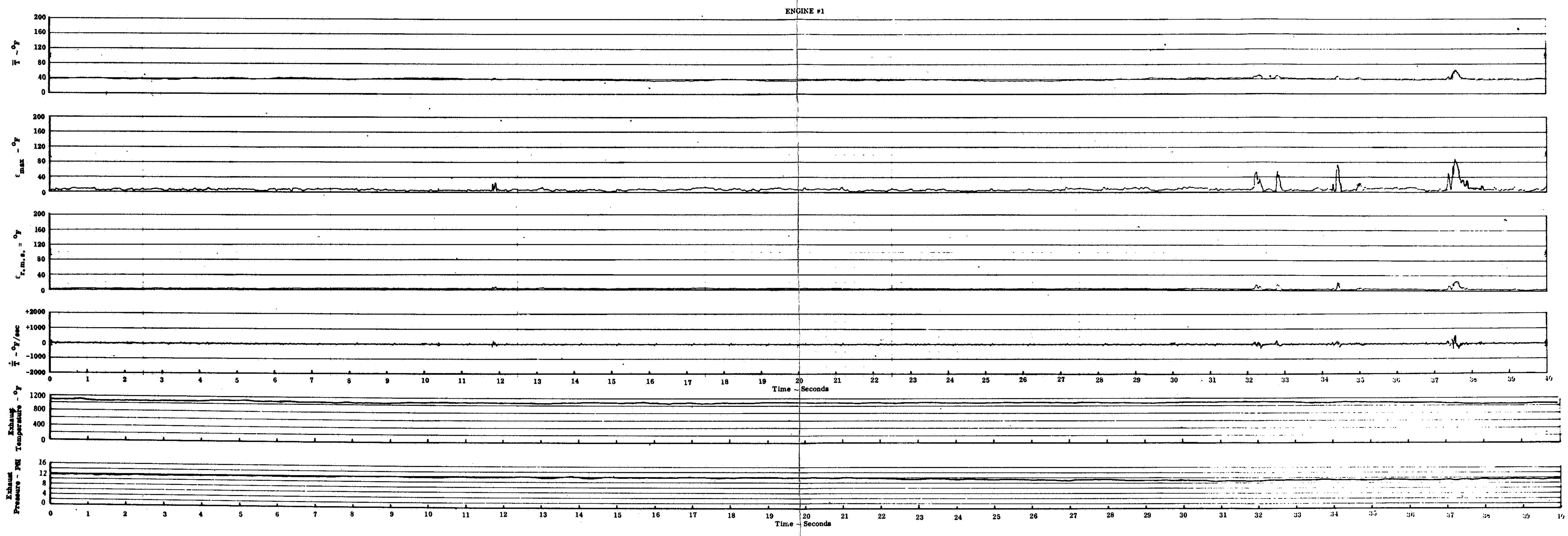

FIGURE A9-1. EXHAUST CONDITIONS AND INGESTION CHARACTERISTICS

Test 9

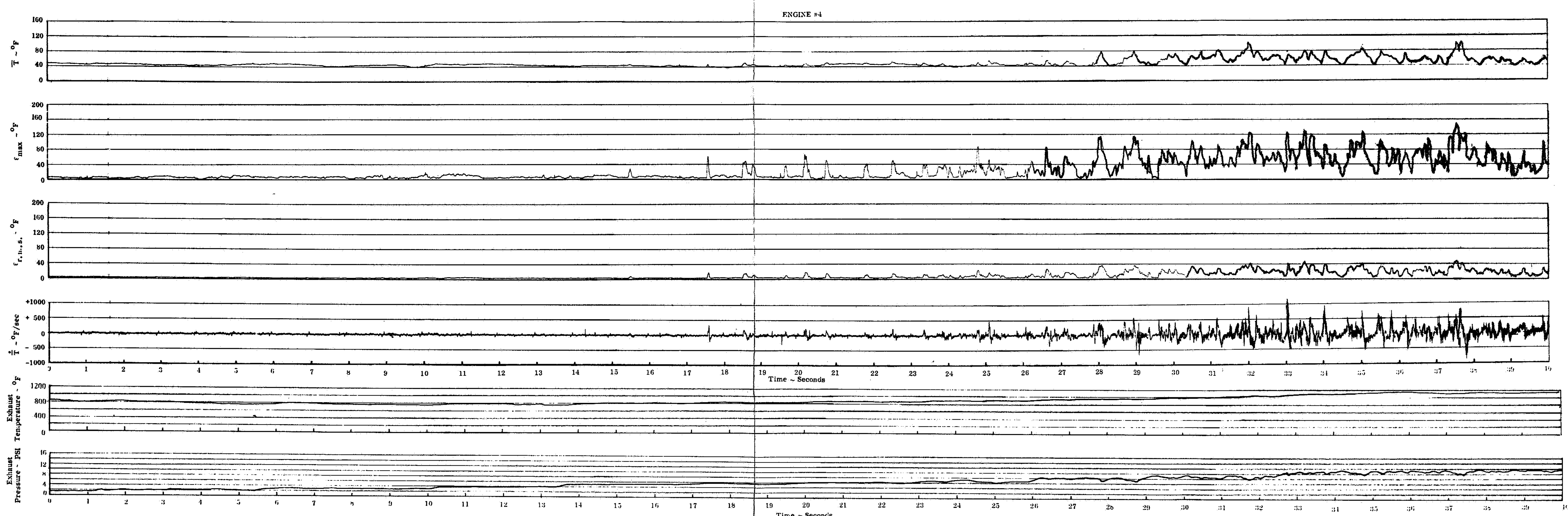

FIGURE A9-2. EXHAUST CONDITIONS AND INGESTION CHARACTERISTICS

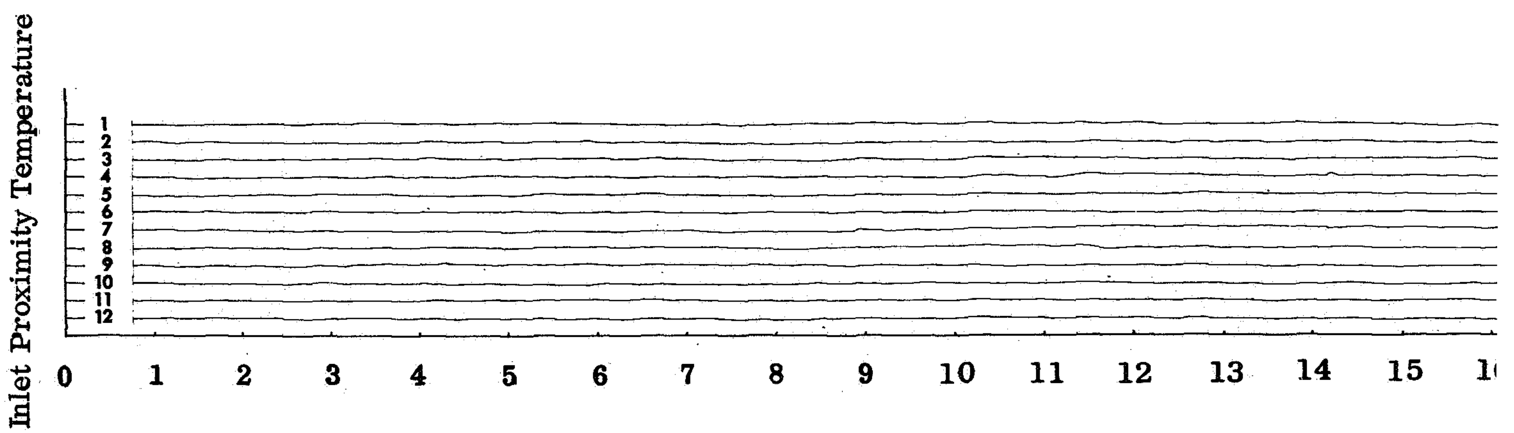
Inlet Proximity Temperature
1
2
3
4
5
6
7
8
9
10
11
12
0
1
2
3
4
5
6
7
8
9
10
11
12
13
14
15

2

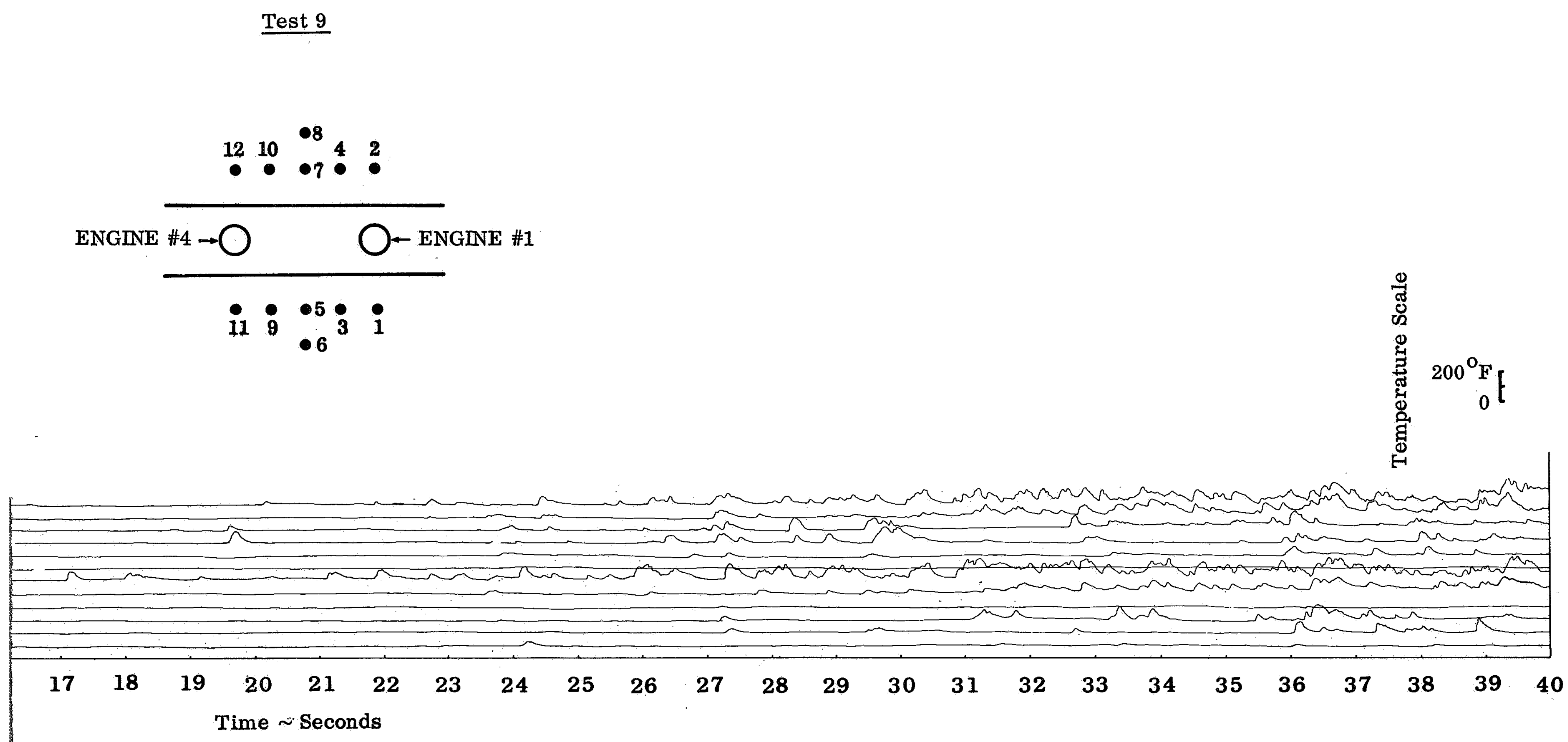

FIGURE A9-3. INLET PROXIMITY TEMPERATURES

Test #10

H/D = 6

α = 0

Wind = < 4 MPH

Engines #1 and #4 operating

INGESTION CHARACTERISTICS

	ENGINE #1	ENGINE #4
$\Delta \hat{\bar{T}}$	16°F	4°F
$\hat{\epsilon}_{max}$	46°F	16°F
$\hat{\epsilon}_{r.m.s.}$	12°F	6°F
$\lvert\hat{\dot{T}}\rvert$	135°F/sec	55°F/sec

Test 10

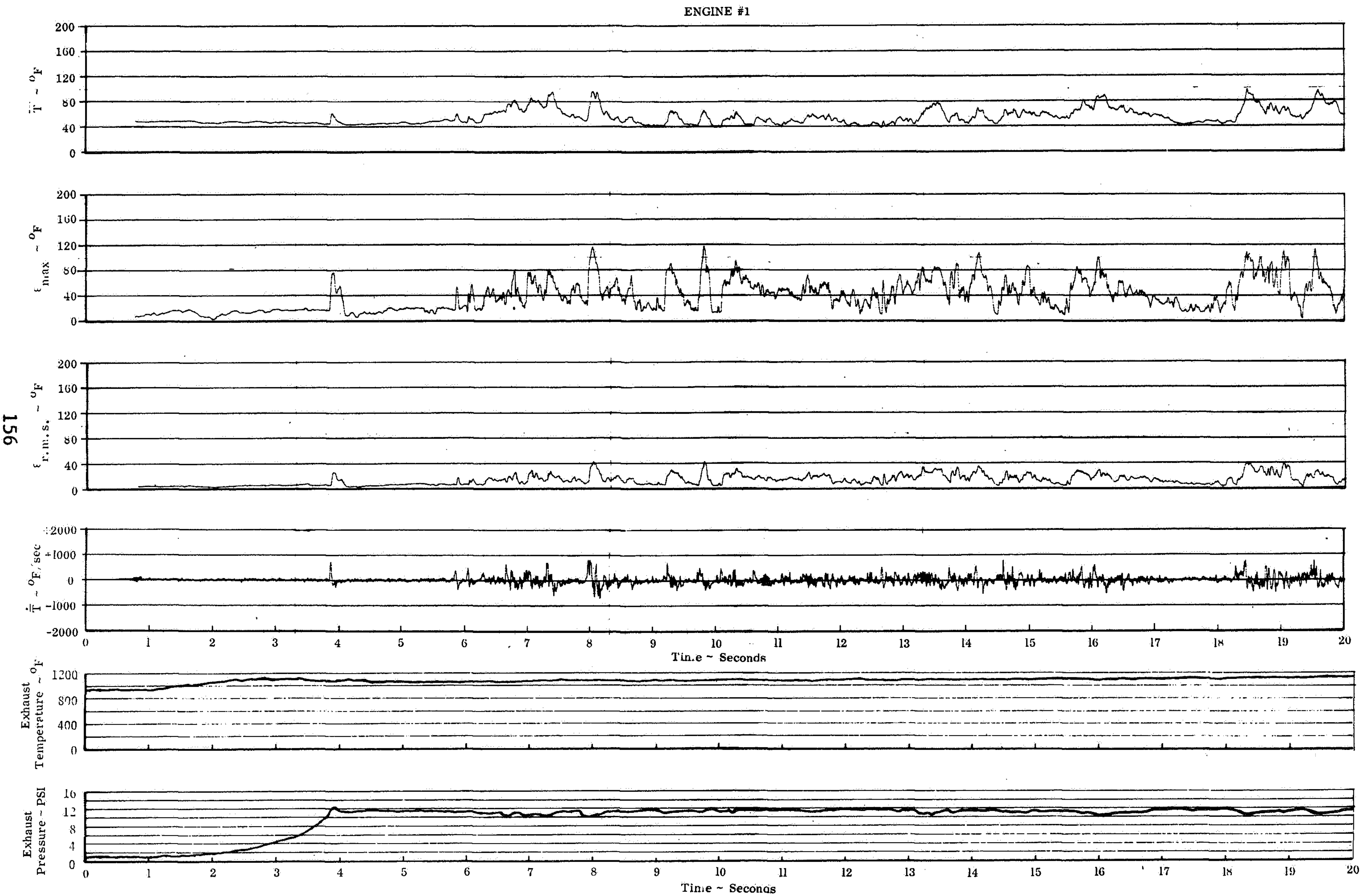

FIGURE A10-1. EXHAUST CONDITIONS AND INGESTION CHARACTERISTICS

Test 10

ENGINE #4

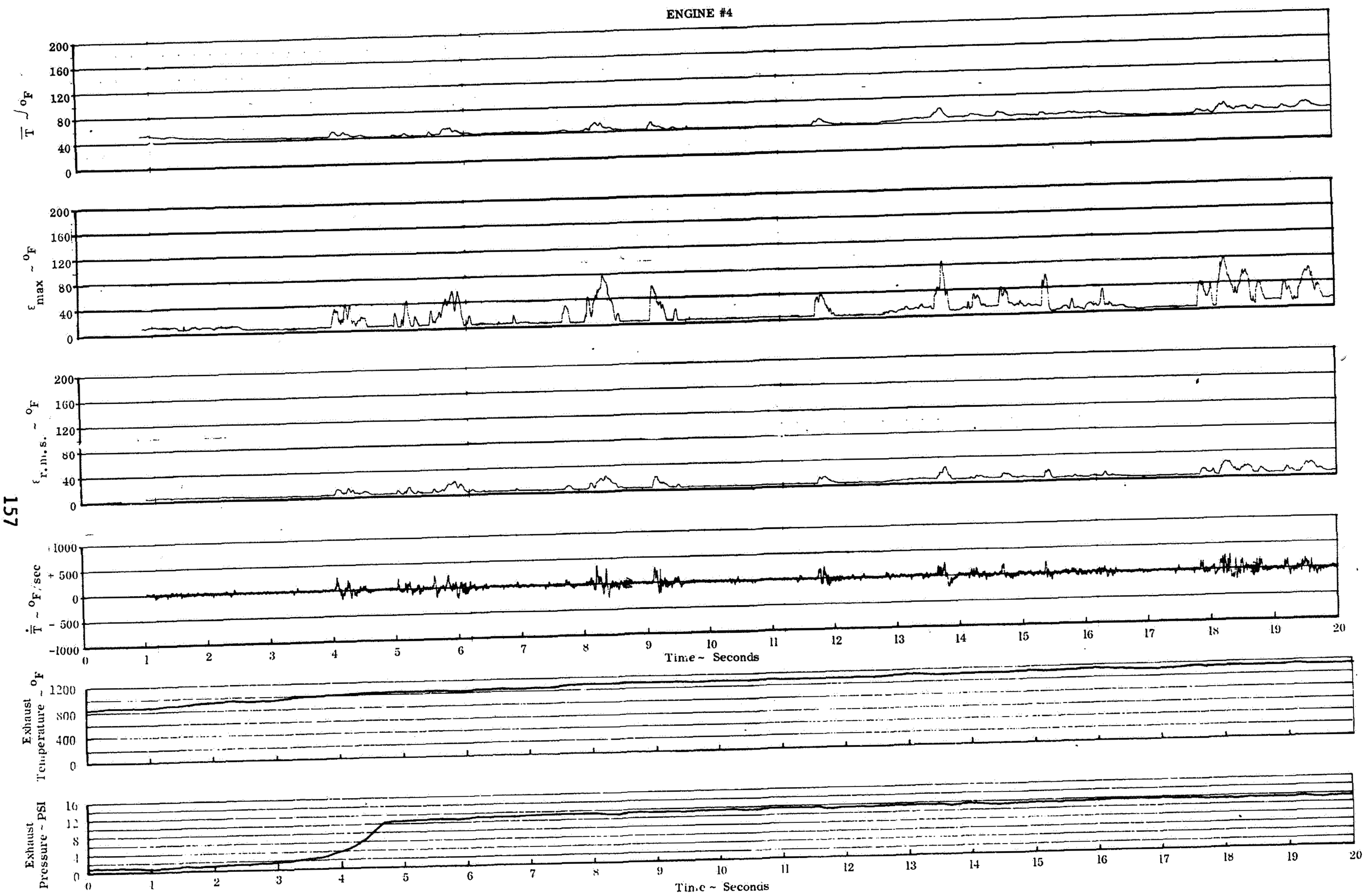

FIGURE A10-2. EXHAUST CONDITIONS AND INGESTION CHARACTERISTICS

Test 10

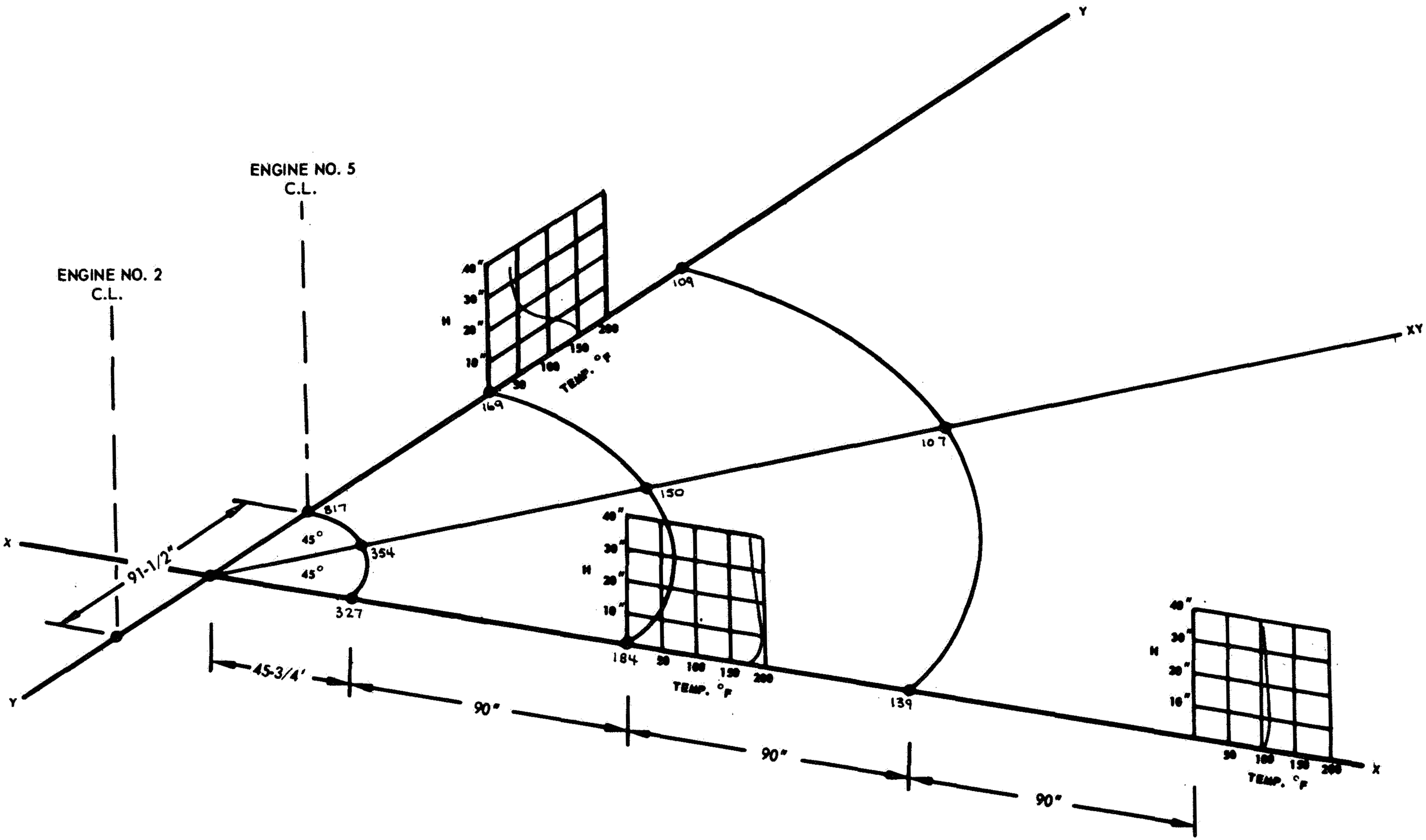

FIGURE A10-3. GROUND JET TEMPERATURE PROFILE

Test 10

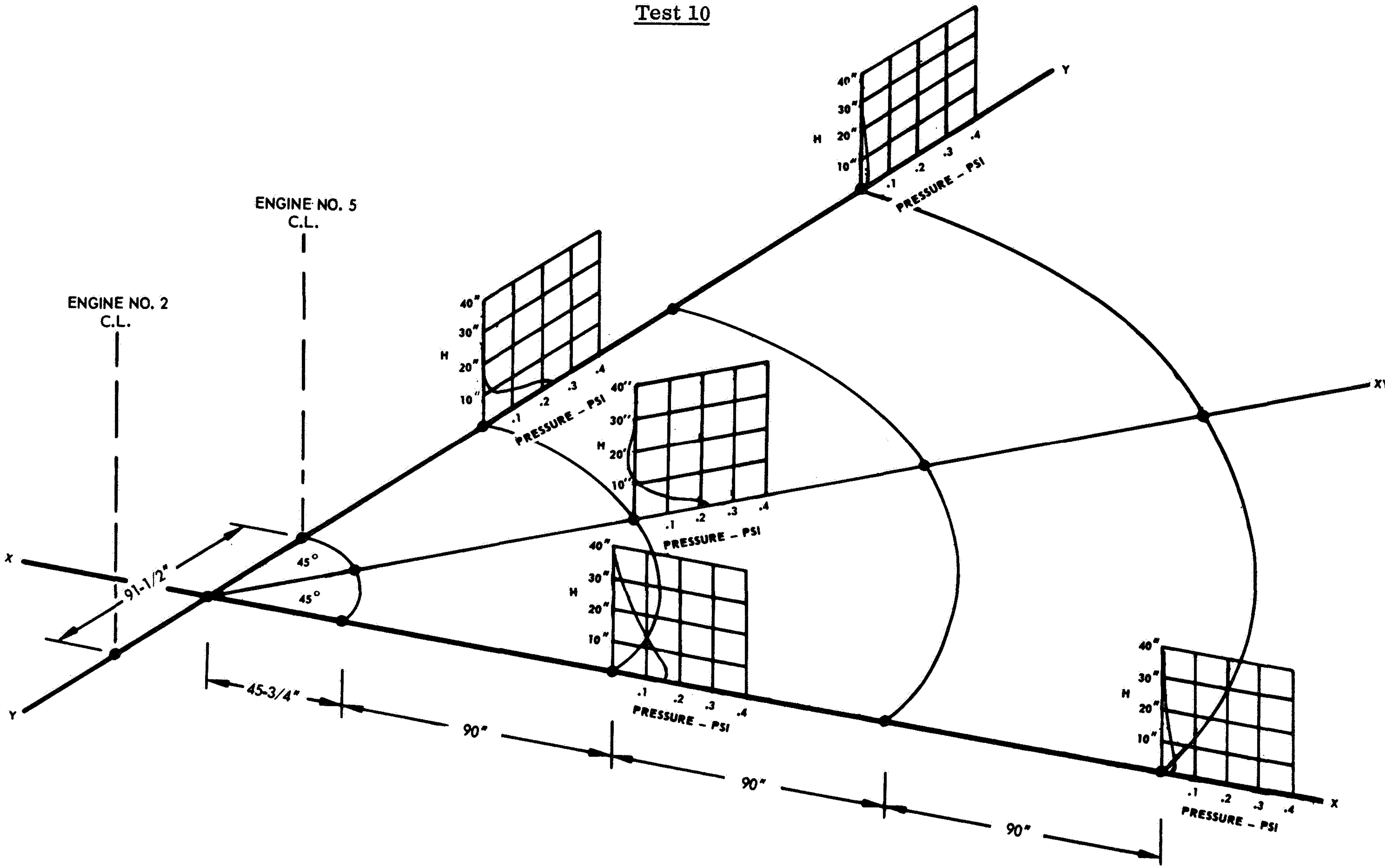

FIGURE A10-4. GROUND JET TEMPERATURE PROFILE

Test 10

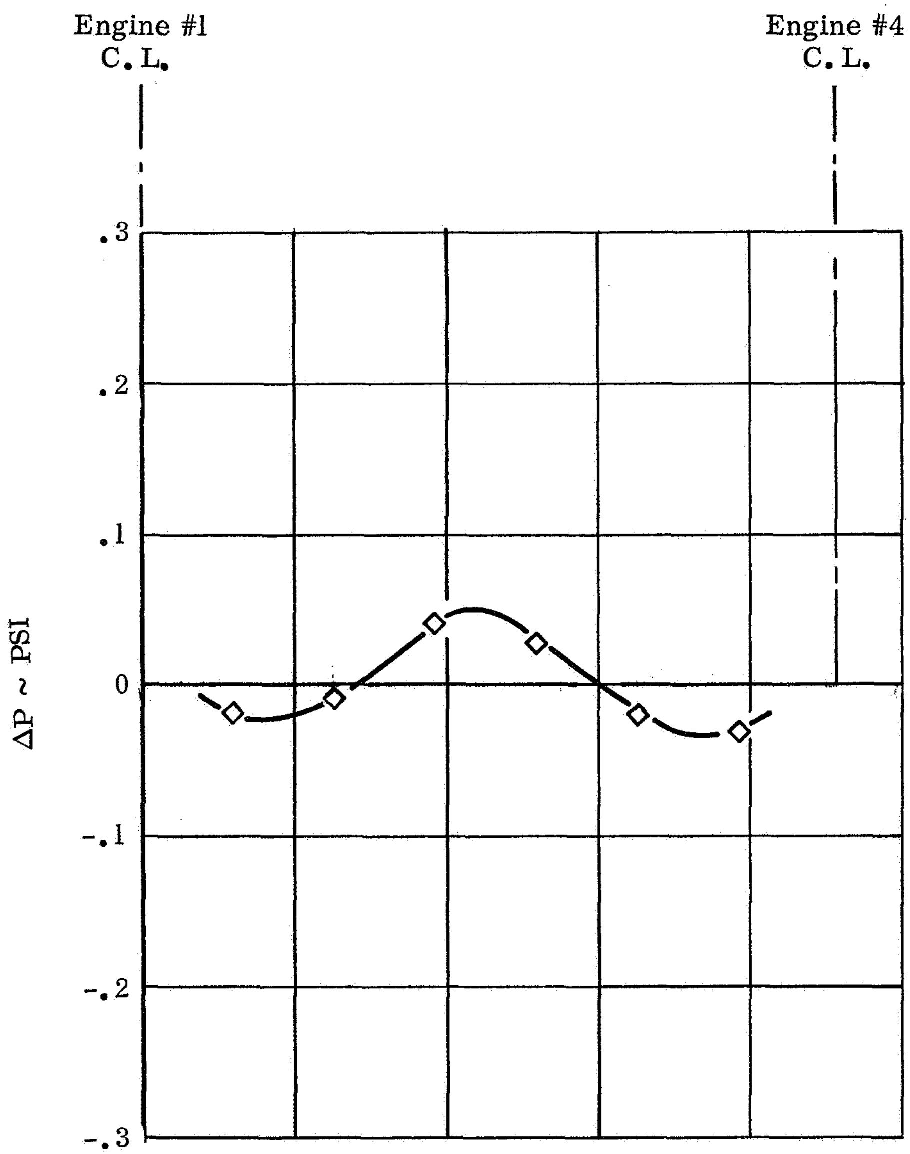

FIGURE A10-5. POD UNDERSURFACE PRESSURE DISTRIBUTION

Test #11

H/D = 8

α = 0

Wind = <4 MPH

Engines #1 and #4 operating

INGESTION CHARACTERISTICS

	ENGINE #1	ENGINE #4
$\Delta \hat{\bar{T}}$	3°F	3°F
$\hat{\epsilon}_{max}$	7°F	4°F
$\hat{\epsilon}_{r.m.s.}$	2°F	2°F
$\lvert\hat{\dot{T}}\rvert$	35°F/sec	—

Test 11

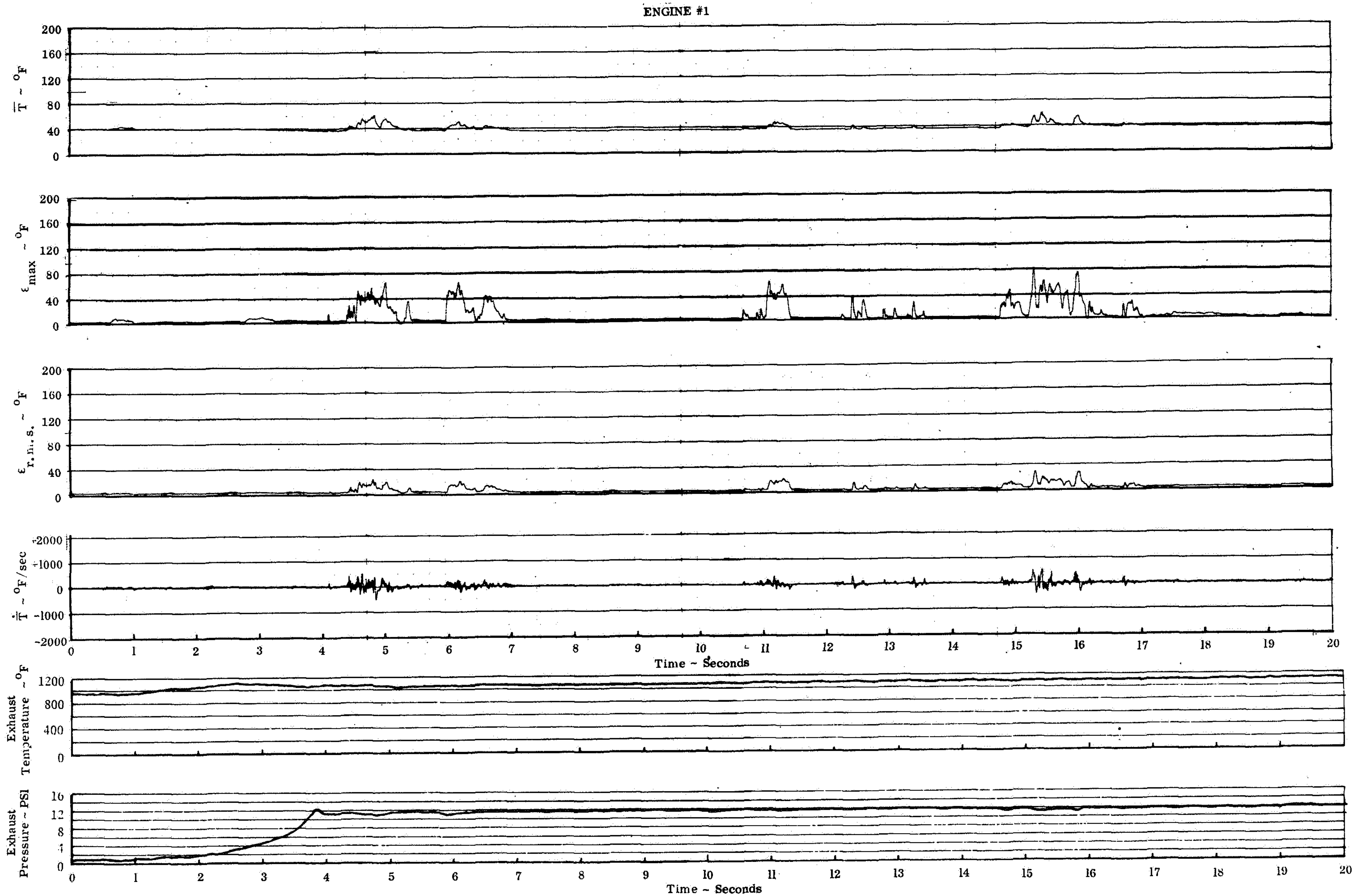

FIGURE A11-1. EXHAUST CONDITIONS AND INGESTION CHARACTERISTICS

Test 11

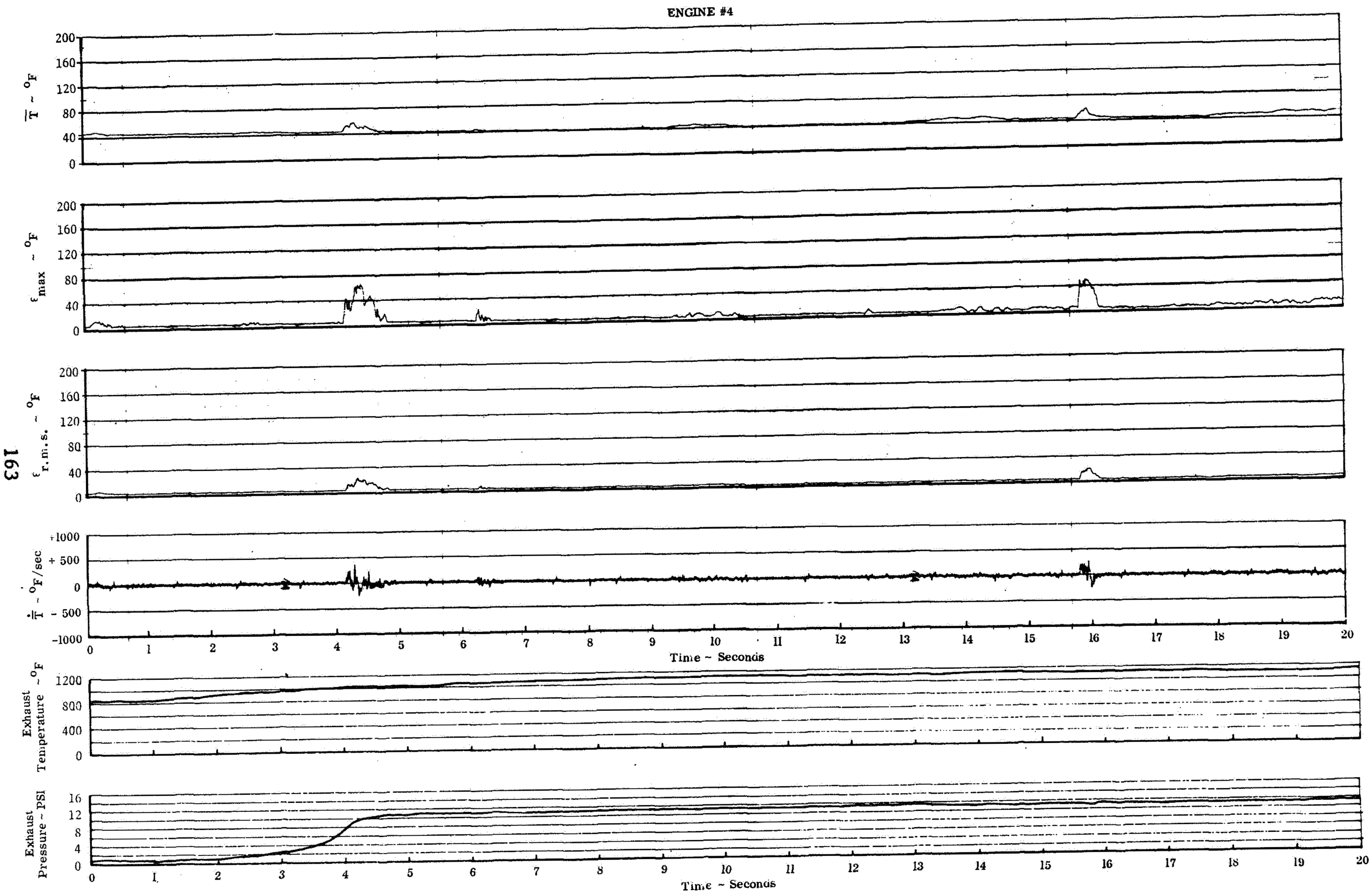

FIGURE A11-2. EXHAUST CONDITIONS AND INGESTION CHARACTERISTICS

Test 11

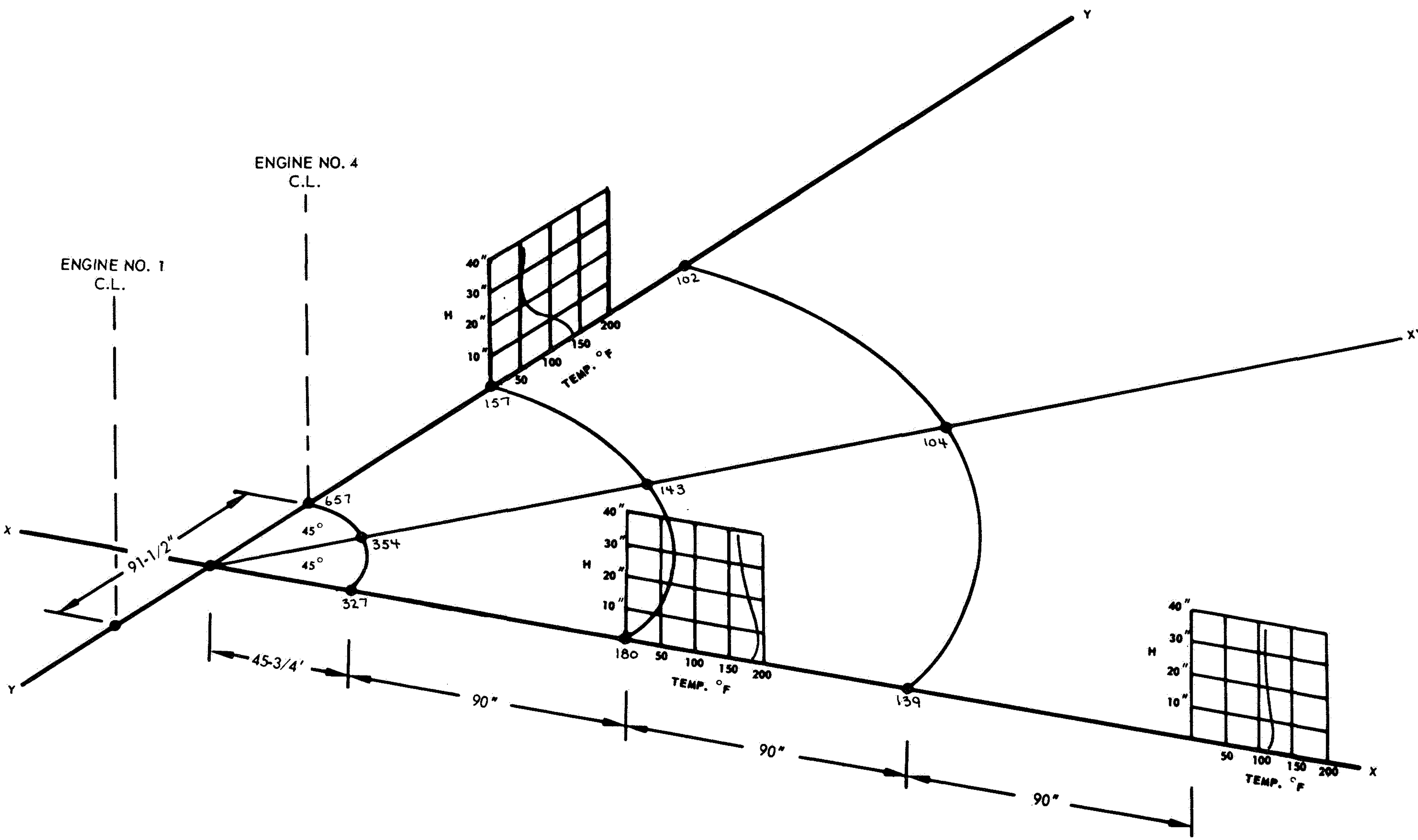

FIGURE A11-3. GROUND JET TEMPERATURE PROFILE

Test 11

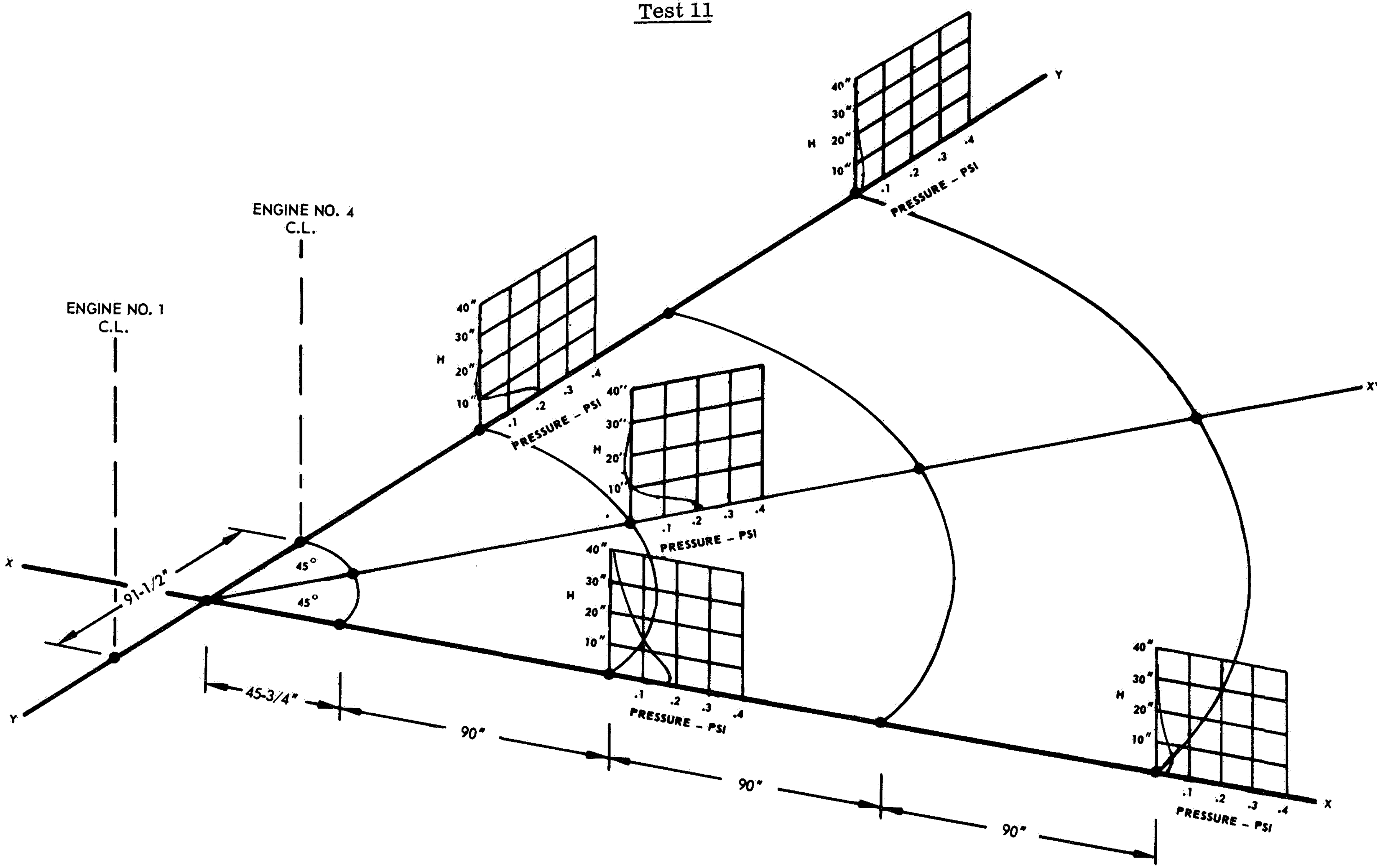

FIGURE A11-4. GROUND JET DYNAMIC PRESSURE PROFILE

Test 11

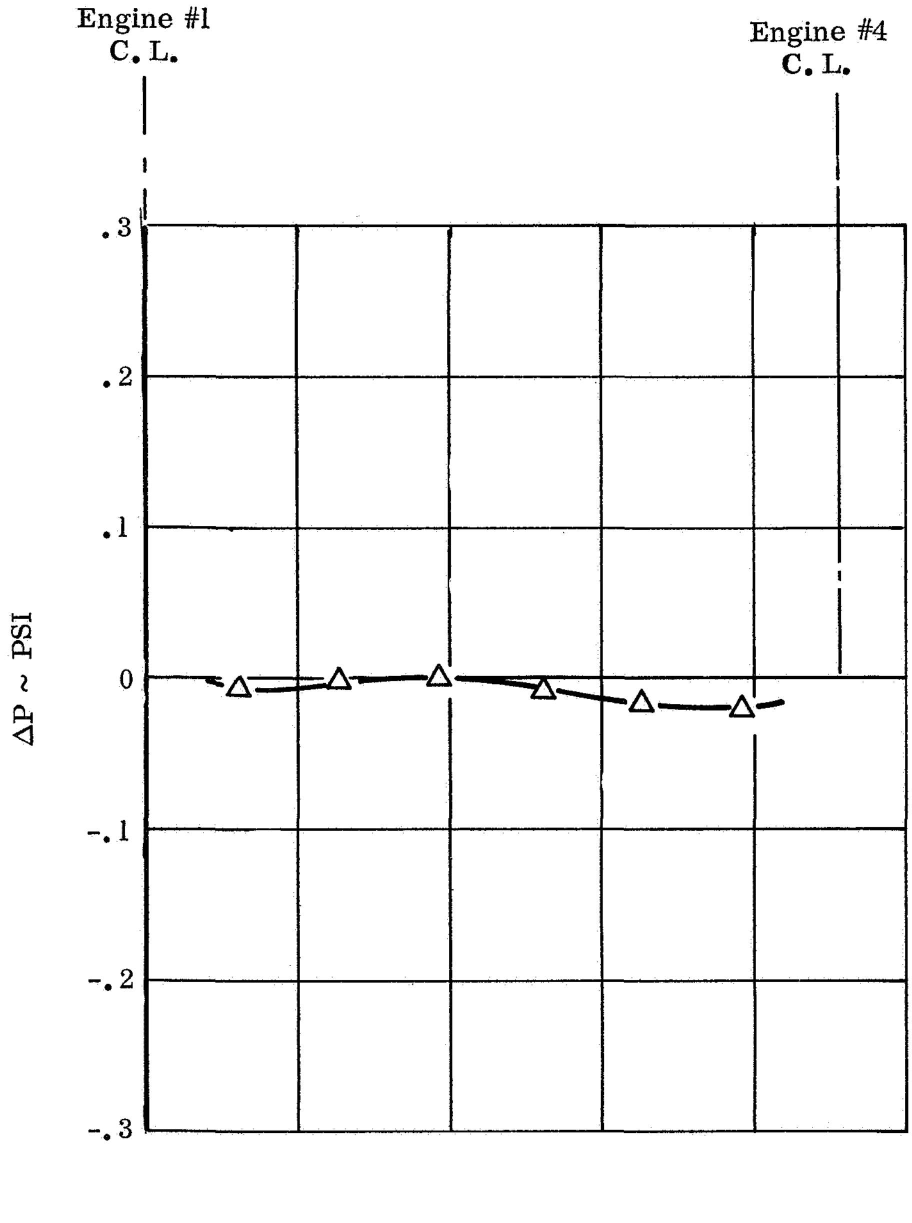

FIGURE A11-5. POD UNDERSURFACE PRESSURE DISTRIBUTION

Test #12

$H/D = 2$

$\alpha = 0$

Wind = <4 MPH

Engine #4 operating

INGESTION CHARACTERISTICS

	ENGINE #1	ENGINE #4
$\Delta\hat{\bar{T}}$		0°F
$\hat{\epsilon}_{max}$		2°F
$\hat{\epsilon}_{r.m.s.}$		0°F
$\lvert\hat{\bar{T}}\rvert$		—

Test 12

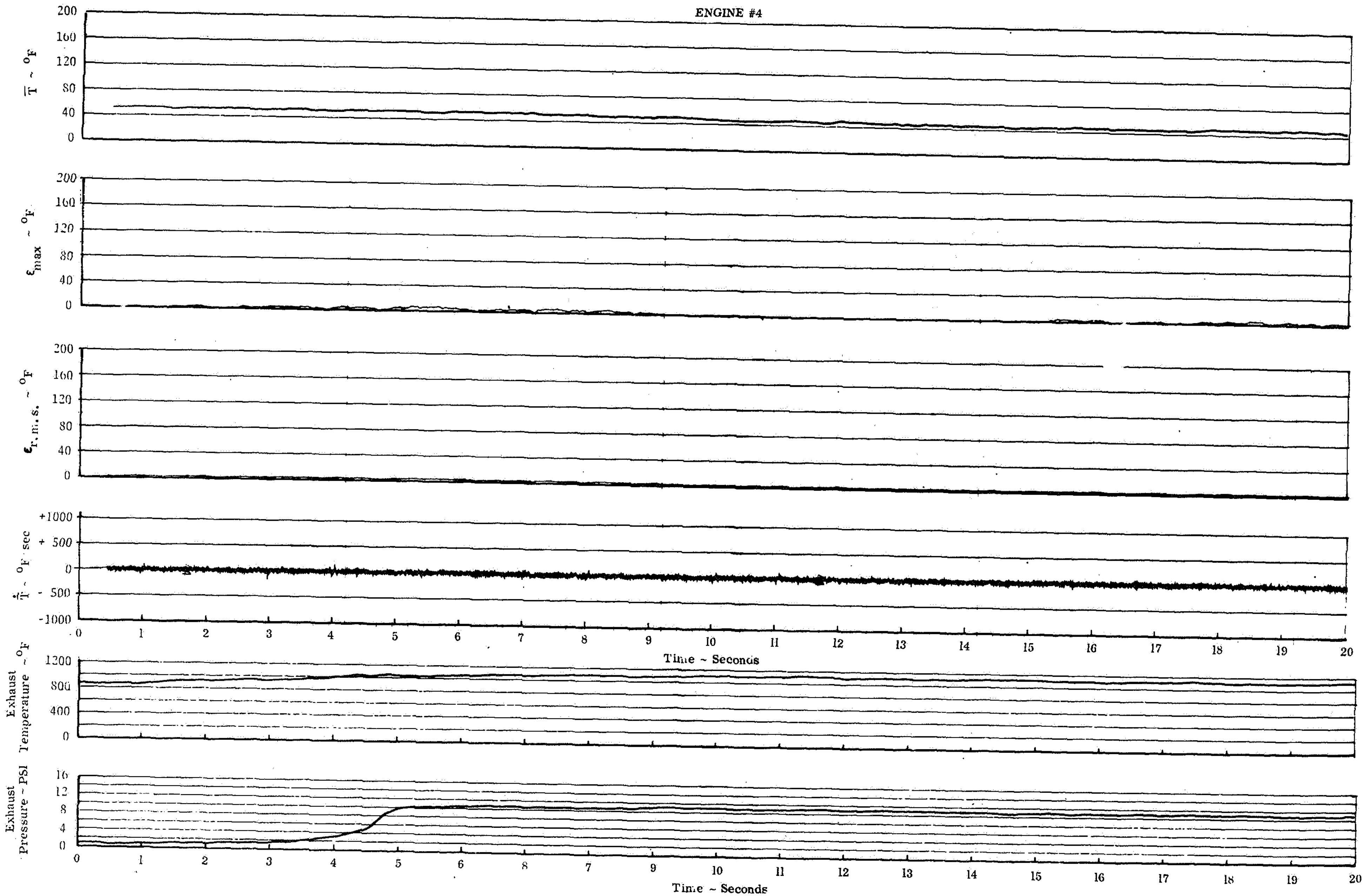

FIGURE A12-1. EXHAUST CONDITIONS AND INGESTION CHARACTERISTICS

Test 12

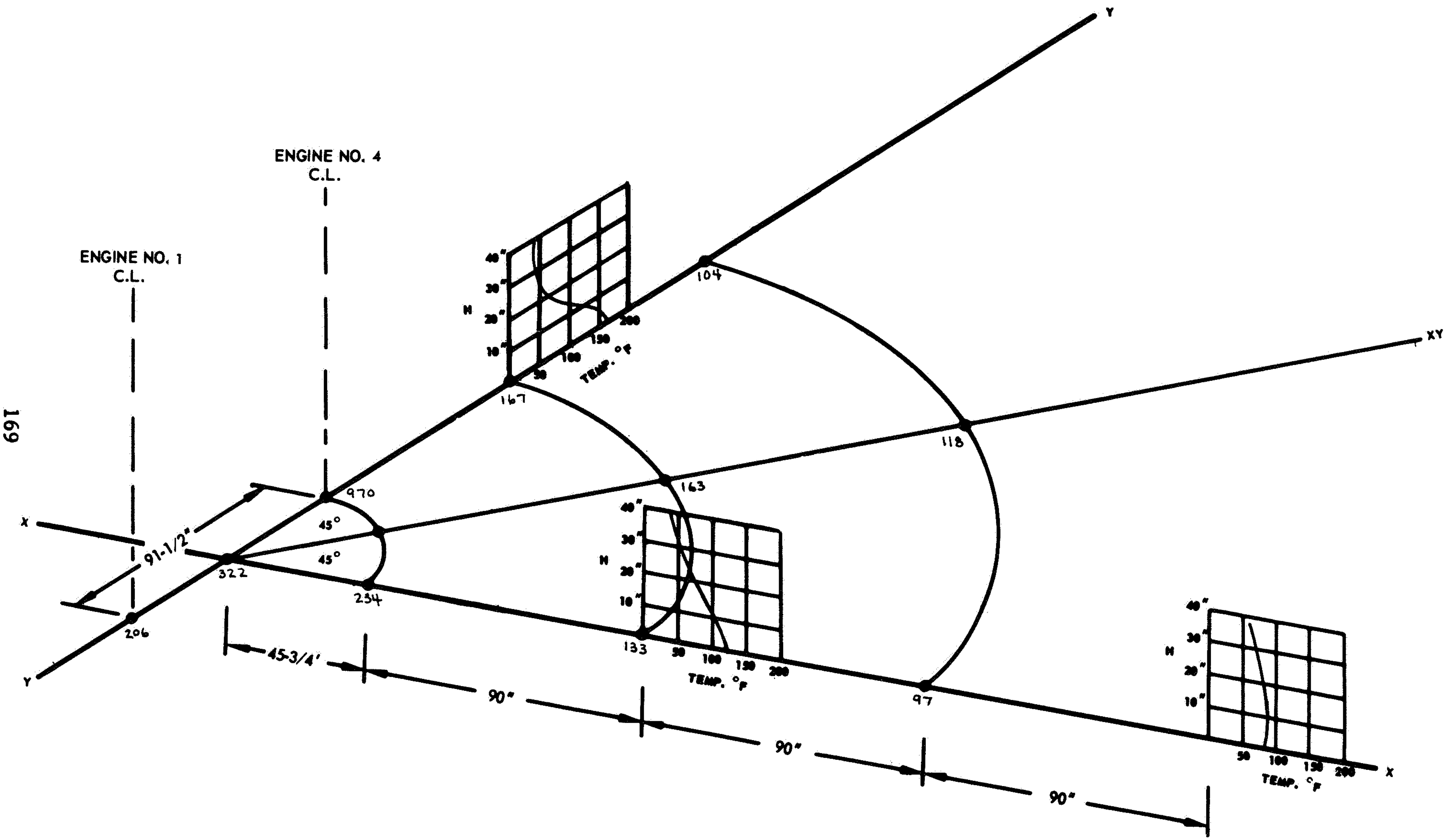

FIGURE A12-2. GROUND JET TEMPERATURE PROFILE

Test 12

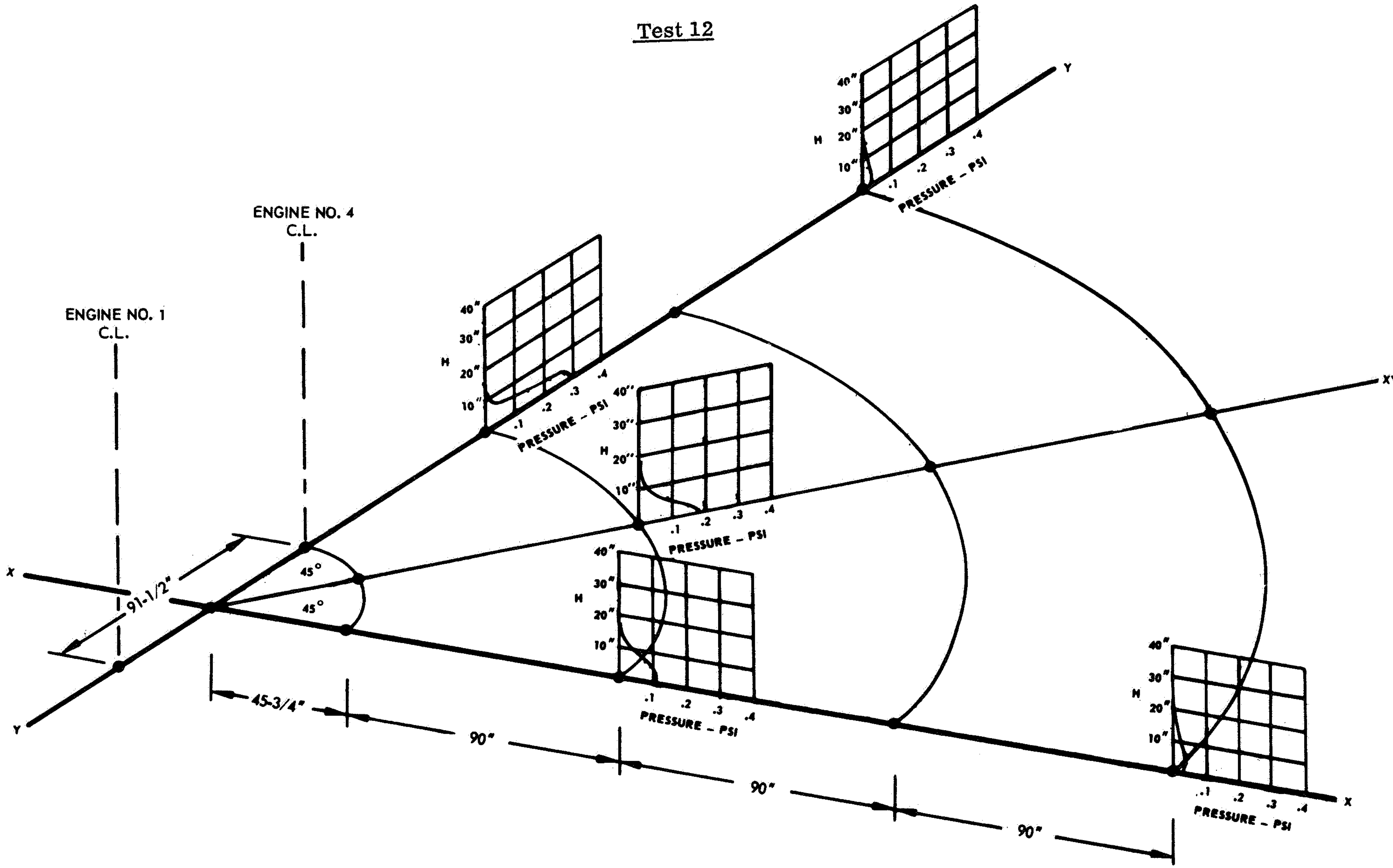

FIGURE A12-3. GROUND JET DYNAMIC PRESSURE PROFILE

Test #13

H/D = 4

α = 0

Wind = <4 MPH

Engine #4 operating

INGESTION CHARACTERISTICS

	ENGINE #1	ENGINE #4
$\Delta\hat{\bar{T}}$	X	0°F
$\hat{\epsilon}_{max}$	X	4°F
$\hat{\epsilon}_{r.m.s.}$	X	2°F
$\lvert\hat{\bar{T}}\rvert$	X	—

Test 13

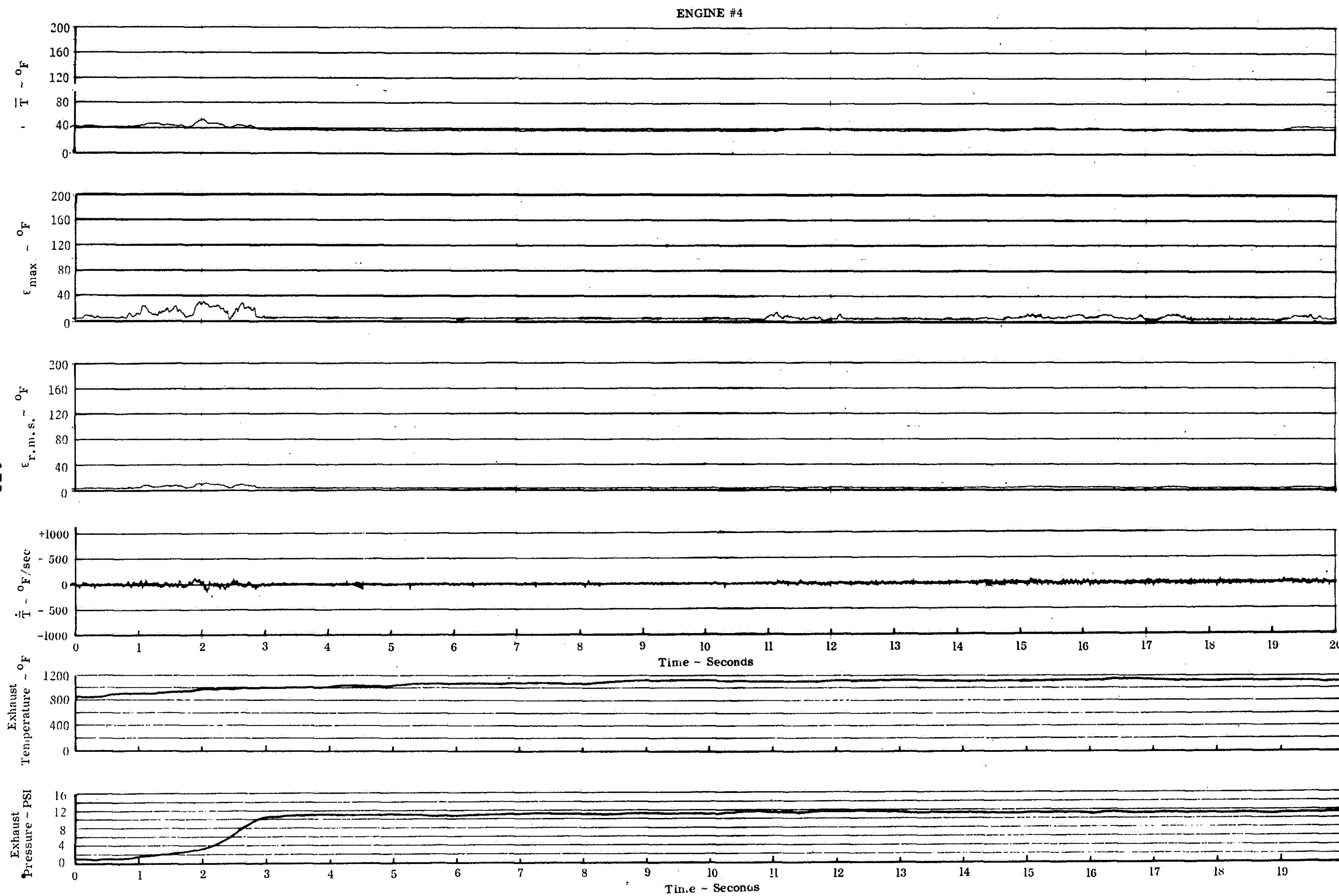

FIGURE A13-1. EXHAUST CONDITIONS AND INGESTION CHARACTERISTICS

Test 13

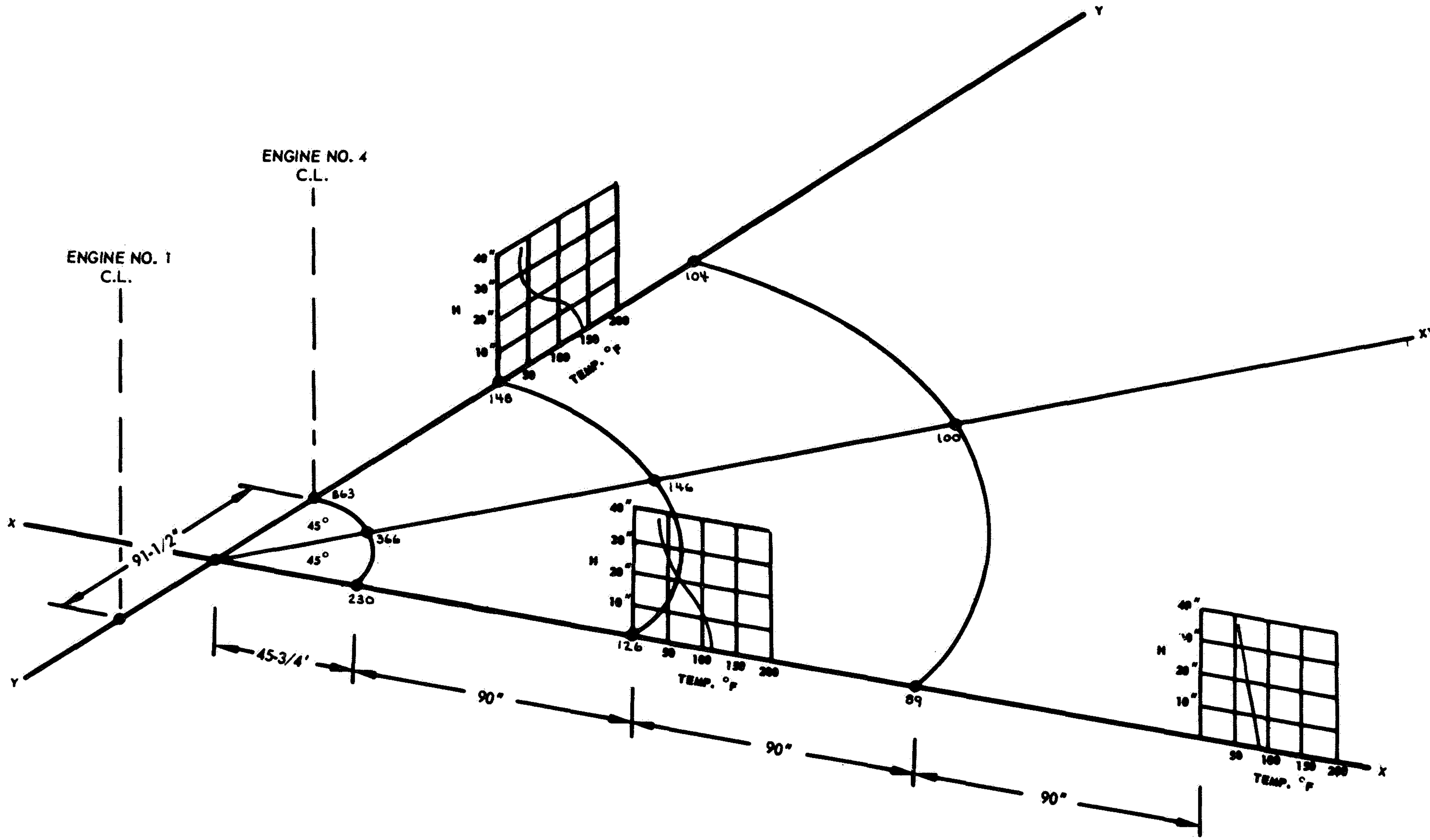

FIGURE A13-2. GROUND JET TEMPERATURE PROFILE

Test 13

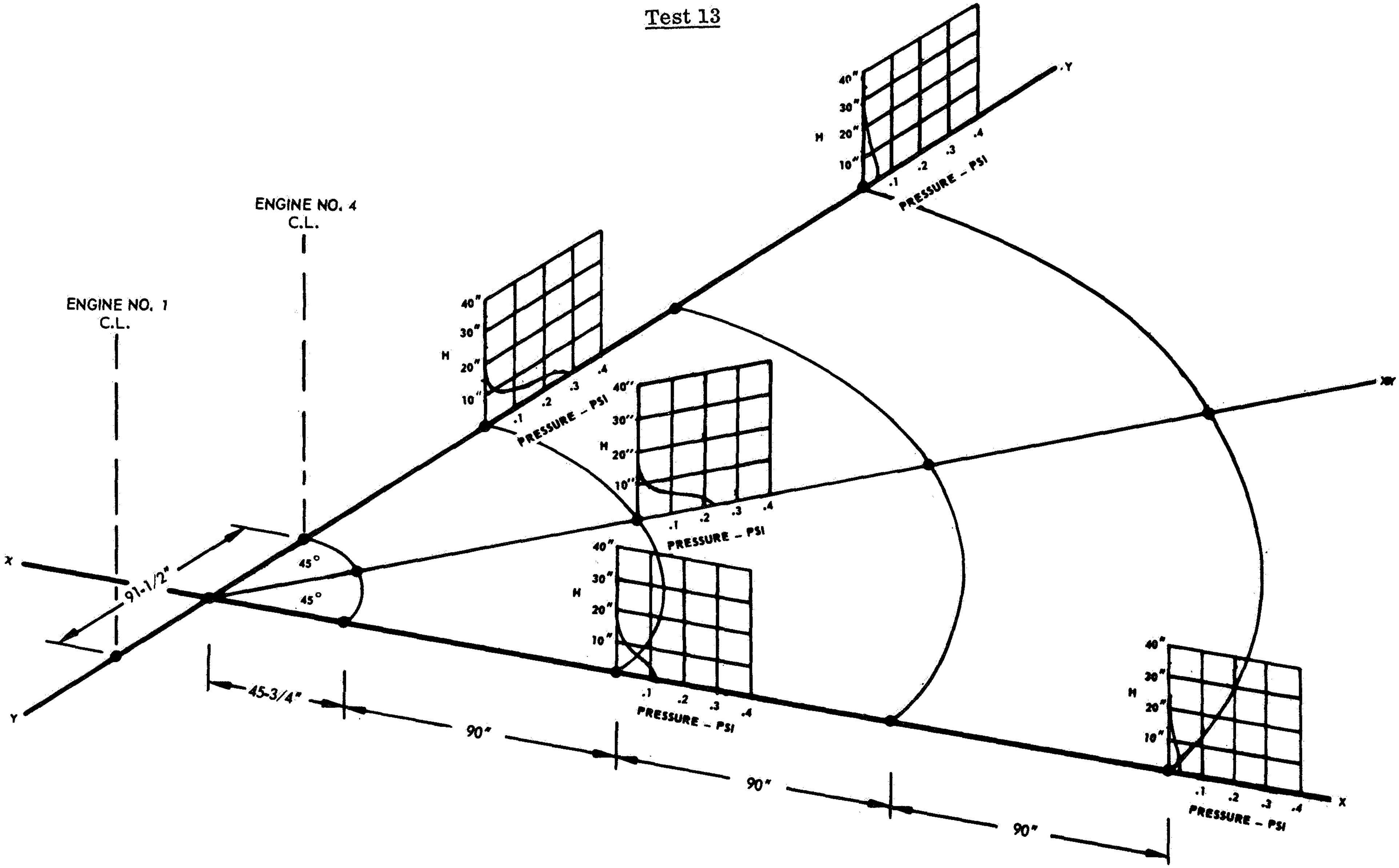

FIGURE A13-3. GROUND JET DYNAMIC PRESSURE PROFILE

Test 13

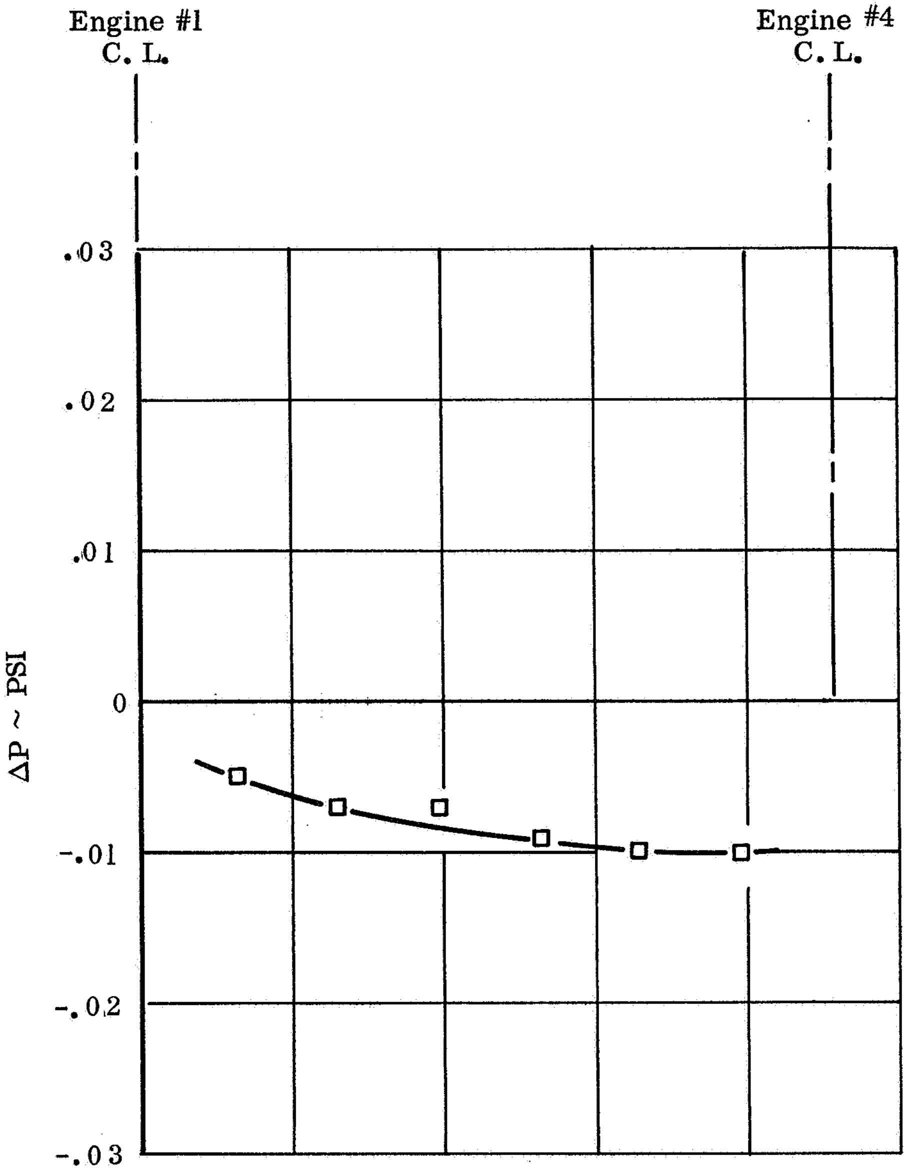

FIGURE A13-4. POD UNDERSURFACE PRESSURE DISTRIBUTION

Test #14

H/D = 6

α = 0

Wind = <4 MPH

Engine #4 operating

INGESTION CHARACTERISTICS

	ENGINE #1	ENGINE #4
$\Delta\hat{\bar{T}}$	X	0°F
$\hat{\epsilon}_{max}$	X	4°F
$\hat{\epsilon}_{r.m.s.}$	X	2°F
$\lvert\hat{\bar{T}}\rvert$	X	—

Test 14

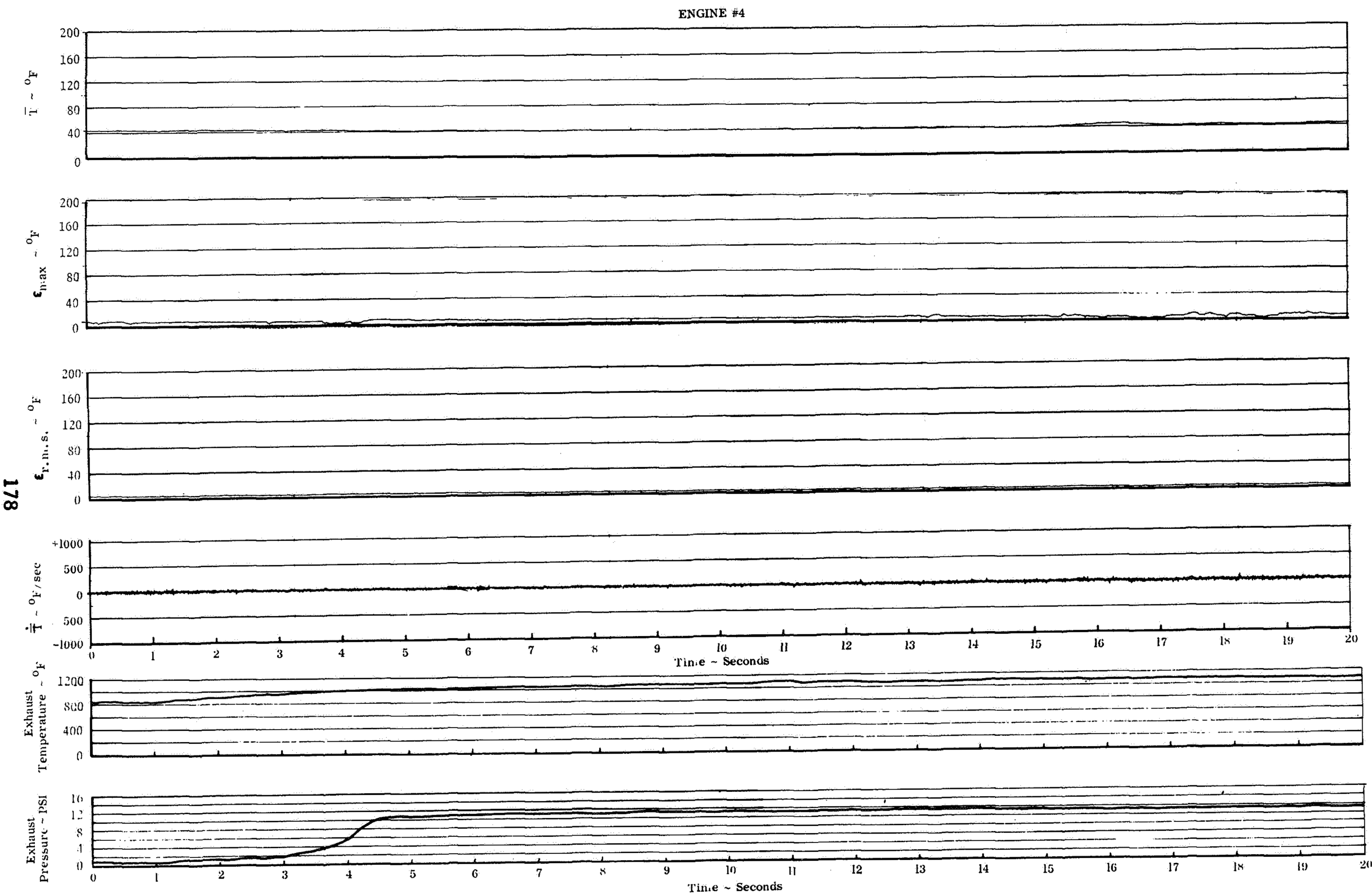

FIGURE A14-1. EXHAUST CONDITIONS AND INGESTION CHARACTERISTICS

Test 14

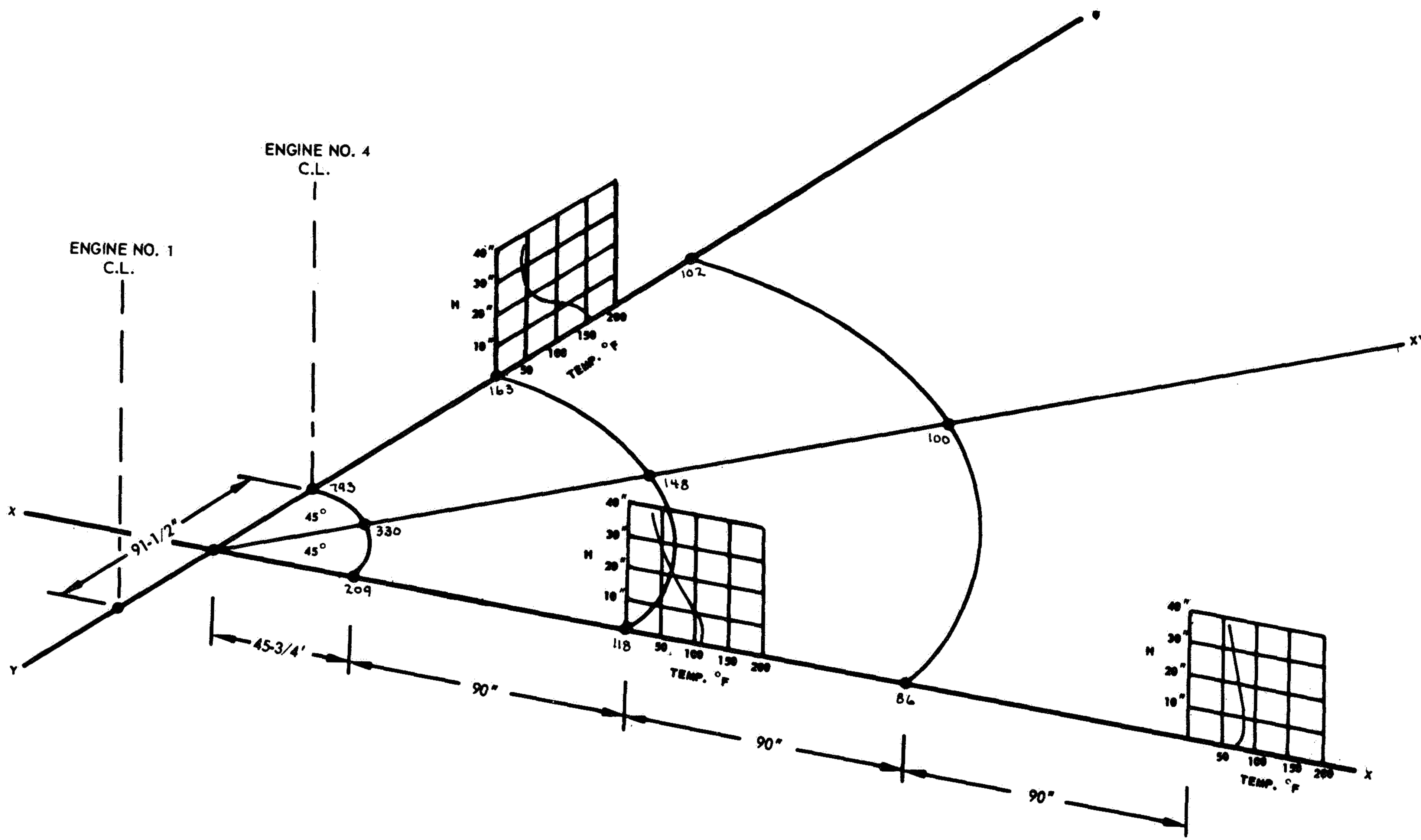

FIGURE A14-2. GROUND JET TEMPERATURE PROFILE

Test 14

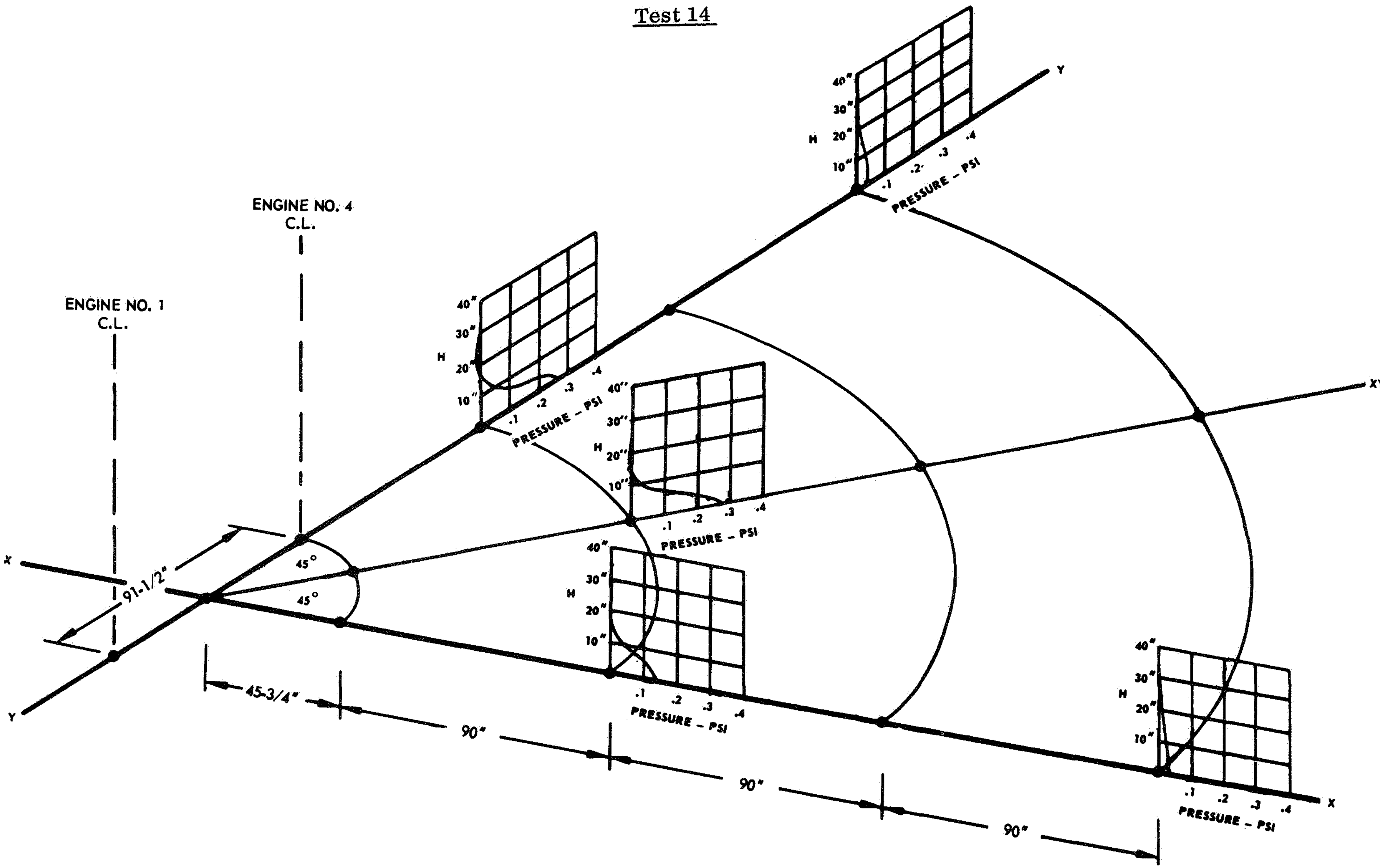

FIGURE A14-3. GROUND JET DYNAMIC PRESSURE PROFILE

Test #15

H/D = 8

α = 0

Wind = <4 MPH

Engine #4 operating

INGESTION CHARACTERISTICS

	ENGINE #1	ENGINE #4
$\Delta\hat{\bar{T}}$	X	1°F
$\hat{\epsilon}_{max}$	X	4°F
$\hat{\epsilon}_{r.m.s.}$	X	1°F
$\lvert\hat{\bar{T}}\rvert$	X	—

Test 15

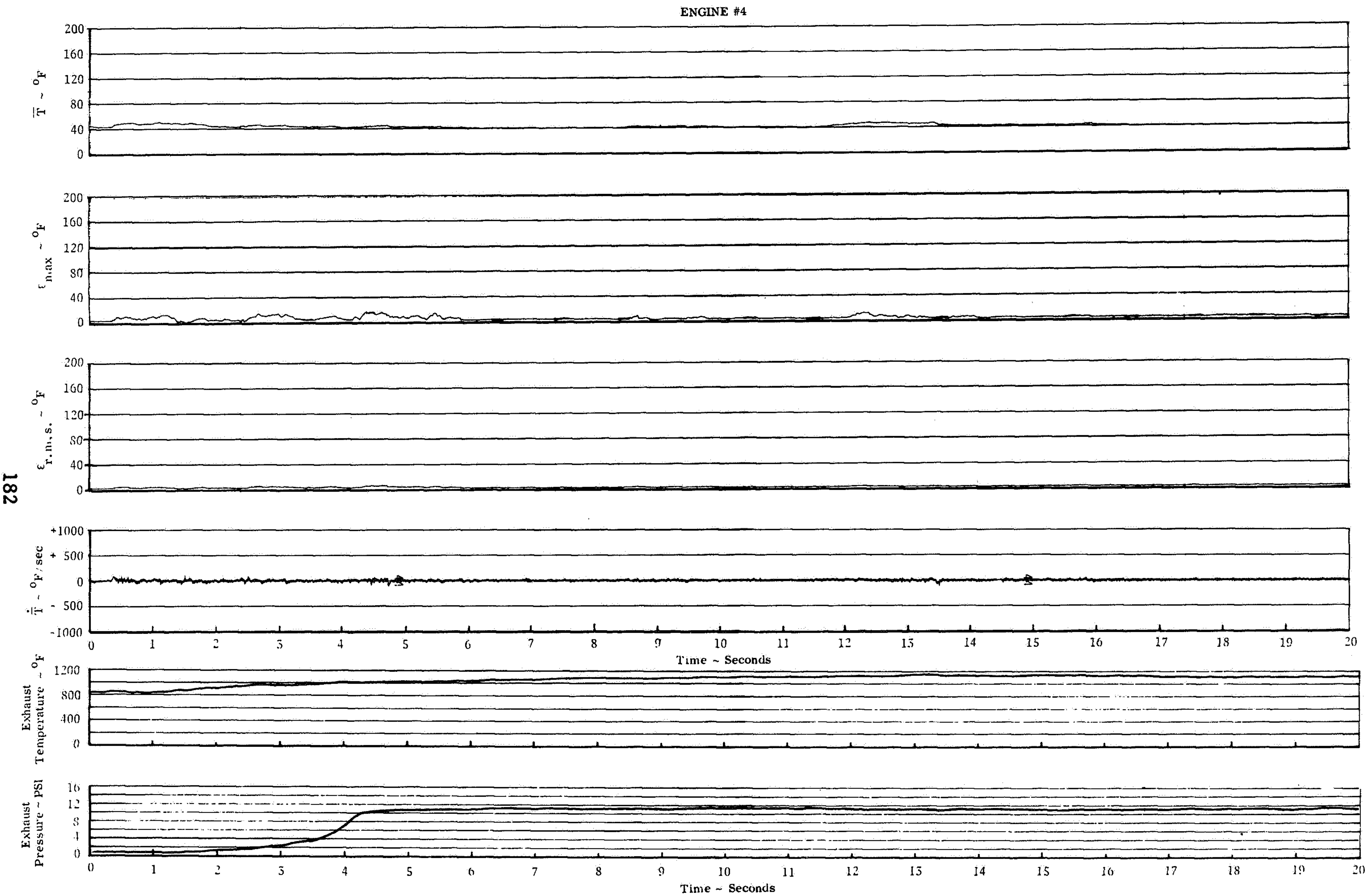

FIGURE A15-1. EXHAUST CONDITIONS AND INGESTION CHARACTERISTICS

Test 15

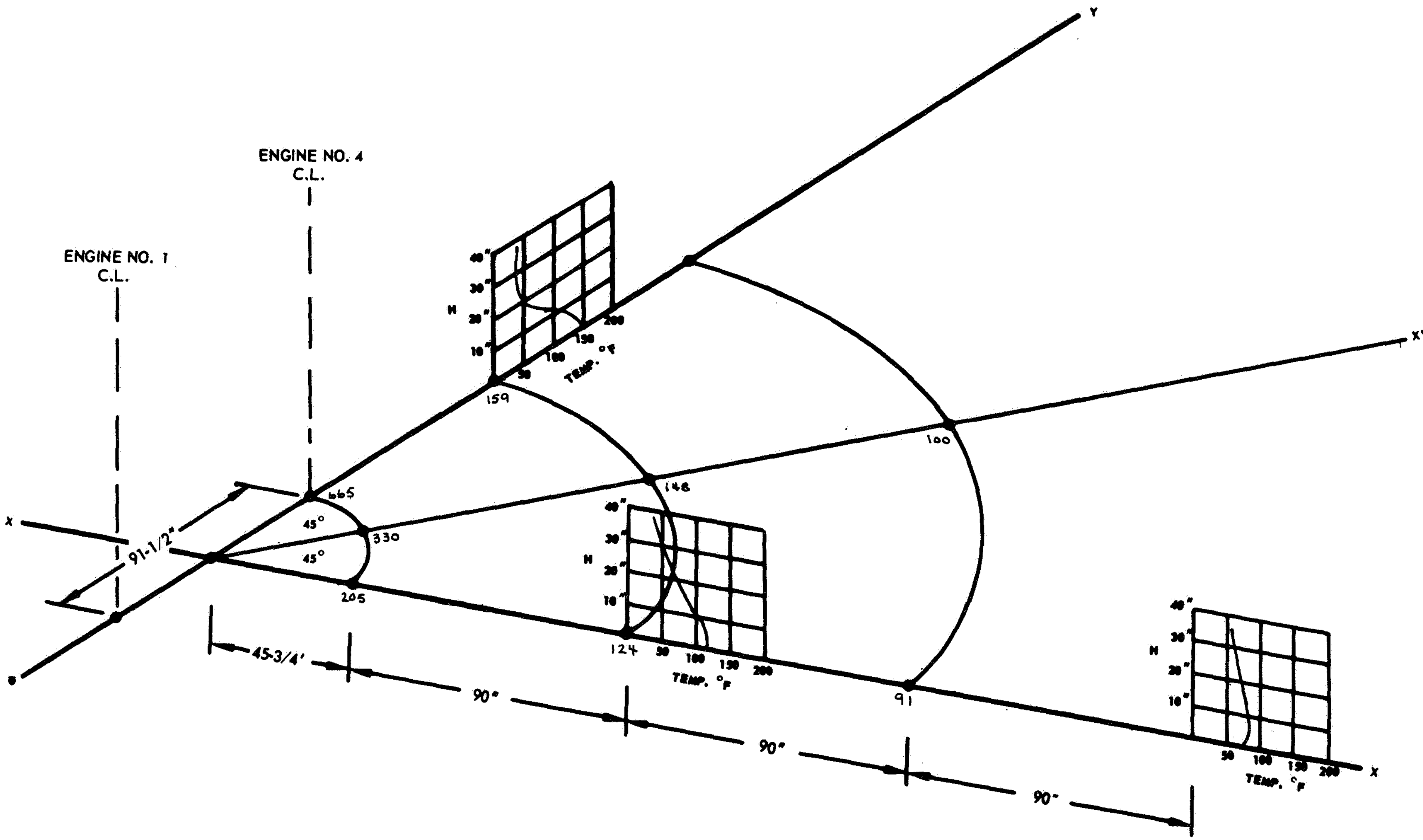

FIGURE A15-2. GROUND JET TEMPERATURE PROFILE

Test 15

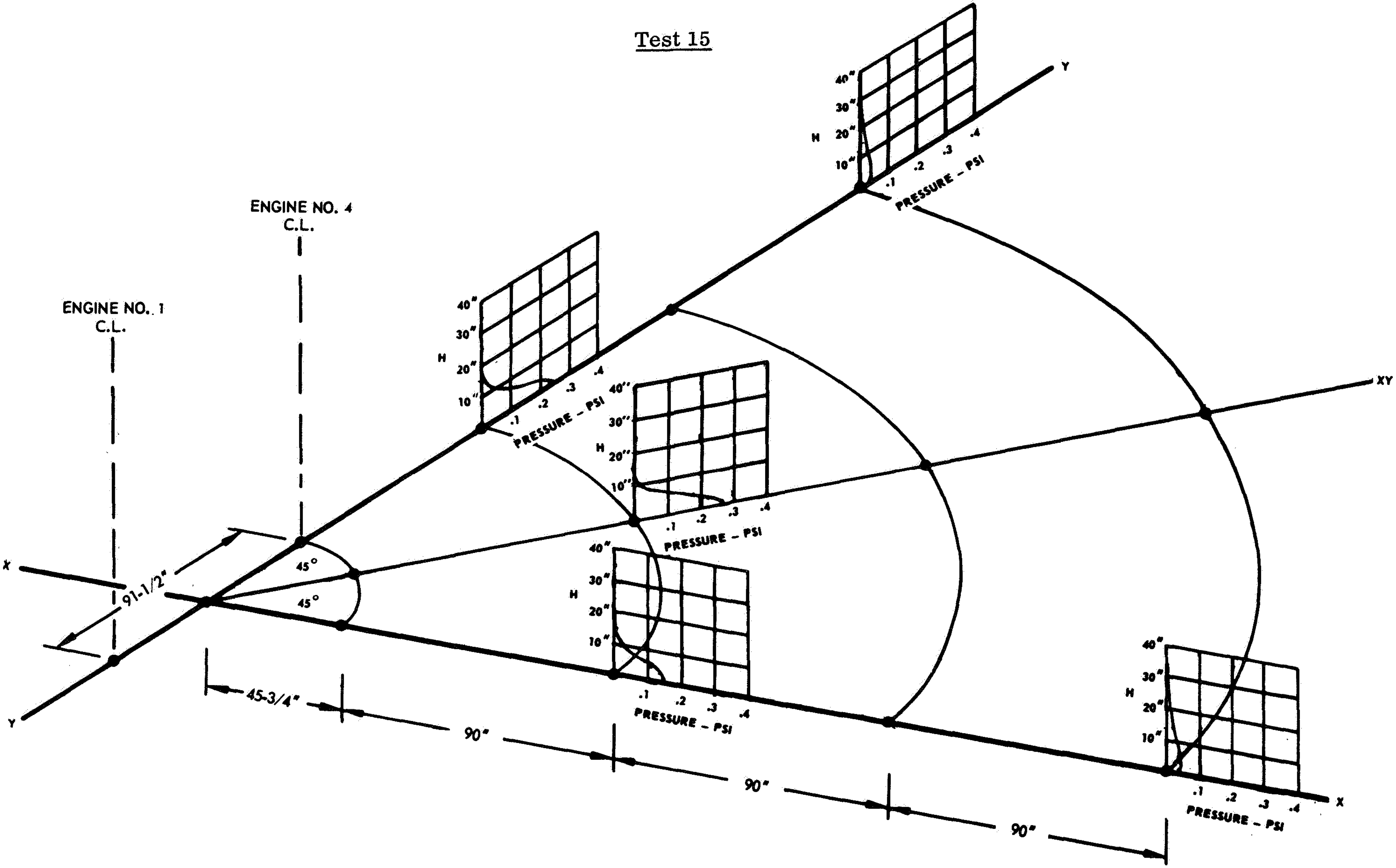

FIGURE A15-3. GROUND JET DYNAMIC PRESSURE PROFILE

Test #16

H/D = 2

α = 0

Wind = 12±2 MPH

Engines #1 and #4 operating

INGESTION CHARACTERISTICS

	ENGINE #1	ENGINE #4
$\Delta \hat{\bar{T}}$	25°F	4°F
$\hat{\epsilon}_{max}$	59°F	8°F
$\hat{\epsilon}_{r.m.s.}$	17°F	4°F
$\lvert\hat{\dot{T}}\rvert$	290°F/sec	50°F/sec

Test 16

ENGINE #1

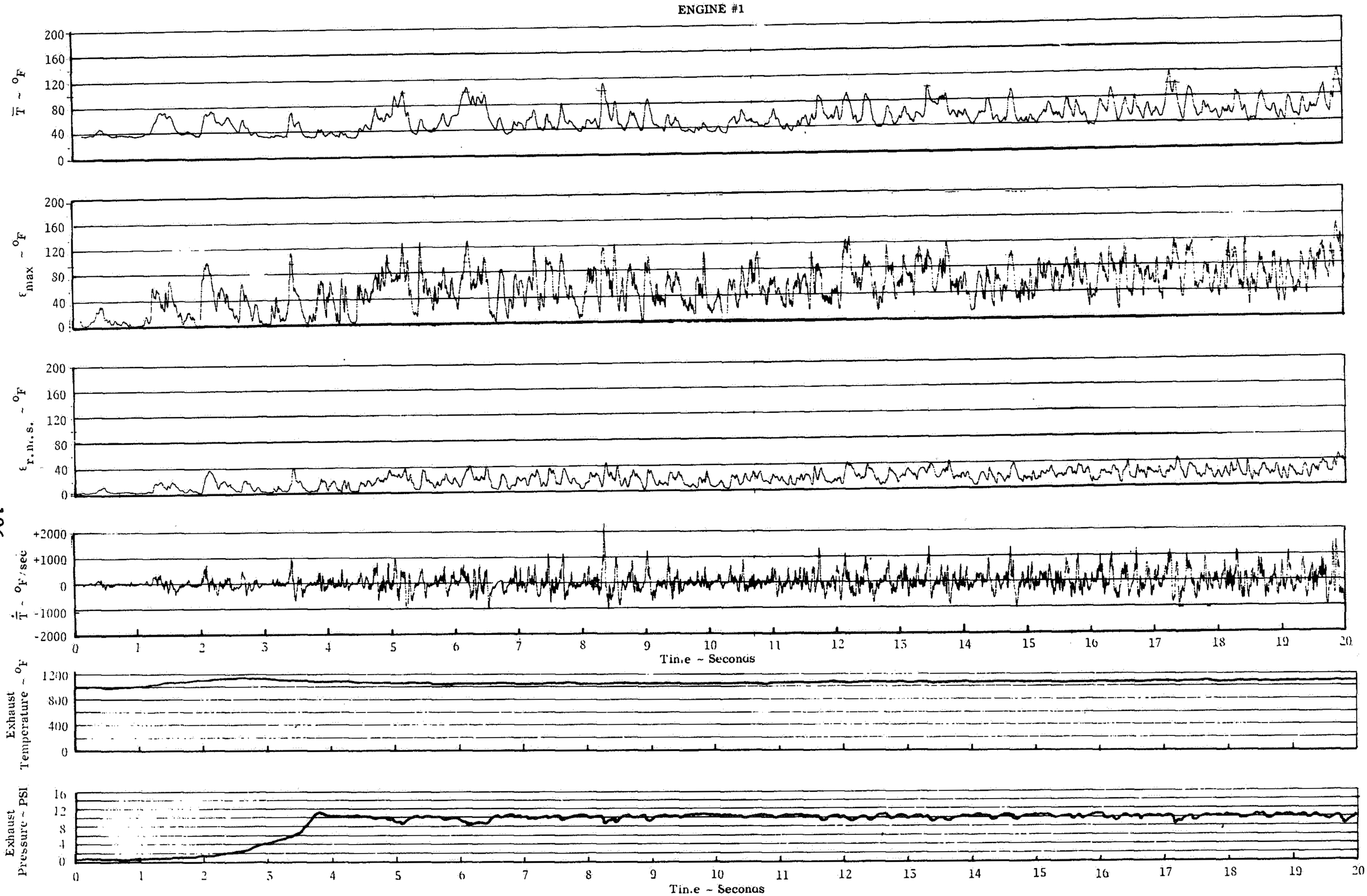

FIGURE A16-1. EXHAUST CONDITIONS AND INGESTION CHARACTERISTICS

Test 16

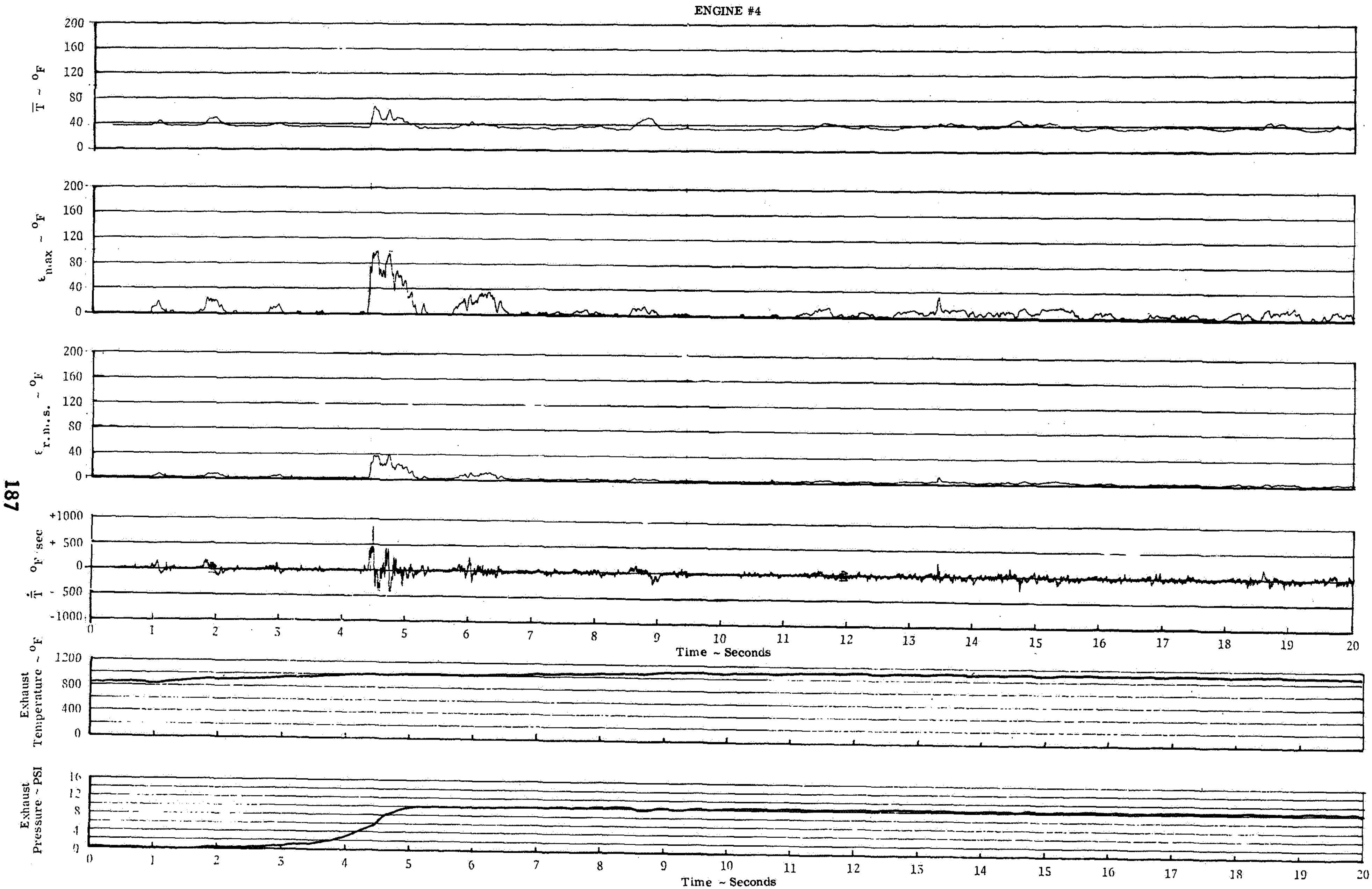

FIGURE A16-2. EXHAUST CONDITIONS AND INGESTION CHARACTERISTICS

Test 16

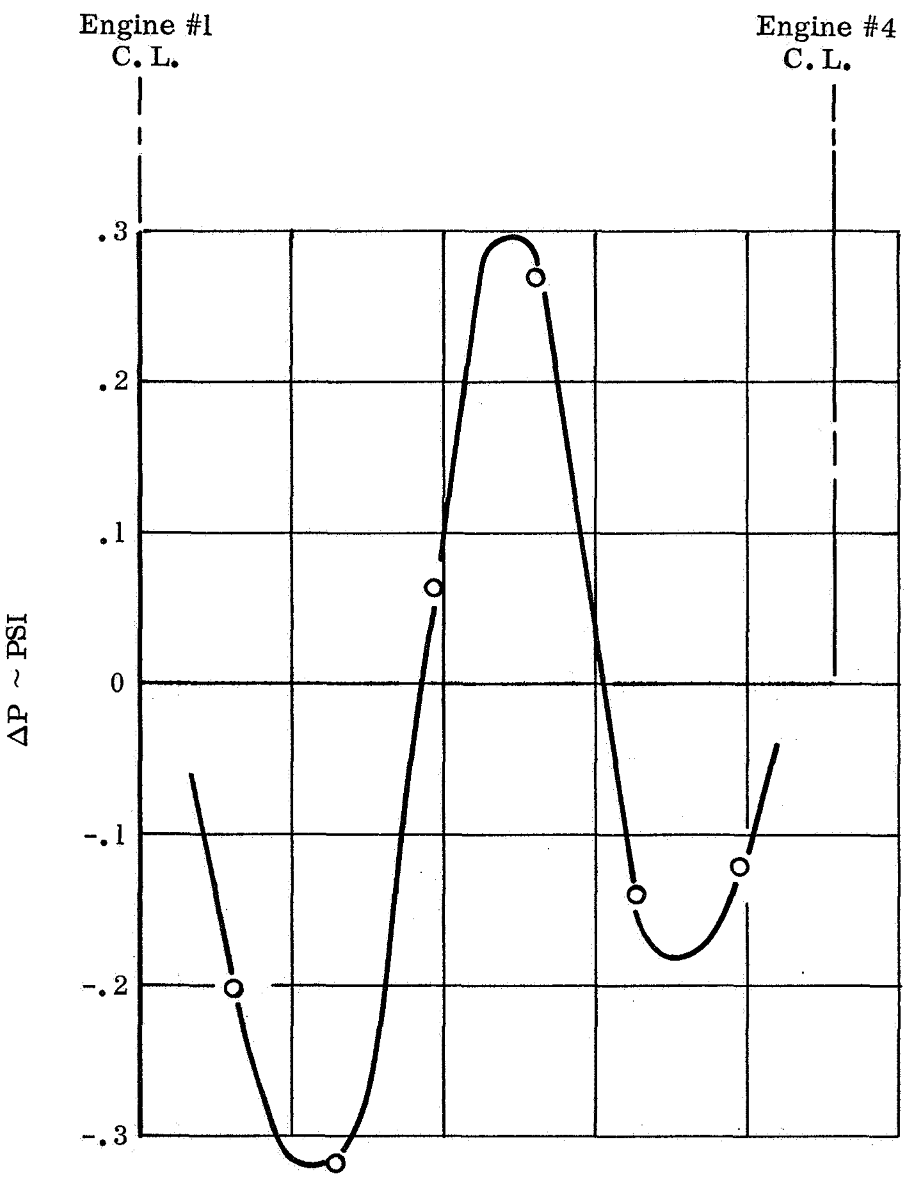

FIGURE A16-3. POD UNDERSURFACE PRESSURE DISTRIBUTION

Test #17

H/D = 4

α = 0

Wind = 16±4 MPH

Engines #1 and #4 operating

INGESTION CHARACTERISTICS

	ENGINE #1	ENGINE #4
$\Delta\hat{\bar{\bar{T}}}$	4°F	3°F
$\hat{\epsilon}_{max}$	11°F	6°F
$\hat{\epsilon}_{r.m.s.}$	3°F	2°F
$\lvert\hat{\bar{\dot{T}}}\rvert$	60°F/sec	50°F/sec

Test 17

ENGINE #1

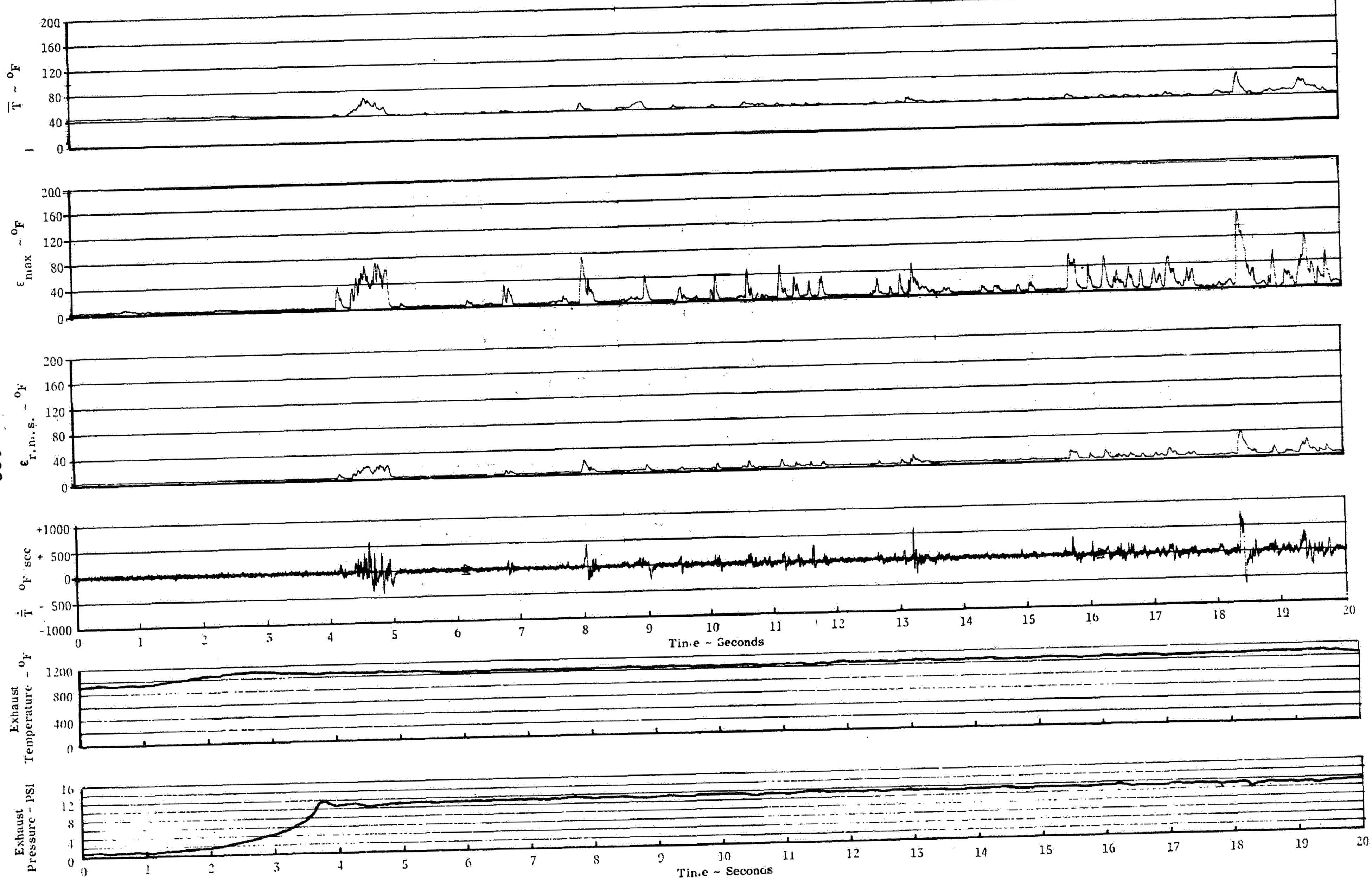

FIGURE A17-1. EXHAUST CONDITIONS AND INGESTION CHARACTERISTICS

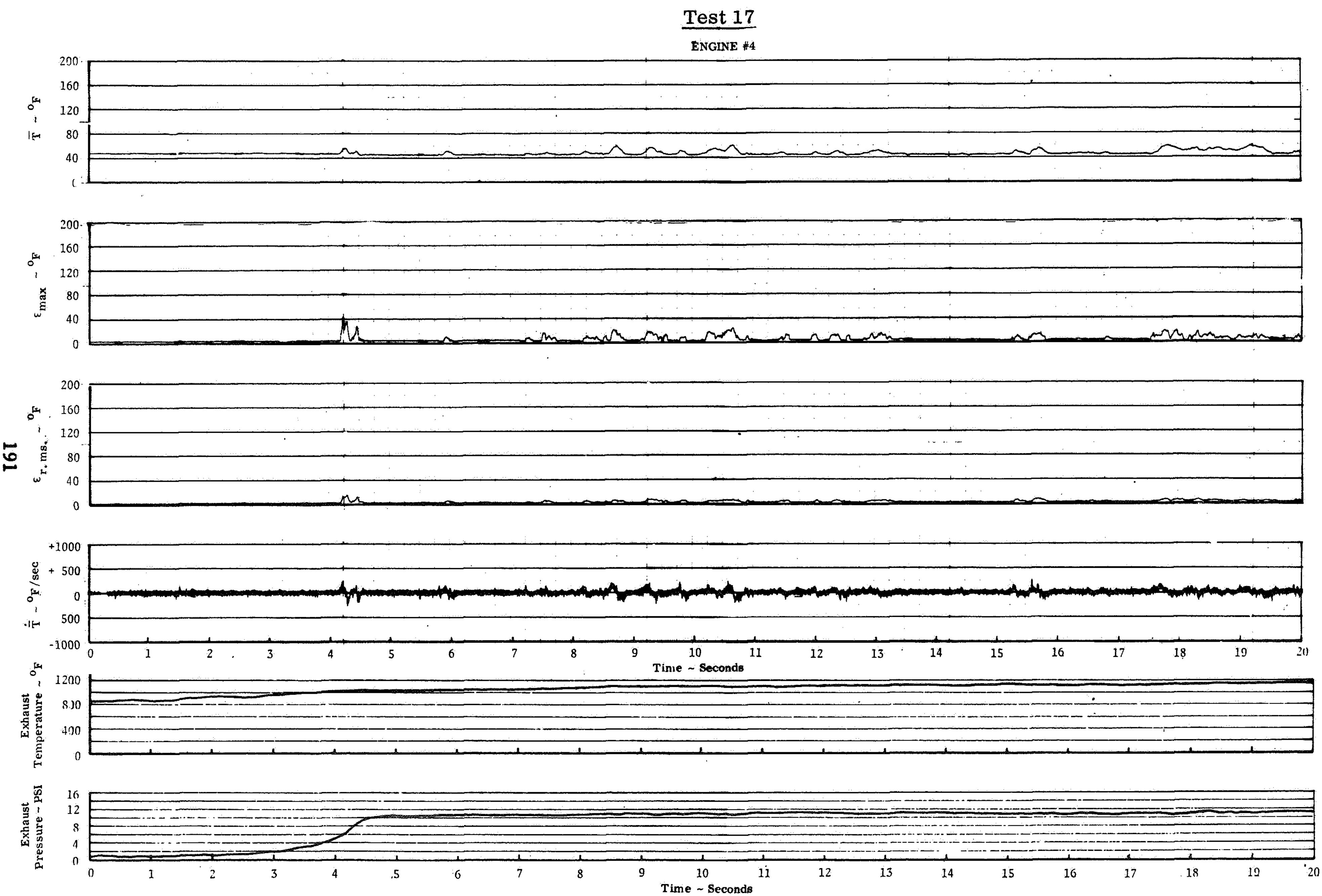

FIGURE A17-2. EXHAUST CONDITIONS AND INGESTION CHARACTERISTICS

Test 17

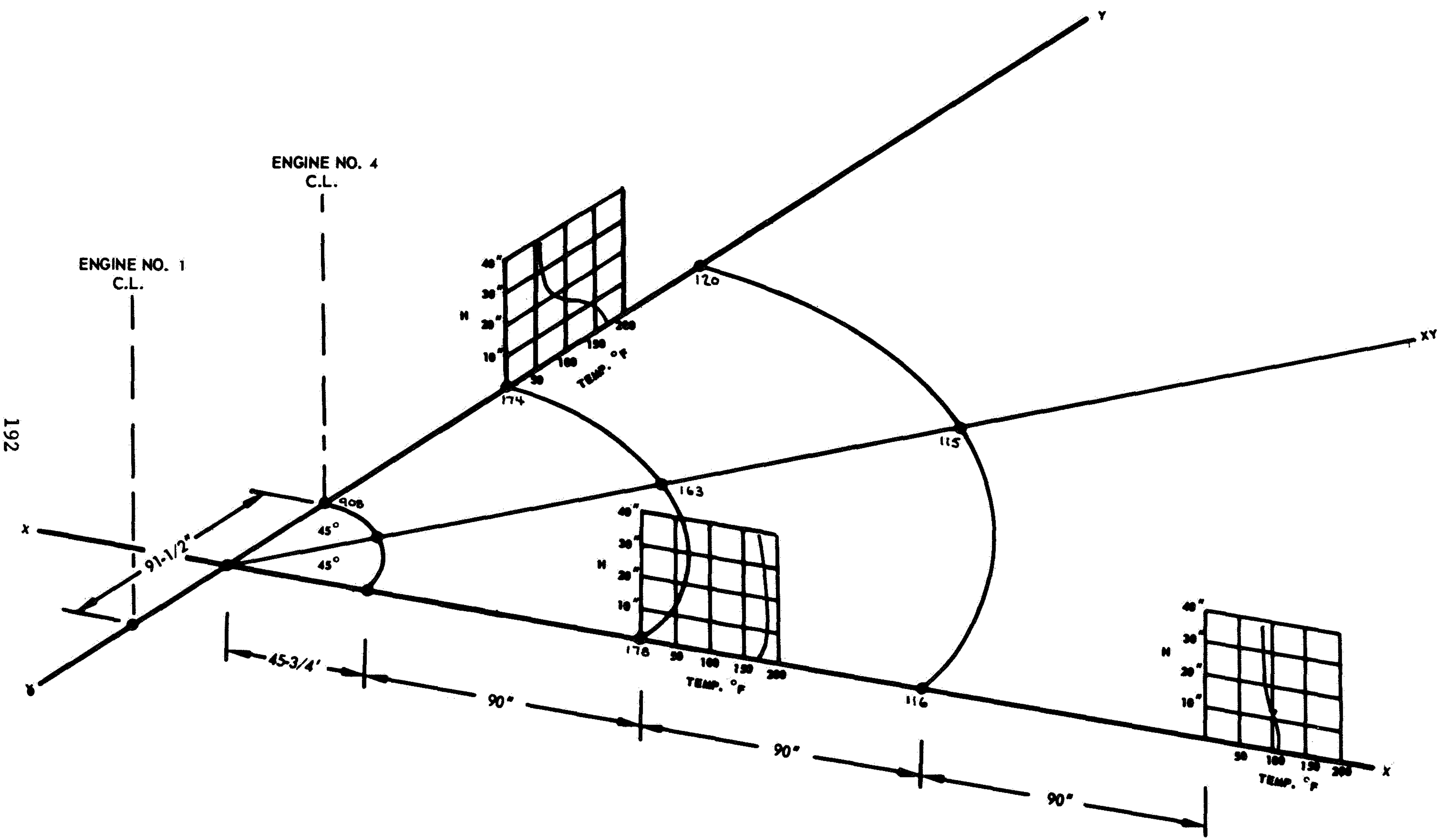

FIGURE A17-3. GROUND JET TEMPERATURE PROFILE

Test 17

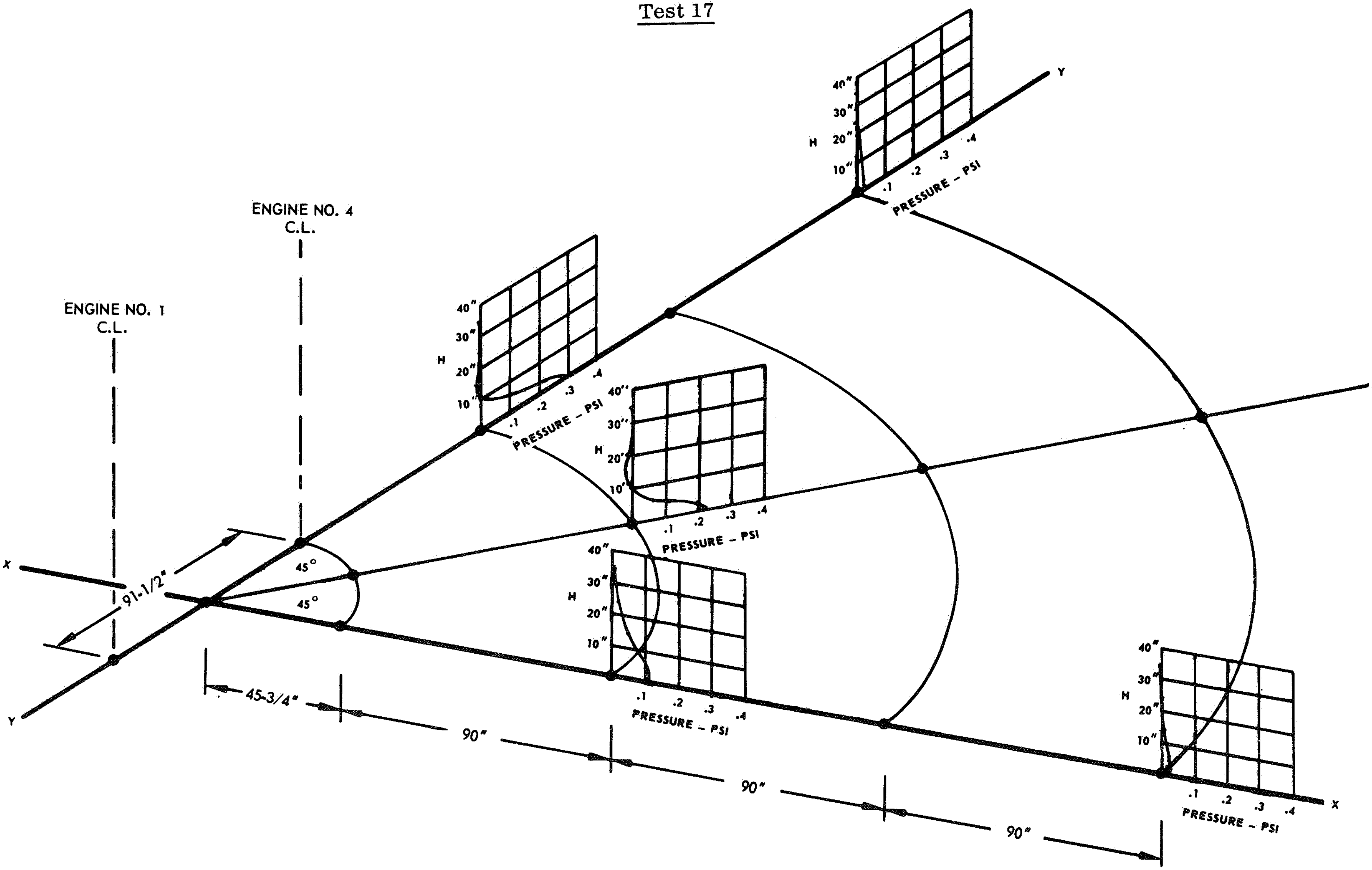

FIGURE A17-4. GROUND JET DYNAMIC PRESSURE PROFILE

Test 17

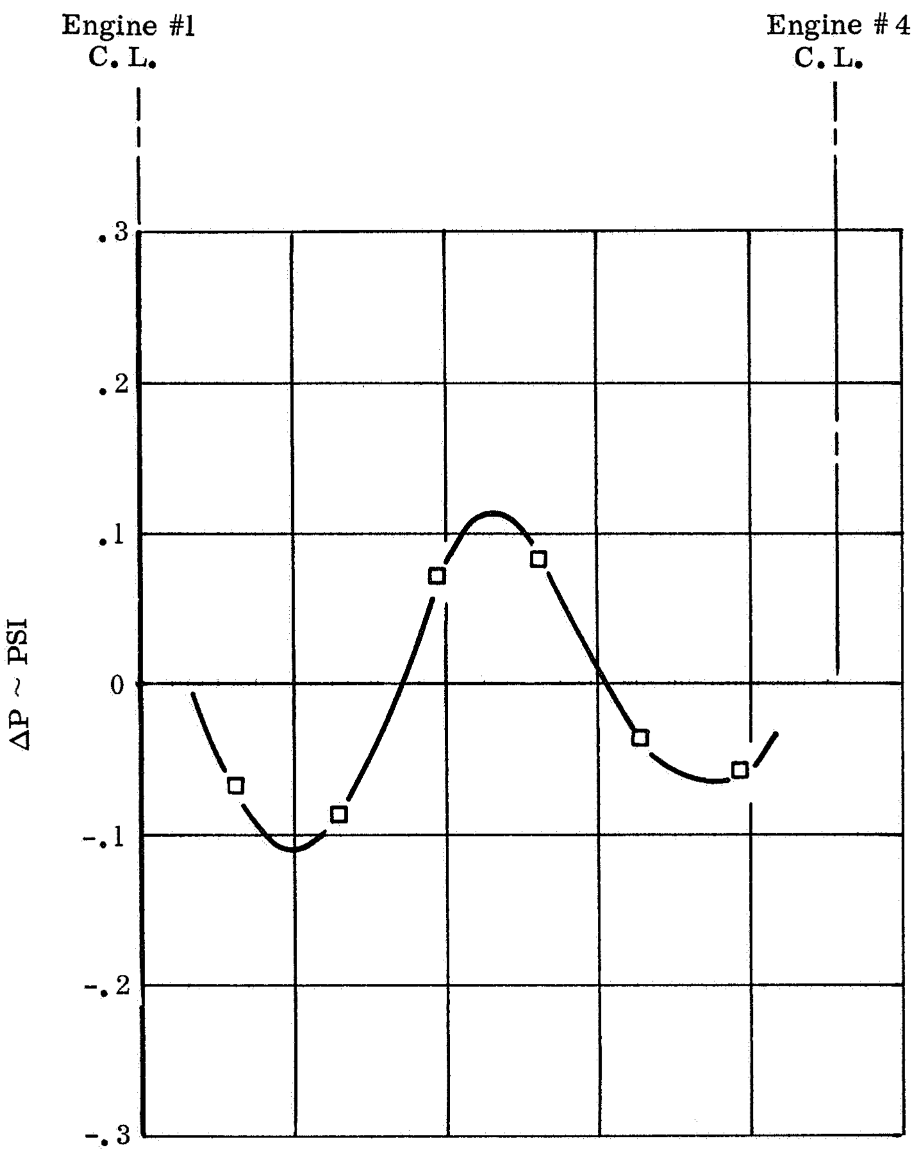

FIGURE A17-5. POD UNDERSURFACE PRESSURE DISTRIBUTION

Test #18

H/D = 6

$\alpha = 0$

Wind = 16±4 MPH

Engines #1 and #4 operating

INGESTION CHARACTERISTICS

	ENGINE #1	ENGINE #4
$\Delta\hat{\bar{T}}$	9°F	4°F
$\hat{\epsilon}_{max}$	20°F	6°F
$\hat{\epsilon}_{r.m.s.}$	5°F	2°F
$\lvert\hat{\dot{T}}\rvert$	85°F/sec	50°F/sec

Test 18

ENGINE #1

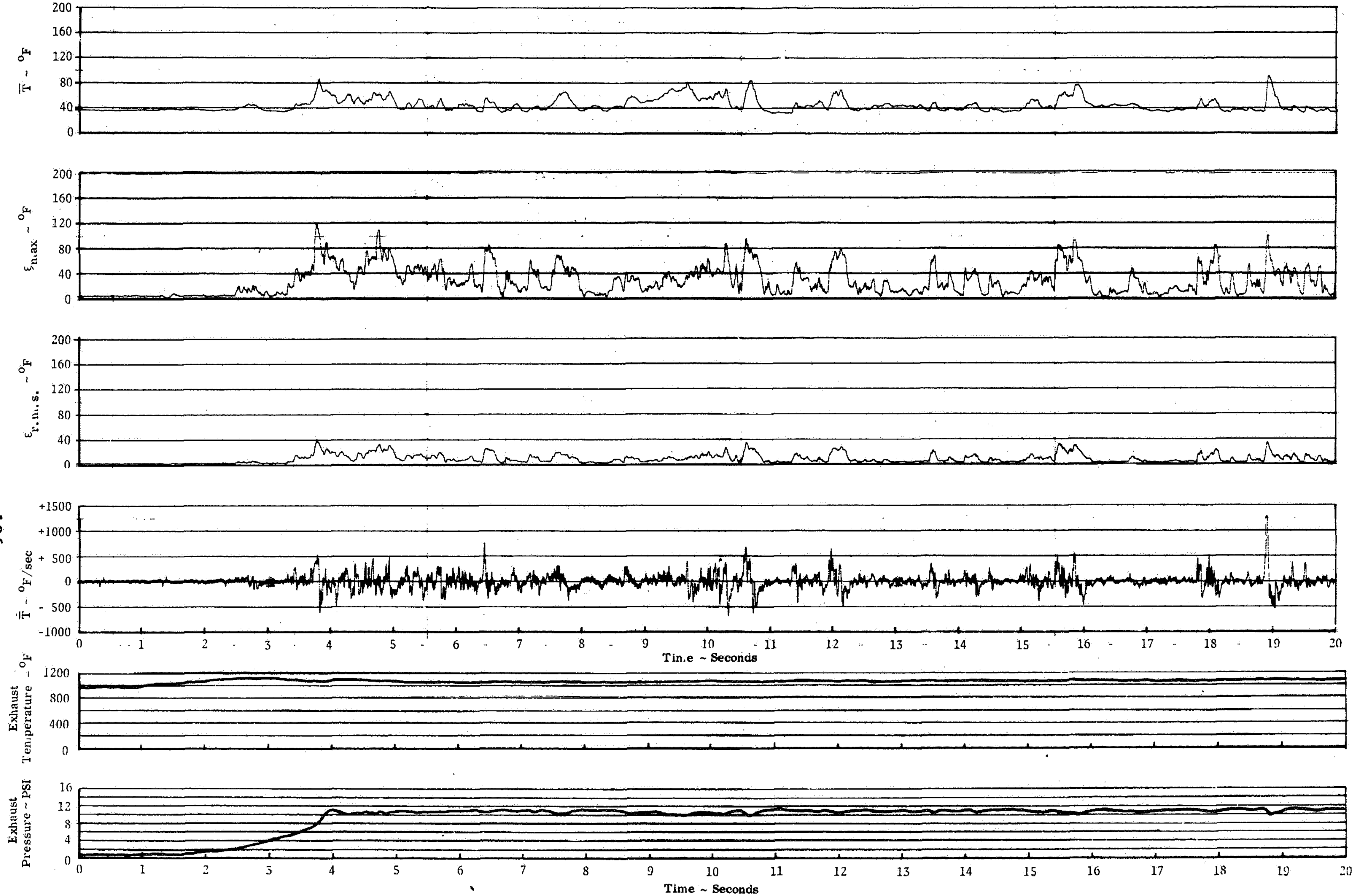

FIGURE A18-1. EXHAUST CONDITIONS AND INGESTION CHARACTERISTICS

Test 18

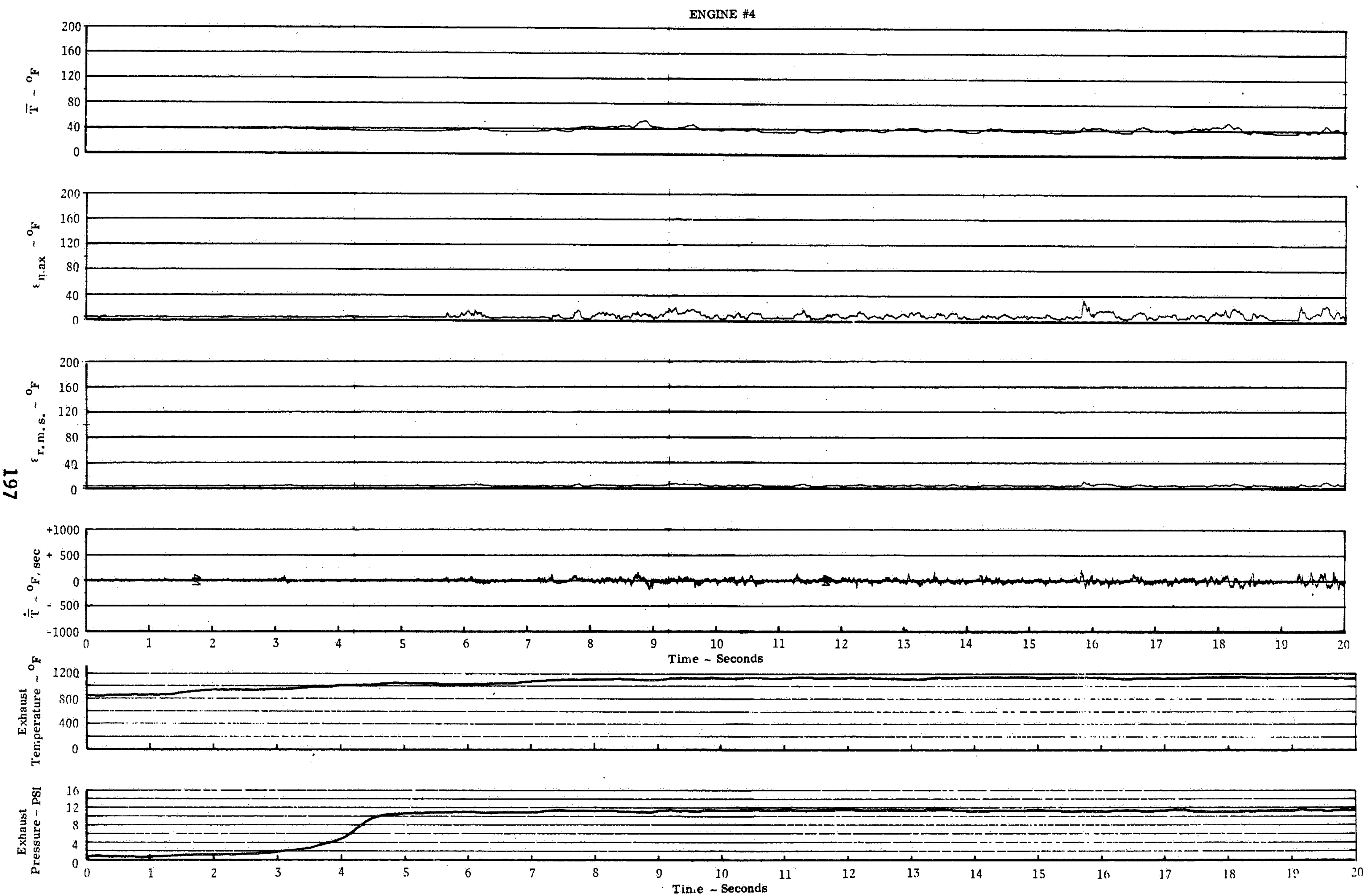

FIGURE A18-2. EXHAUST CONDITIONS AND INGESTION CHARACTERISTICS

Test 18

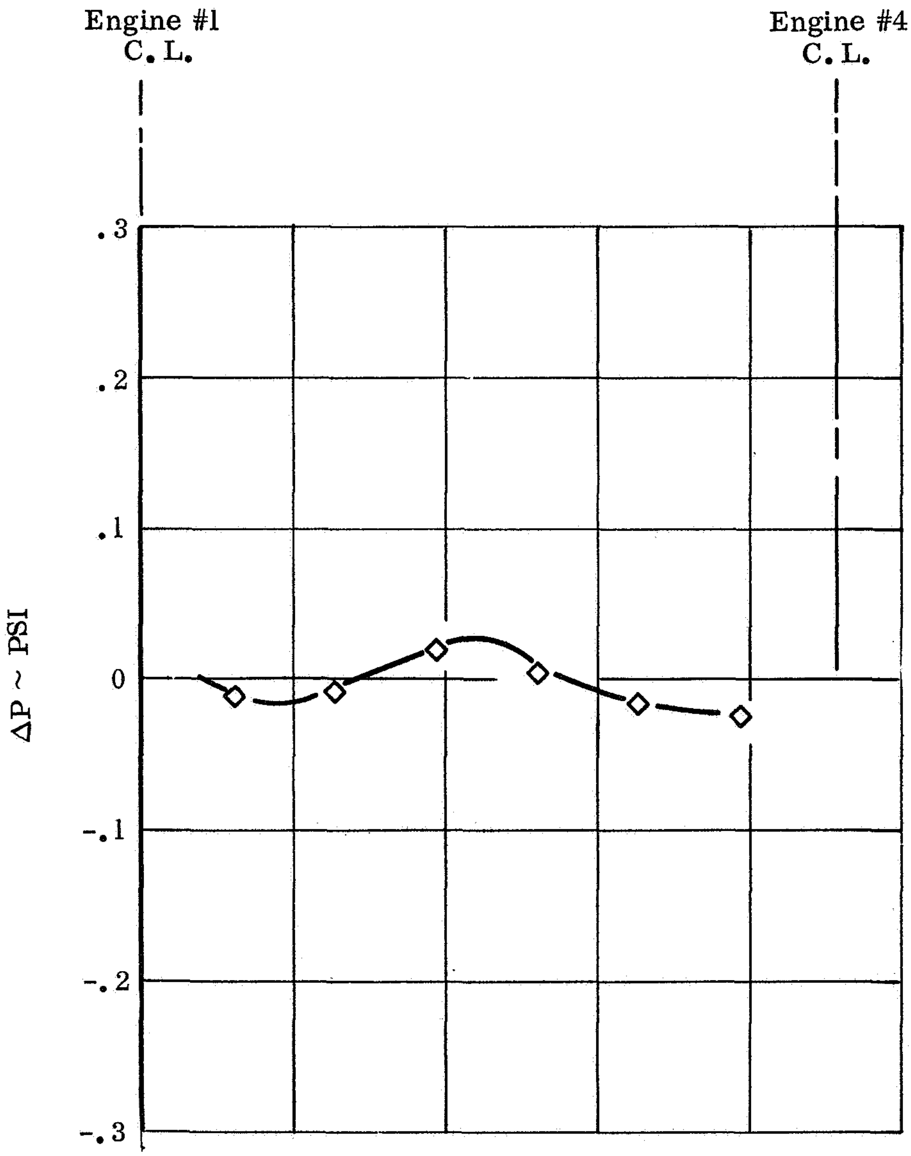

FIGURE A18-3. POD UNDERSURFACE PRESSURE DISTRIBUTION

Test #19

H/D = 8

α = 0

Wind = 16±4 MPH

Engines #1 and #4 operating

INGESTION CHARACTERISTICS

	ENGINE #1	ENGINE #4
$\Delta \hat{\bar{T}}$	1°F	1°F
$\hat{\epsilon}_{max}$	4°F	4°F
$\hat{\epsilon}_{r.m.s.}$	1°F	1°F
$\lvert\hat{\dot{T}}\rvert$	25°F/sec	—

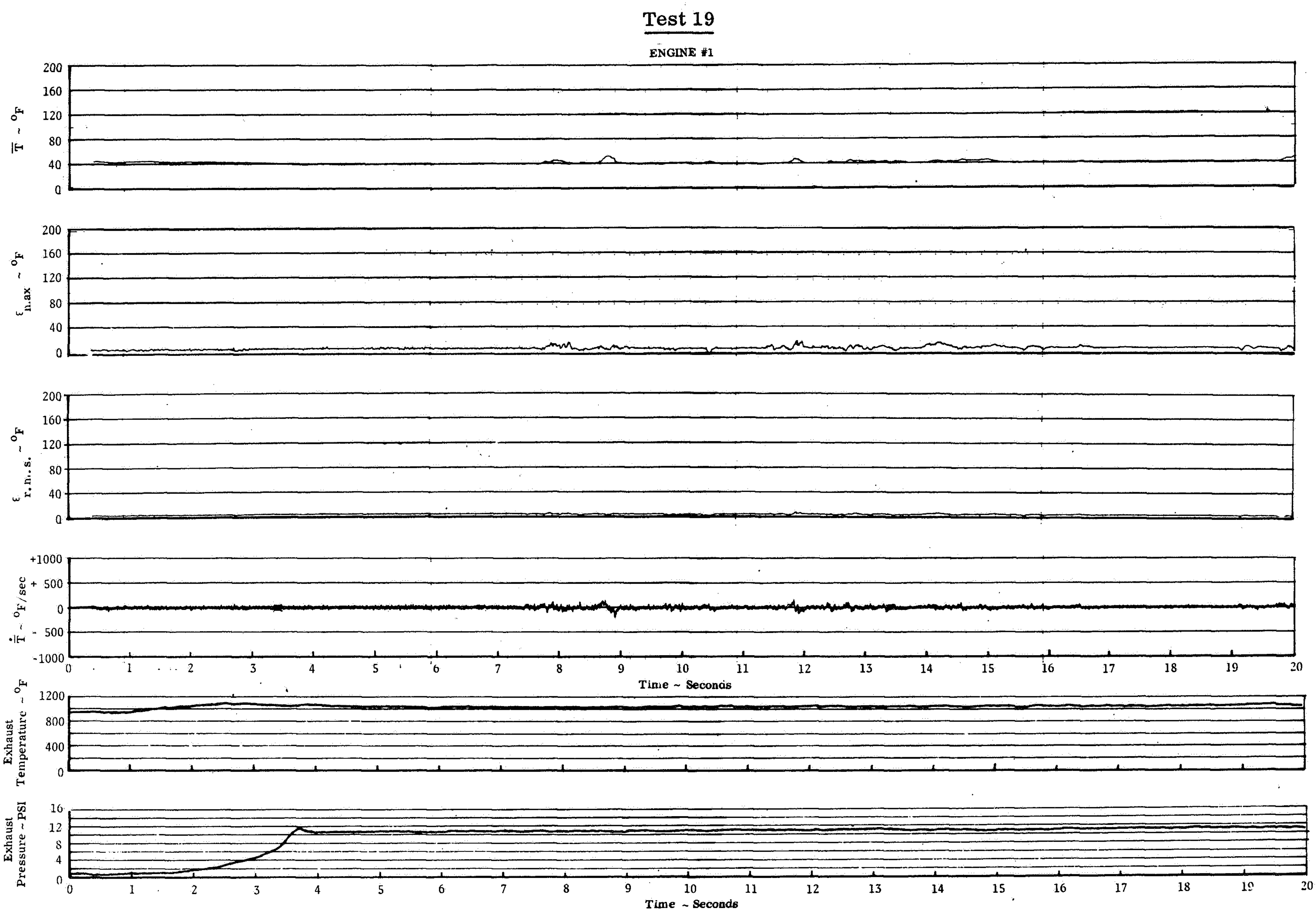

FIGURE A19-1. EXHAUST CONDITIONS AND INGESTION CHARACTERISTICS

Test 19

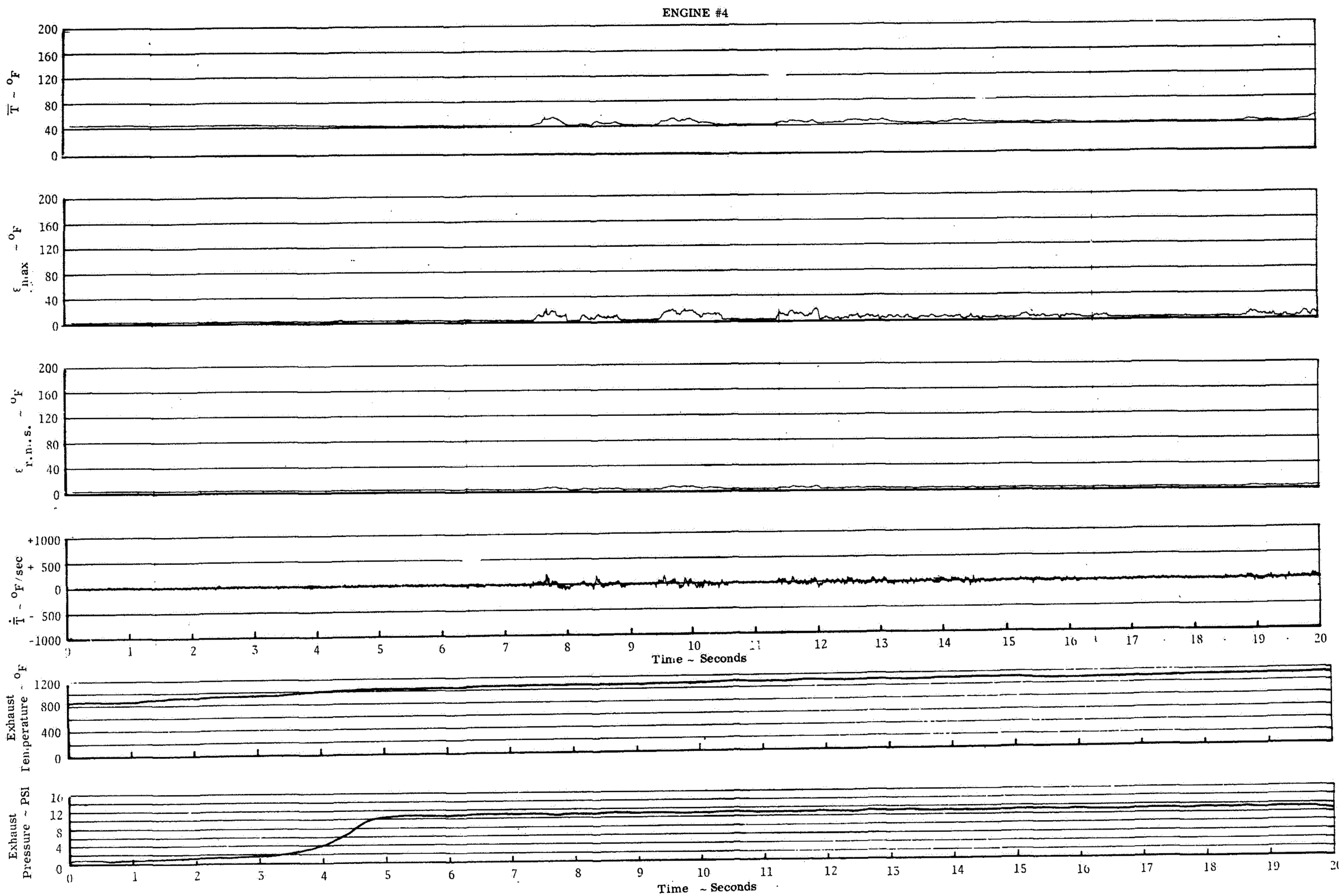

FIGURE A19-2. EXHAUST CONDITIONS AND INGESTION CHARACTERISTICS

Test 19

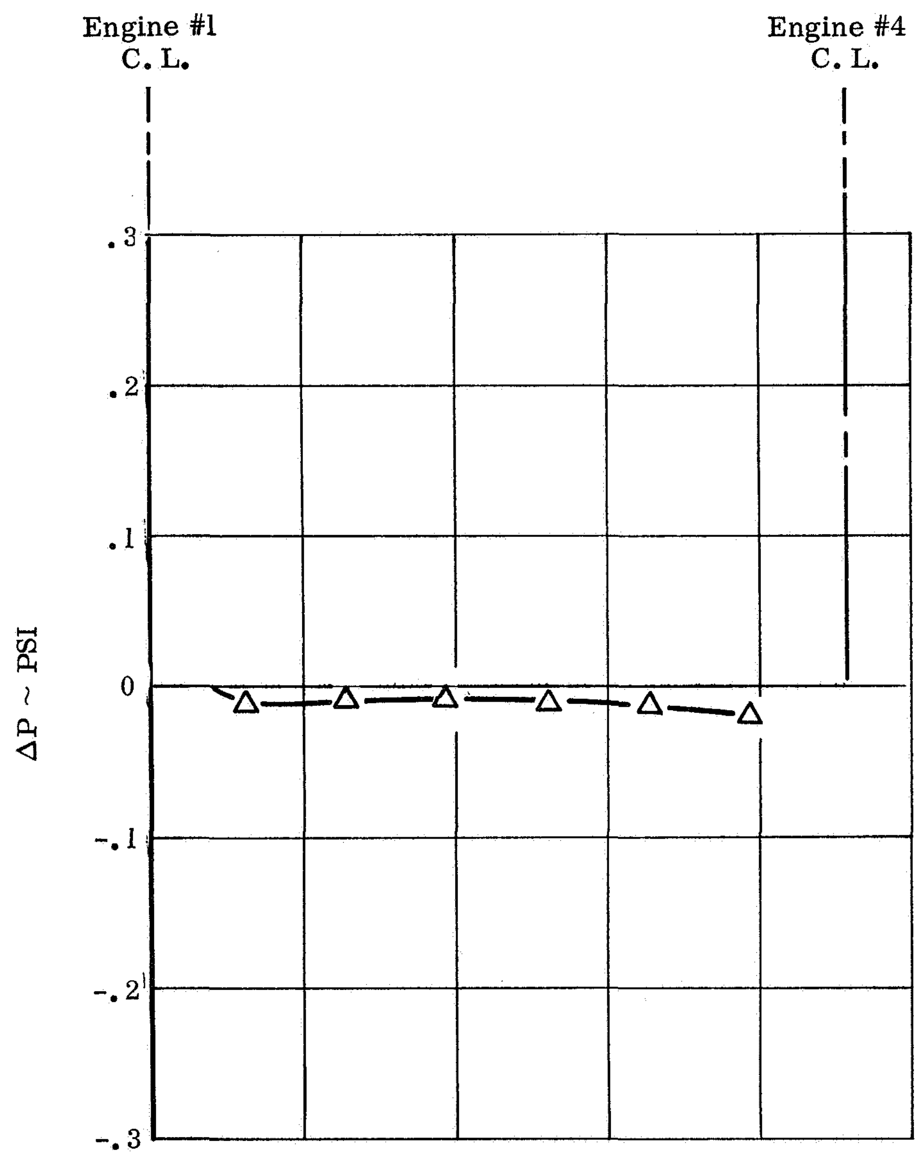

FIGURE A19-3. POD UNDERSURFACE PRESSURE DISTRIBUTION

Test #20

H/D = 2

α = 0

Wind = 10± 2 MPH

Engine #4 operating

INGESTION CHARACTERISTICS

	ENGINE #1	ENGINE #4
$\Delta\hat{\bar{T}}$	X	3°F
$\hat{\epsilon}_{max}$	X	6°F
$\hat{\epsilon}_{r.m.s.}$	X	2°F
$\lvert\hat{\bar{T}}\rvert$	X	——

Test 20

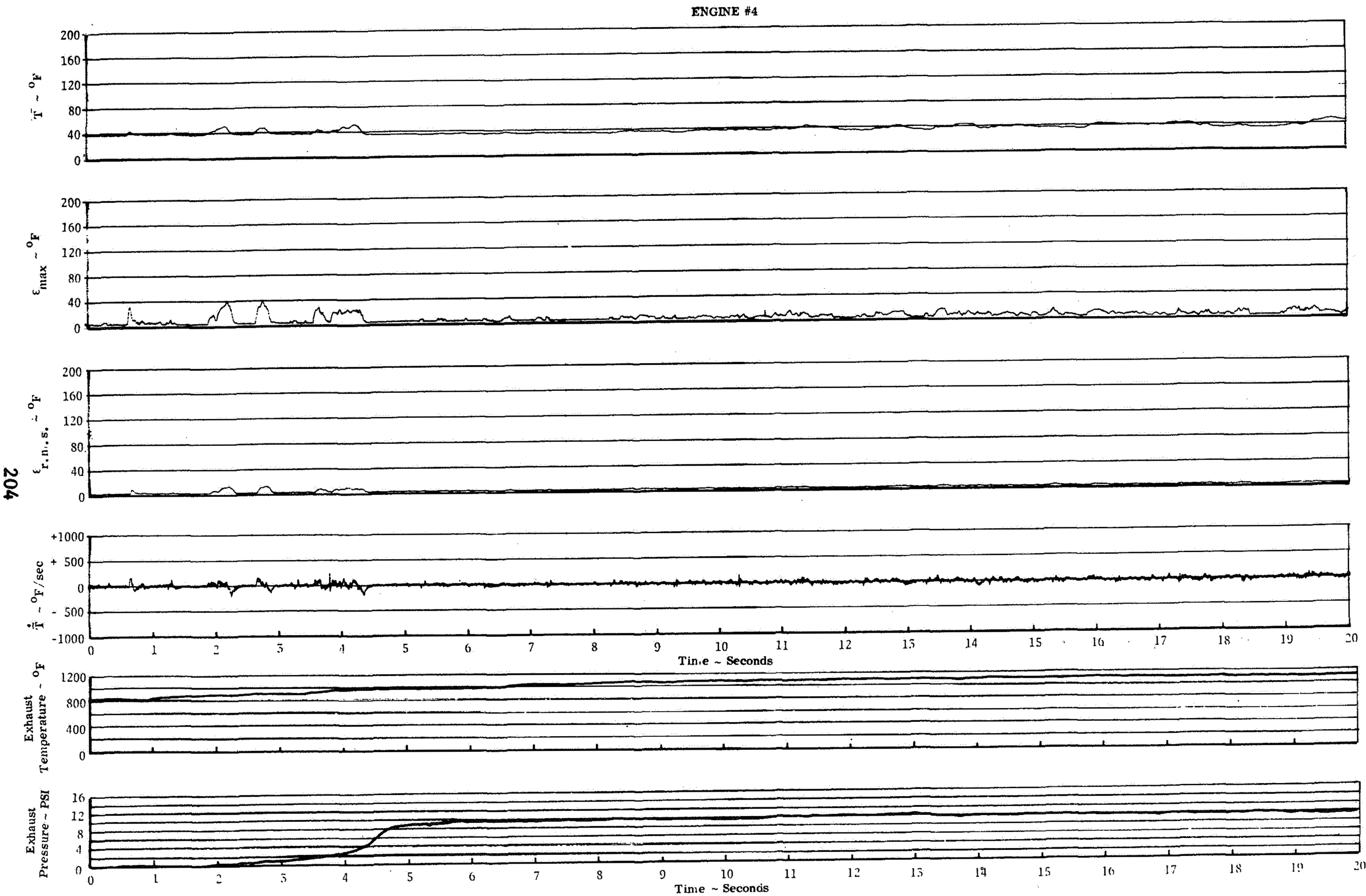

FIGURE A20-1. EXHAUST CONDITIONS AND INGESTION CHARACTERISTICS

Test #21

H/D = 4

α = 0

Wind = 14±4 MPH

Engine #4 operating

INGESTION CHARACTERISTICS

	ENGINE #1	ENGINE #4
$\Delta\hat{\bar{T}}$		4°F
$\hat{\epsilon}_{max}$		6°F
$\hat{\epsilon}_{r.m.s.}$		2°F
$\lvert\hat{\bar{T}}\rvert$		—

Test 21

ENGINE #4

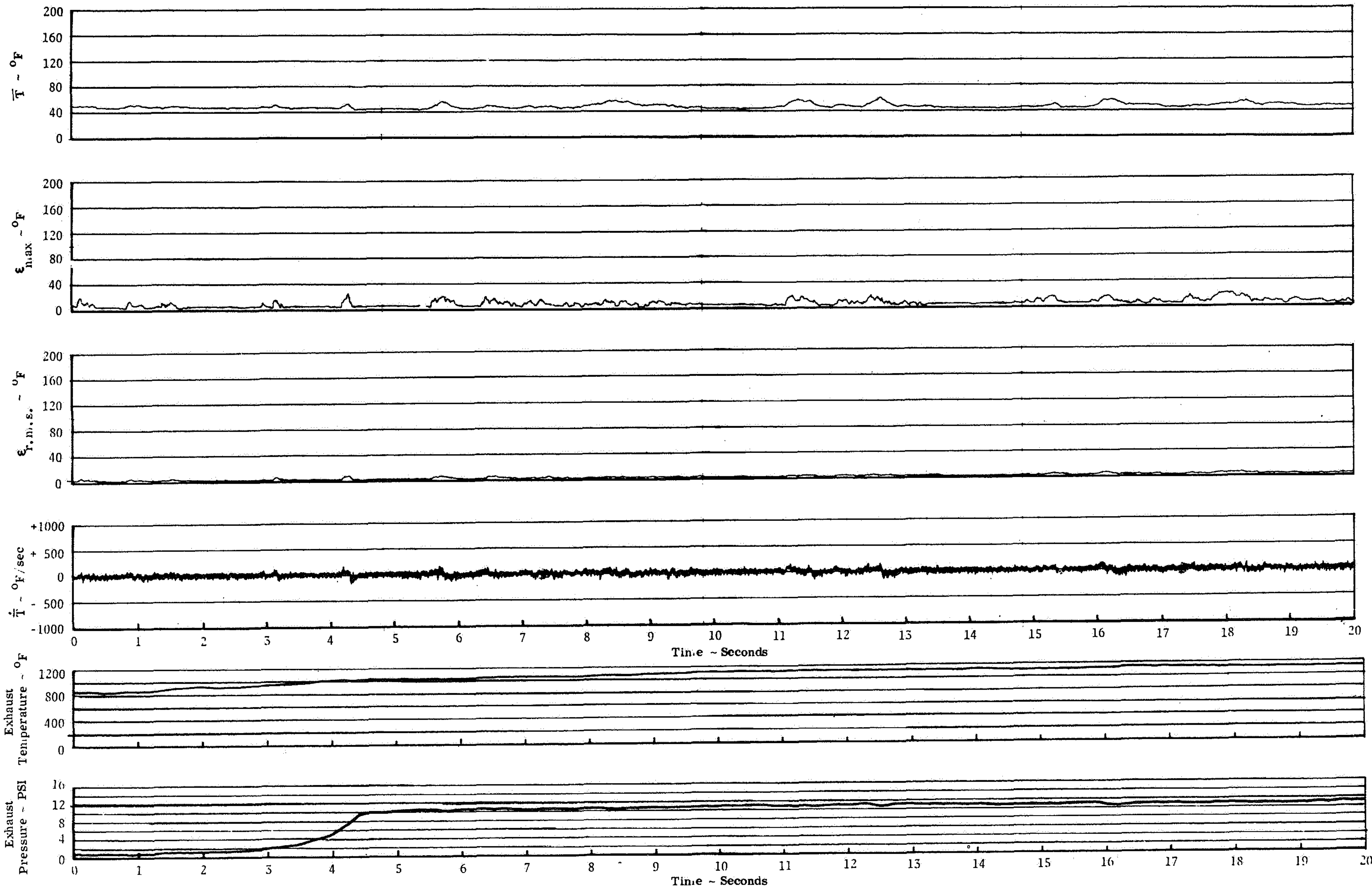

FIGURE A21-1. EXHAUST CONDITIONS AND INGESTION CHARACTERISTICS

Test 21

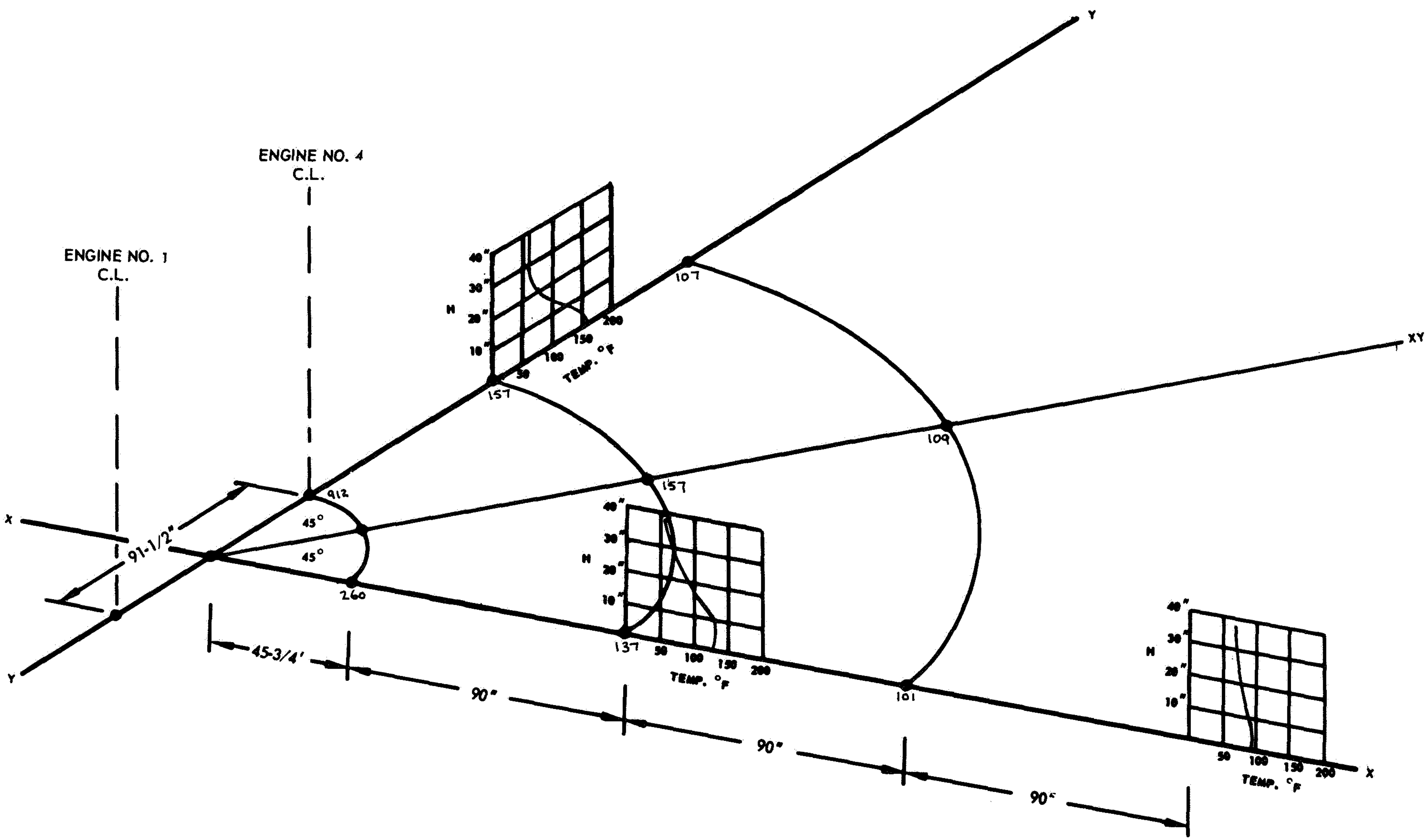

FIGURE A21-2. GROUND JET TEMPERATURE PROFILE

Test 21

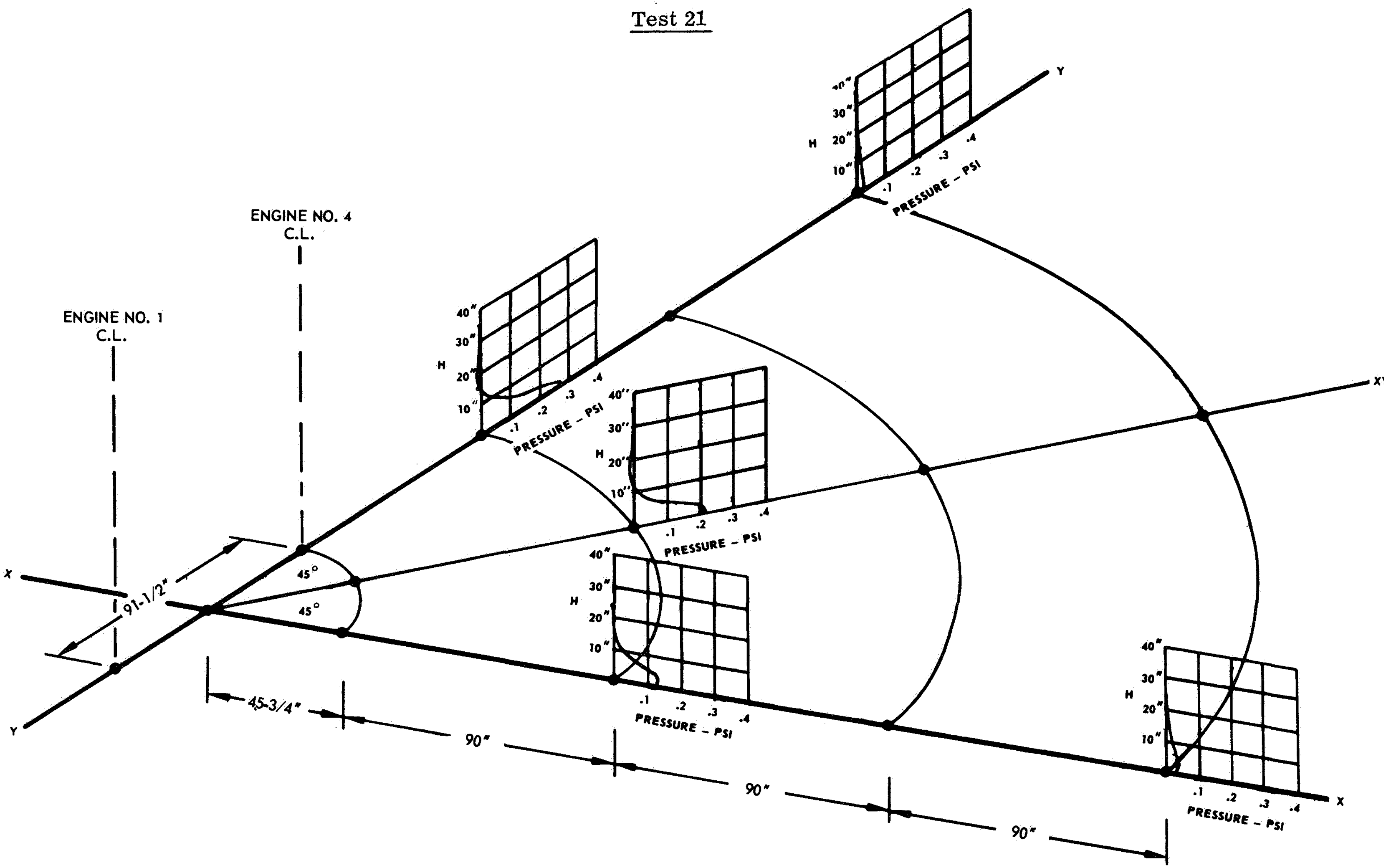

FIGURE A21-3. GROUND JET DYNAMIC PRESSURE PROFILE

Test 21

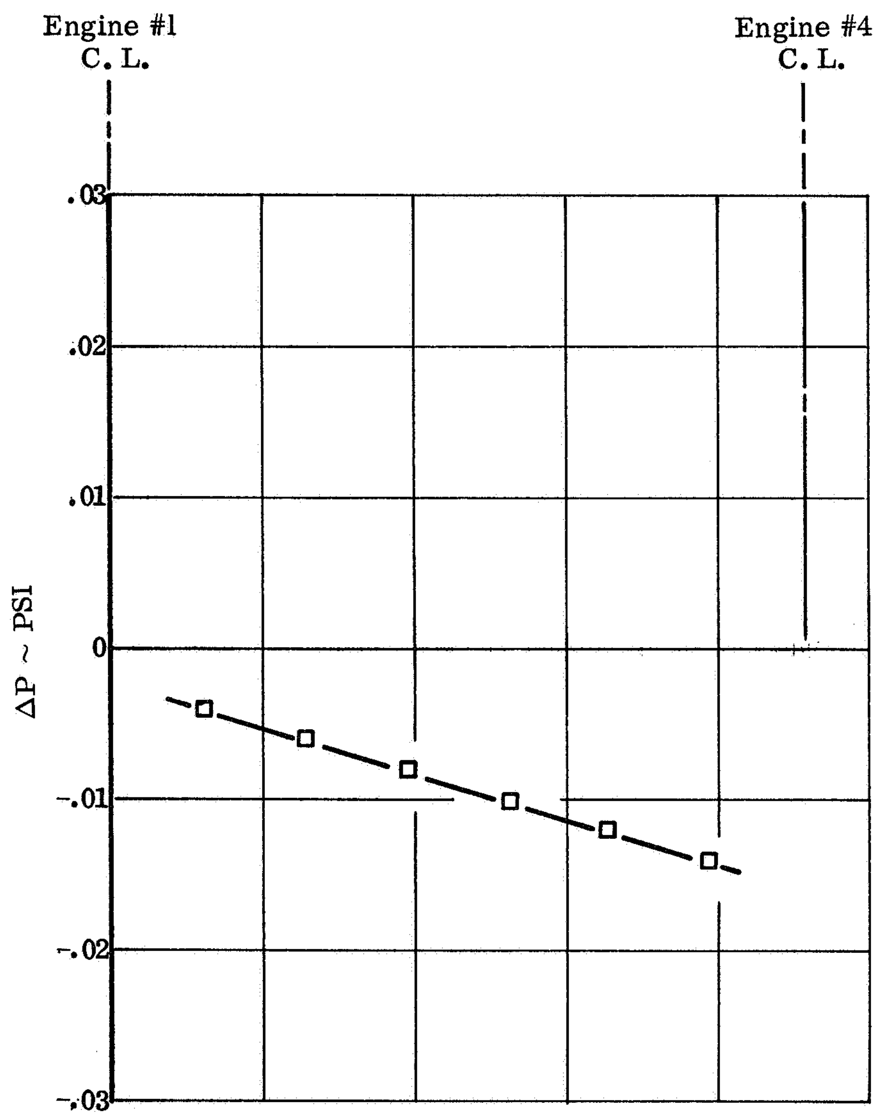

FIGURE A21-4. POD UNDERSURFACE PRESSURE DISTRIBUTION

Test #22

H/D = 6

α = 0

Wind = 16±4 MPH

Engine #4 operating

INGESTION CHARACTERISTICS

	ENGINE #1	ENGINE #4
$\Delta\hat{\bar{T}}$		4°F
$\hat{\epsilon}_{max}$		8°F
$\hat{\epsilon}_{r.m.s.}$		4°F
$\lvert\hat{\bar{T}}\rvert$		—

Test 22

ENGINE #4

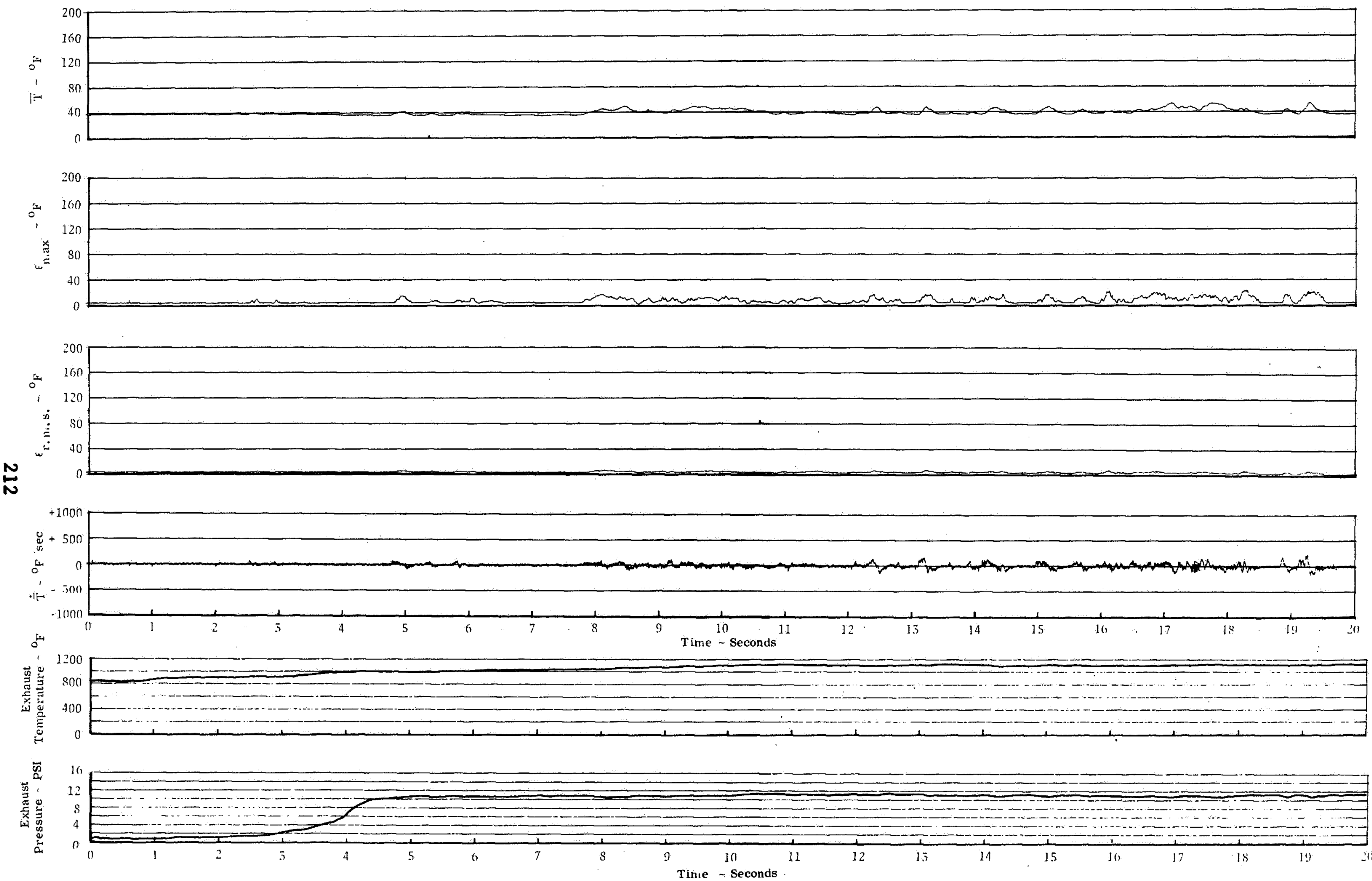

FIGURE A22-1. EXHAUST CONDITIONS AND INGESTION CHARACTERISTICS

Test #23

H/D = 8

α = 0

Wind = 20± 2 MPH

Engine #4 operating

INGESTION CHARACTERISTICS

	ENGINE #1	ENGINE #4
$\Delta\hat{\bar{T}}$		2°F
$\hat{\epsilon}_{max}$		2°F
$\hat{\epsilon}_{r.m.s.}$		0°F
$\lvert\hat{\bar{T}}\rvert$		—

Test 23

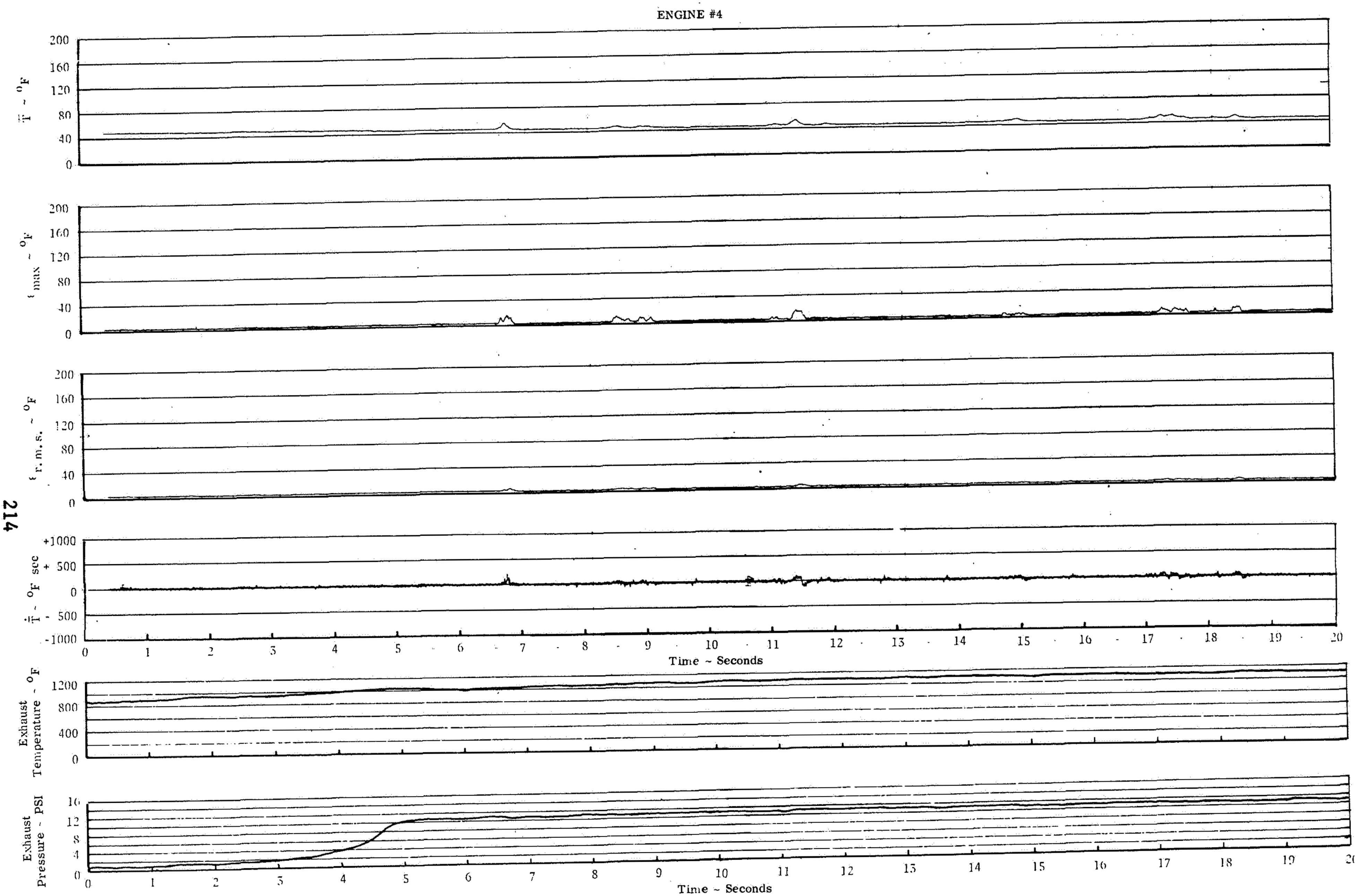

FIGURE A23-1. EXHAUST CONDITIONS AND INGESTION CHARACTERISTICS

Test #24

H/D = 2

α = +6

Wind = <4 MPH

Engines #1 and #4 operating

INGESTION CHARACTERISTICS

	ENGINE #1	ENGINE #4
$\Delta \hat{\bar{T}}$	3°F	2°F
$\hat{\epsilon}_{max}$	14°F	4°F
$\hat{\epsilon}_{r.m.s.}$	4°F	2°F
$\lvert\hat{\dot{T}}\rvert$	45°F/sec	—

Test 24

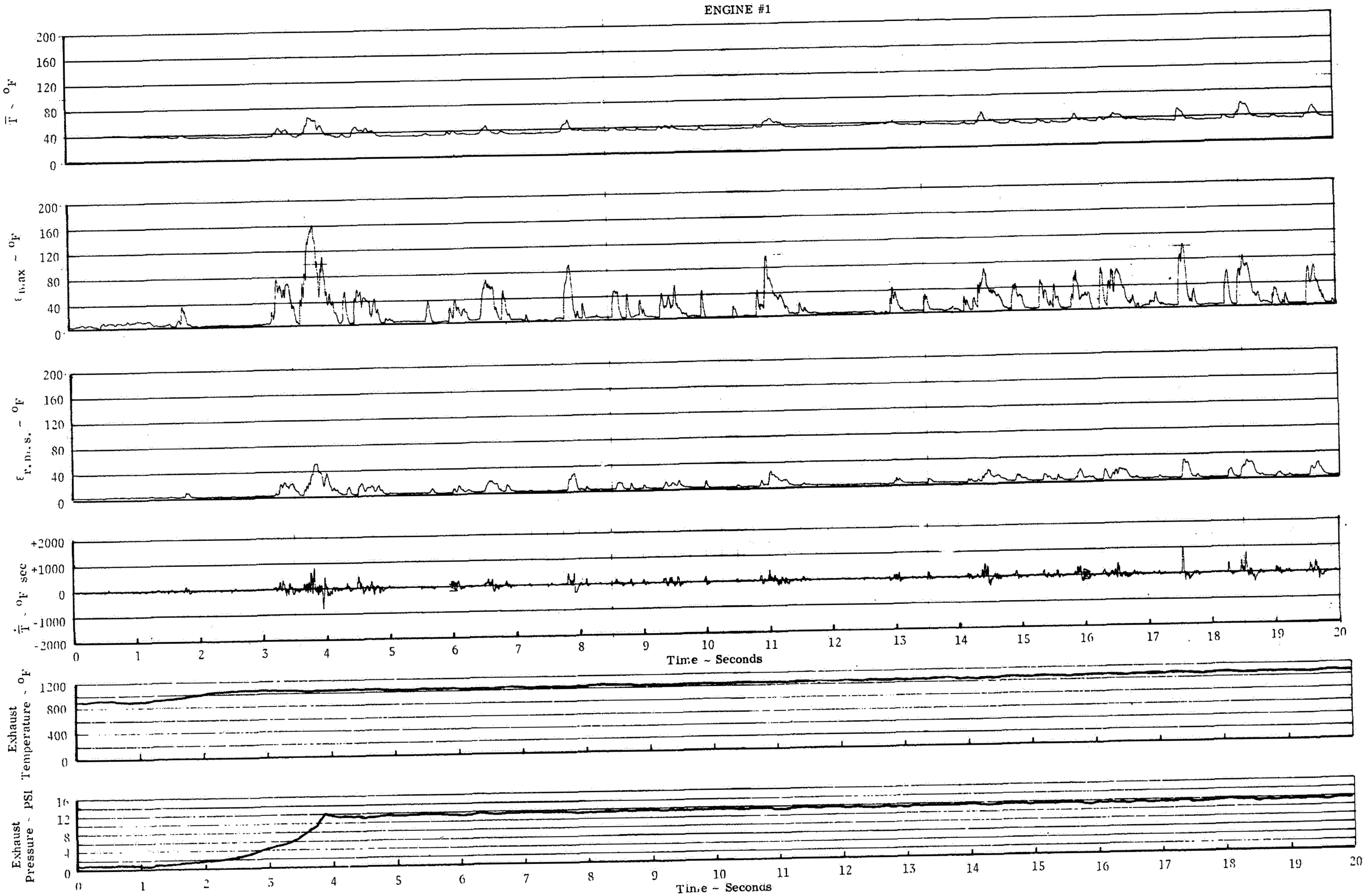

FIGURE A24-1. EXHAUST CONDITIONS AND INGESTION CHARACTERISTICS

Test 24

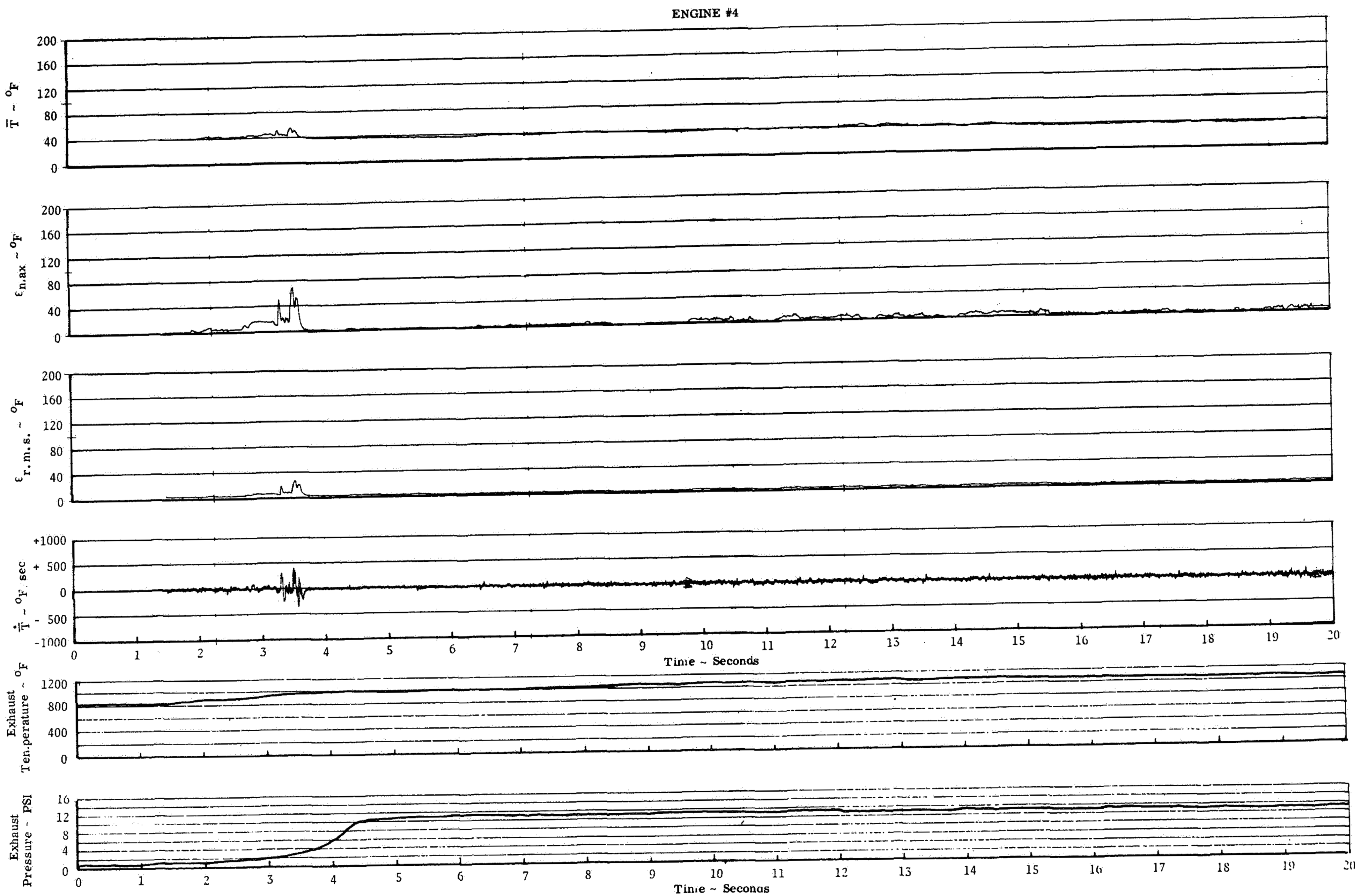

FIGURE A24-2. EXHAUST CONDITIONS AND INGESTION CHARACTERISTICS

Test 24

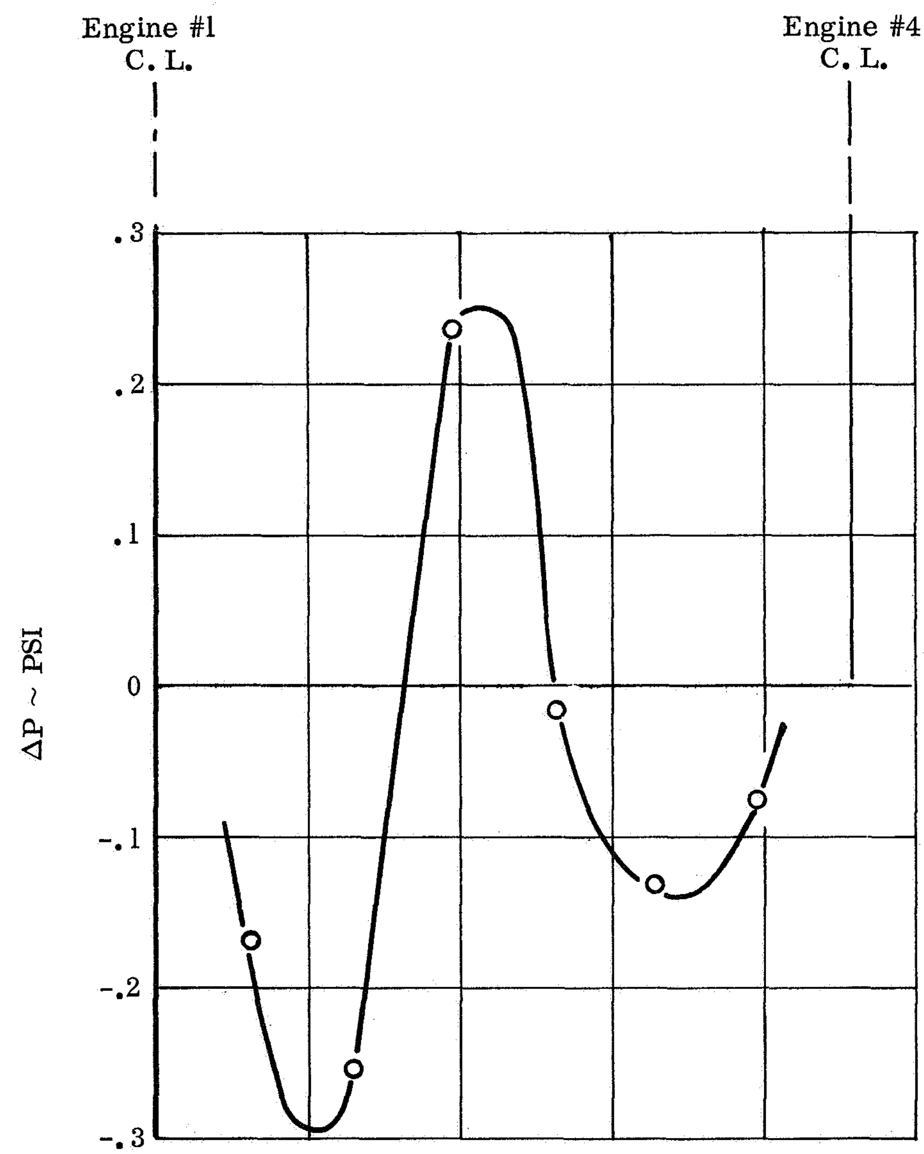

FIGURE A24-3. POD UNDERSURFACE PRESSURE DISTRIBUTION

Test #25

H/D = 4

α = +6

Wind = <4 MPH

Engines #1 and #4 operating

INGESTION CHARACTERISTICS

	ENGINE #1	ENGINE #4
$\Delta \hat{\bar{T}}$	4°F	2°F
$\hat{\epsilon}_{max}$	16°F	8°F
$\hat{\epsilon}_{r.m.s.}$	4°F	2°F
$\lvert\hat{\dot{T}}\rvert$	40°F/sec	—

Test 25

ENGINE #1

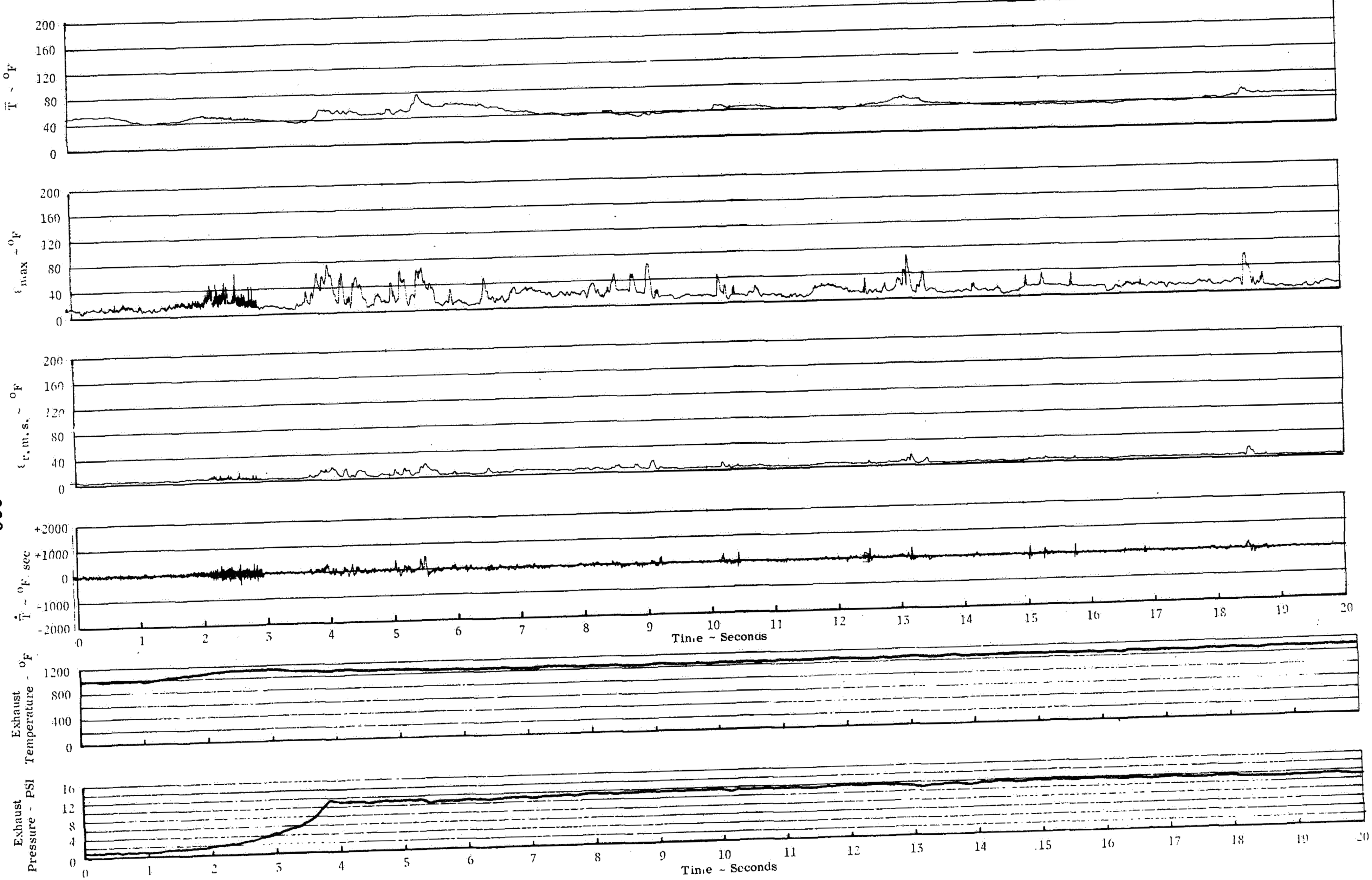

FIGURE A25-1. EXHAUST CONDITIONS AND INGESTION CHARACTERISTICS

Test 25

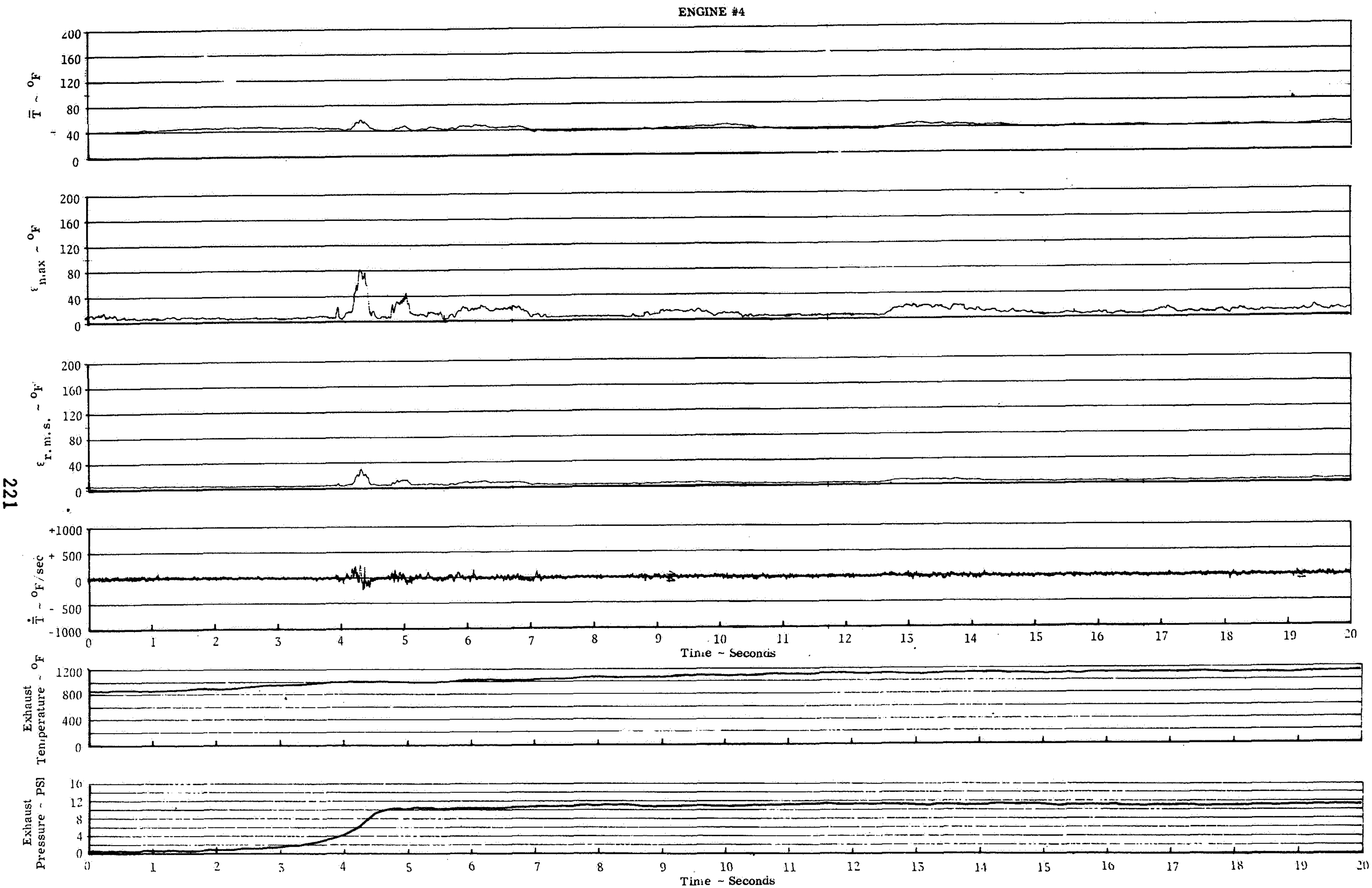

FIGURE A25-2. EXHAUST CONDITIONS AND INGESTION CHARACTERISTICS

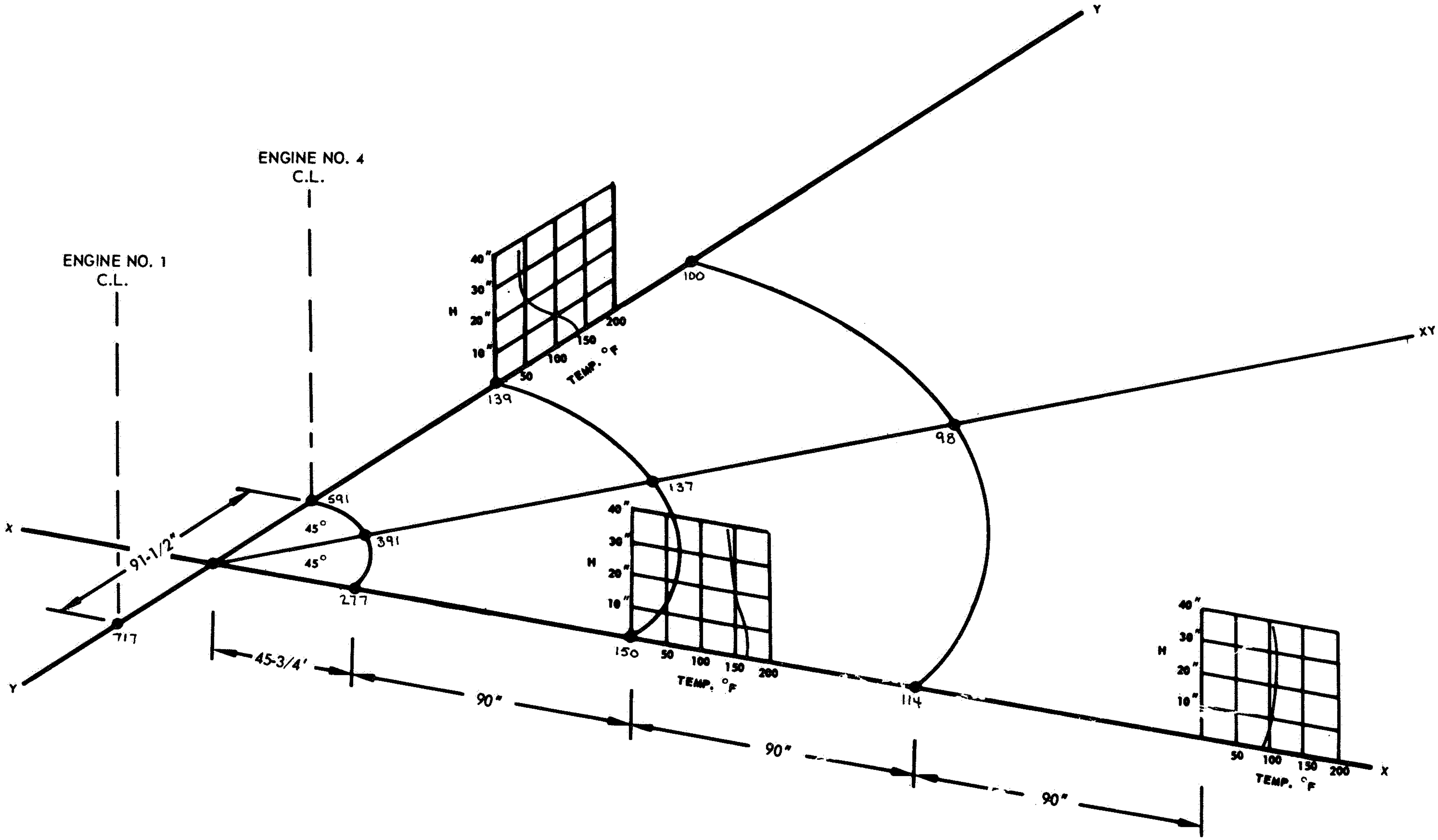

FIGURE A25-3. GROUND JET TEMPERATURE PROFILE

Test 25

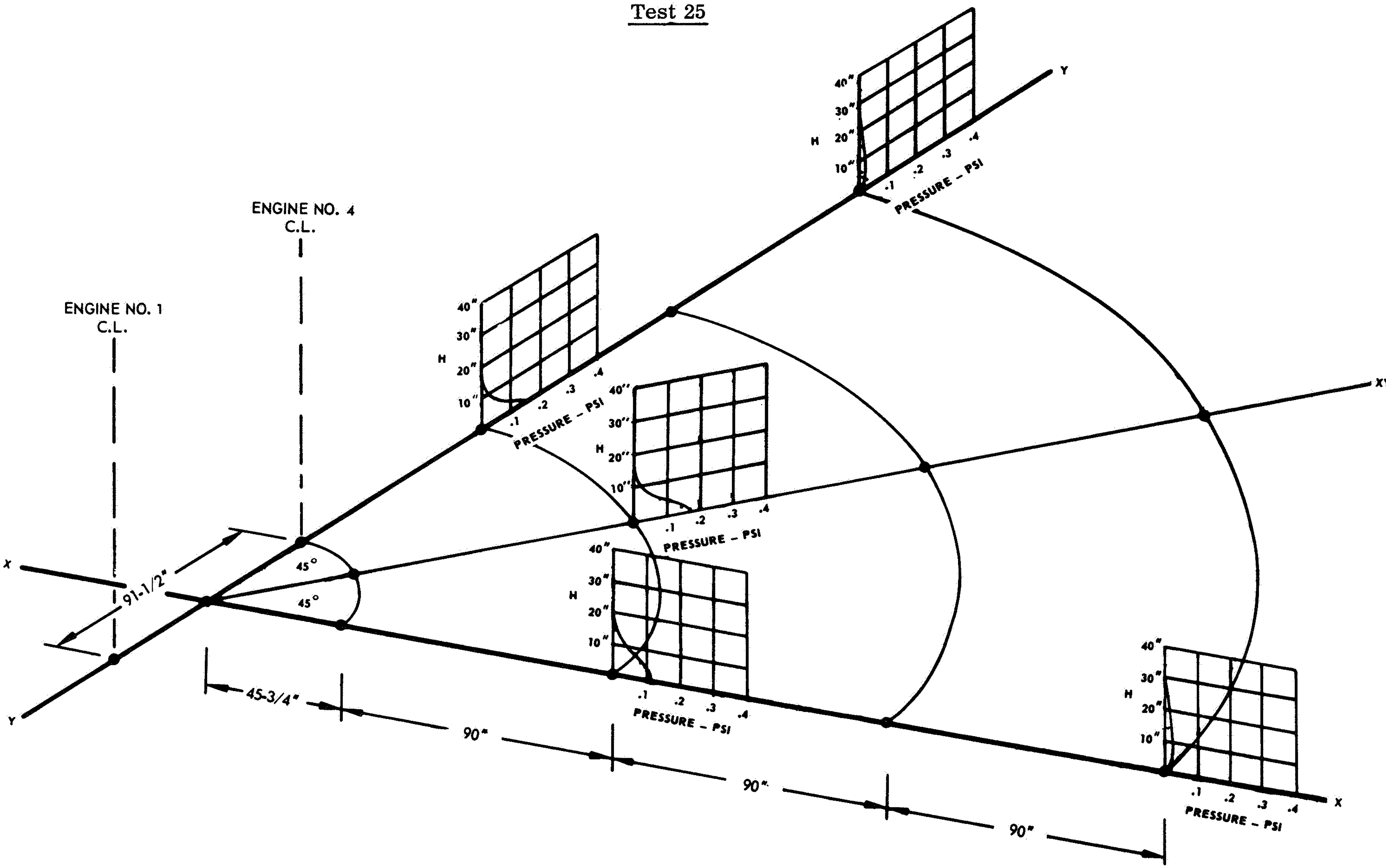

FIGURE A25-4. GROUND JET DYNAMIC PRESSURE PROFILE

Test 25

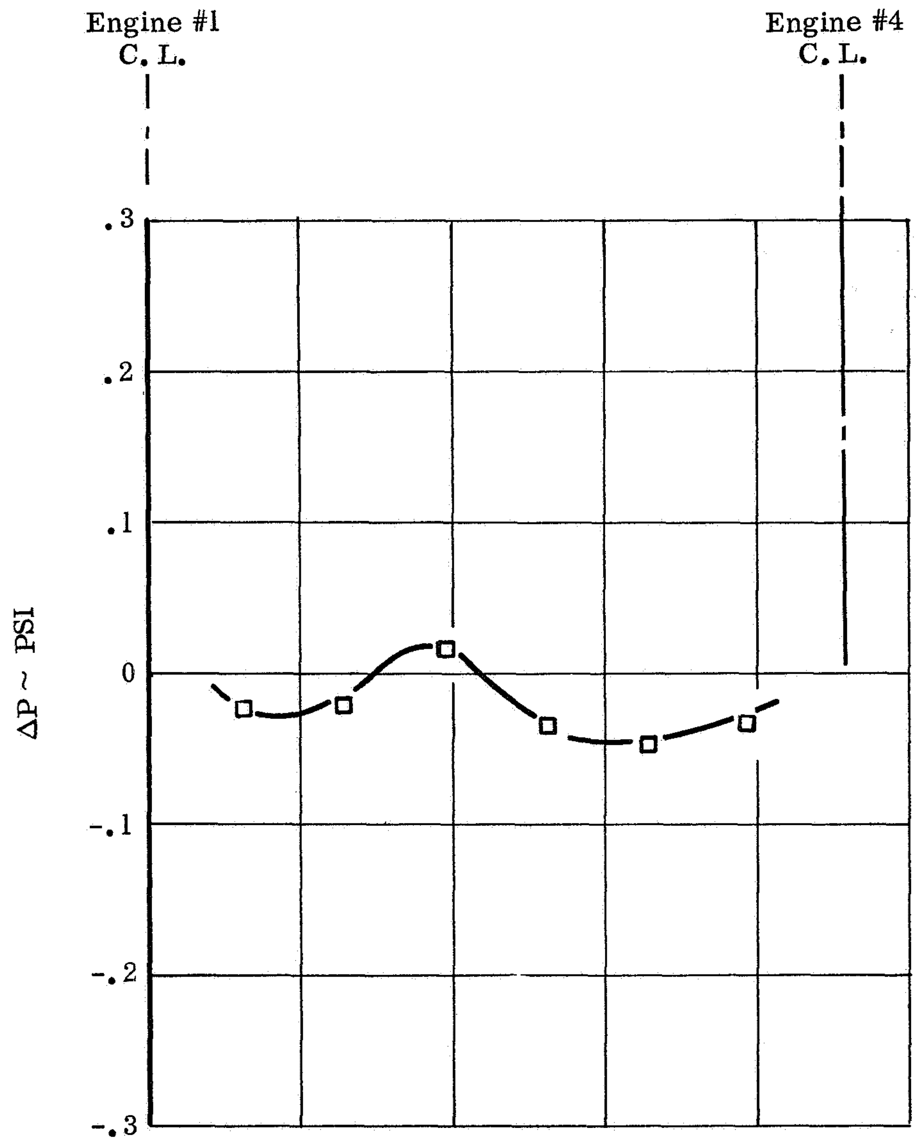

FIGURE A25-5. POD UNDERSURFACE PRESSURE DISTRIBUTION

Test #26

H/D = 4

α = +3

Wind = <4 MPH

Engines #1 and #4 operating

INGESTION CHARACTERISTICS

	ENGINE #1	ENGINE #4
$\Delta\hat{\bar{T}}$	6°F	5°F
$\hat{\epsilon}_{max}$	24°F	10°F
$\hat{\epsilon}_{r.m.s.}$	6°F	4°F
$\lvert\hat{\dot{T}}\rvert$	80°F/sec	—

Test 26

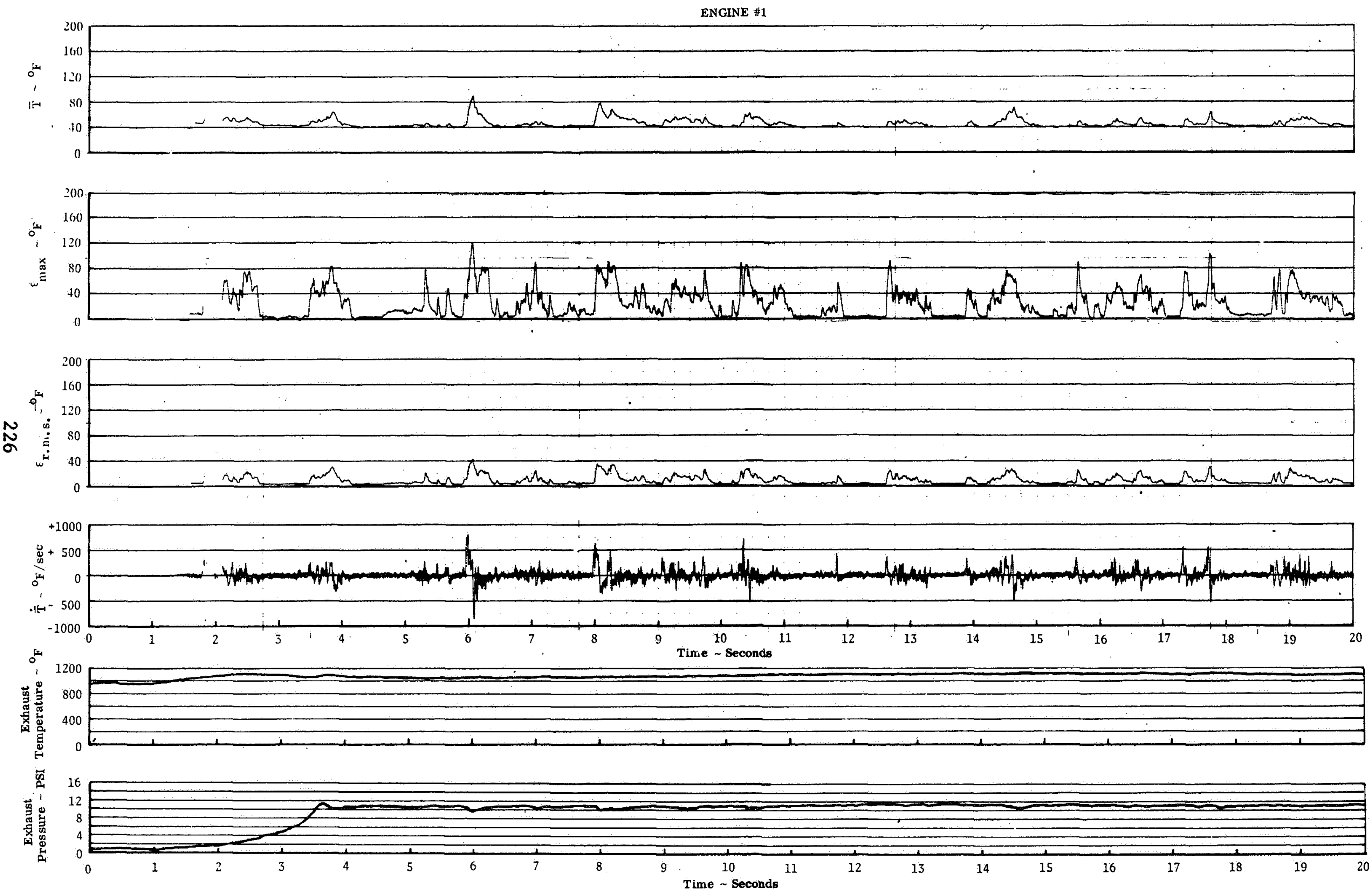

FIGURE A26-1. EXHAUST CONDITIONS AND INGESTION CHARACTERISTICS

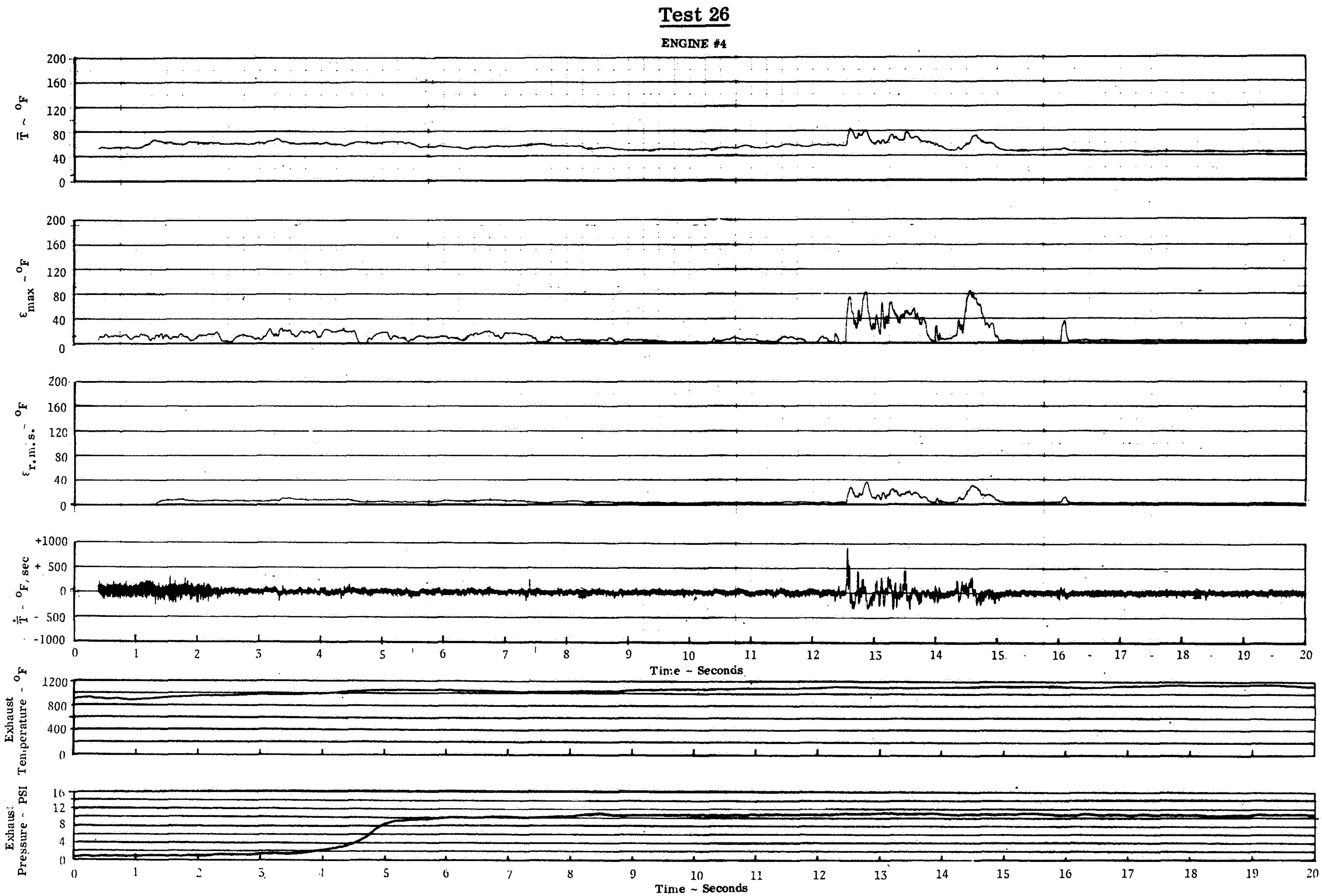

FIGURE A26-2. EXHAUST CONDITIONS AND INGESTION CHARACTERISTICS

Test 26

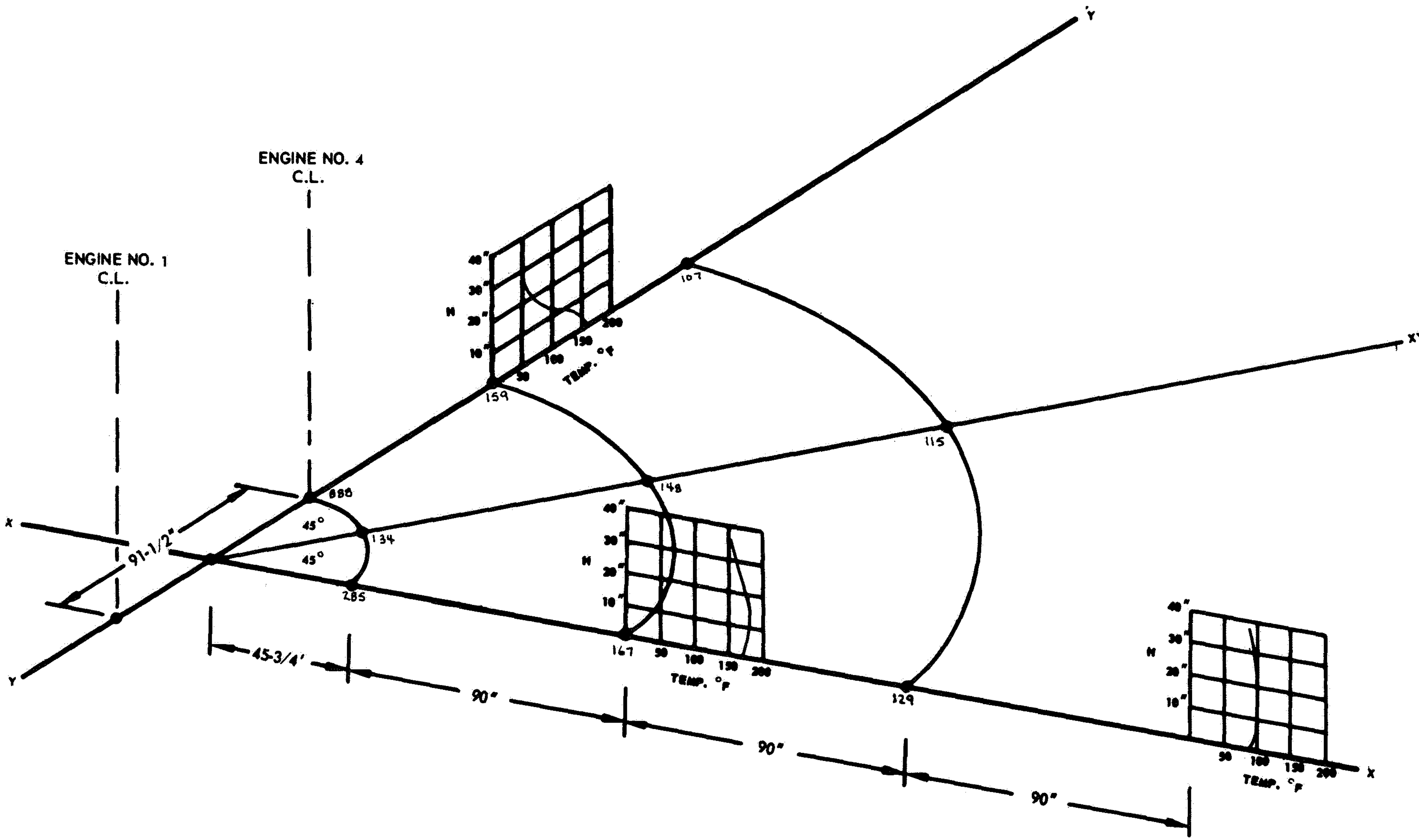

FIGURE A26-3. GROUND JET TEMPERATURE PROFILE

Test 26

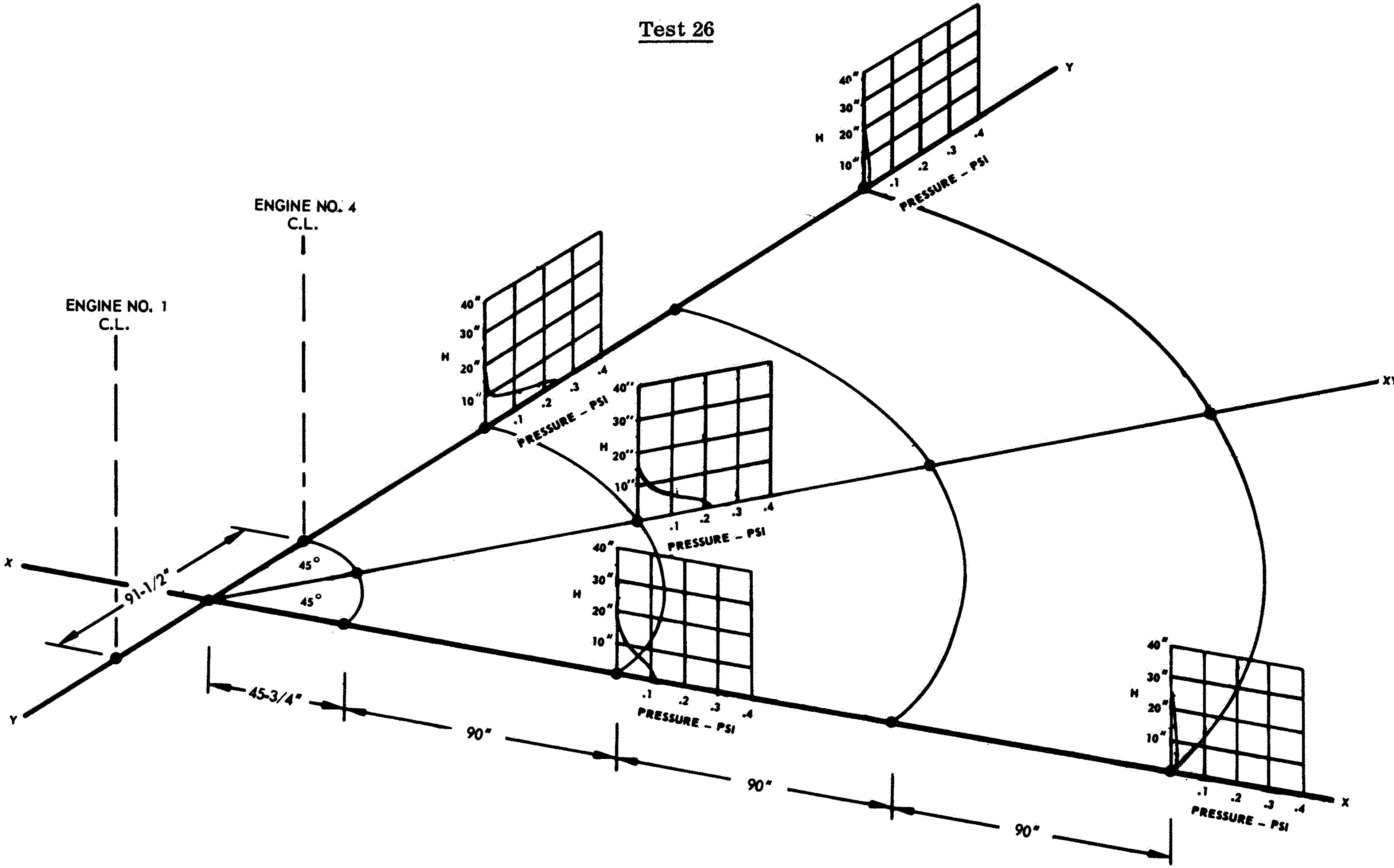

FIGURE A26-4. GROUND JET DYNAMIC PRESSURE PROFILE

Test 26

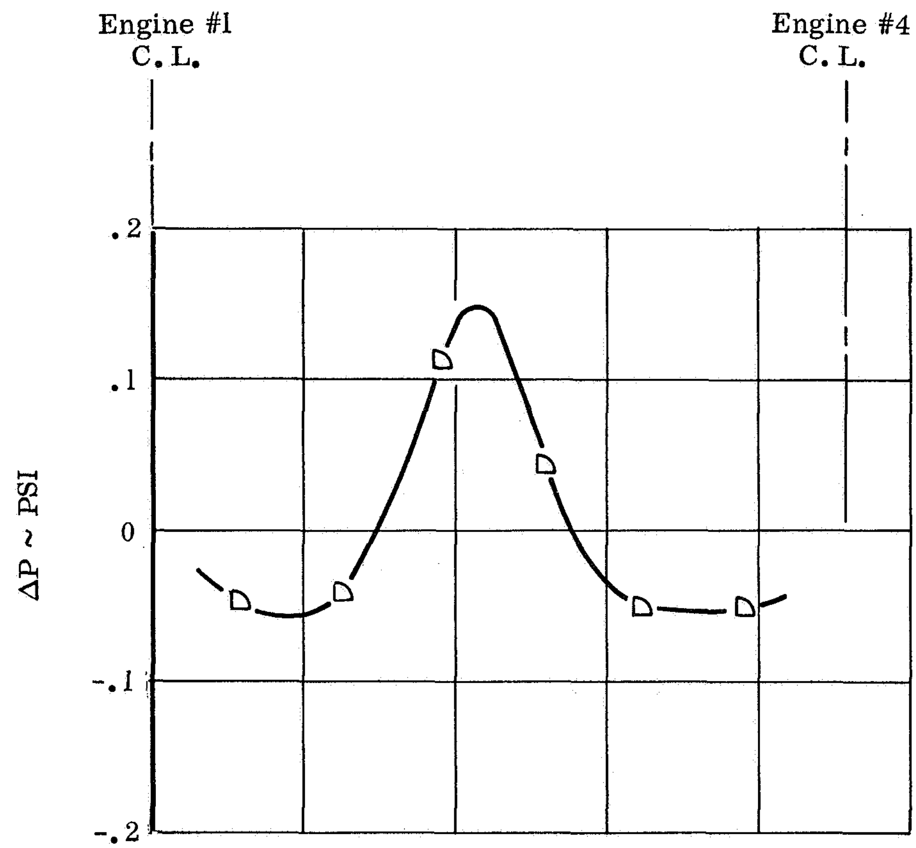

FIGURE A26-5. POD UNDERSURFACE PRESSURE DISTRIBUTION

Test #27

$H/D = 4$

$\alpha = +1$

Wind = <4 MPH

Engines #1 and #4 operating

INGESTION CHARACTERISTICS

	ENGINE #1	ENGINE #4
$\Delta \hat{\bar{T}}$	18°F	2°F
$\hat{\epsilon}_{max}$	52°F	8°F
$\hat{\epsilon}_{r.m.s.}$	14°F	2°F
$\lvert\hat{\dot{T}}\rvert$	140°F/sec	—

Test 27

ENGINE #1

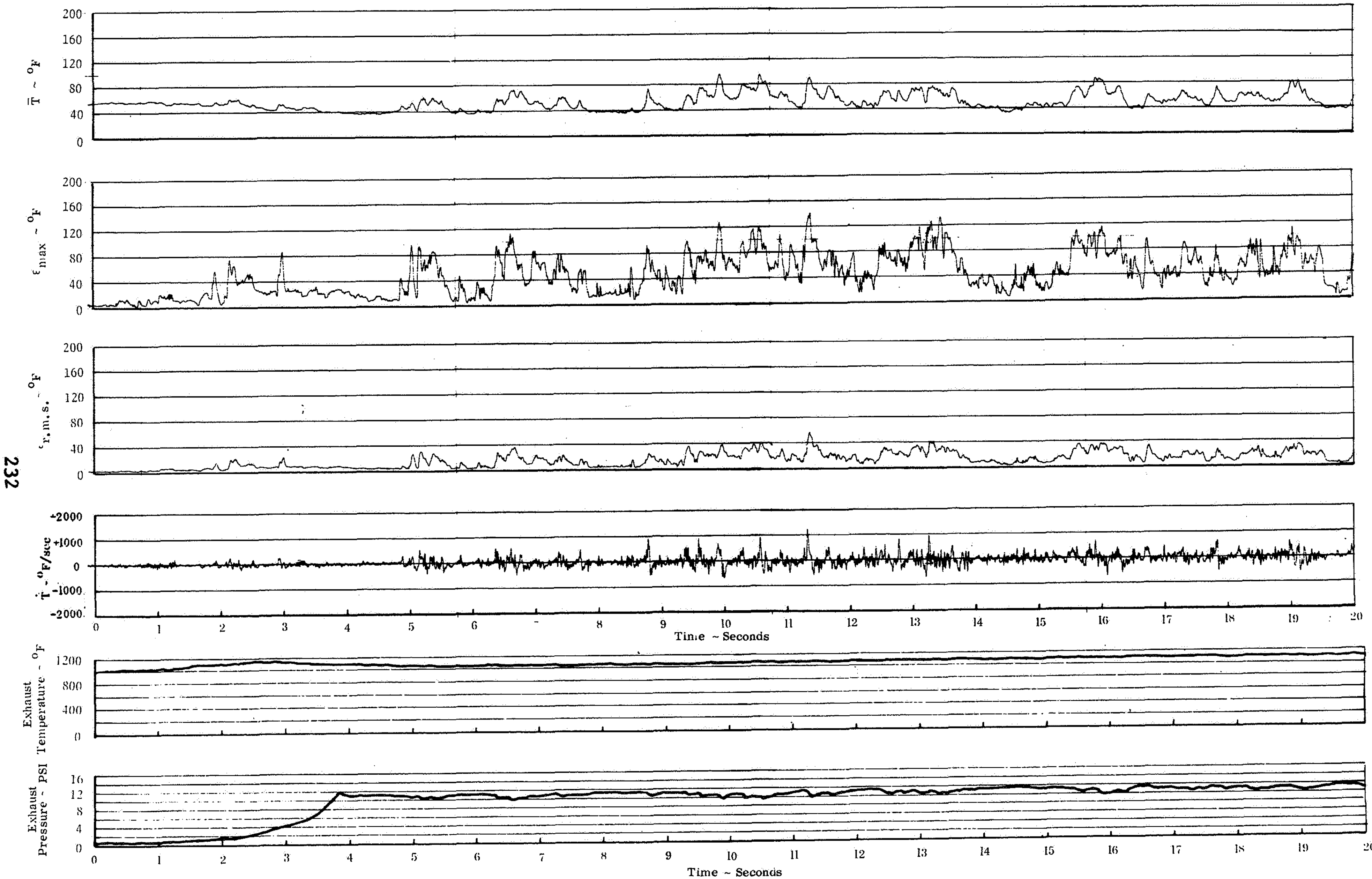

FIGURE A27-1. EXHAUST CONDITIONS AND INGESTION CHARACTERISTICS

Test 27

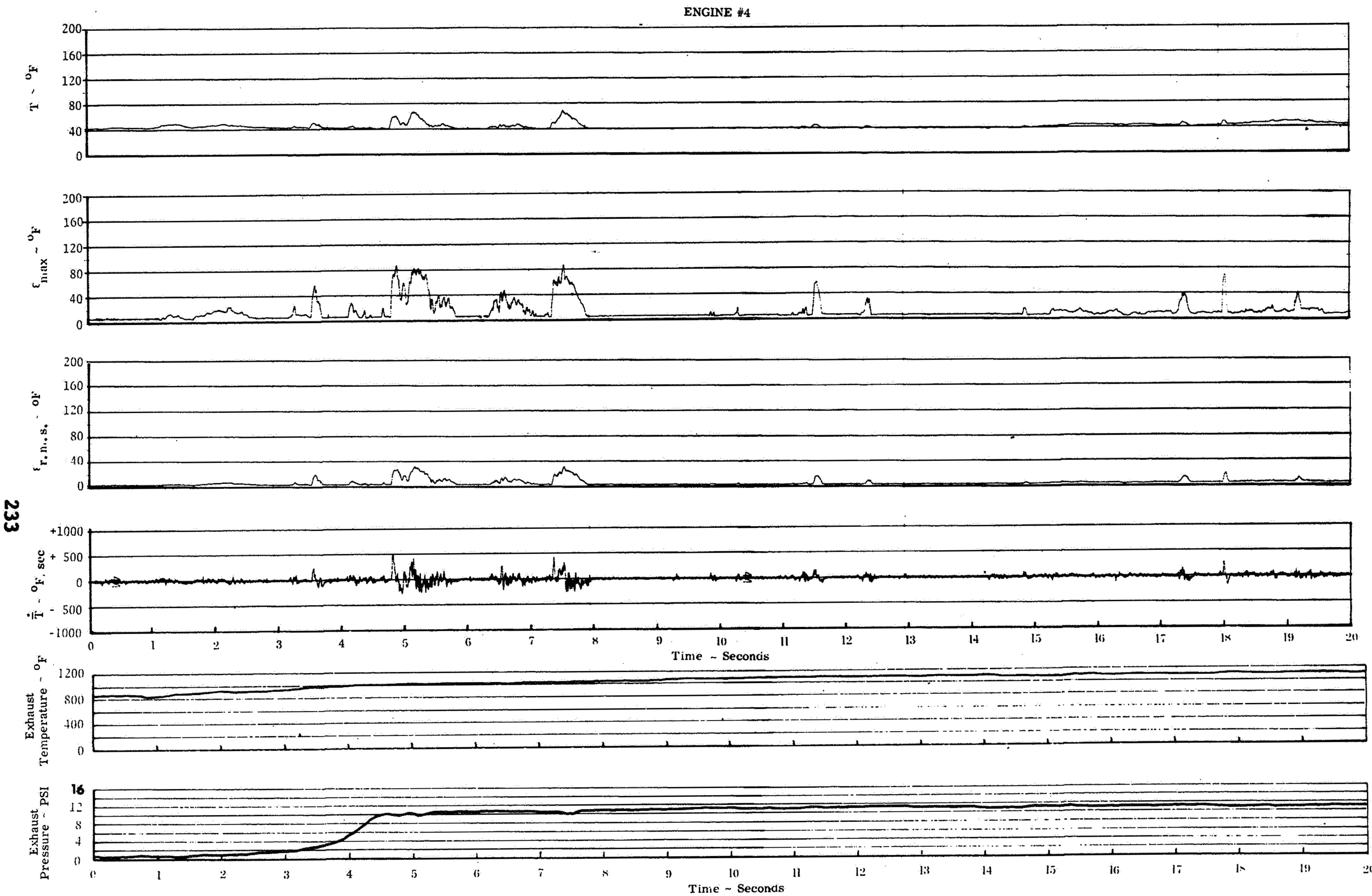

FIGURE A27-2. EXHAUST CONDITIONS AND INGESTION CHARACTERISTICS

Test 27

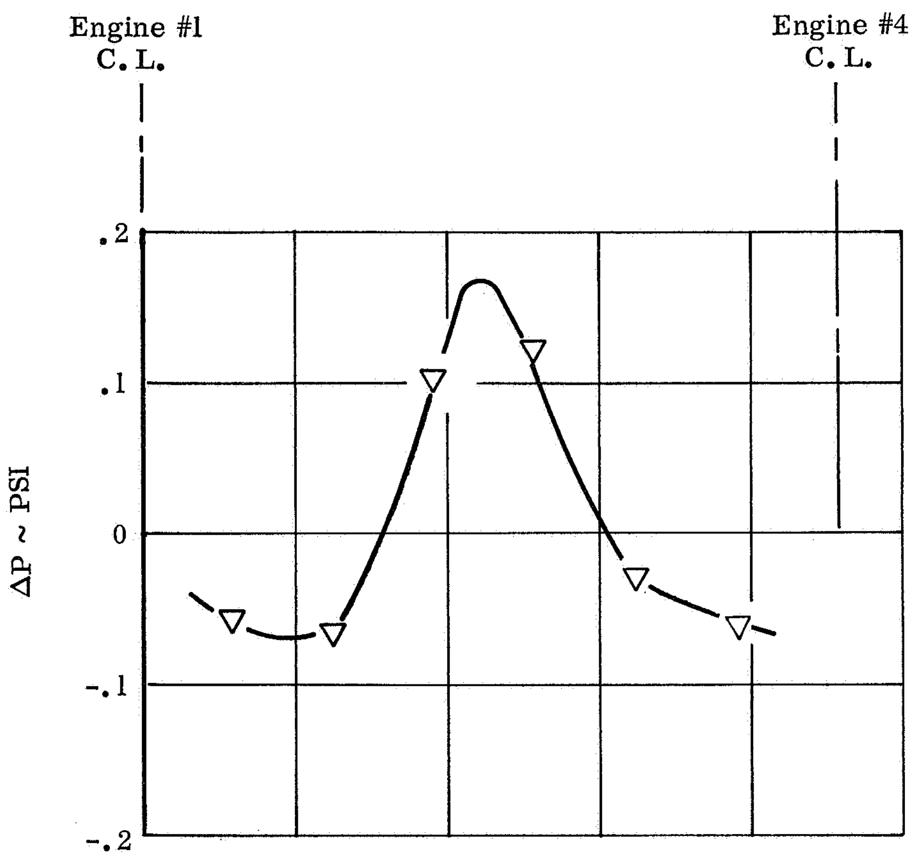

FIGURE A27-3. POD UNDERSURFACE PRESSURE DISTRIBUTION

Test #28

H/D = 4

α = -1

Wind = <4 MPH

Engines #1 and #4 operating

INGESTION CHARACTERISTICS

	ENGINE #1	ENGINE #4
$\Delta\hat{\bar{T}}$	18°F	2°F
$\hat{\epsilon}_{max}$	46°F	8°F
$\hat{\epsilon}_{r.m.s.}$	15°F	4°F
$\lvert\hat{\dot{T}}\rvert$	150°F/sec	—

Test 28

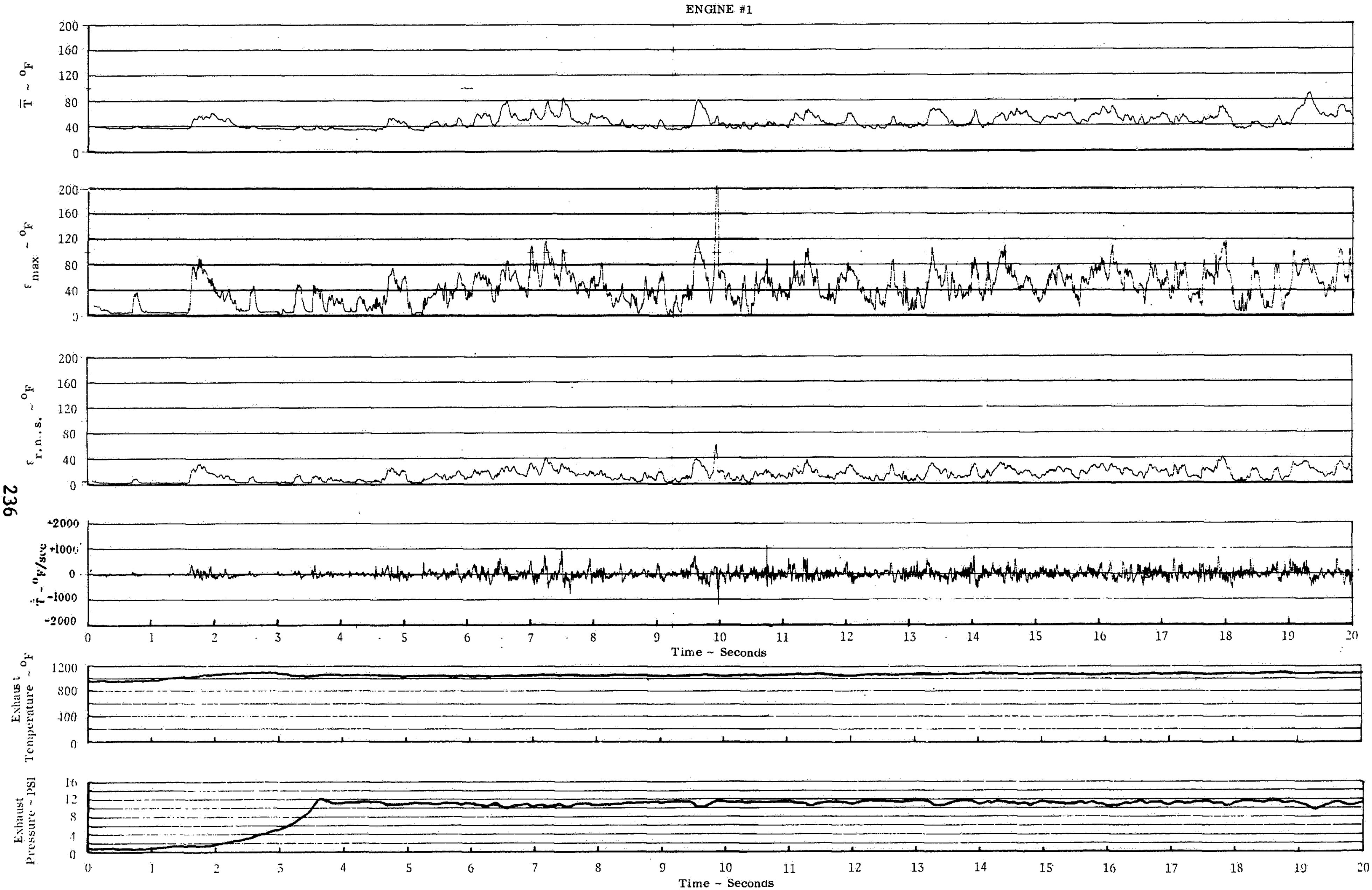

FIGURE A28-1. EXHAUST CONDITIONS AND INGESTION CHARACTERISTICS

Test 28

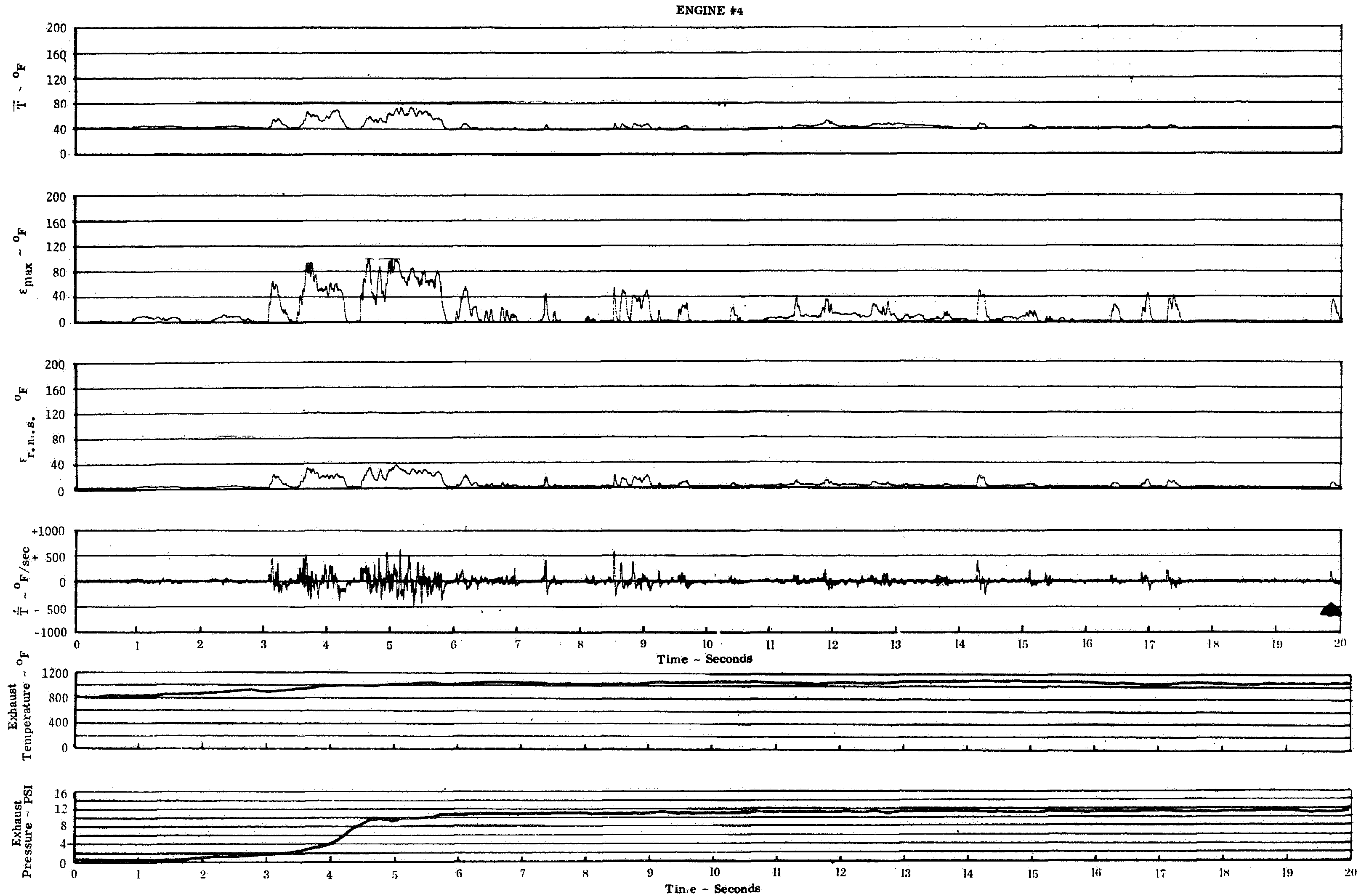

FIGURE A28-2. EXHAUST CONDITIONS AND INGESTION CHARACTERISTICS

Test 28

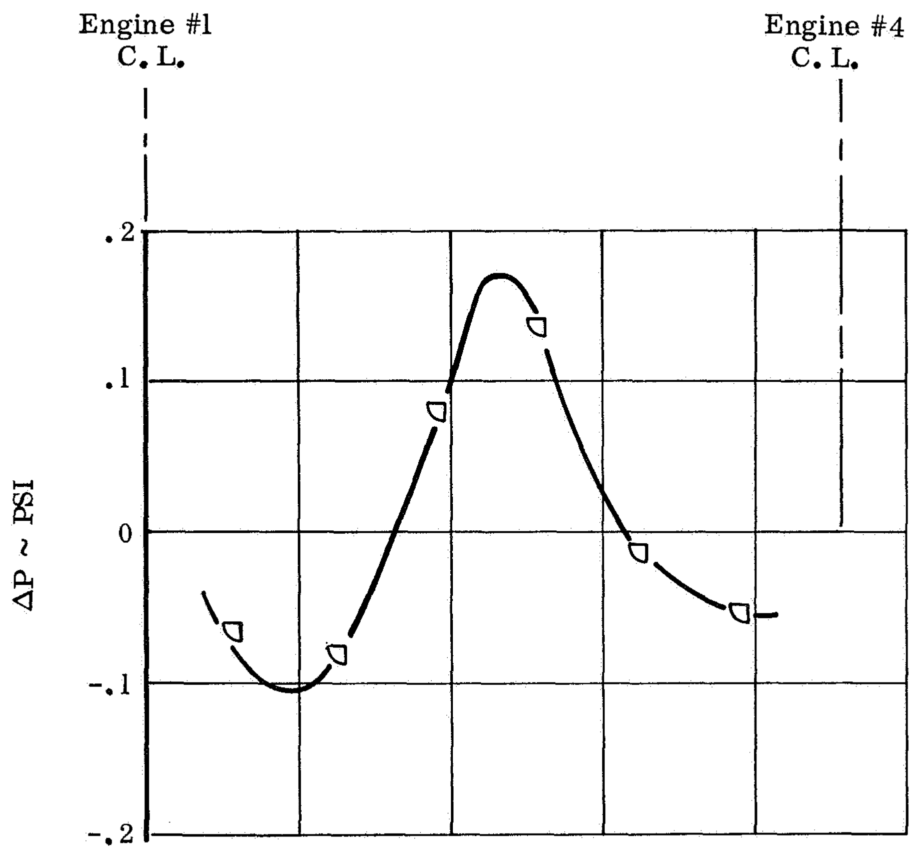

FIGURE A28-3. POD UNDERSURFACE PRESSURE DISTRIBUTION

Test #29

H/D = 4

α = -3

Wind = <4 MPH

Engines #1 and #4 operating

INGESTION CHARACTERISTICS

	ENGINE #1	ENGINE #4
$\Delta\hat{\bar{T}}$	6°F	15°F
$\hat{\epsilon}_{max}$	24°F	42°F
$\hat{\epsilon}_{r.m.s.}$	8°F	13°F
$\lvert\hat{\dot{T}}\rvert$	——	120°F/sec

Test 29

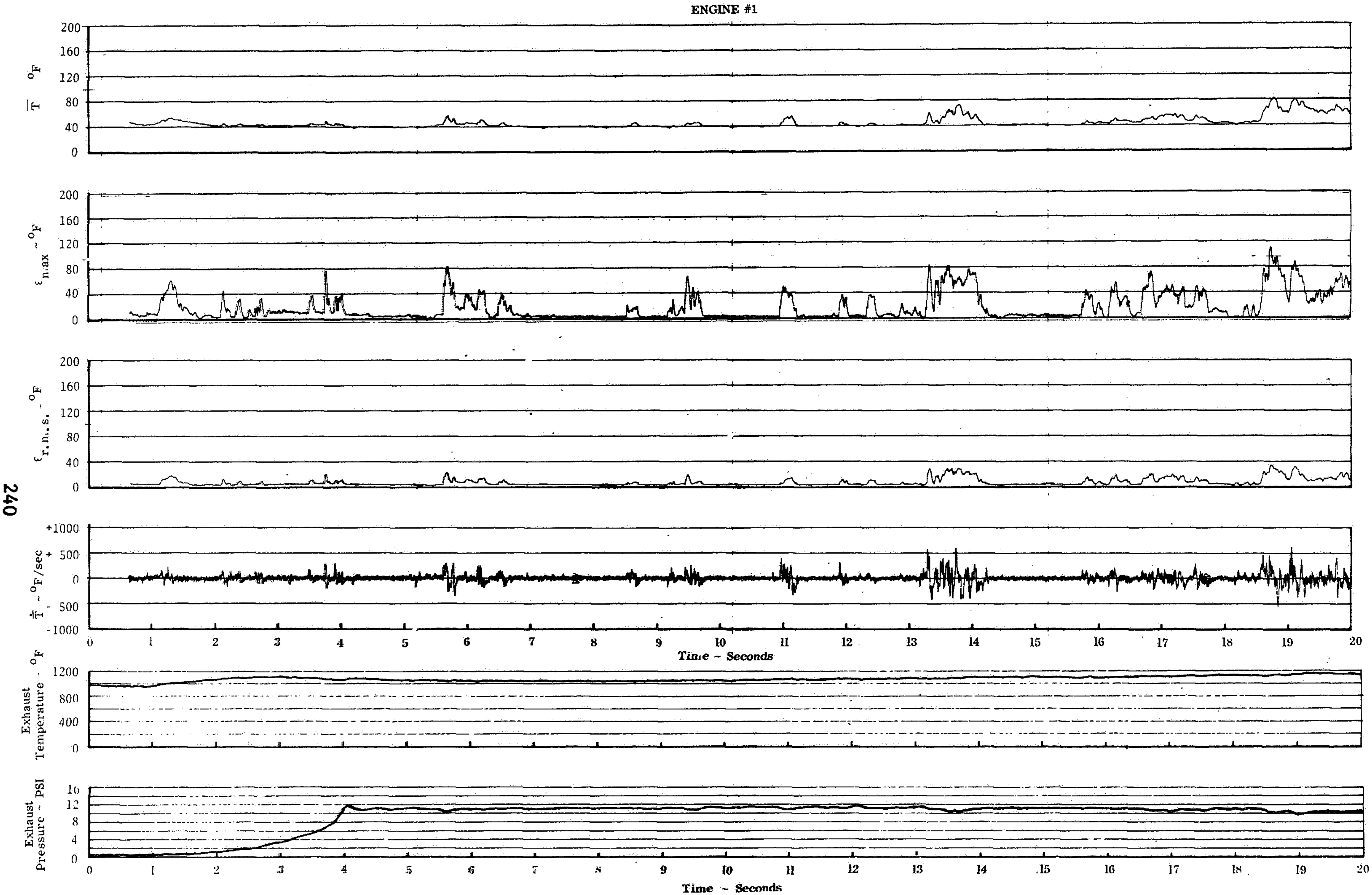

FIGURE A29-1. EXHAUST CONDITIONS AND INGESTION CHARACTERISTICS

Test 29

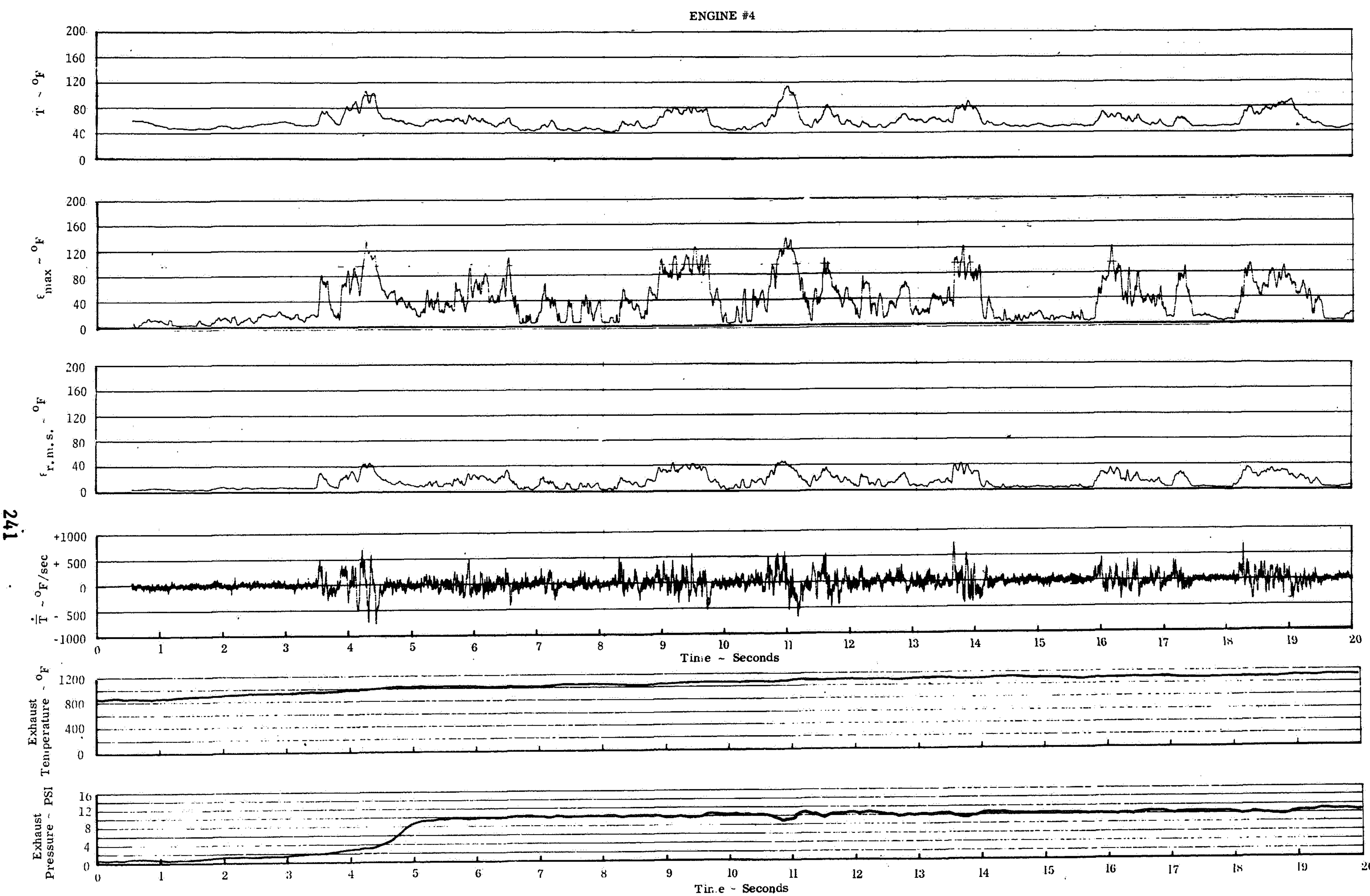

FIGURE A29-2. EXHAUST CONDITIONS AND INGESTION CHARACTERISTICS

Test 29

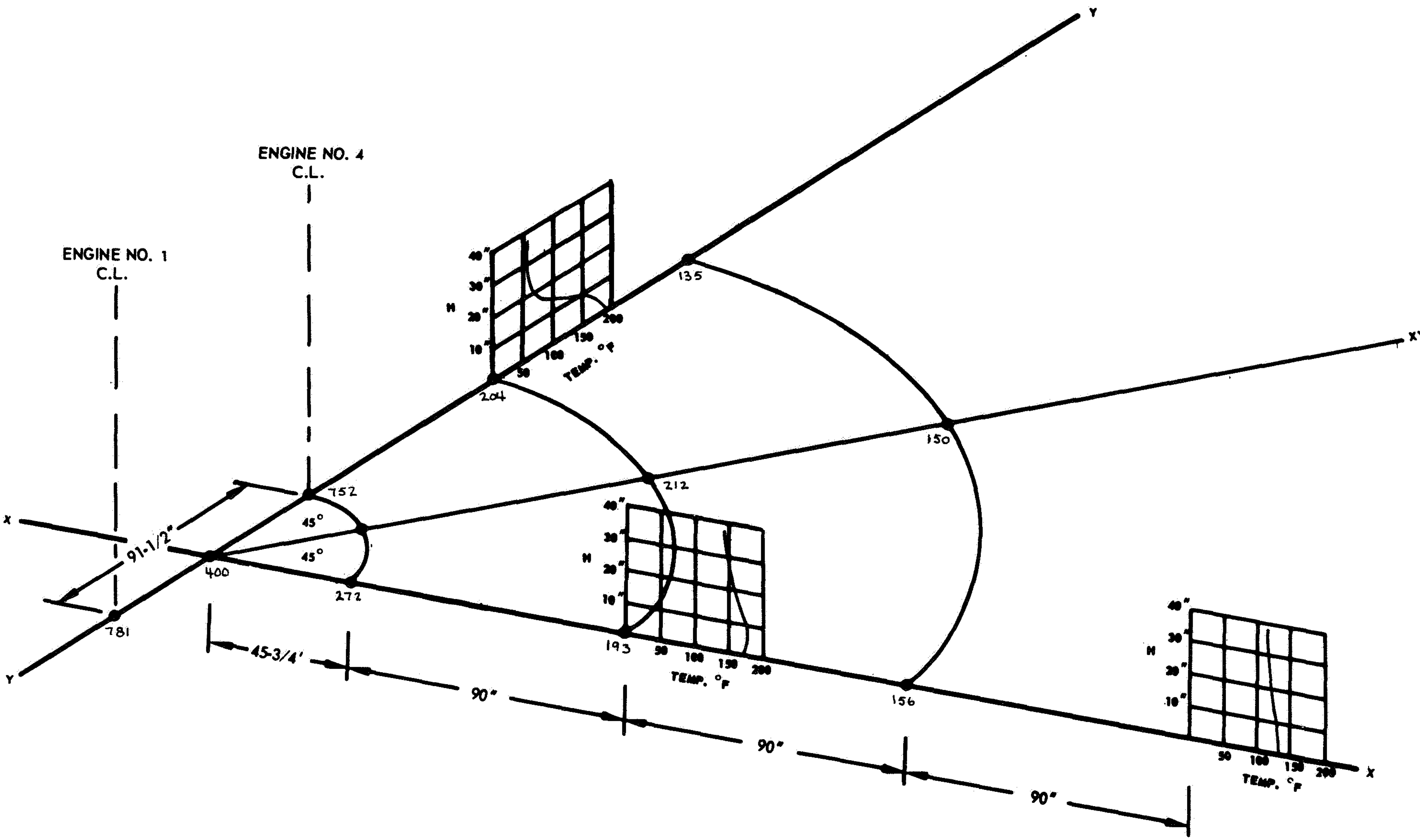

FIGURE A29-3. GROUND JET TEMPERATURE PROFILE

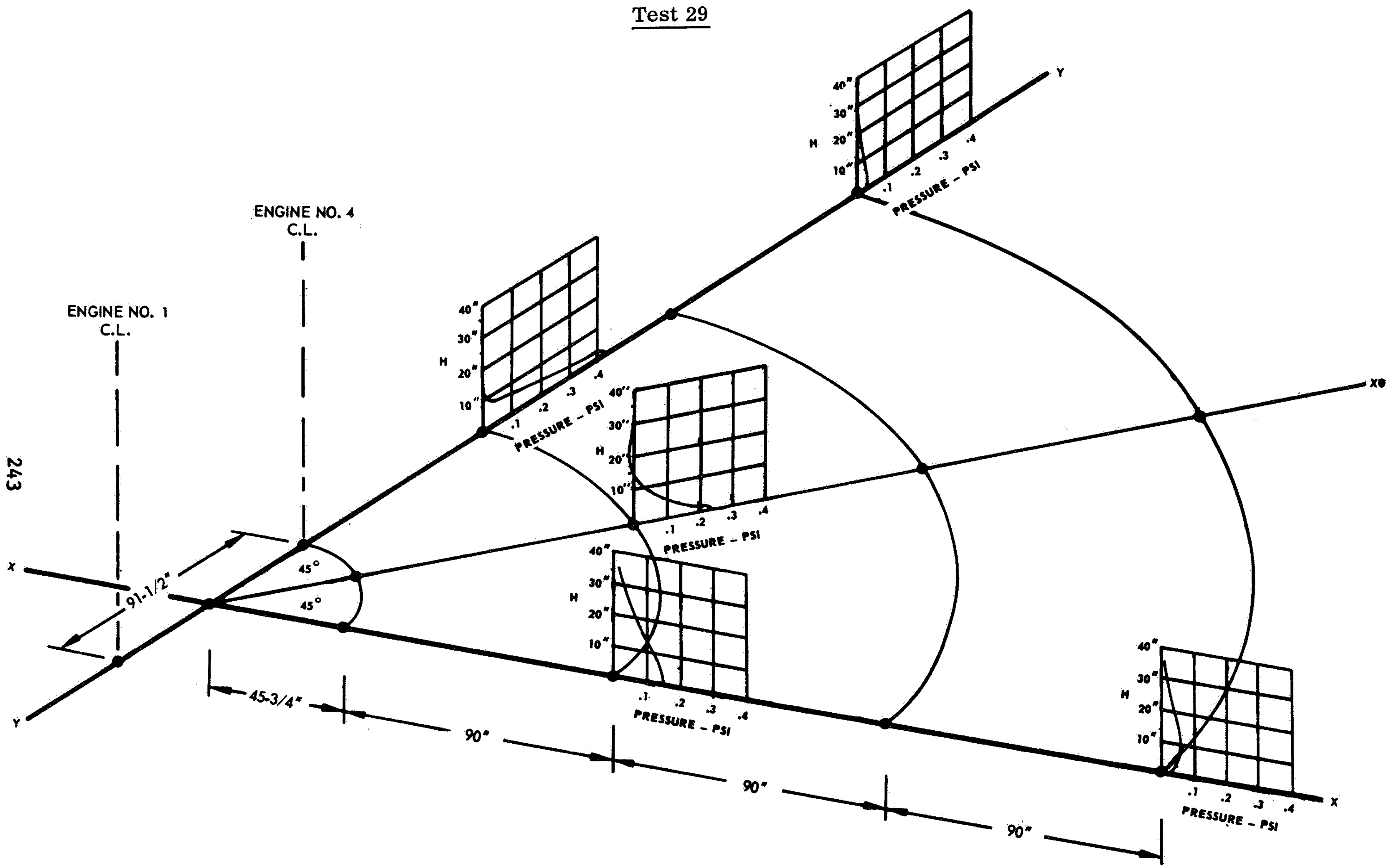

FIGURE A29-4. GROUND JET DYNAMIC PRESSURE PROFILE

Test 29

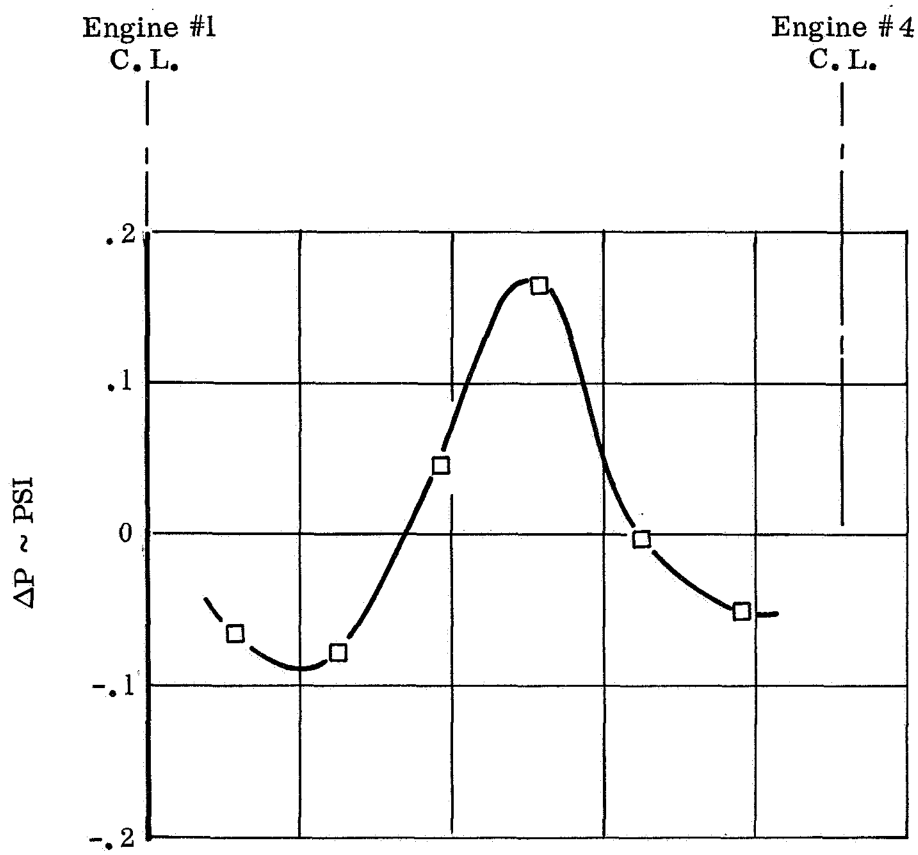

FIGURE A29-5. POD UNDERSURFACE PRESSURE DISTRIBUTION

Test #30

H/D = 4

α = -6

Wind = <4 MPH

Engines #1 and #4 operating

INGESTION CHARACTERISTICS

	ENGINE #1	ENGINE #4
$\Delta\hat{\bar{T}}$	3°F	6°F
$\hat{\epsilon}_{max}$	10°F	24°F
$\hat{\epsilon}_{r.m.s.}$	4°F	6°F
$\lvert\hat{\dot{T}}\rvert$	—	85°F/sec

Test 30

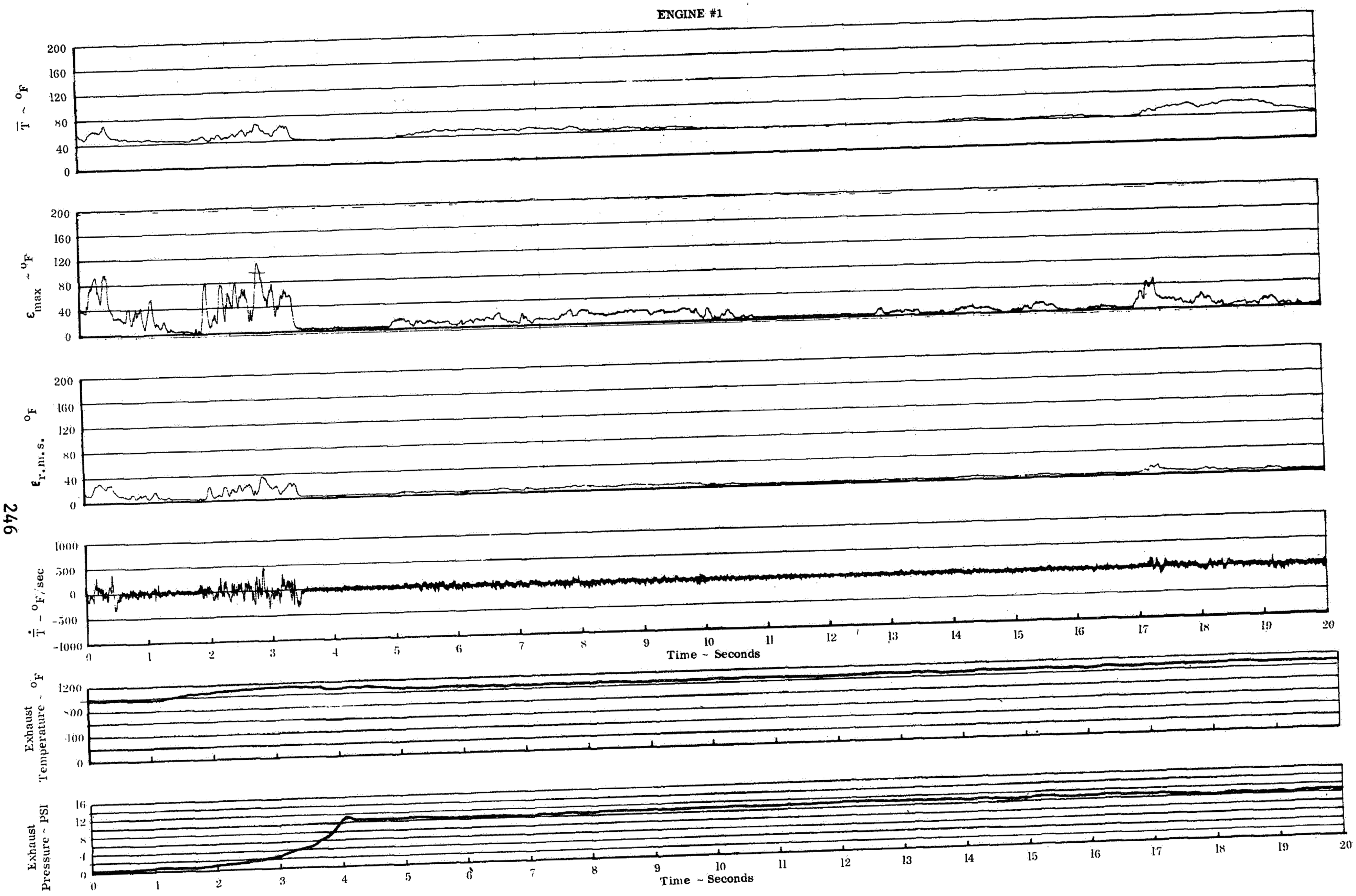

FIGURE A30-1. EXHAUST CONDITIONS AND INGESTION CHARACTERISTICS

Test 30

ENGINE #4

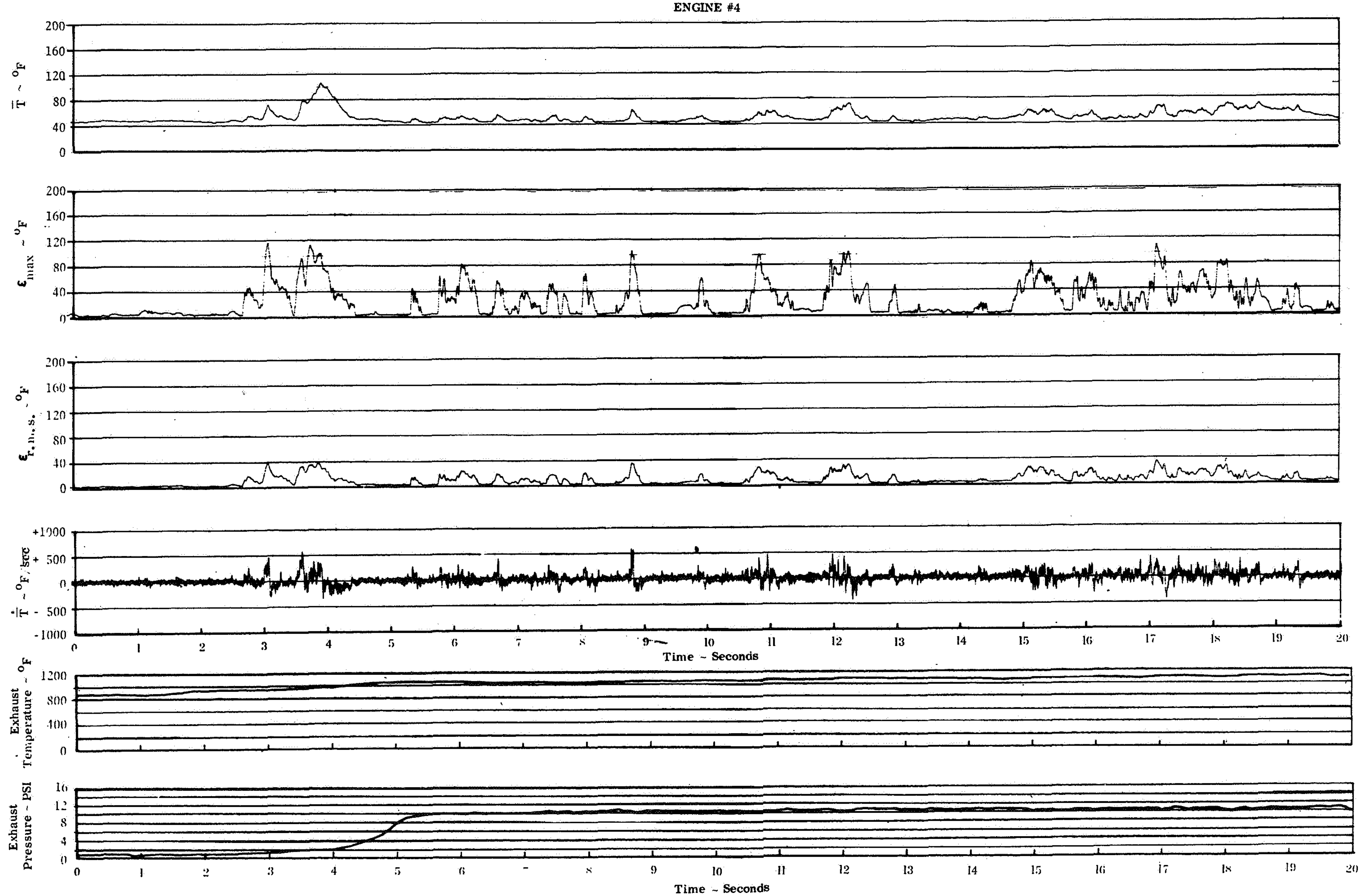

FIGURE A30-2. EXHAUST CONDITIONS AND INGESTION CHARACTERISTICS

Test 30

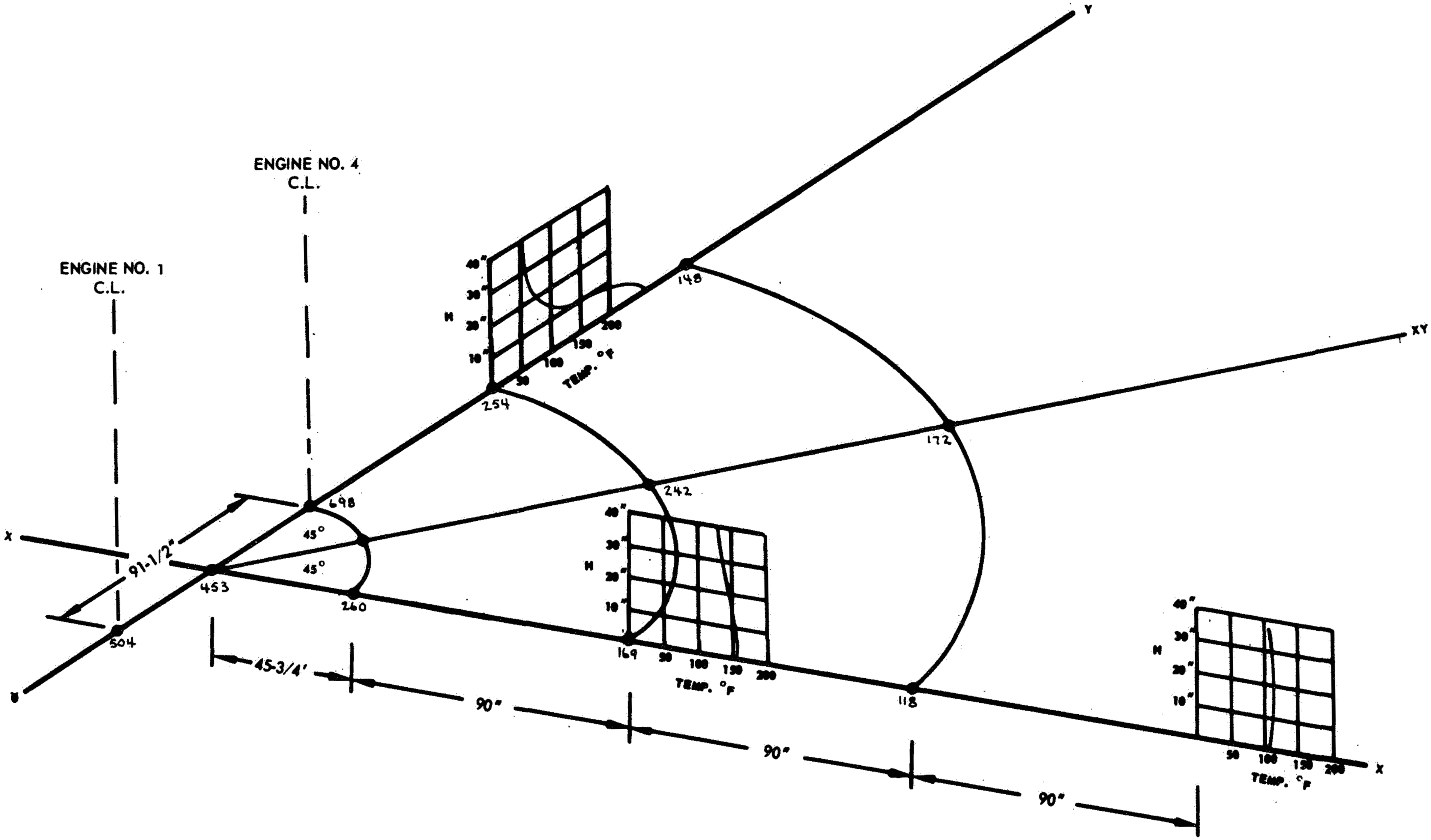

FIGURE A30-3. GROUND JET TEMPERATURE PROFILE

Test 30

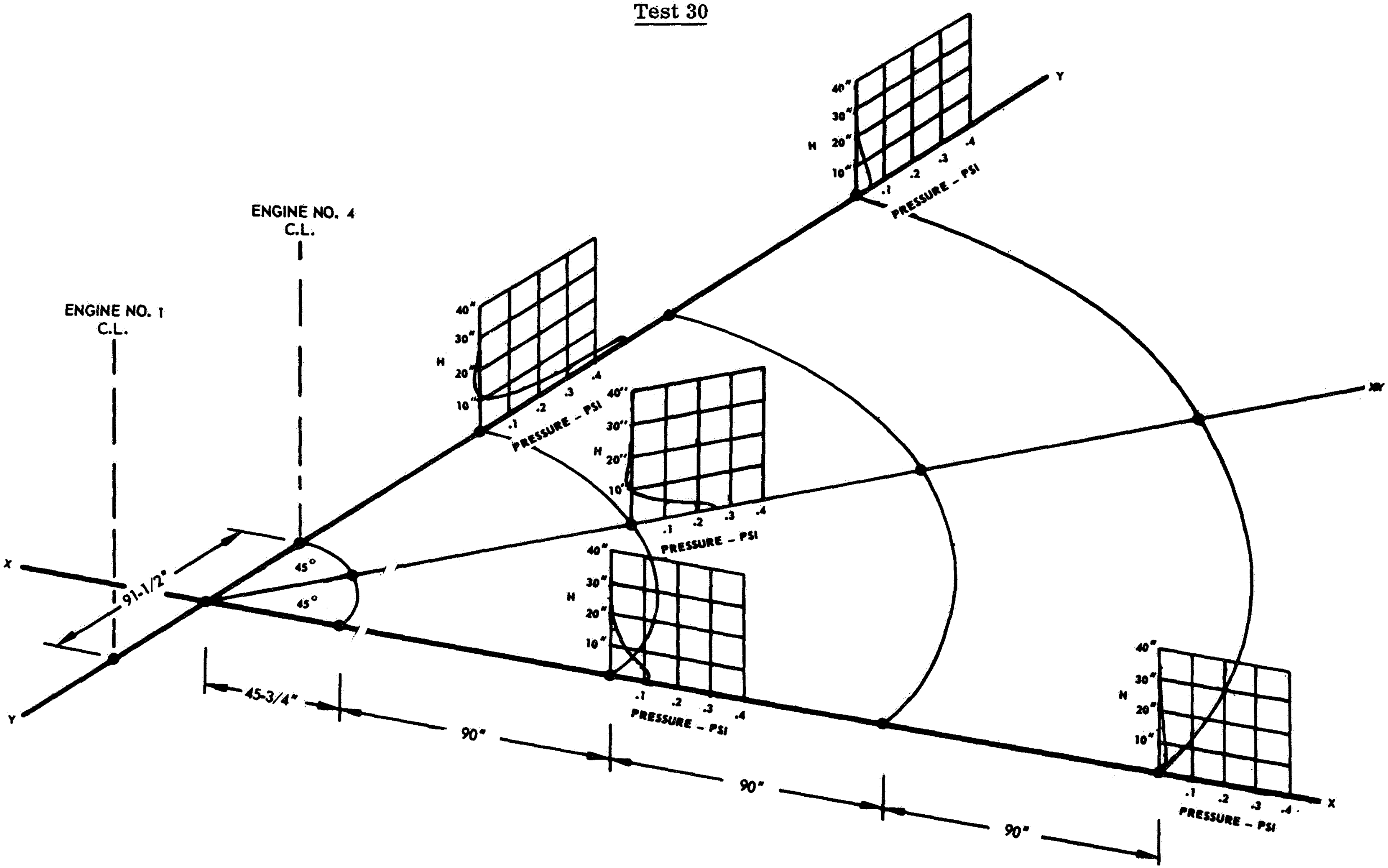

FIGURE A30-4. GROUND JET DYNAMIC PRESSURE PROFILE

Test 30

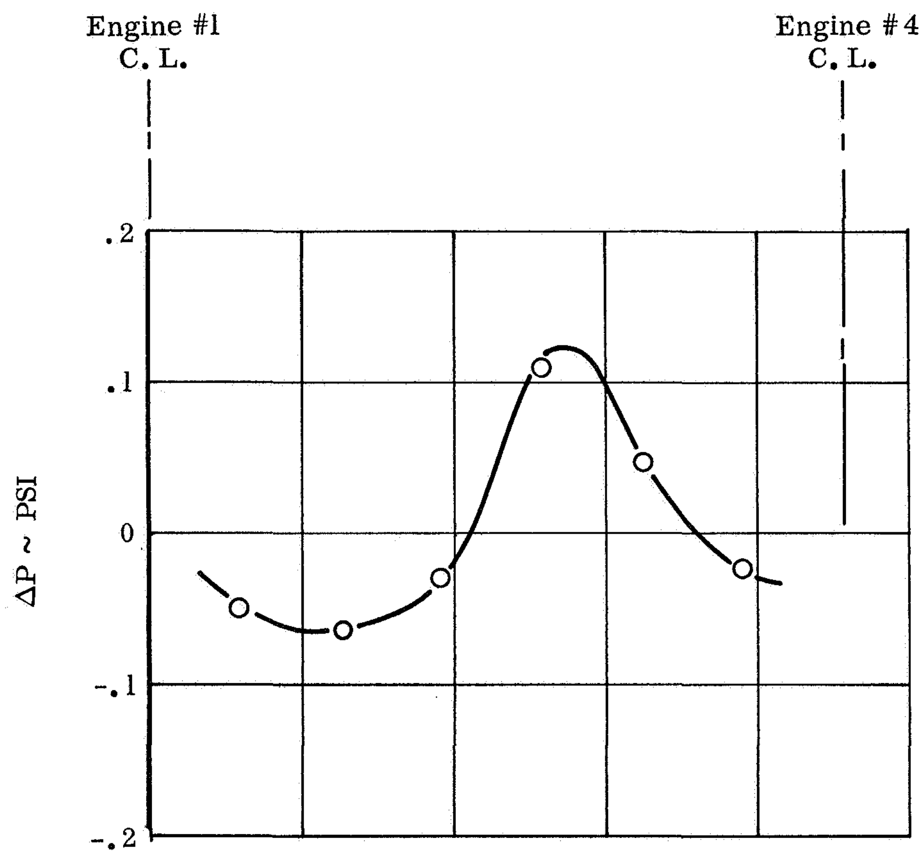

FIGURE A30-5. POD UNDERSURFACE PRESSURE DISTRIBUTION

Test #31

H/D = 6

α = +6

Wind = <4 MPH

Engines #1 and #4 operating

INGESTION CHARACTERISTICS

	ENGINE #1	ENGINE #4
$\Delta \hat{\bar{T}}$	1°F	0°F
$\hat{\epsilon}_{max}$	2°F	2°F
$\hat{\epsilon}_{r.m.s.}$	1°F	1°F
$\lvert\hat{\dot{T}}\rvert$	20°F/sec	—

Test 31

ENGINE #1

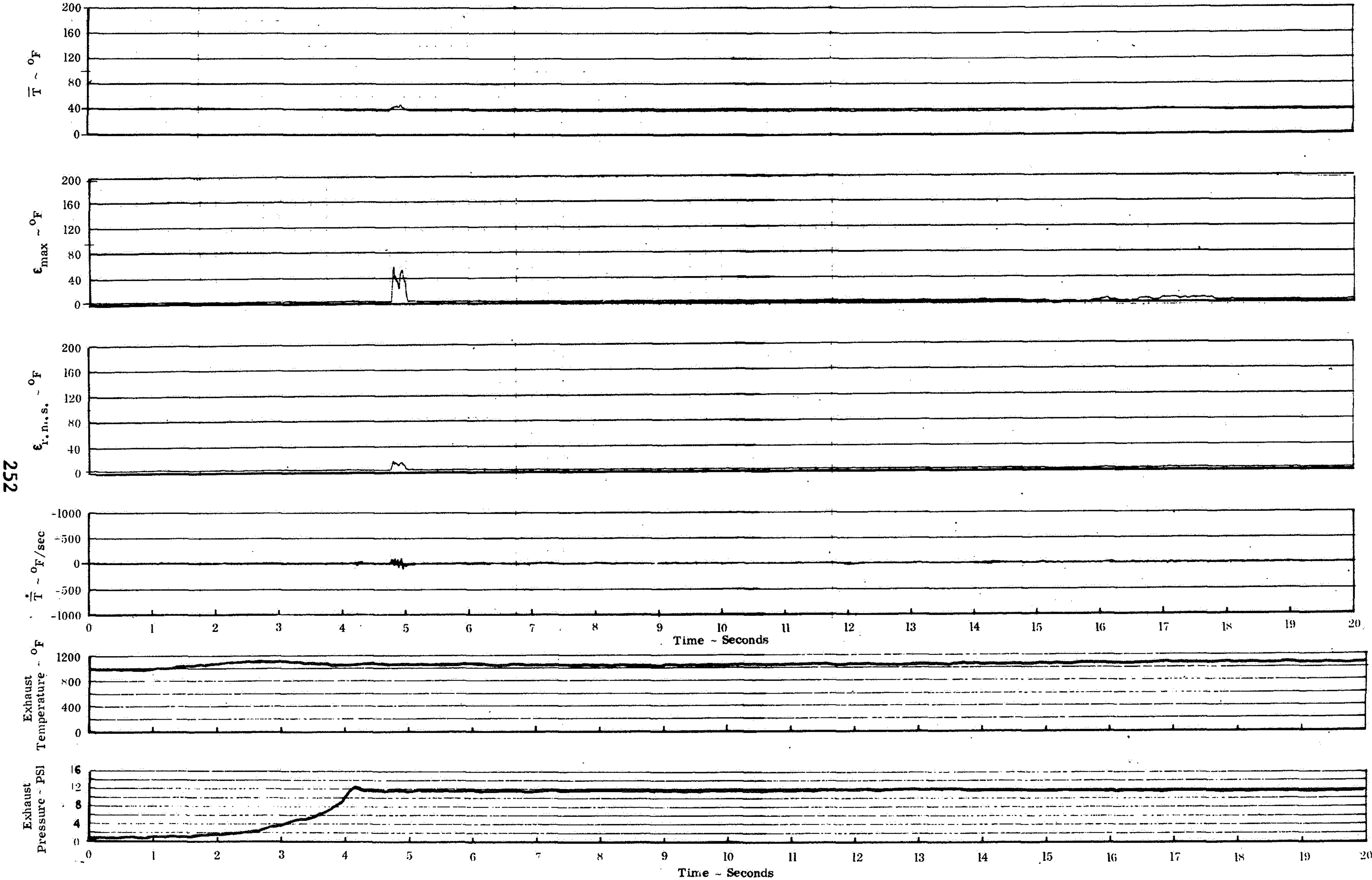

FIGURE A31-1. EXHAUST CONDITIONS AND INGESTION CHARACTERISTICS

Test 31

ENGINE #4

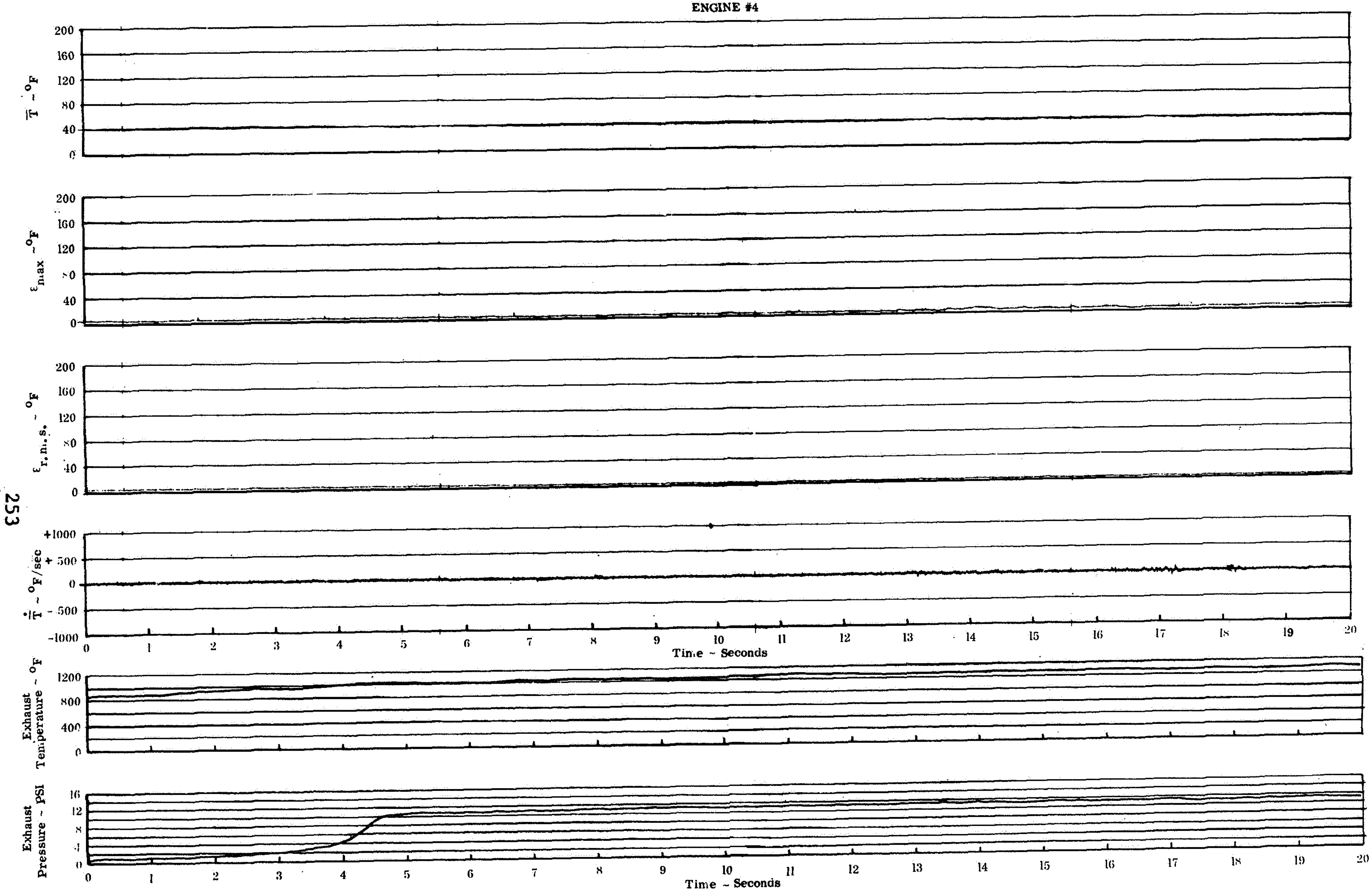

FIGURE A31-2. EXHAUST CONDITIONS AND INGESTION CHARACTERISTICS

Test 31

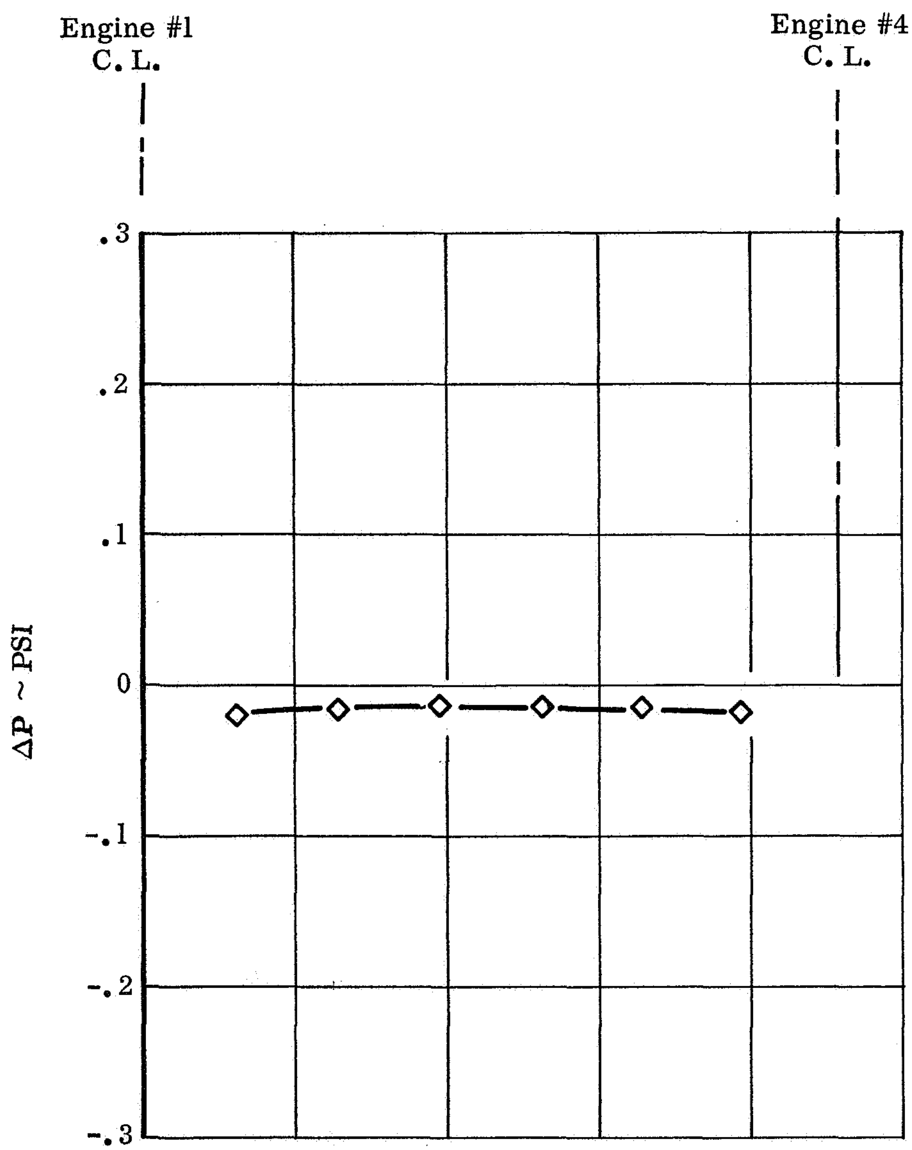

FIGURE A31-3. POD UNDERSURFACE PRESSURE DISTRIBUTION

Test #32

H/D = 8

α = +6

Wind = <4 MPH

Engines #1 and #4 operating

INGESTION CHARACTERISTICS

	ENGINE #1	ENGINE #4
$\Delta\hat{\bar{T}}$	0°F	0°F
$\hat{\epsilon}_{max}$	2°F	2°F
$\hat{\epsilon}_{r.m.s.}$	0°F	0°F
$\lvert\hat{\bar{T}}\rvert$	—	—

Test 32

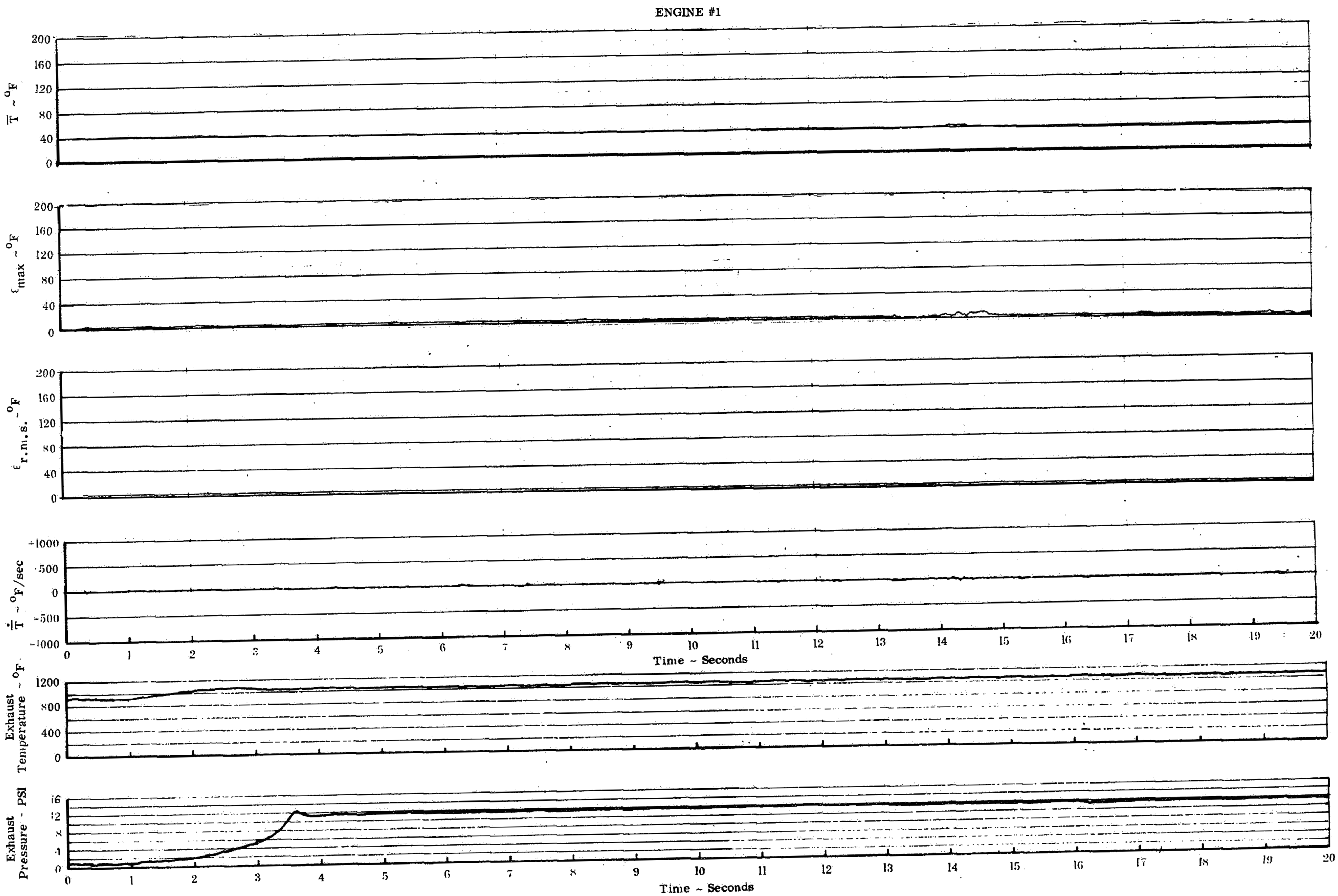

FIGURE A32-1. EXHAUST CONDITIONS AND INGESTION CHARACTERISTICS

Test 32

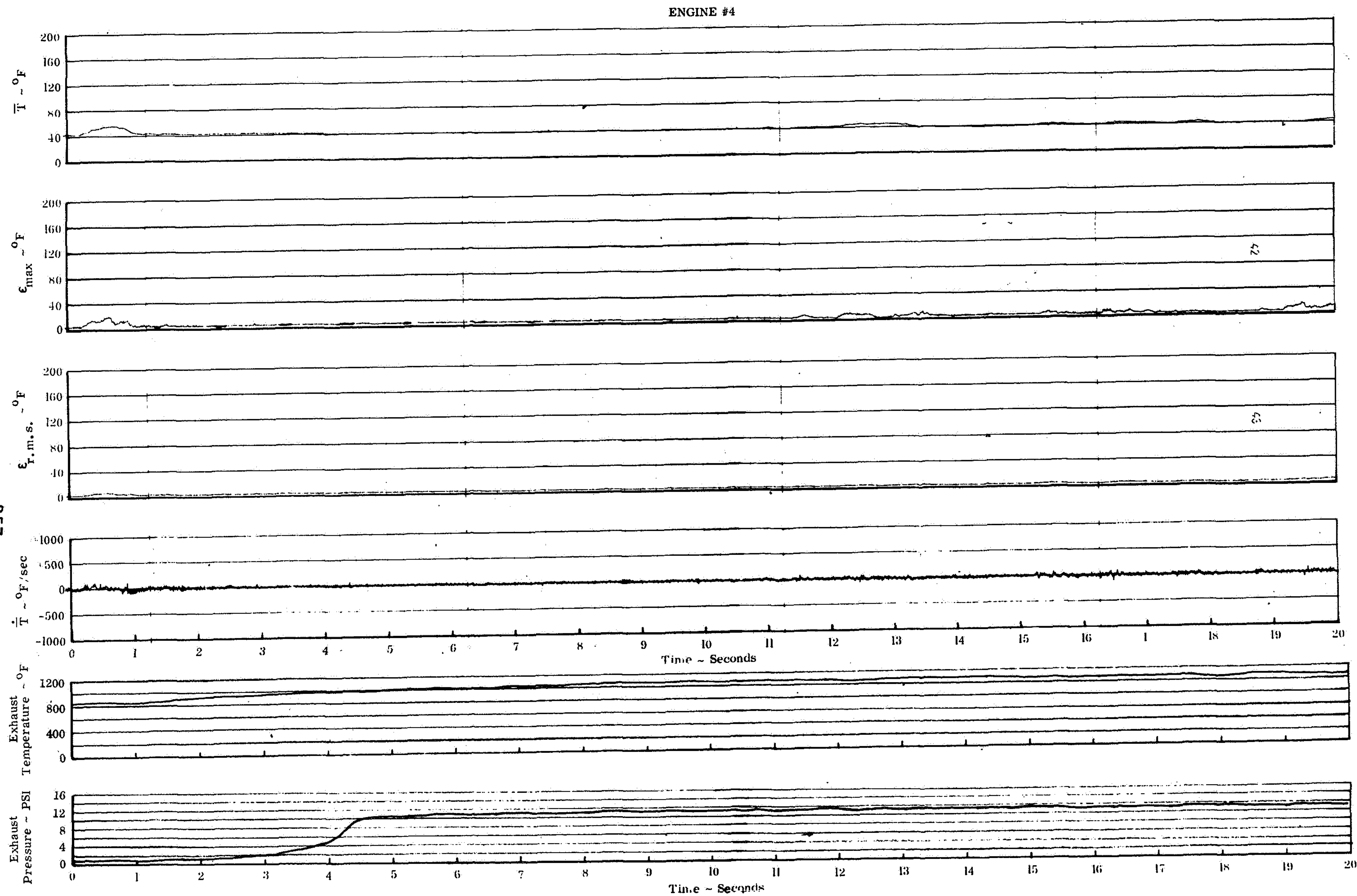

FIGURE A32-2. EXHAUST CONDITIONS AND INGESTION CHARACTERISTICS

Test 32

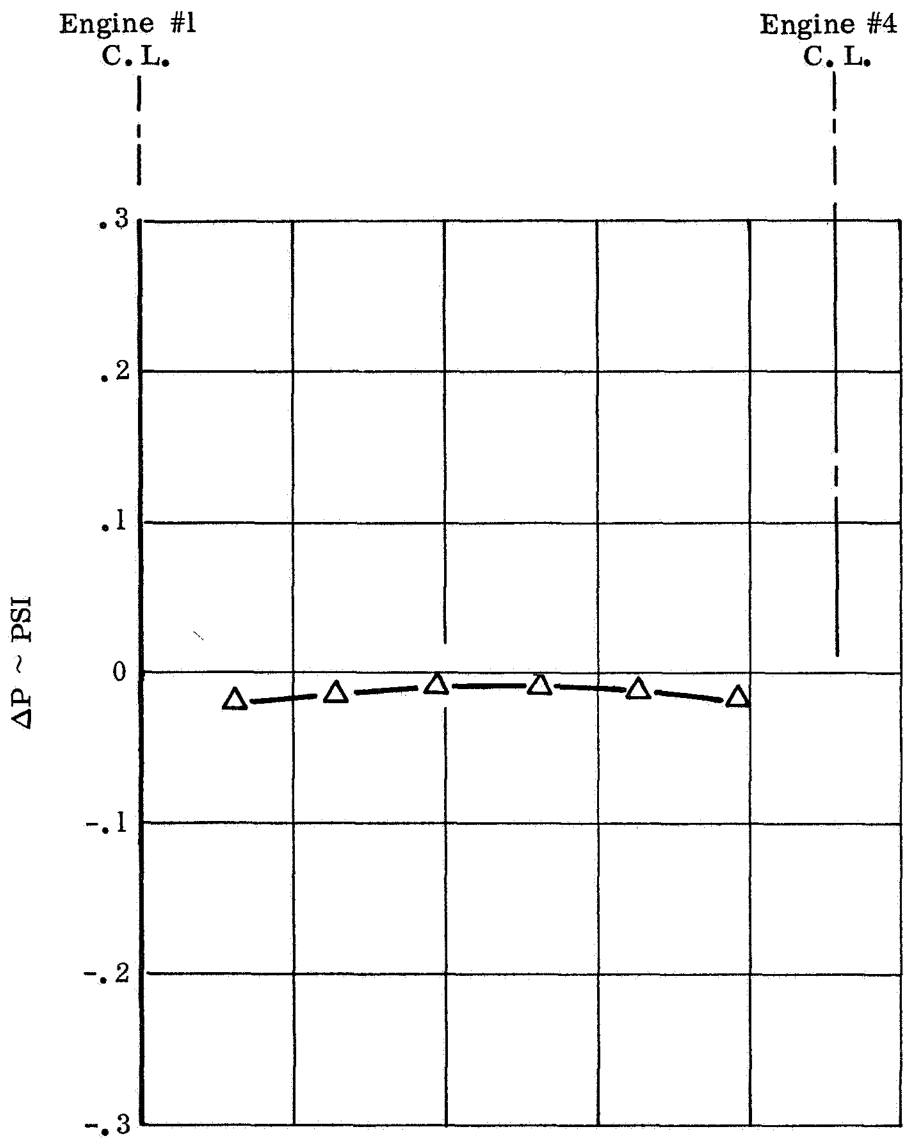

FIGURE A32-3. POD UNDERSURFACE PRESSURE DISTRIBUTION

Report Distribution List

Contract NAS3-10498

			Number of Copies
1. NASA-Lewis Research Center 21000 Brookpark Road Cleveland, OH 44135			
Attention:	Report Control Office	MS5-5	1
	Technical Utilization Office	MS3-19	1
	Library	MS60-3	2
	Special Projects Division	MS302-1	1
	VTOL Branch	MS54-4	6
	L. Crotser	MS100-1	1
	S. Lieblein	MS54-4	1
	N. Clough	MS100-1	3
	L. Macioce	MS60-6	1
	J. H. Diedrich	MS54-4	1
	John H. DeFord	MS77-3	1
2. NASA Scientific and Technical Information Facility P.O. Box 33 College Park, MD 20740			
Attention:	NASA Representative RQT-2448		6
3. FAA Headquarters 800 Independence Avenue, SW Washington, DC 20553			
Attention:	Brig. General J. C. Maxwell		1
	F. B. Howard		1
4. NASA Headquarters Washington, DC 20548			
Attention:	N. F. Rekos (RAP)		1
5. U.S. Army Aviation Materiel Laboraties Fort Eustis, VA 23604			
Attention:	John White		1
6. Headquarters Wright-Patterson Air Force Base, OH 45433			
Attention:	D. Hohler		1
	G. Sealy		1
	R. Krabale		1
	Z. Gershon		1
	Lt. V. K. Smith III		1
	R. Jefferies		1
	R. Hirt		1
7. Department of the Navy Bureau of Weapons Washington, DC 20525			
Attention:	Robert Brown, RAPPI4		1

		Number of Copies
8.	Department of the Navy Bureau of Ships Washington, DC 20360 Attention: G. L. Graves	1
9.	NASA Langley Research Center Hampton, VA 23365 Attention: Library	1
	R. Kuhn	1
	H. C. McLemore	1
	A. D. Hammond	1
10.	NASA Ames Research Center Moffett Field, CA 94040 Attention: Library	1
	W. H. Tolhurst	1
	M. W. Kelly	1
11.	Bell Aerosystems Company Buffalo, NY 14240 Attention: R. F. Speth	1
	P. E. Ryan	1
12.	Lockheed-Georgia Company 86 South Cobb Drive Marietta, GA 30060 Attention: T. W. Tatem	1
	A. Harris	1
13.	North American Aviation, Incorporated International Airport Los Angeles, CA 90009 Attention: Rex Carpenter	1
14.	Pratt & Whitney Aircraft 400 Main Street East Hartford, CT 06108 Attention: W. Sens	1
15.	General Electric Company Flight Propulsion Division Cincinnati, OH 45215 Attention: Jack Klapproth	1
16.	General Electric Company 1000 Western Avenue Lynn, MA 01906 Attention: Klem Gunn	1
17.	Allison Division of General Motors P. O. Box 894 Indianapolis, IN 46206 Attention: C. E. Hockert	1

		Number of Copies
18.	The Boeing Company Commercial Airplane Division P. O. Box 707 Renton, WA 98055 Attention: Walter Swann	1
19.	The Boeing Company Vertol Division Morton, PA 19070 Attention: Bernard L. Fry	1
20.	McDonnell Douglas Box 516 St. Louis, MO 63166 Attention: Ralph Herzmark	1
21.	McDonnell Douglas Aircraft Division 3855 Lakewood Blvd. Long Beach, CA 90808 Attention: W. J. Skillman	1
22.	Lockheed-California Burbank, CA 91503 Attention: Richard Shearer	1
23.	Ryan Aeronautical Company 2701 Harbor Drive San Diego, CA 92101 Attention: John B. Bain	1
24.	Ling-Tempco-Vought Incorporated Dallas, TX 75221 Attention: K. R. Marsh	1
25.	Fairchild Hiller Republic Aviation Division Farmingdale, Long Island, NY 11735 Attention: G. Rosenthal	1